

ISSP

**ACTIVITY
REPORT
OF
SYNCHROTRON
RADIATION
LABORATORY**

2019

© 2020 *The Institute for Solid State Physics, The University of Tokyo*

Activity Report 2019

TABLE OF CONTENTS

pp

7	Preface :	Yoshihisa Harada
8	1	Status of Beamline BL07LSU at the SPring-8
11	2	Status of spin-and angle-resolved photoelectron spectroscopy with laser light at LASOR
13	3	Workshop & Meetings
15	4	Seminar
	5	Activities

Synchrotron Radiation Experiments (SPring-8)

16	1)	SOFT X-RAY EMISSION SPECTROSCOPY STUDY OF A CATHODE MATERIAL FOR LI-ION BATTERIES IN COMBINATION WITH FULL-MULTIPLY CALCULATION Daisuke Asakura, Yusuke Nanba, Eiji Hosono, Hideharu Niwa, Hisao Kiuchi, Jun Miyawaki and Yoshihisa Harada
18	2)	DEVELOPMENT OF ALL-SOLID-STATE LI-ION-BATTERY CELL FOR OPERANDO SOFT X-RAY EMISSION SPECTROSCOPY Daisuke Asakura, Eiji Hosono, Kosuke Yamazoe, Jun Miyawaki and Yoshihisa Harada
20	3)	VERIFICATION OF TWO-CARRIER STATE IN THE CUPRATE SUPERCONDUCTOR $\text{Pr}_{1.4-x}\text{La}_{0.6}\text{Ce}_x\text{CuO}_4$ Kenji Ishii, Shun Asano, Masaki Fujita, Kohei Yamagami, Jun Miyawaki, Yoshihisa Harada
22	4)	SPIN-POLARIZED ELECTRONIC STATE OF SINGLE CRYSTAL Co_2MnSi HEUSLER ALLOY PROBED BY RESONANT INELASTIC SOFT X-RAY SCATTERING (SX-RIXS) IN MAGNETIC FIELD Rie Y. Umetsu, Hidenori Fujiwara, Jun Miyawaki, Kohei Nishimoto, Toshiyuki Kashiuchi, Akira Sekiyama, Akinori Irizawa, Yoshihisa Harada and Shigemasa Suga
24	5)	MULTIORBITAL BOND FORMATION FOR STABLE OXYGEN-REDOX REACTION IN BATTERY ELECTRODES (1) Masashi Okubo
26	6)	MULTIORBITAL BOND FORMATION FOR STABLE OXYGEN-REDOX REACTION IN BATTERY ELECTRODES (2) Masashi Okubo
28	7)	UNDERSTANDING OF SOLVATION AND DESOLVATION STATE OF ACTIVE MATERIALS FOR REDOX-FLOW BATTERIES DERIVED FROM HYDROGEN-BONDING ANALYSIS BY SOFT X-RAY SPECTROSCOPY Akihiro Ohira, Eiji Hosono, Daisuke Asakura, Takashi Funaki, Kosuke Yamazoe, Jun Miyawaki, Yoshihisa Harada
30	8)	PHOTOEXCITED CARRIER DYNAMICS IN LEAD SULFIDE QUANTUM DOT PHOTOVOLTAIC CELL Kenichi Ozawa, Susumu Yamamoto, Iwao Matsuda
32	9)	Photo-induced valence transition dynamics of SmS studied by time-resolved x-ray absorption spectroscopy

H. Watanabe, T. Nakamura, Y. Shibata, K. Yamagami, Y. Hirata, K. Ikeda, Y. Zhang, H. Wadati, K. Imura, H. S. Suzuki, N. K. Sato, S. Kimura

- 34 10) **Relaxation dynamics of Photo-induced valence transition of SmS studied by time-resolved x-ray absorption spectroscopy**
H. Watanabe, T. Nakamura, Y. Shibata, K. Yamagami, Y. Hirata, K. Ikeda, Y. Zhang, H. Wadati, K. Imura, H. S. Suzuki, N. K. Sato, S. Kimura
- 36 11) **LOW-TEMPERATURE METHANE OXIDATIVE COUPLING ON MODIFIED PD MODEL CATALYSTS STUDIED BY *OPERANDO* AMBIENT-PRESSURE XPS**
Takanori Koitaya, Susumu Yamamoto, Iwao Matsuda, Jun Yoshinobu and Toshihiko Yokoyama
- 38 12) **X-ray Spectral Imaging Analysis of Interface States at p^+ -WSe₂/n-MoS₂ Hetero Junctions in TFET Device Structure**
Naoka Nagamura, Keigo Nakamura, Hayami Kawamoto, Naoki Higashitarumi, Keishi Akada, and Kosuke Nagashio
- 40 13) **SOFT X-RAY ADSORPTION AND EMISSION SPECTROSCOPY OF THE INTERMEDIATE WATER IN BIOCOMPATIBLE POLYMERS**
Shin-nosuke Nishimura, Keishi Akada, Daiki Murakami, Kosuke Yamazoe, Tomoya Ueda, Jun Miyawaki, Yoshihisa Harada, Masaru Tanaka
- 42 14) **DEVELOPMENT OF TIME-RESOLVED X-RAY PHOTOELECTRON DIFFRACTION FOR THE OBSERVATION OF THE STRUCTURAL DYNAMICS OF EPITAXIAL SILICENE**
Kouichi Hayashi, Artoni Kevin R. Ang, Koji Kimura, Yuichiro Fukatsu, Susumu Yamamoto, Iwao Matsuda, Takahiro Yonezawa, Antoine Fleurence, Yukiko Yamada-Takamura
- 44 15) **TIME-RESOLVED X-RAY PHOTOELECTRON DIFFRACTION STUDY OF EPITAXIAL SILICENE**
Kouichi Hayashi, Artoni Kevin R. Ang, Koji Kimura, Yuichiro Fukatsu, Susumu Yamamoto, Iwao Matsuda, Takahiro Yonezawa, Antoine Fleurence, Yukiko Yamada-Takamura
- 46 16) **ELECTRIC STRUCTURE OF WATER IN THE VICINITY OF MODEL ORGANIC SURFACES BY X-RAY EMISSION SPECTROSCOPY**
Tomohiro Hayashi
- 48 17) **MEASUREMENT OF THE THICKNESS DEPENDENCE OF THE MAGNET-OPTICAL CONSTANTS OF METAL FE USING FAST POLARIZATION SWITCHING**
Yasuyuki Hirata, Keisuke Ikeda, Kohei Yamagami, Yujun Zhang, Hiroki Wadati, Souliman El Moussaoui, Iwao Matsuda
- 50 18) **Creation of multi-dimensional operando photoelectron spectroscopy (I) Selection of industry-government-academia collaborative model sample**
Hirokazu Fukidome, Takamasa Kamogawa, Naoka Nagamura, Masaharu Oshima, Masato Kotsugi, and Issei Watanabe
- 52 19) **OPERAND MEASUREMENT OF ALL SOLID-STATE LI-ION BATTERYS BY PHOTOELECTRON MICROSPECTROSCOPY**
Eiji Hosono, Wenxiong Zhang, Daisuke Asakura, Naoka Nagamura, Masaharu Oshima, Yoshihisa Harada
- 54 20) **MAPPING MEASUREMENT OF SINGLE CRYSTALLINE LITHIUM METAL OXIDE BY ALL SOLID-STATE LI-ION BATTERYS**
Eiji Hosono, Wenxiong Zhang, Daisuke Asakura, Naoka Nagamura, Masaharu Oshima, Yoshihisa Harada

- 56 21) **Resonant inelastic soft x-ray diffraction of nanoparticles**
J. Miyawaki, T. Yachi, S. Maki, K. Kanie, Y. Harada
- 58 22) **Development of X-ray Polarization Precession Spectroscopy**
J. Miyawaki, Y. Hirata, K. Yamagami, I. Matsuda, Y. Harada
- 60 23) **Resonant Inelastic Soft X-ray Scattering of $Y_3Fe_5O_{12}$**
J. Miyawaki, Y. Harada
- 62 24) **Development of Coherent Soft X-ray Diffraction Imaging Technique for Observation of Ultra-fast Magnetic Dynamics**
Yuichi Yamasaki, Kohei Yamamoto, Yuichi Yokoyama, Yasuyuki Hirata, Hiroki Wadati, and Taka-hisa Arima
- 64 25) **REVERSIBLE AND IRREVERSIBLE ANIONIC REDOX FOR HIGH-CAPACITY BATTERY MATERIALS**
Naoaki Yabuuchi and Daisuke Asakura
- 66 26) **ELECTRONIC STATE OF INTERMEDIATE WATER IN BIOCOMPATIBLE POLYMERS INVESTIGATED BY XAS AND XES**
Koichi Ozaki, Jumpei Yahiro, Masaru Nakada, Masahiro Kunisu, Kosuke Yamazoe, Jun Miyawaki and Yoshihisa Harada
- 68 27) **Present status of the development of time-resolved ambient pressure X-ray photoelectron spectroscopy system at SPring-8 BL07LSU**
Susumu Yamamoto and Iwao Matsuda
- 70 28) **Development of time-resolved X-ray absorption and photoelectron spectroscopy system using time-of-flight electron analyzer**
Susumu Yamamoto, Rei Hobaru, Kenichi Ozawa and Iwao Matsuda
- 72 29) **SOFT X-RAY ABSORPTION SPECTROSCOPY OF Ca_2RuO_4 UNDER ELECTRIC FIELD**
Daiki Ootsuki, Yukie Takasuka, Ayuko Hishikawa, Tatsuhiro Ishida, Teppei Yoshida, Kosuke Yamazoe, Tomoyuki Tsukada, Jun Miyawaki, Yoshihisa Harada, Chanchal Sow, Shingo Yonezawa, Yoshiteru Maeno and Fumihiko Nakamura
- 74 30) **OPERANDO XPS STUDY OF CO_2 HYDROGENATION ON A SINGLE-ATOM ALLOY Pd-Cu MODEL CATALYST**
J. Yoshinobu, S. Tanaka, K. Mukai, W. Osada, T. Matsuda, S. Nakano, Y. Choi, S. Yamamoto and I. Matsuda
- 76 31) **AP-XPS STUDY OF ELECTRONIC STATES OF METAL NANO PARTICLES AND METAL HYDRIDE COMPLEX**
J. Yoshinobu, W. Osada, Y. Choi, S. Tanaka, K. Mukai, T. Koitaya, S. Yamamoto and I. Matsuda
- 78 32) **DYNAMICS OF PHOTOCATALYTIC MATERIALS FOR WATER SPLITTING REACTION STUDIED BY TRANSIENT X-RAY ABSORPTION SPECTROSCOPY**
Yohei Uemura, Ahmed Ismail, Hebatalla Elnaggar, Federica Frati, Hiroki Wadati, Yasuyuki Hirata, Yujun Zhang, Kohei Yamagami, Susumu Yamamoto, Iwao Matsuda, Frank de Groot
- 80 33) **INVESTIGATION OF THE ELECTRONIC STRUCTURE OF COBALT OXIDE SPINEL ON ELECTRODES FOR WATER OXIDATION CATALYSTS USING CO 2P3D RIXS**

- 82 34) **INVESTIGATION OF THE ELECTRONIC STRUCTURE OF ELECTRODEPOSITED COBALT OXIDE FILMS ON ELECTRODES FOR WATER OXIDATION CATALYSTS USING CO 2P3D RIXS**

Minmin Chen, Kosuke Yamazoe, Jun Miyawaki, Yoshihisa Harada, Serena DeBeer, Olaf Rüdiger

Experiments at E-Labo

- 84 1) **SPIN-POLARIZED SURFACE STATES ON MAX PHASE COMPOUND V_2AlC**
Takahiro Ito, Masashi Ikemoto, Damir Pinek, Koichiro Yaji, Shik Shin and Thierry Ouisse
- 86 2) **ABSENCE OF HYBRIDIZATION BETWEEN SPIN-POLARIZED BANDS IN QUASI-ONE-DIMENSIONAL GIANT RASHBA SYSTEM $Bi/InAs(110)-(2 \times 1)$**
Takuto Nakamura, Yoshiyuki Ohtsubo, Ayumi Harasawa, Koichiro Yaji, Shik Shin, Fumio Komori, Shin-ichi Kimura
- 88 3) **TOPOLOGICAL SURFACE STATE MODIFIED BY ADSORPTION OF ORGANIC DONOR MOLECULE**
Tatsuya Kitazawa, Koichiro Yaji, Kosuke Shimozawa, Hiroshi Kondo, Takayoshi Yamanaka, Hiroshi Yaguchi, Yukiaki Ishida, Kenta Kuroda, Ayumi Harasawa, Takashi Iwahashi, Yukio Ouchi, Fumio Komori, Shik Shin and Kaname Kanai
- 90 4) **INVESTIGATION OF TOPOLOGICAL PROPERTIES IN SUPERCONDUCTING $TaSe_3$**
Chun Lin, Ryo Noguchi, Kenta Kuroda, Koichiro Yaji, Ayumi Harasawa, Shik Shin, Atsushi Nomura, Masahito Sakoda, Masakatsu Tsubota, Satoshi Tanda and Takeshi Kondo
- 92 5) **ANGLE- AND SPIN-RESOLVED PHOTOEMISSION SPECTROSCOPY RESEARCH ON TYPE-II WEYL SEMIMETAL WTe_2**
Yuxuan Wan, Lihai Wang, Keisuke Koshiishi, Masahiro Suzuki, Peng Zhang, Jaewook Kim, Kenta Kuroda, Koichiro Yaji, Ryo Noguchi, Ayumi Harasawa, Shik Shin, Atsushi Fujimori, Sang-Wook Cheong, Takeshi Kondo
- 94 6) **DEVELOPMENT OF TIME-, SPIN- AND ANGLE-RESOLVED PHOTOEMISSION SPECTROSCOPY MACHINE AT ISSP**
K. Kawaguchi, K. Kuroda, Z. Zhao, A. Harasawa, K. Yaji, R. Noguchi, S. Tani, M. Fujisawa, S. Shin, F. Komori, Y. Kobayashi, T. Kondo
- 96 7) **THE WEAK TOPOLOGICAL INSULATOR STATE IN $ZrTe_5$**
Peng Zhang, Ryo Noguchi, Kenta Kuroda, Chun Lin, Kaishu Kawaguchi, Koichiro Yaji, Ayumi Harasawa, Simin Nie, Hongming Weng, V. Kandyba, A. Giampietri, A. Barinov, Qiang Li, G.D. Gu, Shik Shin and Takeshi Kondo
- 98 8) **Observation of spin polarized surface states in polar Weyl semimetal T_d-MoTe_2**
M. Sakano, Y. Tanaka, M. S. Bahramy, H. Takahashi, K. Kuroda, A. Harasawa, K. Yaji, S. Shin, S. Ishiwata, K. Ishizaka
- 100 9) **SARPES STUDY OF A Pb ATOMIC LAYER ON $Ge(111)$**
Koichiro Yaji and Fumio Komori
- 102 10) **HIGH-RESOLUTION SPIN-RESOLVED ELECTRONIC STRUCTURE OF TOPOLOGICAL HEAVY-FERMION MATERIALS**
Andrés F. Santander-Syro, Franck Fortuna, Maximilian Thees, Cris Adriano

103	11)	Study of spin structure in domain-regulated alloy of atomic layer Ting-Yu Chen, Li-Cheun Yang, Santosh Chiniwar, H. -T. Jeng, Woei Wu Pai, S. -J. Tang
106	12)	Spin resolved ARPES on interfacial electronic states of Bi/NbSe₂ R. Stania, H. Jung, H.W. Yeom
108	13)	HIGH-RESOLUTION SPIN- AND ANGLE-RESOLVED PHOTOEMISSION SPECTROSCOPY ON DOPED MAGNETIC TOPOLOGICAL INSULATORS Keisuke Fukutani, Chandan De, Roland Stania, Koichiro Yaji, Kenta Kuroda, Jaeyoung Kim and Han-Woong Yeom
110		Half-metallicity of the ferrimagnet Mn₂VAl revealed by resonant inelastic soft x-ray scattering in a magnetic field R.Y. Umetsu, H. Fujiwara, K. Nagai, Y. Nakatani, M. Kawada, A. Sekiyama, F. Kuroda, H. Fujii, T. Oguchi, Y. Harada, J. Miyawaki, and S. Suga PHYSICAL REVIEW B 99, 134414 (2019)
120		Influence of interface dipole layers on the performance of graphene field effect transistors Naoka Nagamura, Hirokazu Fukidome, Kosuke Nagashio, Koji Horiba, Takayuki Ide, Kazutoshi Funakubo, Keiichiro Tashima, Akira Toriumi, Maki Suemitsu, Karsten Horn, Masaharu Oshima Carbon 152 (2019) 680-687
128		Spectrum adapted expectation-maximization algorithm for high-throughput peak shift analysis Tarojiro Matsumura, Naoka Nagamura, Shotaro Akaho, Kenji Nagata, Yasunobu Ando SCIENCE AND TECHNOLOGY OF ADVANCED MATERIALS (2019), VOL. 20, NO. 1, 733–745
142	6	Staff
143	7	Publication List

Preface

The Synchrotron Radiation Laboratory (SRL) of the Institute for Solid State Physics (ISSP) has been cooperating with the Synchrotron Radiation Research Organization of the University of Tokyo since 2006 to operate the BL07LSU soft X-ray beamline and experimental end-stations in SPring-8. The beamline has a 27-m-long polarization-controlled undulator and a monochromator covering the photon energy range from 250 eV to 2 keV with an average photon flux of 10^{12} photons/sec. As one of the central facilities for promoting advanced materials science and development of unique spectroscopic methods in the soft X-ray region, the SRL fully opened the beamline to public users in 2009. Since then, the SRL staff members have played an essential role in promoting both domestic and international joint researches. Four end-stations, i.e. time-resolved photoelectron spectroscopy, ambient pressure X-ray photoelectron spectroscopy, three dimensional nanoESCA, and high-resolution soft X-ray emission spectroscopy stations, have excellent time resolution (~ 50 ps), high pressure (~ 20 mbar), spatial resolution (~ 70 nm), and energy resolution ($E/\Delta E \approx 10,000$), respectively. They have been installed in the beamline to accept joint-research proposals, while a free-port station equipped with a focusing mirror is available to outside users.

In 2018, the Japanese government has decided to construct a next generation synchrotron radiation facility dedicated to the soft and tender x-ray regions in Sendai. SRL has also decided to make a significant commitment and will gradually transfer the techniques cultivated in SPring-8 to the new synchrotron facility.

In addition to the cutting-edge activities using synchrotron radiation, SRL joined the Laser and Synchrotron Research (LASOR) Center as a member in 2012. Since then, SRL has promoted the scientific use of high-harmonic generation by lasers in the vacuum ultraviolet and soft X-ray regions at the Kashiwa Campus. In 2014, SRL constructed a new high-resolution laser spin- and angle-resolved photoelectron spectroscopy (SARPES) apparatus that is designed to provide high-energy (1.7 meV) and -angular resolutions with high-efficiency spin detectors for various types of solids, such as spin-orbit coupled materials and ferromagnetic materials. Since 2015, the SARPES system has been open for users and accepting joint-research proposals.

Our goal is to provide users with a platform that uses both synchrotron radiation and high-harmonic generation by lasers by strong collaboration with other LASOR group members.

June 30, 2020

Yoshihisa Harada
Director of SRL-ISSP

1. Status of Beamline BL07LSU at SPring-8

The University-of-Tokyo high-brilliance synchrotron soft X-ray outstation beamline BL07LSU at SPring-8 has been maintained by the permanent staff members with adjuncts for user operations. The scientific aim of the beamline is to promote advanced spectroscopy for solid state and soft (including bio-) materials. There are four regular endstations for time-resolved soft X-ray spectroscopy (TR-SX spectroscopy), ambient pressure X-ray photoelectron spectroscopy, 3D-scanning photoelectron microscope (3D nano-ESCA) and high-resolution soft X-ray emission spectroscopy (HORNET) that are open for users. There is also a free port station for users who bring their own experimental apparatus.

The beamline BL07LSU is equipped with a segmented cross-type undulator. By using phase shifter among the undulator segments, a polarization control of soft X-ray was started since 2016. Circularly and linearly polarized soft X-rays at full energy range (250 – 2000 eV) have been available by tuning the permanent magnet type phase shifter.

At the endstations, various scientific researches were carried out by both the laboratory staffs and general users (G-type and S-type applications). In addition, from this fiscal year, we started to accept priority issues (P type problem) for the purposes of utilizing the advanced synchrotron radiation light source technology, especially high-speed polarization switching, at BL07LSU and of promoting developments of the beamline and endstation technologies for the next generation synchrotron light source.

Recent activities at each station is briefly introduced below.

(1) Time-Resolved soft X-ray spectroscopy station (TR-SX spectroscopy)

The station is to perform time-resolved photoemission spectroscopy experiments by synchronizing the high-brilliant soft X-ray and the ultra-short laser pulses. A two-dimensional angle-resolved time-of-flight (ARTOF) analyzer has been equipped for the efficient time-resolved measurements and the measurement temperature can be controlled from 15 K to 1150K. The station adopts two different optical laser systems synchronized with synchrotron soft X-ray; low repetition rate and high pulse energy (1 kHz, mJ) and high repetition rate and low pulse energy (208 kHz, μ J).

In 2019, Hayashi group succeeded in observing the temporal variation of the Si $2p$ photoelectron diffraction pattern of a silicene layer after the laser pulse irradiation. The time-resolved pattern agreed with the simulation results and revealed the lattice dynamics. The research paper is submitted as the world's first time-resolved photoelectron diffraction data. The system of time-resolved photoelectron spectroscopy will be transferred to Kashiwa Campus in 2020 for experiments with the vacuum ultraviolet/soft

X-ray lasers. The time-resolved photoemission measurement will be continued users with the AP-XPS system, see the following section, that has been updated for this purpose recently.

(2) Ambient-pressure X-ray photoelectron spectroscopy (AP-XPS)

AP-XPS station allows *Operando* observation of catalysts under reaction conditions. The AP-XPS station was constructed in 2014 by an external funding (JST ACT-C project), and was opened to external users since 2018. The AP-XPS system is equipped with a differentially pumped electron analyzer (SPECS, PHOIBOS 150 NAP) and an ambient-pressure gas cell. XPS measurements can be performed both under ultrahigh vacuum and in near-ambient gas pressure up to 20 mbar. Catalytic activity is monitored by mass spectrometer, and simultaneous evaluation of adsorbate and catalyst electronic states is performed. In addition to the experiments using synchrotron soft X-ray, off-line experiments using a twin-anode X-ray source can be performed.

In 2019, a variety of research projects have been conducted using the AP-XPS station: (i) Methanol synthesis on Cu-Zn catalysts, (ii) Sabatier reaction on Ni catalysts, (iii) H₂ adsorption/absorption in Pd nanoparticles and Pd alloys (PdAg and PdCu), (iv) CH₄ partial oxidation on Pd catalysts, (v) CO₂ adsorption on graphene support, (vi) band alignment at a semiconductor photoelectrode and electrolyte interface, and (vii) development of time-resolved AP-XPS. Koitaya *et al.* published a research paper on CO₂ hydrogenation on a Zn modified Cu surface in ACS Catalysis (IF 11.384). Tang *et al* reported *articles* on H₂ adsorption and storage on a PdCu alloy surface in Appl. Surf. Sci.

(3) 3D-scanning photoelectron microscope (3D nano-ESCA)

3D-nano-ESCA can be used for sub-100 nm range microscopic 2D mapping and depth profile of the chemical structure of functional materials and devices.

In 2019, elucidation of facet-wise Li de-insertion characteristics of LTO in all-solid-state LIB was carried out as a joint research by Asakura and Hosono group at AIST. By changing the solid electrolyte from LLZ and dry polymer to sulfide solid electrolyte, the degas rate was reduced, and a clearer image was obtained. Also conducted was photoelectron spectromicroscopy of SnS as a joint research by Nagamura at NIMS and Prof. Nagashio group at UTokyo. The reason behind the monolayer growth of SnS by the simple PVD remains unclear. A single SnS film was not grown from high-purity SnS powder. By nano-ESCA observation, it is confirmed that the lateral growth of monolayer SnS is facilitated due to the enhanced surface diffusion of SnS precursor molecules by Sn₂S₃ contaminants in low-purity powder. Lastly, super-resolution imaging and depth profiling analysis of hetero-junction transistor fine structures using III-V compound

semiconductors were performed as a joint research by Fukidome group at Tohoku Univ. In the viewpoint of measurement informatics, sparse modeling approach is applied to overcome the limits of spatial resolution and make it possible to observe objects in the size of several nms.

(4) Ultra high-resolution soft X-ray emission spectroscopy (HORNET)

The station is dedicated for soft X-ray emission (or resonant inelastic X-ray scattering: RIXS) spectroscopy measurements with high-resolution ($E/\Delta E > 10,000$) and under various environmental conditions (gas, liquid, and solid).

In 2019 the station accepted 19 joint researches. Studies on solid state physics include i) O K-edge RIXS of holes doped in $\text{Pr}_{1.4-x}\text{La}_{0.6}\text{Ce}_x\text{CuO}_4$, ii) Observation of magnon-induced state of spintronics material $\text{Y}_3\text{Fe}_5\text{O}_{12}$ by operando RIXS by application of high-frequency electromagnetic wave, iii) XAS and RIXS studies of the electric-field-induced metal insulator transition of $\text{Ca}_3(\text{Ru}_{1-x}\text{Ti}_x)_2\text{O}_7$, iv) Fe L-edge RIXS of diluted magnetic semiconductors (Ga, Fe)Sb and (In, Fe)As. For the battery and catalyst materials, the valence state of Li-ion battery electrode materials $\text{LiMn}_{1-x}\text{Fe}_x\text{PO}_4$ and $\text{Li}(\text{Li}_{2/3}, \text{Mn}_{4/3})\text{O}_4$ during charge and discharge as well as water decomposition catalyst $\text{Co}_x\text{Fe}_y\text{O}_4$ were observed by operando RIXS. For the studies on the behavior of interfacial water, water hydrating thermo-responsive polymer PNIPAM, polyvinyl alcohol aqueous solution, water confined in a subnanopore of liquid crystalline membrane, interfacial water in the polymer-brush form of PBuA and PMEA were observed. All the measurements were successful in the determination of specific hydrogen bond structure of water responsible for materials functions such as phase transition, folding, ice nucleation process, water filtration, and biocompatibility.

Status of spin- and angle-resolved photoelectron spectroscopy with laser light at Laser and Synchrotron Research Laboratory

Spin- and angle-resolved photoelectron spectroscopy (SARPES) is a powerful technique to investigate the spin-dependent electronic states in solids. This has been used for studying exchange splitting of ferromagnetic materials over 50 years. Recently, spin textures have been intensively studied in strongly spin-orbit coupled materials, such as Rashba spin-split systems and topological insulators. We have been developing a SARPES apparatus using vacuum-ultraviolet (VUV) lasers at Laser and Synchrotron Research Laboratory in the Institute for Solid State Physics, named LOBSTER (Laser-Optics-Based Spin-vecTor Experimental Research) machine. The LOBSTER machine is currently utilized to obtain precise information on spin-dependent electronic structures near the Fermi level in solids. We started a project to construct the LOBSTER machine from FY 2014 and joint researches at this station have started from FY2015.

Figure 1 represents an overview of the LOBSTER machine [1]. The apparatus consists of an analysis chamber, a carousel sample-bank chamber connected to a load-lock chamber, and a molecular beam epitaxy (MBE) chamber, which are kept in an ultra-high vacuum (UHV) environment and are connected with each other via UHV gate valves. The hemispherical electron analyzer is a

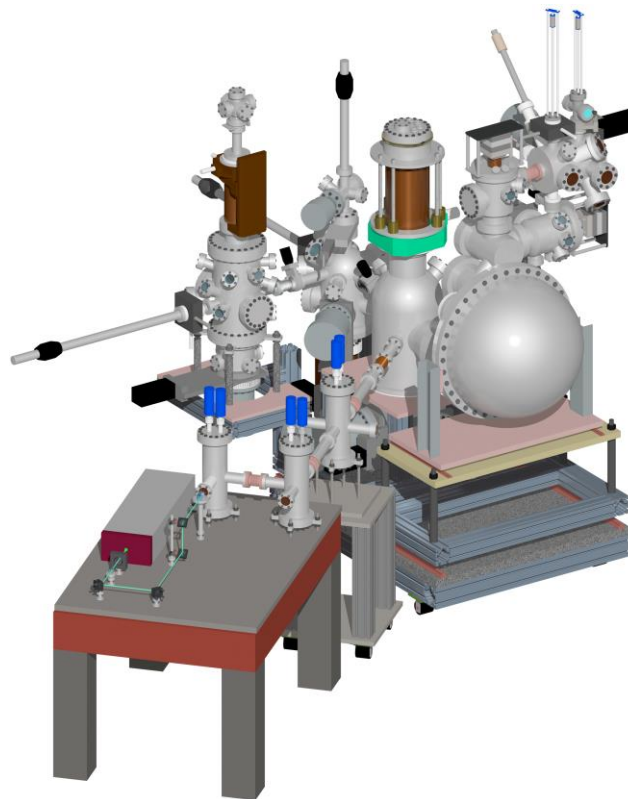


Fig. 1. Overview of the LOBSTER machine developed at the Laser and Synchrotron Research Laboratory at the Institute for Solid State Physics [1].

custom-made ScientaOmicron DA30-L, modified to attach the very-low-energy-electron-diffraction type spin detectors. The electrons are currently excited by 6.994-eV photons, yielded by 6th harmonic of a Nd:YVO₄ quasi-continuous wave laser with repetition rate of 120 MHz. A helium discharge lamp (VG Scienta, VUV5000) is also available as a photon source. At the MBE chamber, samples can be heated by a direct current heating or electron bombardment. The surface evaluating and preparing instruments, such as evaporators, low energy electron diffraction, sputter-gun and quartz microbalance, can be installed. At the carousel chamber, 16 samples can be stocked in the UHV environment.

In FY2019, eleven research proposals from outside of the institute were accepted and conducted. Spin-polarized states were investigated in both bulk and surface of various topological materials including magnetic and superconducting ones, atomic layers, and ferromagnetic compounds. For extending the use of laser-SARPES to time-resolved study, we have been developing a new laser beamline of 10.7 eV femtosecond laser pulses based on the Yb-doped fiber with the high repetition rate (1 MHz) [2].

References

- [1] K. Yaji, A. Harasawa, K. Kuroda, S. Toyohisa, M. Nakayama, Y. Ishida, A. Fukushima, S. Watanabe, C.-T. Chen, F. Komori and S. Shin, *Rev. Sci. Instrum.* **87**, 053111 (2016).
- [2] Z. Zhao and Y. Kobayashi., *Opt. Exp.* **25**, 13517 (2017).

3. Workshops & Meetings

ISSP workshop: *Innovations to the Next-Generation Synchrotron Radiation*

Date: 2020/2/14(Fri)

Place: Lecture Room (A632), 6th Floor, ISSP, The University of Tokyo

Program:

10:30- **Address**

Hatsumi Mori (ISSP, The University of Tokyo)

10:35- **Conceptual design of public beamlines at the next generation synchrotron facility**

Takahasi Masamitsu (National Institutes for Quantum and Radiological Science and Technology)

11:05- **Overview of the partner beamlines design in the next generation synchrotron radiation facility**

Tetsuya Nakamura (Tohoku University, PhoSIC)

11:35- **Poster short presentation**

12:00- **lunch**

13:00- **Poster session**

14:15- **AI-Robot-driven inorganic materials research**

Ryota Shimizu (Tokyo Institute of Technology, JST-PRESTO)

14:45- **Expanding Availability of Spectromicroscopy by Informatics**

Naoka Nagamura (National Institute for Materials Science, JST-PRESTO)

15:15- **Soft X-ray Focusing using Ellipsoidal mirrors**

Hiroto Motoyama (Center for Ultrafast Intense Laser Science, School of Science, The University of Tokyo)

15:45- **Coffee Break**

16:00- **Operando spectroscopic studies of heterogeneous catalysts by soft X-ray ambient-pressure XPS**

Takanori Koitaya (Institute for Molecular Science, JST-PRESTO)

16:30- **Challenges towards Ultrahigh Resolution Resonant Inelastic Soft X-ray Scattering**

Jun Miyawaki (ISSP, The University of Tokyo)

17:00- **High-Brilliance Soft-X-Ray Beamline for Magnetic and Spintronic Materials Science**

Tetsuro Ueno (National Institutes for Quantum and Radiological Science and Technology)

17:30- **Closing Address**

Takahisa Arima (SRRO, The University of Tokyo)

A plan for the next-generation synchrotron radiation facility was launched in Japan and the user-experiments are expected from 2023. Ten beamlines are planned by the Photon Science Innovation Center (PhoSIC) and the National Institutes for Quantum and Radiological Science and Technology (QST). There have been vigorous discussions on experimental methods for the individual beamlines that are expected to innovate our science and technology, including novel X-ray optics, advanced measurements, informatics analyses and automatic controls by AI robots.

To promote our project toward the new synchrotron radiation facility, we organized this workshop at the ISSP lecture room with broadcast live at SPring-8. It has successfully brought together 91 participants with fruitful discussion on these new technologies and foresights of the coming science. The program started with invite talks by Dr. Tetsuya Nakamura (PhoSIC) and Dr. Masamitsu Takahashi (QST), introducing their beamlines. In the following, there were invited talks by leading young researchers who made presentations on technical innovations for synchrotron radiation. We had a poster session by graduate students and postdocs who shared their new results and actively discussed with each other. Participants were confident to find that our next-generation synchrotron radiation facility would be developed by our next generations.



4. Seminar

Date: August 5, 2019

Title: Prospect of Solid State Physics Research using Coherent Soft X-ray in Next-generation Synchrotron Radiation

Speaker: Dr. Yuichi Yamasaki (National Institute for Materials Science)

Date: August 6, 2019

Title: Spectroscopic study of High- T_c cuprates and ARPES beamline at SSRL

Speaker: Dr. Makoto Hashimoto (SSRL, SLAC National Accelerator Laboratory)

Date: August 21, 2019

Title: State-of-the-art ARPES by third-generation synchrotron light source

Speaker: Dr. Hideaki Iwasawa (Graduate School of Science, Hiroshima University)

Date: September 30, 2019

Title: Novel X-ray Imaging Optics for Coherent X-ray Light Sources

Speaker: Dr. Takashi Kimura (Graduate School of Engineering, The University of Tokyo)

Date: October 11, 2019

Title: Development of hardware and software for observation of material 'in action' by single crystal structure analysis

Speaker: Dr. Manabu Hoshino (Institute of Physical and Chemical Research)

Date: October 16, 2019

Title: Image type multichannel spin polarimeter and related studies

Speaker: Dr. Shan Qiao (Shanghai institute of microsystem and information technology, Chinese academy of sciences, P. R. China)

Date: March 24, 2020

Title: Development of soft X-ray microscope using Wolter mirrors and its future prospects

Speaker: Dr. Satoru Egawa (Graduate School of Engineering, The University of Tokyo)

SOFT X-RAY EMISSION SPECTROSCOPY STUDY OF A CATHODE MATERIAL FOR LI-ION BATTERIES IN COMBINATION WITH FULL-MULTIPLY CALCULATION

Daisuke Asakura^{1,2}, Yusuke Nanba^{1,#}, Eiji Hosono^{1,2}, Hideharu Niwa^{3,4,†}, Hisao Kiuchi^{5,\$}, Jun Miyawaki^{3,4}, and Yoshihisa Harada^{2,3,4}

¹Research Institute for Energy Conservation, National Institute of Advanced Industrial Science and Technology (AIST)

²AIST-UTokyo Advanced Operando-Measurement Technology Open Innovation Laboratory, AIST

³Synchrotron Radiation Laboratory, The Institute for Solid State Physics, The University of Tokyo

⁴Synchrotron Radiation Research Organization, The University of Tokyo

⁵Department of Applied Chemistry, The University of Tokyo

Present affiliations: #Shinshu University, †University of Tsukuba, \$Kyoto University

Enhancement of the energy-density and power-density of electrode materials is one of the important subjects in the research field of Li-ion batteries (LIBs). To improve the performances of electrode materials, the redox mechanisms due to Li-ion extraction/insertion should be clarified. In this study, high-energy-resolution soft x-ray emission spectroscopy (XES) was applied to understand changes in the electronic structure of LiMn₂O₄ cathode [1] by Li-ion extraction/insertion[2]. The Mn *2p-3d-2p* resonant XES spectra were analyzed by the configuration-interaction full-multiplet (CIFM) calculation, which reproduced both *dd* and charge-transfer (CT) excitations.

The LiMn₂O₄ sample was fabricated by a sol-gel method. For electrochemical experiments, LiMn₂O₄ (75 wt%), acetylene black (20 wt%), and polytetrafluoroethylene (5 wt%) were ground into a paste. Lithium metal was used as the counter and reference electrodes, and 1M ethylene carbonate (EC)/diethyl carbonate (DEC) solutions of LiClO₄ were used as electrolytes for a three-electrode beaker cell. We prepared three samples for initial (before charging), charged, and discharged states by constant-current charge-discharge experiments with a current density of 10 mA/g. The corresponding voltages for the three states were 3.2, 4.3 and 3.2 V vs. Li/Li⁺, respectively. Mn *2p-3d-2p* resonant XES measurements for the LiMn₂O₄ samples were carried out at BL07LSU in SPring-8 using a high resolution XES spectrometer, HORNET[3]. The total energy resolution for XES was set to $E/\Delta E = 3200$ at the Mn *L*₃ edge. All the XES measurements were carried out at room temperature in a high vacuum. The CIFM calculation for the electronic-structure analysis of Mn atoms in LiMn₂O₄ was carried out by assuming an octahedral MnO₆ cluster in which the Mn *3d* and O *2p* orbitals and the charge-transfer effect were taken into account[4].

The resonant XES spectra taken with an excitation energy of 642.0 eV corresponding to a Mn *L*₃-edge absorption peak showed drastic changes between the initial and charged states (Fig. 1). The initial state should be attributed to a mixed valence state of Mn³⁺/Mn⁴⁺. For the initial state, all the Mn³⁺ should be oxidized to Mn⁴⁺. For

the discharged state, the Mn ions should partially be reduced to Mn³⁺. Between the initial and discharged state, the small changes of the ratio of Mn³⁺/Mn⁴⁺ was detected by the use of resonant XES.

To confirm the changes and separately understand the Mn³⁺ and Mn⁴⁺ states, we analyzed the XES spectra by using the CIFM calculation (Fig. 2), while the Mn⁴⁺ state was regarded as unchanged during charge-discharge. Both the oxidation states have strong ligand-to-metal CT effect. In particular for the Mn⁴⁺ (charged) state, the CT energy Δ was highly negative, resulting in the dominant $d^4\bar{L}$ and $d^5\bar{L}^2$ charge transfer configurations. The present results

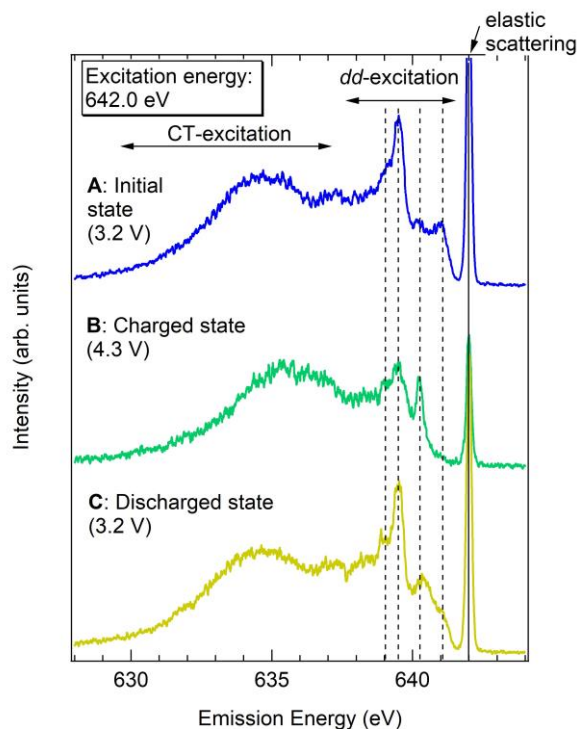


Fig. 1. Mn $2p$ - $3d$ - $2p$ resonant XES spectra for LiMn_2O_4 at the initial, charged and discharged states[2].

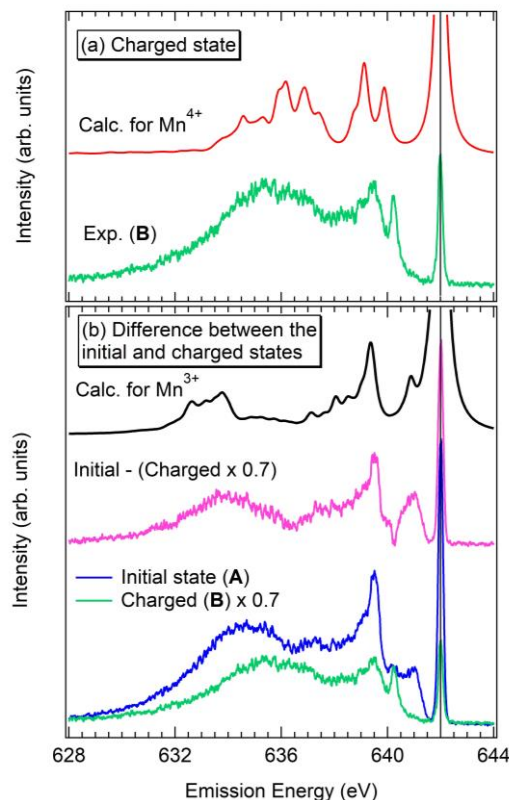


Fig. 2. CIFM calculation for (a) Mn^{4+} with the charged state and (b) Mn^{3+} states with a difference spectrum between the initial and charged states[2].

indicate possible reasons for the capacity fading in LiMn_2O_4 : instability of the crystal-structure during charge-discharge and Jahn-Teller distortion at the Mn^{3+} site.

In summary, we measured Mn $2p$ - $3d$ - $2p$ resonant XES for LiMn_2O_4 . Detailed information of the electronic-structure change such as the strong CT effect was obtained. In the near future, we will perform O $1s$ - $2p$ - $1s$ XES measurement to further understand the redox reaction.

REFERENCES

- [1] For example, M. M. Thackeray, *Prog. Solid State Chem.* **25**, 1 (1997).
- [2] D. Asakura *et al.*, *Phys. Chem. Chem. Phys.* **21**, 18363 (2019).
- [3] Y. Harada *et al.*, *Rev. Sci. Instrum.* **83**, 013116 (2012).
- [4] For example, D. Asakura *et al.*, *J. Phys. Chem. Lett.* **5**, 4008 (2014).

DEVELOPMENT OF ALL-SOLID-STATE LI-ION-BATTERY CELL FOR OPERANDO SOFT X-RAY EMISSION SPECTROSCOPY

Daisuke Asakura^{1,2}, Eiji Hosono^{1,2}, Kosuke Yamazoe^{3,4}, Jun Miyawaki^{3,4}, and Yoshihisa Harada^{2,3,4}

¹Research Institute for Energy Conservation, National Institute of Advanced Industrial Science and Technology (AIST)

²AIST-UTokyo Advanced Operando-Measurement Technology Open Innovation Laboratory, AIST

³Synchrotron Radiation Laboratory, The Institute for Solid State Physics, The University of Tokyo

⁴Synchrotron Radiation Research Organization, The University of Tokyo

Development of high-performance lithium-ion battery (LIB) for electric vehicles is a one of the important research subjects to realize a sustainable low-carbon society. However, the trade-off relationships among the performances such as energy density, power performance, cycle performance, and safety property make the development difficult. Moreover, the combination of the materials among the cathode, anode, and electrolyte is crucial for the improvement of total performances of LIB. Thus, comprehensive researches and developments are highly important. In addition to the materials design, cutting-edge analyses are inevitable because understanding of the redox reactions and structural/electronic properties for the materials in LIBs is necessary to design/create innovative materials for LIBs.

Synchrotron radiation X-ray spectroscopy is a powerful technique to understand the crystal structure and electronic structure in LIB materials. We have been studying the charge-discharge mechanisms in LIBs based on the electronic-structure analysis by using soft X-ray spectroscopy at HORNET, BL07LSU. Especially, the redox reactions of electrode materials have been investigated by *operando* soft x-ray emission spectroscopy under the charge-discharge operation [1,2]. The *operando* cell consists of special electrode chip directly grown on Si₃N₄ thin-film window, counter electrode and electrolyte solution. On the other hand, all-solid-state LIB with solid-state electrolyte is of particular importance. We have already developed an all-solid-state-type *operando* cell for *operando* photoemission spectromicroscopy at 3DnanoESCA, BL07LSU [3,4].

In this study, we tried to install the all-solid-state-type *operando* cell for the HORNET chamber to perform *operando* soft x-ray emission spectroscopy for the all-solid-state LIBs. A special transfer vessel was developed to transfer the *operando* cell from a glove box filled with Ar gas to vacuum chamber without air exposure, because the *operando* cell includes a Li-metal counter electrode. The transfer vessel was fixed to the HORNET chamber and the *operando* cell was moved to the beam position (Figs. 1(a) and 1(b)).

The working electrode of the *operando* cell was LiCoO₂, a cathode material, which was single crystalline particles. The particles were mixed with a binder as a slurry and fixed on a carbon micro grid with an Au mesh (Fig. 1(d)). Then, the working electrode was stacked with the solid-state electrolyte sheets and Li-metal counter electrode as shown in Fig. 1(d).

Figure 1(c) shows the Co L₃-edge soft X-ray emission spectra for different 4 positions on the working electrode. For all the points, the intensity was too small, indicating that there were few LiCoO₂ particles. Because the size of the particles (μm order) is comparable with the beam size, it was difficult to find the positions of the small number of the particles. The density of the particles on the Au mesh should be much higher. On the other hand, we succeeded in the electrochemical charge-discharge using the *operando* cell and detecting the

signals of Co L_3 -edge soft X-ray absorption by the total-electron yield detection mode.

In summary, we installed an all-solid-state-type *operando* cell for the HORNET chamber. The intensity of the Co L_3 -edge soft X-ray emission spectra for the LiCoO_2 working electrode was too weak due to the small number of the μm -order particles. In the near future, we will increase the number of the particles by modifying the cell structure in order to perform soft X-ray emission measurement for the all-solid-state-type *operando* cell.

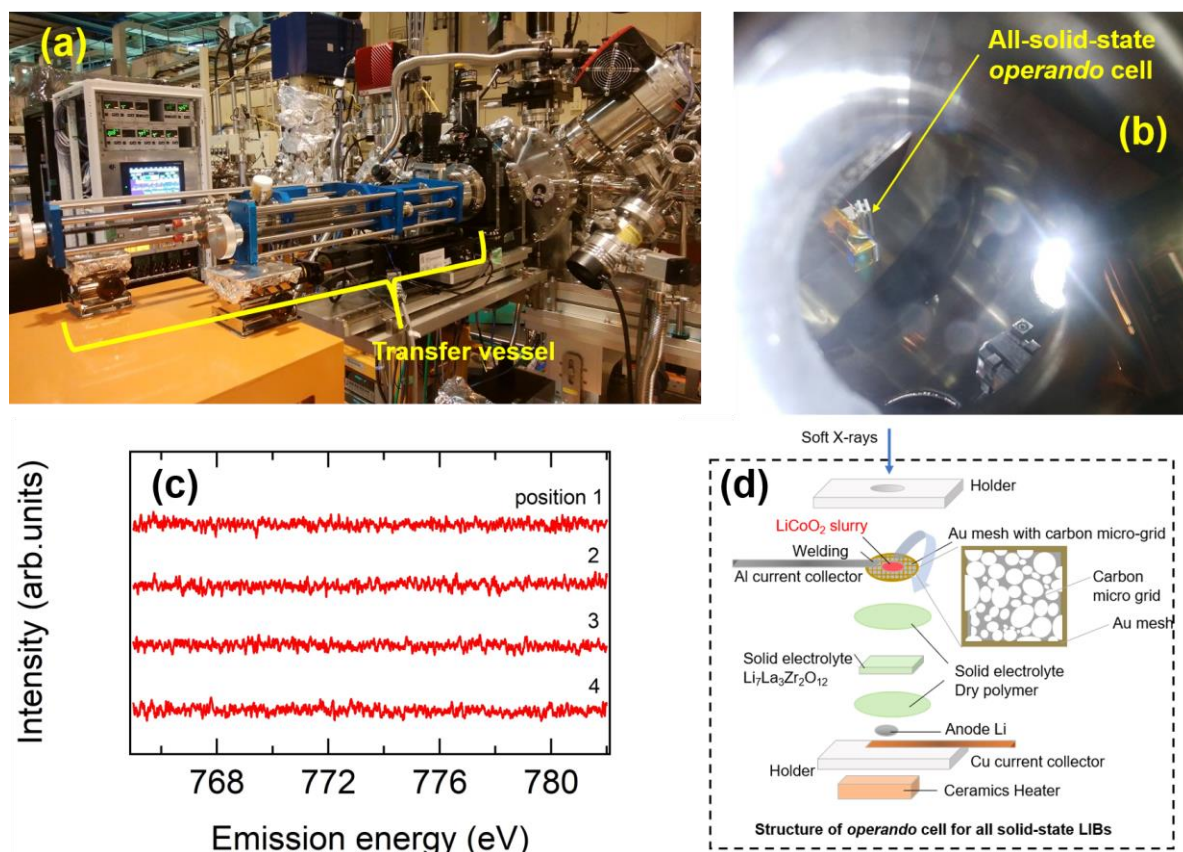


Fig.1. (a) A picture of the transfer vessel fixed with the HORNET chamber. (b) A picture of the inserted all-solid-state-type *operando* cell into the main chamber taken via a viewport. (c) Co L_3 -edge soft X-ray emission spectra for different 4 positions on the working electrode. (d) A schematic picture of the all-solid-state-type *operando* cell [3,4].

REFERENCES

- [1] D. Asakura *et al.*, Electrochem. Commun. **50**, 93 (2015).
- [2] D. Asakura *et al.*, Phys. Chem. Chem. Phys. **21**, 26351 (2019).
- [3] K. Akada *et al.*, J. Electron Spectrosc. Relat. Phenom. **233**, 64 (2019).
- [4] K. Akada *et al.*, Sci. Rep. **9**, 12452 (2019).

VERIFICATION OF TWO-CARRIER STATE IN THE CUPRATE SUPERCONDUCTOR $\text{Pr}_{1.4-x}\text{La}_{0.6}\text{Ce}_x\text{CuO}_4$

Kenji Ishii¹, Shun Asano², Masaki Fujita²,
Kohei Yamagami³, Jun Miyawaki³, Yoshihisa Harada³

¹*Synchrotron Radiation Research Center, National Institutes for Quantum and Radiological Science and Technology*

²*Institute for Materials Research, Tohoku University*

³*Synchrotron Radiation Laboratory, The Institute for Solid State Physics, The University of Tokyo*

High-transition-temperature superconductivity in the cuprates occurs when either holes or electrons are doped into parent antiferromagnetic Mott insulators. Doped holes occupy the oxygen $2p$ orbitals predominantly. In contrast, electrons are doped into the Cu $3d$ orbital but doping evolution of the electronic states of the “nominally” electron-doped cuprates is not so simple. Most electron-doped cuprate superconductors have the chemical formula $RE_{2-x}\text{Ce}_x\text{CuO}_4$ ($RE = \text{La, Pr, Nd, Sm, Eu}$) and electrons are doped via partial substitution of trivalent RE with tetravalent Ce. At low Ce concentration (x), Hall and Seebeck coefficients, which are often used to determine the sign and number of carriers, are negative as expected. However, the coefficients change the sign in the temperature dependence in the intermediate concentration and the sign becomes positive in entire measured temperature at high concentration ($x > 0.155$ for $RE = \text{Pr}$ and $x > 0.135$ for $RE = \text{La}$) [1-3]. Furthermore, reconstruction of the Fermi surface with increasing the Ce concentration is observed in ARPES [4] and quantum oscillation [5]. Recently, it was reported in a transport study [6] that superconductivity in the nominally electron-doped cuprates emerges under the coexistence of holes and electrons and a relation between the superfluid density of holes and the superconducting transition temperature agrees with that of hole-doped cuprates. This result indicates that the superconductivity in the nominally electron-doped cuprates is driven by the holes rather than the electrons and a unified mechanism of the superconductivity exists irrespective of the type of carriers.

In this study, we aim to verify the two-carrier states in the nominally electron-doped cuprates, especially to prove the existence of the holes by means of x-ray absorption spectroscopy (XAS) and resonant inelastic x-ray scattering (RIXS) at the oxygen K -edge. In the hole-doped cuprates, O K -edge XAS gave a direct evidence of the holes in the O $2p$ orbitals [7]; a peak at the pre-edge is ascribed to the hole state. In addition, we recently demonstrated that O K -edge RIXS is sensitive to the charge excitations of the doped holes [8].

The experiment was performed using the HORNET spectrometer at BL07LSU of SPring-8. Total energy resolution of RIXS was 150 meV. For the present study, we selected $\text{Pr}_{1.4-x}\text{La}_{0.6}\text{Ce}_x\text{CuO}_4$ (PLCCO), in which superconductivity is observed in wide Ce concentration (x). We prepared single crystals of superconducting $x = 0.16$ and non-superconducting $x = 0.08$. The crystals were cleaved in the air just before the measurement and σ -polarized x-rays were irradiated on the ab -plane of the crystal. The ac -plane was parallel to the horizontal scattering plane and momentum transfer in the CuO_2 plane (q) was scanned by rotating the crystal along the vertical b -axis. Scattering angle (2θ) was kept at 135° and temperature of the crystals was about 15 K.

The inset of Fig. 1 shows an XAS spectrum of PLCCO $x = 0.16$. The peak at 528.8 eV originates from the absorption to the Cu $3d$ upper Hubbard band (UHB) hybridized with the O $2p$ states. In the hole doped cuprates, absorption to the O $2p$ hole states appears at lower energy of the UHB peak but we cannot find any trace of the hole states in PLCCO. The main panel of Fig. 1 shows incident energy (E_i) dependence across the UHB peak in XAS as indicated by vertical bars in the inset. A Raman feature at 0.4 eV is observed at $E_i \leq 528.7$ eV and it gradually changes to fluorescence at higher E_i .

Figure 2 shows momentum dependence of RIXS measured at $E_i = 528.5$ eV. In the four spectra from the bottom, lines in light color present raw data and elastic scattering is subtracted for the lines in deep color. The subtracted spectra are overlaid at the top. Most of the spectral weight below 1eV is independent of the momentum and two-magnon excitation is a possible origin. In stark contrast, spectral weight in O K -edge RIXS exhibits large momentum dependence in hole-doped cuprates [8]. Though it is tiny, a momentum-dependent component is discernible in Fig. 2. Because the component follows the momentum dependence of the charge excitations observed in Cu K - and L_3 -edge RIXS [9,10], it is reasonably ascribed to the same charge origin through the hybridization between Cu $3d$ and O $2p$ orbitals. Regarding the doping dependence, the momentum-independent spectral weight is similarly observed, intensity of the momentum-dependent component is weaker in $x = 0.08$.

In summary, present XAS and RIXS results of PLCCO are comprehensible without assuming the existence of the holes in the O $2p$ orbitals. Even if the holes exist in the nominally electron-doped cuprates, their orbital character is qualitatively different from that of the O $2p$ holes in hole-doped cuprates.

REFERENCES

- [1] Y. Dagan et al., Phys. Rev. Lett. **92**, 167001 (2004).
- [2] P. Li et al., Phys. Rev. B **75**, 020506 (2007).
- [3] R. L. Greene et al, Annu. Rev. Condens. Matter Phys. **11**, 213 (2020).
- [4] N. P. Armitage et al., Phys. Rev. Lett. **88**, 257001 (2002).
- [5] T. Helm et al., Phys. Rev. B **92**, 094501 (2015).
- [6] Y. Li et al., Sci. Adv. **5**, eaap7349 (2019).
- [7] C. T. Chen et al., Phys. Rev. Lett. **66**, 104 (1991).
- [8] K. Ishii et al., Phys. Rev. B **96**, 115148 (2017).
- [9] K. Ishii et al., Phys. Rev. Lett. **94**, 207003 (2005).
- [10] K. Ishii et al., Nat. Commun. **5**, 3714 (2014).

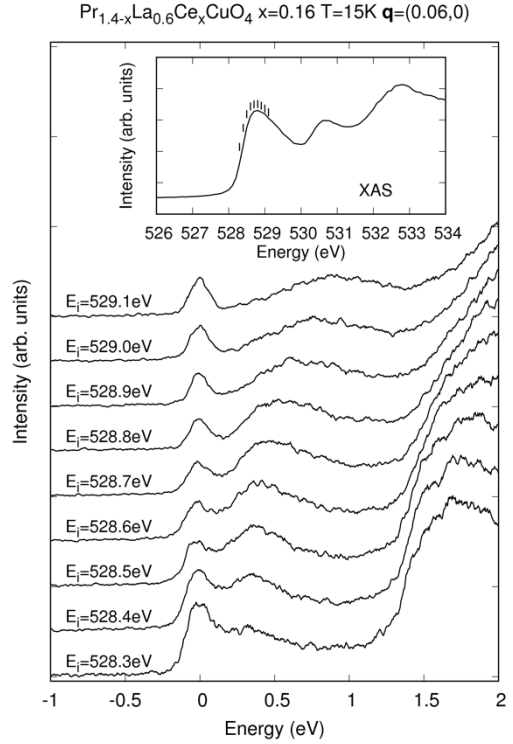


FIG. 1: Incident energy dependence of O K -edge RIXS in PLCCO $x = 0.16$. Inset shows XAS at the edge.

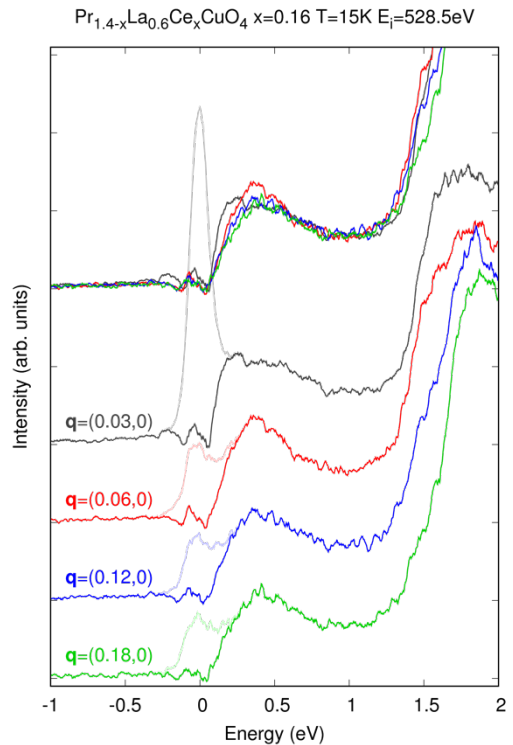


FIG. 2: Momentum dependence of O K -edge RIXS in PLCCO $x = 0.16$.

SPIN-POLARIZED ELECTRONIC STATE OF SINGLE CRYSTAL Co_2MnSi HEUSLER ALLOY PROBED BY RESONANT INELASTIC SOFT X-RAY SCATTERING (SX-RIXS) IN MAGNETIC FIELD

Rie Y. Umetsu¹, Hidenori Fujiwara², Jun Miyawaki^{3,4}, Kohei Nishimoto², Toshiyuki Kashiuchi², Akira Sekiyama², Akinori Irizawa⁵, Yoshihisa Harada^{3,4} and Shigemasa Suga⁵

¹*Institute for Materials Research (IMR), Tohoku University*

²*Graduate School of Engineering Science, Osaka University, Osaka, Japan*

³*The Institute for Solid State Physics (ISSP), The University of Tokyo, Japan*

⁴*Synchrotron Radiation Research Organization, The University of Tokyo, Japan*

⁵*Institute of Scientific & Industrial Research, Osaka University, Osaka, Japan*

Introduction

It has been predicted from theoretical calculations that some of Mn- and Co-based Heusler alloys are half-metallic ferro- or ferri-magnets with the spin polarization of $\sim 100\%$ around the Fermi energy (E_F) [1-3]. If the electrons are completely polarized around E_F , it is very efficient as a magnetic electrode in various spin dependent devices in the field of spintronics.

In the aspect of the fundamental investigations for half-metallic materials, it has been considered how to show the real evidence of the characteristic electronic structure. Attempts have been made worldwide to observe the detailed electronic state of Heusler alloys by photoelectron spectroscopy. Although a magnetic field must be applied in order to make a sample into a single domain state, the photoelectron orbit is greatly affected by the magnetic field. In our previous work, we have first studied the detailed electronic structure and magnetic properties of a single crystal Mn_2VAI by SX-RIXS measurements in magnetic field [4]. The RIXS is a bulk sensitive photon-in and photon-out spectroscopy, and very powerful to investigate such as $d-d$ excitations for open shell $3d$ orbitals and magnetic excitations for spin systems as well as $2p-3d$ transitions in element- and symmetry-specific ways. In this study, we performed the RIXS experiments for single crystal of Co_2MnSi Heusler alloy, which was predicted to be a half-metallic ferromagnet.

Experiments

a) Sample preparation

A single crystal of Co_2MnSi was prepared by the Bridgman method after preparing a master alloy by arc melting in Ar gas atmosphere, and subjected to homogenizing heat treatment at 1373 K. The sample composition identified by an electron probe microanalyzer is Co:50.0, Mn:25.9, Si:24.1 at.%. Crystal orientation was checked by the Laue method and the specimens were cut out in the stripe form with the length of 6 mm along the $\langle 100 \rangle$ with about $1 \times 1 \text{ mm}^2$ cross section. Magnetic properties were investigated with SQUID magnetometer and the spontaneous magnetization at 5 K was 142.2 emu/g ($= 5.1 \mu_B/\text{f.u.}$), being comparable to the literature [5].

b) RIXS experiment

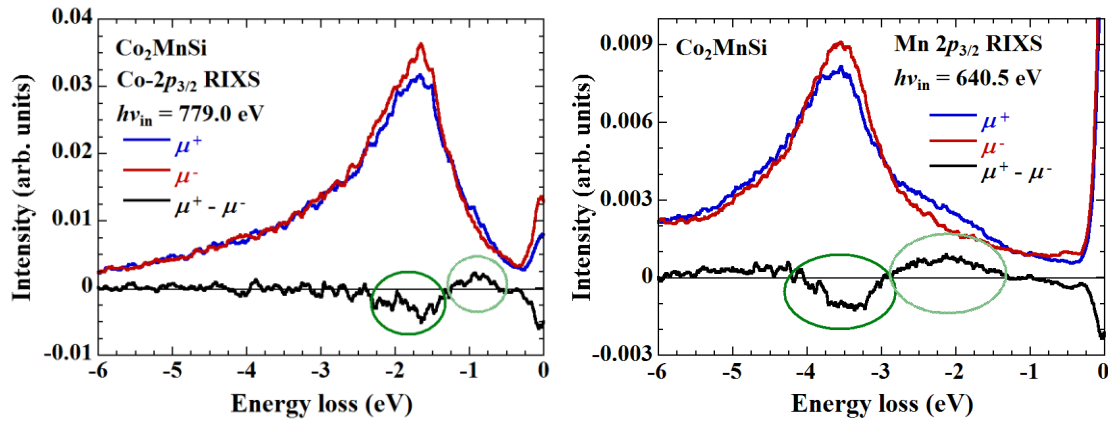
RIXS experiments were performed using a high-resolution soft X-ray emission spectrometer installed at the end of the BL07LSU of SPring-8. The specimen with the (001) plane was fractured in a glove box with Ar gas atmosphere, and then transferred into the analyzer chamber without exposure to the air. The RIXS spectra for Co and Mn $2p$ core excitation were measured with use of the right and left helicity circularly polarized light at room temperature. A permanent magnet with the field of 0.25 T was installed in the chamber and arranged as the X-ray incidence direction and the magnetic field direction become parallel [6].

Results

Figures indicate RIXS spectra obtained in parallel (μ^+) and antiparallel (μ^-) configurations between the photon helicity and the magnetic field at incoming photon energy, $h\nu_{\text{in}}$ of 779.0 eV (left figure) and 640.5 eV (right figure) for the Co and Mn- $2p_{3/2}$ edges, respectively. These photon energies correspond to the peak positions of the Co and Mn- $2p_{3/2}$ absorption spectra for the Co_2MnSi . Intensity peaks without any energy loss are the elastic component, and the other peaks in the larger energy loss region are the so-called fluorescence peaks. As shown in the figures, clear fluorescence components were observed and their circular polarization dependence (MCD = $\mu^+ - \mu^-$) was also confirmed. This RIXS-MCD signals originate from the spin-selective dipole-transition from $m_j = \pm 3/2$ which is separated by the Zeeman splitting due to the effective magnetic field of $3d$ electron states [4]. It was found that the positive and negative MCD fluorescence components in both Co and Mn have a large contribution of fluorescence from $m_j = +3/2$ and $-3/2$, respectively, suggesting that the valence band electronic structures of Co_2MnSi is highly spin-polarized.

References

- [1] R.A. de Groot, F.M. Mueller, P.G.van Engen, K.H.J. Buschow, Phys. Rev. Lett. 50 (1983) 2024-2027.
- [2] J.J. Kübler, A.R. Williams, C.B. Sommers, Phys. Rev. B 28 (1983) 1745-1755.
- [3] S. Ishida, S. Akazawa, Y. Kubo, J. Ishida, J. Phys. F 12 (1982) 1111-1122.
- [4] R.Y. Umetsu, H. Fujiwara, K. Nagai, Y. Nakatani, M. Kawada, A. Sekiyama, F. Kuroda, H. Fujii, T. Oguchi, Y. Harada, J. Miyawaki, S. Suga, Phys. Rev. B 99 (2019) 134414.
- [5] R.Y. Umetsu, K. Kobayashi, A. Fujita, R. Kainuma, K. Ishida, Scripta Mater. 58 (2008) 723-726
- [6] J. Miyawaki, S. Suga, H. Fujiwara, H. Niwa, H. Kiuchi, Y. Harada, J. Synchro. Rad. 24 (2017) 449-455.



Figs. RIXS spectra recorded for parallel (μ^+) and antiparallel (μ^-) configurations of the photon helicity at Co- $2p_{3/2}$ with incident photon energy, $h\nu_{\text{in}}$ of 779.0 eV (left figure) and at Mn- $2p_{3/2}$ of 640.5 eV (right figure). Black lines indicate MCD ($=\mu^+ - \mu^-$).

MULTIORBITAL BOND FORMATION FOR STABLE OXYGEN-REDOX REACTION IN BATTERY ELECTRODES

Masashi Okubo

Department of Chemical System Engineering, School of Engineering, The University of Tokyo

The development of advanced electrochemical energy storage devices has been an active research field because it offers sustainability prospects, for instance, reduction of fossil fuel reliance by realizing an electric vehicle range of 500 km per charge or integrating renewable energy sources to an electrical grid. Market-leading lithium-ion batteries (LIBs) efficiently store energy by lithium-ion (de)intercalation associated with redox reactions. However, their energy density approaches the theoretical limit, in part owing to the small capacity of the positive electrode materials, which severely obstructs the wide deployment of LIBs. Therefore, it is important to find an alternative battery chemistry that can exceed the existing positive-electrode capacity limits.

The use of the extra redox reactions of oxygen in addition to conventional transition-metal redox reactions is an attractive way to increase the capacity of transition-metal oxides.⁷ In general, most oxygen 2*p* orbitals in conventional electrode materials LiMO_2 (*M*: transition metal) form σ -type bonds with axial *M* 3*d* orbitals (e_g orbitals in an O_h symmetry). As the atomic energy level of oxygen 2*p* orbitals is usually lower than that of *M* e_g orbitals, the σ -type bonding orbitals are predominantly from oxygen 2*p* orbitals. Therefore, it is difficult to oxidize oxygen 2*p* orbitals that have a σ -type bonding character. However, research groups led by Bruce and Ceder postulated that oxygen in Li-excess transition-metal oxides $\text{Li}_{1+x}\text{M}_{1-x}\text{O}_2$ (Fig. 1a) intrinsically have localized ('orphaned') 2*p* orbital along the Li–O–Li axis without the σ -type bonding character, which can contribute to an additional oxygen-redox capacity. Indeed, large capacities exceeding the capacity limit of *M* redox reactions have been reported for many Li-excess transition-metal oxides including Li_2MnO_3 - LiMO_2 solid solution, layered honeycomb Li_2IrO_3 , random rock salt $\text{Li}_{1.2}\text{Ti}_{0.4}\text{Mn}_{0.4}\text{O}_2$, three-dimensional β - Li_2IrO_3 , and anti-fluorite Li_5FeO_4 . However, despite the theoretical adequacy of the proposed 'orphaned' oxygen 2*p* orbital hypothesis, the existence of the localized oxygen 2*p* orbitals in Li-excess transition-metal oxides has not been verified

experimentally.

Furthermore, although localized, the oxygen 2*p* orbital along the Li–O–Li axis still has a π -type interaction with the *M* t_{2g} orbital, which should play an essential role in oxygen-redox reactions. It is important to emphasize that the rigid-band model, which was frequently used for

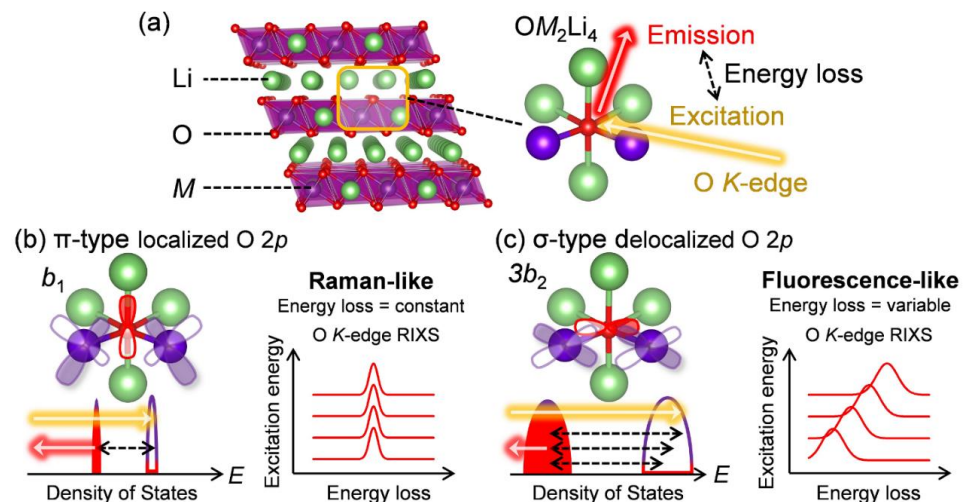


Figure 1. Resonant inelastic X-ray scattering (RIXS) spectra for delocalized and localized oxygen 2*p* orbitals. (a) Crystal structure of Li-excess layered transition-metal oxides $\text{Li}[\text{Li}_x\text{M}_{1-x}]\text{O}_2$ (*M*: transition metal). (b) π -type localized occupied/unoccupied states consisting of oxygen 2*p* and *M* t_{2g} orbitals (b_1/b_1^* bands in a C_{2v} -symmetry OM_2Li_4 cluster). (c) σ -type delocalized occupied/unoccupied states consisting of oxygen 2*p* and *M* e_g orbitals ($3a_1/3a_1^*$ and $3b_2/3b_2^*$ bands in a C_{2v} -symmetry OM_2Li_4 cluster).

consideration of oxygen-redox electrodes, cannot qualitatively discuss M–O interaction (*e.g.*, covalency), because it only considers a bandwidth and a band center energy of each band. Therefore, for a thorough understanding of the reversible oxygen-redox reactions occurring in Li-excess transition-metal oxides, it is necessary to clarify the nature of the π -type bonds during the oxygen-redox reactions from the molecular orbital viewpoint. In this work, we used oxygen *K*-edge resonant inelastic X-ray scattering (RIXS) spectroscopy combined with *ab initio* computations to demonstrate ($\sigma + \pi$) multiorbital bond formation as a firm criterion for stable oxygen-redox reactions.

Oxygen *K*-edge RIXS spectroscopy was used to examine the existence of π -type localized oxygen *2p* orbitals in Li_2MnO_3 , a standard Li-excess layered transition-metal oxide. Oxygen *K*-edge RIXS spectroscopy records the inelastic scattering during core excitation–relaxation ($1s \rightarrow 2p \rightarrow 1s$), in which the energy loss corresponds to valence excitation between occupied and unoccupied *2p* bands. RIXS spectroscopy has a probing depth of approximately 100 nm (bulk sensitive). Importantly, when occupied/unoccupied oxygen *2p* bands have a localized character with weak orbital hybridization, the inelastic scattering becomes Raman-like and has constant energy loss regardless of the incident photon energy (Fig. 1b). Conversely, delocalized occupied/unoccupied oxygen *2p* bands with a large orbital hybridization gives fluorescence-like inelastic scattering with variable energy loss depending on the incident photon energy (Fig. 1c). Therefore, oxygen *K*-edge RIXS spectroscopy allows us to diagnose localized or delocalized oxygen *2p* bands.

The *ab initio* calculations using HSE06 hybrid functional for Li_2MnO_3 indicates that a localized oxygen *2p* orbital exists along the Li–O–Li axis with an orbital energy of approximately -0.9 to 0.0 eV versus the Fermi energy (Fig. 2a). The RIXS spectra and the corresponding second differential RIXS map (Fig. 2b and 2c) exhibit two broad fluorescence-like peaks, which could be related to the valence excitation between the σ -type wide oxygen *2p* bands strongly hybridized with axial Mn e_g orbitals (Fig. 1c). Based on the C_{2v} symmetry of an OMn_2Li_4 cluster, these bands are labelled as $3a_1/3b_2$ bands. More importantly, the RIXS spectra show an intense Raman-like peak with constant energy loss of approximately 2.5 eV. This Raman-like peak clearly indicates the existence of the π -type narrow oxygen *2p* bands weakly hybridized with Mn t_{2g} orbitals (b_1/b_1^* bands based on the C_{2v} -symmetry labelling, Fig. 1b). It is important to note that the Raman-like feature is not the simple projection of the *d-d* excitation of Mn *L*-edge, because O *K*-edge XAS and RIXS involve charge-transfer processes through O–Mn interactions. In contrast, for a non-Li-excess layered oxide $\text{LiNi}_{1/3}\text{Co}_{1/3}\text{Mn}_{1/3}\text{O}_2$, the RIXS spectra show only fluorescence-like peaks with variable energy loss depending on the incident photon energy because most oxygen *2p* orbitals form σ -type wide bands with axial *M* *3d* orbitals. Therefore, this is the first experimental verification of the ‘orphaned’ oxygen *2p* orbital hypothesis for Li-excess transition-metal oxides, and oxygen *K*-edge RIXS spectroscopy is definitely an effective diagnostic tool to detect electrochemically active oxygen states.

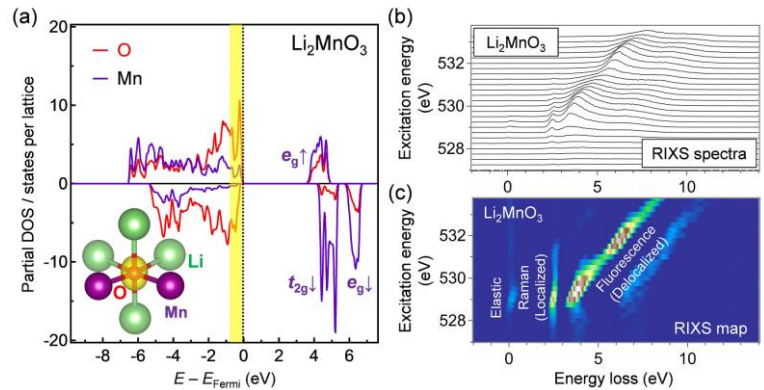


Figure 2. Direct observation of orphaned oxygen *2p* orbitals in Li_2MnO_3 . (a) Calculated partial density of states for oxygen and manganese in Li_2MnO_3 . The inset shows the spatial electron density at the energy range from -0.9 to 0 eV versus the Fermi energy. (b) Oxygen *K*-edge RIXS spectra, and (c) second differential RIXS map for Li_2MnO_3 with excitation photon energy from 527 to 533.75 eV.

MULTIORBITAL BOND FORMATION FOR STABLE OXYGEN-REDOX REACTION IN BATTERY ELECTRODES

Masashi Okubo

Department of Chemical System Engineering, School of Engineering, The University of Tokyo

High energy density batteries are a long-standing target for sustainability efforts, but the energy density of the state-of-the-art lithium-ion batteries is limited in part owing to the small capacity of positive electrode materials. Although the additional oxygen-redox reaction of Li-excess transition-metal oxides is an attractive approach to increase the capacity, an atomic-level understanding of the reaction mechanism has not been established. Here, using bulk-sensitive resonant inelastic X-ray scattering (RIXS) spectroscopy combined with *ab initio* computations, we prove the existence of an orphaned oxygen 2*p* orbital that was theoretically predicted to play a key role in oxygen-redox reactions.

As a target Li-excess layered transition metal oxide, $\text{Li}_{1.2}\text{Ni}_{0.13}\text{Co}_{0.13}\text{Mn}_{0.54}\text{O}_2$ was used as an oxygen-redox electrode material. Before measuring the RIXS spectra, the *ab initio* calculations using the HSE06 hybrid functional were carried out for $\text{Li}_{1.2-x}\text{Ni}_{0.13}\text{Co}_{0.13}\text{Mn}_{0.54}\text{O}_2$. The calculated electronic structures show that the averaged Bader charges of Ni and Co decrease only during the early stage of Li^+ extraction ($x < 0.4$), whereas that of oxygen continuously decreases during the whole delithiation process, suggesting the occurrence of the additional oxygen-redox reactions for $x > 0.4$. Indeed, $\text{Li}_{1.2}\text{Ni}_{0.13}\text{Co}_{0.13}\text{Mn}_{0.54}\text{O}_2$ delivers a large capacity of approximately 250 mAh/g exceeding the theoretical capacity (123 mAh/g) of the $\text{Ni}^{4+}/\text{Ni}^{2+}$ and $\text{Co}^{4+}/\text{Co}^{3+}$ redox reactions.

The oxygen *K*-edge X-ray absorption spectrum (XAS) in a bulk sensitive partial fluorescence yield mode for the pristine $\text{Li}_{1.2}\text{Ni}_{0.13}\text{Co}_{0.13}\text{Mn}_{0.54}\text{O}_2$ shows two absorption peaks (528.5 and 531 eV) of 1*s* core-electron excitation to unoccupied σ -type bands (oxygen 2*p*-Mn $e_g^\downarrow/e_g^\uparrow$, $3a_1^*/3b_2^*$ in C_{2v}) and an unoccupied π -type band (oxygen 2*p*-Mn t_{2g}^\downarrow , b_1^* in C_{2v}). This band picture agrees with the calculated partial density of states (pDOS) for Mn. Upon charging to 4.4 V vs. Li/Li⁺, a new XAS shoulder emerged at 527 eV owing to hole generation in σ -type (oxygen 2*p*-Ni e_g) and π -type (oxygen 2*p*-Co t_{2g}) bands. After oxygen oxidation, a new absorption emerged at a relatively high absorption-energy region of approximately 530.5 eV. Similar spectral changes were also observed during the second cycle. The XAS signal at 530.5 eV can be ascribed to an unoccupied π -type band (oxygen 2*p*-Mn t_{2g}^\uparrow) resulting from oxygen oxidation. The emergence of the absorption at a relatively high energy region is reasonable because oxygen oxidation increases the effective nuclear charge, which lowers the initial energy level of an oxygen 1*s* core and hence raises the excitation energy¹⁸. Similar changes in the XAS signals by oxidation (the emergence of new absorption at a high energy region) are often observed for transition-metal *K*-edge absorption spectra.

The RIXS spectra and the second differential RIXS map of pristine $\text{Li}_{1.2}\text{Ni}_{0.13}\text{Co}_{0.13}\text{Mn}_{0.54}\text{O}_2$ (Fig. 1) exhibit a Raman-like peak with constant energy loss corresponding to a π -type narrow oxygen 2*p* band ($\pi \rightarrow \pi^*$), in addition to the fluorescence-like peaks ($\sigma \rightarrow \sigma^*$). The *ab initio* calculations for pristine $\text{Li}_{1.2}\text{Ni}_{0.13}\text{Co}_{0.13}\text{Mn}_{0.54}\text{O}_2$ supports the existence of the localized oxygen 2*p* orbitals along the Li-O-Li axes with an orbital energy near the Fermi level. The $\pi \rightarrow \pi^*$ RIXS peak intensified after charging to 4.4 V vs. Li/Li⁺ (transition-metal oxidation, Fig. 1b), which indicates accumulation of the localized oxygen 2*p* states to the Fermi level. The initial Li⁺ extraction associated with Co and Ni oxidation gives an oxygen coordination environment with a $\square\text{-O-Li}^+$ or $\square\text{-O-}\square$ axis (\square : Li⁺ vacancy), which electrostatically raises the energy level of the localized oxygen 2*p* orbitals. Indeed, the fact that the energy loss of the Raman-like RIXS peak decreased from 2.5 to 2.0 eV supports the rise in the energy level of the localized oxygen 2*p* orbitals. We presume that the accumulation of the localized oxygen 2*p* states to the Fermi level should be an essential

preceding process to trigger the oxygen-redox reactions. For example, it is well known that the electrochemical properties of Li_2MnO_3 is poor even though oxygen has a $\text{Li}^+\text{-O-Li}^+$ axis and hence a localized oxygen $2p$ orbital. Most likely, as Li_2MnO_3 cannot exhibit the initial Li^+ extraction owing to the electrochemically inactive Mn^{4+} , it is difficult to generate the $\text{Li}^+\text{-O-Li}^+$ and $\text{Li}^+\text{-O-O-Li}^+$ axes, and the energy level of the localized oxygen $2p$ orbital remains too low to undergo oxidation within the electrolyte stability window. Conversely, when redox-active transition metals are present, such as in $\text{Li}_2\text{MnO}_3\text{-LiMO}_2$ solid solution, the $\text{Li}^+\text{-O-Li}^+$ and $\text{Li}^+\text{-O-O-Li}^+$ axes are easily formed by the initial Li^+ extraction to raise the energy level of the localized oxygen $2p$ orbital, unlocking the redox activity of oxygen. Once the oxygen-redox reaction is triggered, the $\text{Li}^+\text{-O-Li}^+$ and $\text{Li}^+\text{-O-O-Li}^+$ axes are continuously generated to achieve a large oxygen-redox capacity.

After charging to 4.8 V vs. Li/Li^+ (oxygen oxidation, Fig. 1c), the Raman-like $\pi \rightarrow \pi^*$ RIXS peaks disappear, and all the RIXS peaks become fluorescence-like. Importantly, a new intense fluorescence-like peak emerges at an energy loss of approximately 7.0 eV with an incident photon energy of 530.5 eV. Recalling that an incident photon of 530.5 eV excited $1s$ core electron to an unoccupied π -type band (oxygen $2p\text{-Mn } t_{2g}^\uparrow$), the inelastic scattering resonance with the 530.5 eV incident photon includes the valence excitation between the π -type bands ($\pi \rightarrow \pi^*$). Therefore, a large energy loss of approximately 7 eV for this RIXS peak corresponds to π -type splitting. This large π -type splitting should be induced by the hole generation in the antibonding π -type band, and makes the Mn-O bonds more bonding (more delocalized). Therefore, the RIXS peak is observed as fluorescence-like. The enhanced π -type interaction stabilizes the oxidized oxygen, leading to reversible oxygen-redox reactions. Indeed, the Raman-like RIXS peak of the localized oxygen $2p$ orbitals was recovered after full discharge (Fig. 1d), and the changes in the RIXS spectra were reversible even during the subsequent cycle.

To summarize the reaction mechanism, the $\text{Li}^+\text{-O-Li}^+$ coordination in the pristine state forms localized oxygen $2p$ orbital weakly hybridized with the $\text{Mn } t_{2g}$ orbital. When the initial Li^+ extraction occurs in association with M redox reactions, the $\text{Li}^+\text{-O-Li}^+$ and $\text{Li}^+\text{-O-O-Li}^+$ coordination axes are generated, which raises the energy level of the localized oxygen $2p$ states to the Fermi level. After this accumulation, oxygen oxidation occurs to delocalize the hole within a Mn-O-Mn bond. The resulting large b_1/b_1^* splitting stabilizes the oxidized oxygen, enabling a reversible oxygen-redox reaction.

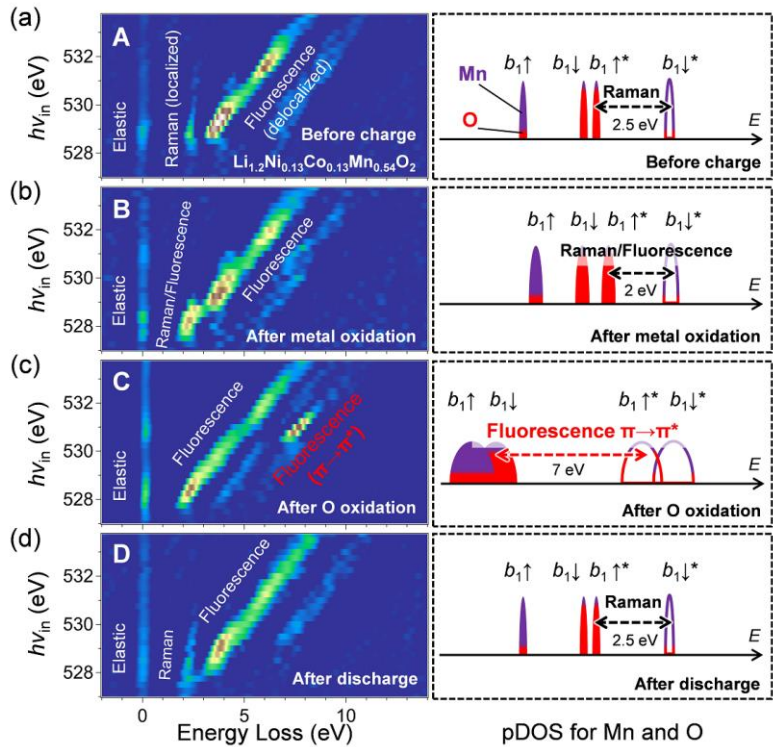


Figure 1. Monitoring oxygen $2p$ orbitals during oxygen-redox reaction of $\text{Li}_{1.2}\text{Ni}_{0.13}\text{Co}_{0.13}\text{Mn}_{0.54}\text{O}_2$. Oxygen K -edge second differential RIXS map for the samples (a) before charge, (b) after transition-metal oxidation, (c) after oxygen oxidation, and (d) after discharge, with excitation photon energy from 527 to 533.75 eV. The schematic partial density of states (pDOS) for $\text{Mn } 3d$ and oxygen $2p$ orbitals are shown for comparison.

UNDERSTANDING OF SOLVATION AND DESOLVATION STATE OF ACTIVE MATERIALS FOR REDOX-FLOW BATTERIES DERIVED FROM HYDROGEN-BONDING ANALYSIS BY SOFT X-RAY SPECTROSCOPY

Akihiro Ohira¹, Eiji Hosono^{1,2,3}, Daisuke Asakura^{1,3}, Takashi Funaki¹, Kosuke Yamazoe⁴, Jun Miyawaki^{4,5}, Yoshihisa Harada^{4,5}

¹Research Institute for Energy Conservation, National Institute of Advanced Industrial Science and Technology (AIST), ²Department of Energy and Environment, Global Zero Emission Research Center, AIST, ³AIST-UTokyo Advanced Operando-Measurement Technology Open Innovation Laboratory (OPERANDO-OIL), ⁴Synchrotron Radiation Laboratory, The Institute for Solid State Physics, The University of Tokyo ⁵Synchrotron Radiation Research Organization, The University of Tokyo

Power generation systems that use natural energy, such as sunlight and wind, and that do not generate greenhouse gases have been actively introduced globally. Although they do not generate carbon dioxide, compared to power sources like thermal and hydroelectric power, these renewable energy sources provide an unstable power supply that is affected by various situations. In order to use renewable energy efficiently and smoothly, the generated electricity must be stored and discharged as required; thus, a storage battery (secondary battery) that can adjust the constantly fluctuating output over short and long cycles is significantly desired. Large scale storage batteries are famous for lithium ion batteries, sodium-sulfur batteries, lead storage batteries and redox flow batteries.[1-3] Lead storage batteries have been used as batteries for automobiles and motorcycles for a long time and have abundant achievements as small storage batteries. Lithium ion batteries also have many achievements as small batteries. Sodium-sulfur batteries have an extremely high energy density and are widely used in load leveling applications in substations due to their high charge and discharge efficiency.

Redox flow batteries (RFBs) have been successfully developed by NASA around 1974.[4] At the beginning of development, the Fe/Cr system was mainstream,[5] but it was not put into practical use due to the disadvantage that mixing of the positive/negative electrolyte through the membrane leads to a decrease in capacity of the battery. In around 1984, Kazacos et al. has developed a vanadium-based RFB (VRFB).[6] Since that time, the awareness of RFBs have increased and research and development has been accelerating.

The significant issue in studying RFBs is to correctly evaluate the reactivity of electrodes and active materials in addition to newly active material search and clarify material properties necessary for improving battery performance.

In addition to the search for new active materials, it is important to precisely understand the reactivity of the electrodes and active materials. In particular, the state of solvation and desolvation associated with the electrochemical reaction between active material and solvent has not been well-understood at all, and a detailed understanding of the dynamics of solvation/desolvation at the interface between the active material and the electrode is required. This will lead to a dramatic increase in solubility and redox activity, which will lead to the realization of high-performance RFBs. In this study, to obtain a guideline for the design of the interface between the active material and the electrode, which is indispensable for the realization of a high-performance RFB, the hydration state of water-soluble active materials was investigated by X-ray absorption and emission spectroscopy.

A dendrimer molecule with a viologen unit [7] dissolved in methanol was cast on the SiN window and after drying the membrane, the cell was assembled and mounted in a chamber. Water vapor was introduced while bubbling with nitrogen gas to control the relative humidity in the cell. We observed changes in the O1s soft x-ray emission spectra of oxygen upon hydration and dehydration of the dendrimer molecules.

Figure 1 shows the change in the O1s XES spectrum of water in dendrimer molecules during the hydration and dehydration processes. With increasing humidity, emission spectra similar to those of bulk water were obtained. In addition, in the spectrum of the dehydration process (the change from wet to dry state indicated by the sign Re), 1b' is relatively small, and the change is not reversible when comparing the each spectra of the hydration and dehydration processes. To irreversible change in the spectra, optical microscopy observations of the cast films before and after the measurements were performed. Since the film disappeared in the area irradiated by X-rays, it is inferred that the film was dissolved during the hydration process.

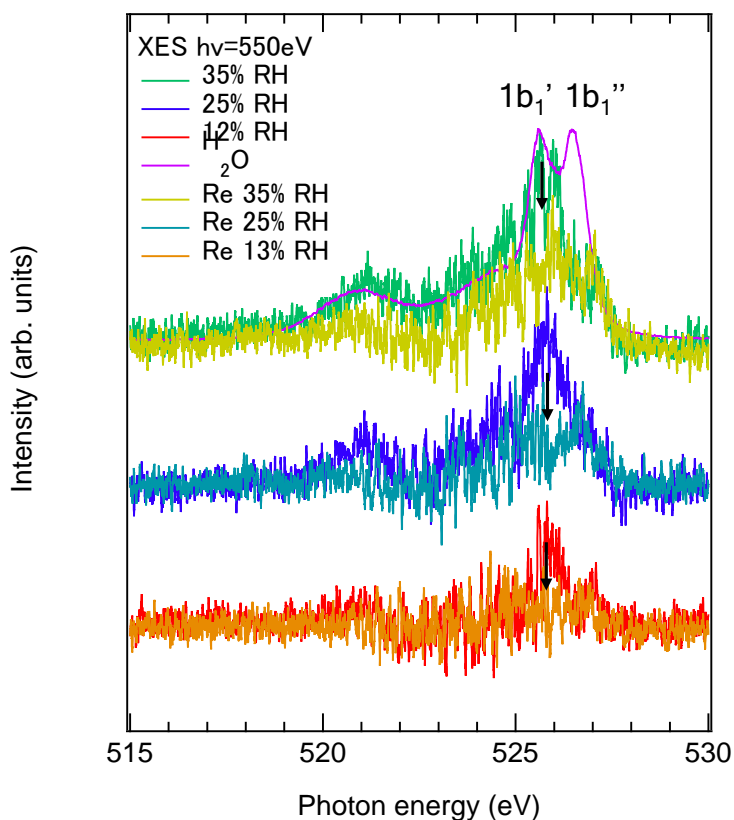


Figure 1 Change in the O1s XES spectrum of water in dendrimer molecules under humidity control.

In the future, we plan to immobilize the molecules on the substrate to check the changes in hydration and dehydration.

REFERENCES

- [1] B. Zakeri, S. Syri, *Renewable and Sustainable Energy Reviews*, **42**, 569 (2015).
- [2] F. Shi, *Reactor and Process Design in Sustainable Energy Technology*, Elsevier Amsterdam (2016).
- [3] B. Dunn, H. Kamath, J.-M. Tarascon, *Science*, **334**, 928 (2011).
- [4] L. H. Theller, NASA TM X-71540, 1 (1974).
- [5] R. F. Gahn, N. Hagedorn, NASA Tech Briefs February, 42 (1987).
- [6] M. S. Kazacos, M. Rychcik, R. G. Robin, A. G. Fane, *J. Electrochem. Soc.*, **133**, 1057 (1986).
- [7] A. Ohira, T. Funaki et al. *ACS Appl. Energy Mater.*, **3**, 4377 (2020)

PHOTOEXCITED CARRIER DYNAMICS IN LEAD SULFIDE QUANTUM DOT PHOTOVOLTAIC CELL

Kenichi Ozawa^{a,b}, Susumu Yamamoto^c, Iwao Matsuda^d

^aDepartment of Chemistry, Tokyo Institute of Technology, ^bInstitute of Materials Structure Science, High Energy Accelerator Research Organization, ^cInstitute of Multidisciplinary Research for Advanced Materials, Tohoku University, ^dThe Institute for Solid State Physics, The University of Tokyo

INTRODUCTION

For realizing a sustainable society, uses of solar energy are essential. Photovoltaic (PV) devices are one of solutions to utilize the solar energy. It has been recognized that there is the Shockley-Queisser limit, which is the theoretical maximum light-electricity conversion efficiency of a PV cell using a single p/n junction. The limit is 34% at a band gap of 1.34 eV [1]. One of techniques to exceed this limit is tandemization of multiple p/n junctions composed of different materials to cover several photon energies. Another solution is the use of quantum dots (QDs) in a light-receiving layer. The QDs allow to absorb lights of various wavelengths owing to the formation of quantum-well states. One of advantages of the QD PV cells is that the absorption band can be controlled simply by changing the QD size so that the production cost can be kept low in comparison with the multijunction PV cells.

Preceding studies on the QD PV cells have mainly focused on synthesis methods of various kinds of QDs as well as their optical properties. On the other hand, accumulation of knowledge of photoexcited carrier dynamics in the QD PV cells is still insufficient. In the present study, therefore, we shed the light on the dynamics of carriers generated in the QDs by using time-resolved soft X-ray photoelectron spectroscopy (TRXPS). TRXPS has been proved to be a powerful tool to clarify the carrier dynamics in model organic PV cells [2, 3].

EXPERIMENTAL

The QDs employed in this work were lead sulfide (PbS) nanoparticles with average sizes of 3 and 9 nm (Quantum Solutions). PbS QD films were prepared under ambient conditions by spin-coating the PbS QD solutions on 0.05 and 0.5 wt% Nb-doped rutile TiO₂(110) substrates. Since PbS and TiO₂ are p-type and n-type semiconductors, respectively, a p/n junction is realized at the PbS/TiO₂ interface. The prepared QD films were treated with 3-mercaptopropionic acid (3-MPA) by dropping a 3-MPA solution onto the films and then by removing the solution. This procedure allowed to replace a capping layer of the PbS QD from original oleic acid to 3-MPA.

The TRXPS measurements were carried out at BL07LSU of SPring-8 in the H operation mode [4]. Visible (807 nm) and ultraviolet (404 nm) lasers with a repetition rate of 208 kHz were used to generate the photoexcited carriers in the PbS QD films, and the excited states were monitored through synchrotron-radiation excited Pb 4f and S 2p peaks of PbS and Ti 2p peak of TiO₂.

RESULTS AND DISCUSSION

Fig. 1 shows S 2p and Pb 4f spectra of the 3-nm PbS QD film. Four peaks are observed in the S 2p spectrum; two of them originate from the spin-orbit splitting S 2p levels of the S atoms in the PbS QD

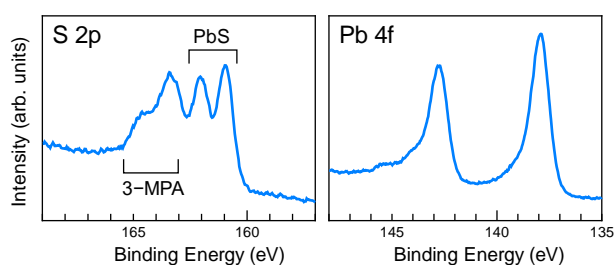


FIGURE 1. S 2p and Pb 4f core-level peaks of the 3-nm PbS QD film on TiO₂(110). The photon energy was 370 eV.

film, and the other two arise from 3-MPA. The lower and higher binding-energy components are associated with PbS and 3-MPA, respectively. This assignment is rationalized because (1) the PbS/3-MPA intensity ratio is higher in the film composed of the 9-nm QDs than the 3-nm QDs and (2) the low binding-energy component is transiently shifted upon laser pulse irradiation (this will be described below). The Pb $4f_{7/2}$ and $4f_{5/2}$ peaks have a tailing towards higher binding energies (Fig. 1). This suggests an existence of oxidation species such as PbO. Although the PbS QD films were prepared and treated under ambient conditions, oxidation of the PbS QD is limited because of a relatively low intensity of the tail structure.

As the PbS QD films are irradiated by either visible or ultraviolet laser, the PbS-originated peaks move to the higher binding energies. Fig. 2a compares the S 2p and Pb $4f_{7/2}$ spectra of the 3-nm PbS QD film acquired with and without the visible laser (807 nm = 1.54 eV). Except for the S 2p component of 3-MPA, all peaks move by ~100 meV upon laser irradiation. The direction of the peak shift can be interpreted by a loss of an excited electron in the PbS QD by charge transfer from PbS to TiO₂.

Fig. 2b shows that the magnitude of the laser-induced shift of the PbS peaks diminishes with a delay time. This suggests that electron-hole recombination should proceed with time if the magnitude of the shift is proportional to the number of the PbS cations. It is apparent that the decay curve can be reproduced neither by a biexponential function nor by a triexponential function. This is in contrast to decay curves obtained from model organic PV cells [2], where the curves are reproduced by a biexponential function. A gradual decrease of the peak shift in the present case implies that there should be several PbS cations with different lifetimes. A certain distribution of the QD size, though the average size is 3 nm in the case of Fig. 2b, may be responsible for a wide range of the lifetime.

A point to be noted is that the peak shift remains even after 4.8 μ s, the longest delay time examined in the present study. A long lifetime of the excited state of PbS, i.e., the cationic state of PbS, is one of advantages for the efficient light-electricity conversion because there is an enough time for the free electrons and holes to be transported to the electrodes before they are quenched via electron-hole recombination. Thus, the PbS QD/TiO₂ system can be a good candidate for a PV cell with high efficiency.

ACKNOWLEDGEMENT

The TRXPS study was conducted using the facilities of the Synchrotron Radiation Research Organization, The University of Tokyo (Proposal No. 2019B7460). A financial support from MEXT, Japan (KAKENHI 16H06027) is appreciated.

REFERENCES

- [1] S. Rühle, *Sol. Energy* **130**, 139–147 (2016).
- [2] K. Ozawa *et al.*, *J. Phys. Chem. C* **123**, 4388–4395 (2019).
- [3] F. Roth *et al.*, *Phys. Rev. B* **99**, 020303(R) (2019).
- [4] S. Yamamoto *et al.*, *J. Synchrotron Radiat.* **21**, 352–365 (2014).

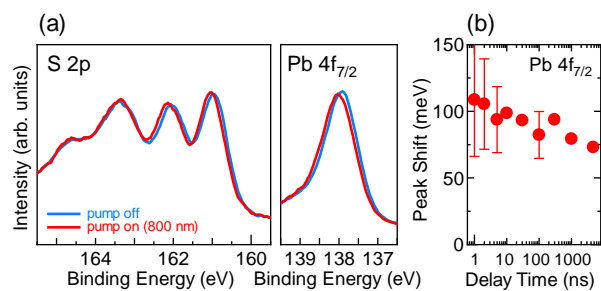


FIGURE 2. (a) Comparison of the S 2p and Pb $4f_{7/2}$ peaks of 3-nm PbS QD with and without 800-nm laser pulse irradiation. The photon energy was 370 eV. The spectra with laser irradiation were acquired at a delay time of 1 ns. (b) Change in the magnitude of the Pb $4f_{7/2}$ peak shift as a function of a delay time.

Photo-induced valence transition dynamics of SmS studied by time-resolved x-ray absorption spectroscopy

H. Watanabe^A, T. Nakamura^A, Y. Shibata^A, K. Yamagami^B, Y. Hirata^C, K. Ikeda^B, Y. Zhang^D, H. Wadati^D, K. Imura^E, H. S. Suzuki^B, N. K. Sato^E, S. Kimura^A

^AOsaka University, ^BISSP, The University of Tokyo, ^CNational Defense Academy, ^DUniversity of Hyogo, ^ENagoya University

Samarium monosulfide (SmS) is known to show a phase transition (namely BG transition) from a black insulator phase to a valence-fluctuating golden metal phase by applying pressure and/or elemental substitution (yttrium doping) [1]. Although the research has a long history for about 50 years, the origin of the BG transition has not been revealed yet. One possibility of the origin is due to an instability of excitonic states, namely excitonic instability [2]. If so, when the exciton states are produced by photo-irradiation, a phase transition like the BG transition is supposed to occur. So far, we have reported the existence of a metastable state of yttrium-doped SmS accompanied by high carrier density by photo-irradiation [3]. However, it has not been revealed that the metastable state is related to the valence transition. In this study, to clarify the valence change of Sm ions by photo-irradiation, we measured the temporal structure of the Sm $3d_{5/2}$ XAS after the photo-irradiation.

The time-resolved pump-probe XAS experiment was performed at BL07LSU of SPring-8 using the H mode (11/29-filling + 1-bunch). The Sm $3d_{5/2}$ core level absorption peak at about 1080 eV was used to evaluate the ratio between Sm^{2+} and Sm^{3+} ions. A Ti:sapphire laser (pulse width: 50 fs, photon energy: 1.55 eV, repetition rate: 1 kHz) synchronized with the synchrotron radiation x-ray (pulse width: 50 ps) was used as the pump light.

Figure 1 shows the time evolution of the signal intensity of 1077 eV (Sm^{2+} $3d_{5/2}$ core level) before and after the one-laser-pulse irradiation at 0 ps, but no significant change was observed after the photo-irradiation. The same result was obtained at the Sm^{3+} $3d_{5/2}$ peak at 1080 eV. These suggest that the spectral change due to the one-pulse irradiation was less than the experimental accuracy of about 1 % estimated from the variation in strength before the pump pulse irradiation ($t < 0$ ps) as shown in Fig. 1. According to our time-resolved reflectance measurements, a 20-% change of the reflectivity was observed just after the photo-irradiation, but the change was relaxed to less than 1 % within 1 ps. Therefore, no spectral change in the

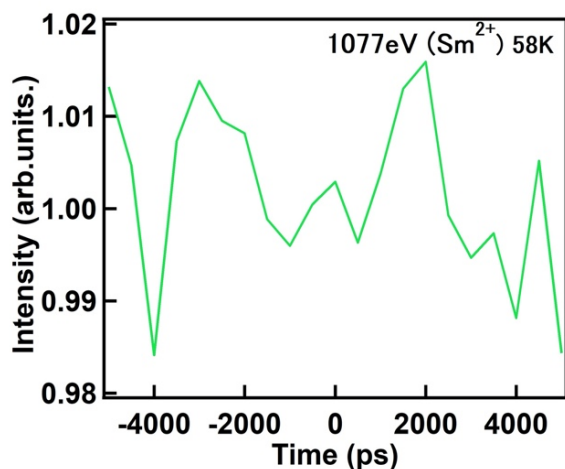


Fig. 1. Time development of the peak intensity at 1077 eV before and after photo-irradiation at the time of 0 ps.

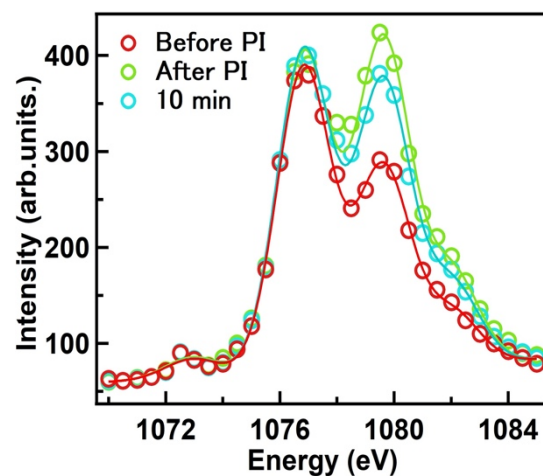


Fig. 2. XAS spectra of the Sm $3d_{5/2}$ core level before (red), just after (green) and 10 minutes after (blue) the photo-irradiation (PI). The spectra were normalized by the peak intensity at 1077 eV.

XAS result by one laser pulse is consistent with our previous time-resolved reflectance measurement.

Next, the time evolution of the Sm $3d_{5/2}$ XAS spectrum after many light pulses irradiation was measured. Figure 2 shows the Sm $3d_{5/2}$ core absorption spectra before (red), immediately after (green) and 10 minutes after (blue) the photo-irradiation for 1 hour at a temperature of 58 K. The absorption shape obviously changes by time suggesting the temporal change of the mean valence. Also, combined with no temporal change by one pulse excitation, the valence change by one pulse is too small to be observed and it is piled up by many pulses because it does not relax completely before the next pulse after 1 ms.

Before the photo-irradiation, not only the peak at 1077 eV (mainly originating from a Sm^{2+} component) but also the peak at 1080 eV (mainly from Sm^{3+}) was observed suggesting the intermediate valence of Sm ions. From Figure 2, combined with core level calculations, the mean valence can be roughly evaluated from the ratio of peak intensity at 1077 eV and 1080 eV as shown in Fig. 3. The mean valence before the photo-irradiation was evaluated as 2.40. Just after the photo-irradiation shown by blue circles, the intensity of the Sm^{3+} peak increased compared to that of Sm^{2+} suggesting the mean valence of Sm increased to 2.51 by many laser pulses. After 10 minutes, the mean valence of Sm decreased to 2.47, but the mean valence does not come back to the original value even after 1 hour. The origin of the remained higher valence cannot be explained by a very long relaxation time because surface oxidation also makes a valence change from Sm^{2+} to Sm^{3+} . However, since the decrease of the mean valence after 10 min is the opposite change to the oxidation, it suggests the relaxation from Sm^{3+} to Sm^{2+} without photo-irradiation. This implies that the photo-excited Sm^{3+} intermediate state decays to the Sm^{2+} ground state by a very long relaxation time for several 10 min. The detailed relaxation dynamics is reported in a separate report [4].

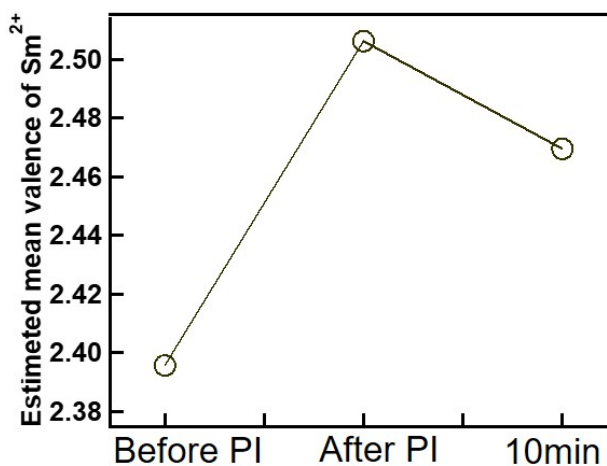


Fig. 3. Time evolution of the mean valence before and after one-hour laser pulse irradiation (PI). The mean valence is obtained by the ratio between the 1077-eV and 1080-eV peaks.

REFERENCES

- [1] K. Matsubayashi *et al.*, J. Phys. Soc. Jpn. **76**, 064601 (2007).
- [2] T. Mizuno *et al.*, J. Phys. Soc. Jpn. **77**, 113704 (2008).
- [3] R. Ikeda *et al.*, J. Phys.: Conf. Ser. **1220**, 012005 (2019).
- [4] H. Watanabe *et al.*, ACTIVITY REPORT OF SYNCHROTRON RADIATION LABORATORY 2019, ISSP, The University of Tokyo.

Relaxation dynamics of Photo-induced valence transition of SmS studied by time-resolved x-ray absorption spectroscopy

H. Watanabe^A, T. Nakamura^A, Y. Shibata^A, K. Yamagami^B, Y. Hirata^C, K. Ikeda^B, Y. Zhang^D,
H. Wadati^D, K. Imura^E, H. S. Suzuki^B, N. K. Sato^E, S. Kimura^A

^AOsaka University, ^BISSP, The University of Tokyo, ^CNational Defense Academy,
^DUniversity of Hyogo, ^ENagoya University

Samarium monosulfide (SmS) is known to show a phase transition (BG transition) from a black insulator phase to a valence-fluctuating golden metal phase by applying pressure and/or elemental substitution (yttrium doping) [1]. We have reported the existence of a metastable state of yttrium-doped SmS accompanied with high carrier density by photo-irradiation [2] and the valence transition from Sm²⁺ to Sm³⁺ could be occurred by photo-irradiation at 58 K by the time-resolved x-ray absorption spectroscopy (trXAS) [3]. In the trXAS, the valence change of Sm could not be observed by one-pulse excitation, but after the many pulse irradiation, the valence finally changes from 2.40 to 2.51. This suggests that the photo-excited metastable state has a very long life-time than the interval of the pump pulse (1 ms) and it is piled up by the multi-pulse excitation, and finally, the photo-excited state could be observed. The origin of the metastable state is related to the pressure-induced BG transition and recently observed non-linear conduction phenomena of black-SmS [4].

The origin of the metastable state, as well as the valence transition by the photo-irradiation, has not been clarified yet. One possibility is the BCS-to-BEC transition of the photo-excited exciton state, namely “excitonium” [5]. The excitonium is expected to have carriers, so the other experiment to detect the time-dependence of carrier density, band structure, and lattice constants must be combined with trXAS. In this study, to evaluate the lifetime of the photo-excited state, we measured the relaxation dynamics after multi-pulse excitation.

The time-resolved pump-probe XAS experiment was performed at BL07LSU of SPring-8 using the H mode (11/29-filling + 1-bunch). The Sm 3d_{5/2} core level absorption peak at about 1080 eV was used to evaluate the ratio between Sm²⁺ and Sm³⁺ ions. A Ti:sapphire laser (pulse width: 50 fs, photon energy: 1.55 eV, repetition rate: 1 kHz) synchronized with the synchrotron radiation x-ray (pulse width: 50 ps) was used as the pump light.

Figure 1 shows the temporal structure of the 1080-eV peak after the 5-min (about 300,000 laser pulse) laser irradiation. The valence of the photo-excited state has been evaluated as about 2.5 [3], which is smaller than that of the golden phase (2.6-2.7) induced by pressure [6]. So, the consistency between the photo-excited state and the golden phase is still unclear but it is obviously different from that of the divalent black phase. The photo-excited state might be a new

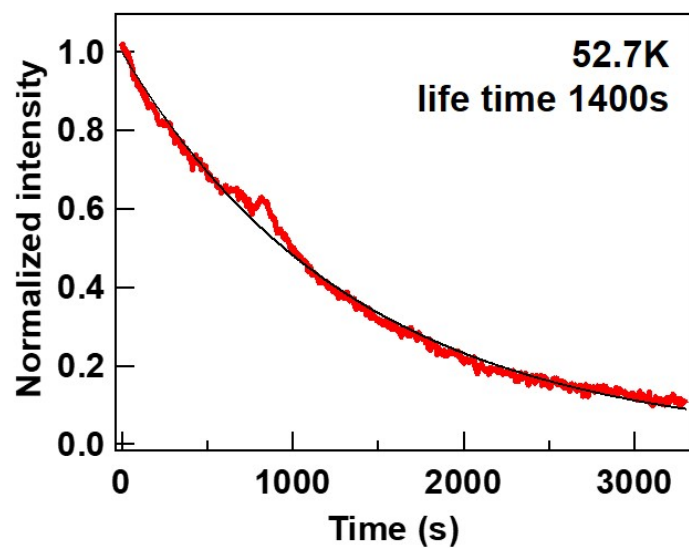


Fig. 1. Temporal structure of the 1080-eV peak at 52.7 K. The time dependence can be fitted by an exponential decay curve with a lifetime of 1400 s.

intermediate state. The decay curve can be fitted by an exponential relaxation with ~~the~~a lifetime of 1400 s (about 23 min), i.e., the photo-excited intermediate state has a very long time. To clarify the origin of the photo-excited state, a further trXAS and other time-resolved experiments are needed.

REFERENCES

- [1] K. Matsubayashi *et al.*, J. Phys. Soc. Jpn. **76**, 064601 (2007).
- [2] R. Ikeda *et al.*, J. Phys.: Conf. Ser. **1220**, 012005 (2019).
- [3] H. Watanabe *et al.*, ACTIVITY REPORT OF SYNCHROTRON RADIATION LABORATORY 2019, ISSP, The University of Tokyo.
- [4] H. Ando *et al.*, JPS Conf. Proc. **30**, 011132 (2020).
- [5] B. I. Halperin and T. M. Rice, Rev. Mod. Phys. **40**, 755 (1968).
- [6] K. Imura *et al.*, JPS Conf. Proc. **30**, 011131 (2020).

LOW-TEMPERATURE METHANE OXIDATIVE COUPLING ON MODIFIED PD MODEL CATALYSTS STUDIED BY *OPERANDO* AMBIENT-PRESSURE XPS

Takanori Koitaya,[†] Susumu Yamamoto,[‡] Iwao Matsuda,[‡] Jun Yoshinobu[‡] and Toshihiko Yokoyama[†]

[†] *Department of Materials Molecular Science, Institute for Molecular Science*

[‡] *The Institute for Solid State Physics, The University of Tokyo*

Direct observation of heterogeneous catalysts under operation condition is important for understanding reaction mechanism and nature of active sites on the catalysts. Various *operando* methods have been developed to investigate surface chemistry on heterogeneous catalysts. We have investigated reactions of inert molecules, such as carbon dioxide and methane, using an ambient-pressure XPS (AP-XPS) system at SPring-8 soft X-ray beam line BL07LSU [1, 2]. The XPS measurements can be currently performed in the presence of reactant gases up to 2000 Pa using synchrotron radiation or a conventional X-ray source. In the gas environment, the sample can be heated up to around 900 K to investigate thermal reaction on the surface of catalysts.

In this study, oxidation of methane on the Pd(110) surface was studied by AP-XPS and QMS. Fig. 1 shows QMS spectra of reaction products and sample temperature of the Pd(110) surface in the presence of 2.0 mbar oxygen and 5.6 mbar methane. As shown in Fig. 1, reactivity of the Pd(110) sample was very low, when the sample was heating from room temperature to 615 K in the presence of the feed gases. However, the amount of the products increased significantly after heating to 780 K.

Chemical states of the surface during the reaction were investigated by *operando* AP-XPS. Fig. 2 shows AP-XPS spectra measured at sample temperature of 615 K. Before heating to 780 K, the surface of the sample was oxidized, and PdO thin film was formed as indicated by Pd 3d and O 1s spectra. In addition, peaks of adsorbed species were observed in O 1s and C 1s, which can be attributed to oxidized carbon species (CO_x). Since the surface before heating to 780 K is less reactive, the observed adsorbate is not an important reaction intermediate, but a spectator or poisoning species. After the activation process, Pd 3d and O 1s spectra shows that the sample was still (partially) oxidized. In O 1s and C 1s spectra, gas-phase peaks of the produced species (water and CO₂) were observed, indicating that this surface is much more reactive. Note that the adsorbed CO_x was not observed after the activation process. This indicates that coverage of the intermediates is negligible during the methane oxidation reaction. Therefore, the rate-limiting step for the methane oxidation is dissociative adsorption of methane. Once the formation of CH₃ species occurs, following reactions, including desorption of products, proceed at much faster rates compared to the initial methane dissociation.

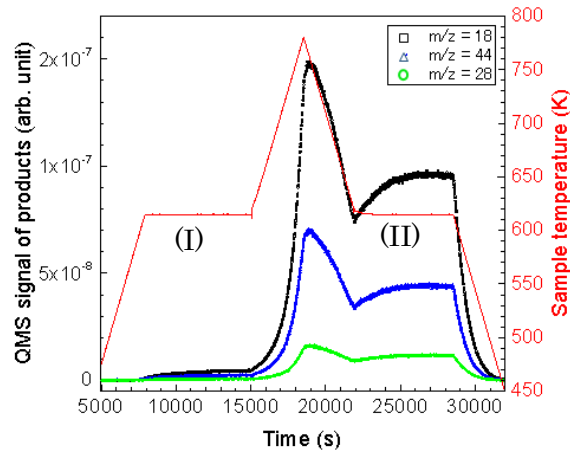


Figure 1. QMS spectra of oxidation products (water, CO, CO₂) on the Pd(110) surface in the presence of 2.0 mbar oxygen and 5.6 mbar methane. Sample temperature is also shown in the figures.

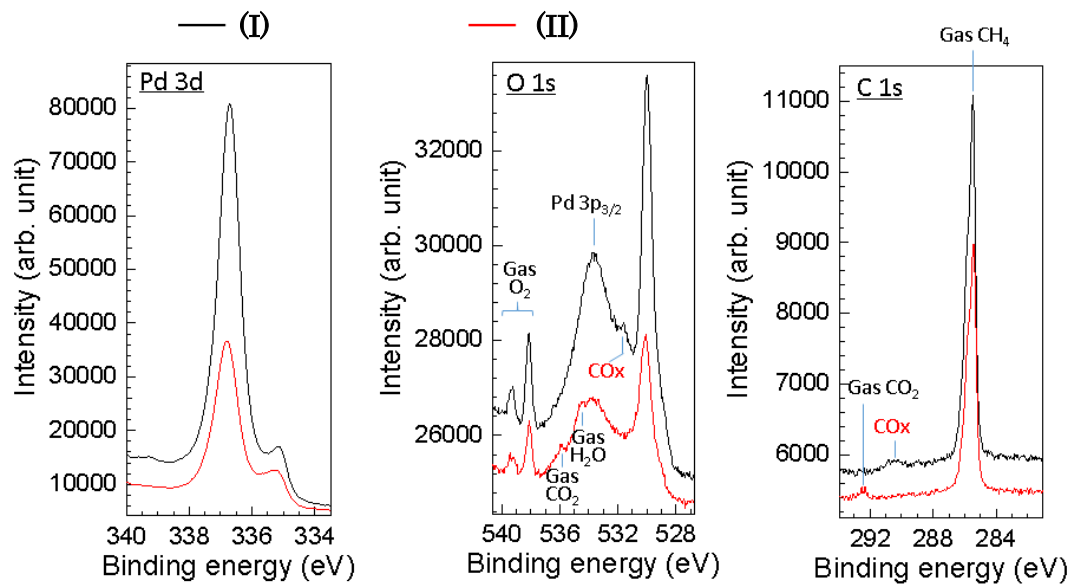


Figure 2. AP-XPS spectra measured at region (I) and (II) indicated in Fig. 1. During the measurement, the Pd(110) sample was kept at 615 K in the presence of 2.0 mbar oxygen and 5.6 mbar methane gases.

REFERENCES

- [1] Koitaya, T. et al., *Top. Catal.* **59**, 526-531 (2016).
- [2] Koitaya, T. et al., *e-J. Surf. Sci. Nanotech.* **17**, 169-178 (2019).

X-ray Spectral Imaging Analysis of Interface States at p^+ -WSe₂/ n -MoS₂ Hetero Junctions in TFET Device Structure

Naoka Nagamura^{1,2}, Keigo Nakamura³, Hayami Kawamoto³, Naoki Higashitarumi³, Keishi Akada⁴, and Kosuke Nagashio³

¹National Institute for Materials Science (NIMS), Tsukuba, Ibaraki, Japan.

²PRESTO, Japan Science and Technology Agency, Honcho, Saitama, Japan.

³Department of Materials Engineering, The University of Tokyo, Hongo, Tokyo, Japan.

⁴Institute for Solid State Physics, The University of Tokyo, Kashiwa, Chiba, Japan.

Reducing power consumption in semiconductor devices is an imminent challenge, but the present field effect transistors (FETs) require at least 60 mV of gate voltage to increase the current by one order of magnitude at room temperature. Tunnel FETs can overcome this limitation because of the band-to-band tunnelling (BTBT).

Two-dimensional materials are promising for TFETs. Recently, using p^+ -WSe₂ source doped by charge transfer from a WO_x surface oxide layer, we succeeded in observing a clear BTBT in the stable TFET system of p^+ -WSe₂/ n -MoS₂[1].

In this study, we systematically study the local band alignment in the p^+ -WSe₂/MoS₂ TFET device structure as shown in Fig. 1 by scanning photoelectron emission microscopic (SPEM) measurements using a three-dimensional nanoscale electron- spectroscopy chemical analysis (3D nano-ESCA) system installed at BL07LSU of SPring-8.

2D materials used in the sample are fabricated by exfoliation of bulk crystals. WO_x side of WSe₂ film is transferred onto h -BN on a SiO₂/ n^+ -Si substrate after forming WSe₂/WO_x by O₃ annealing. Then, the p^+ -WSe₂/MoS₂ heterostructures were fabricated via dry transfer method using PDMS under the alignment system. Ni/Au was deposited as source/drain electrodes by EB lithography.

Figure 2a shows an intensity mapping image for the Mo $3d$ $5/2$ peak for the 3L- n -MoS₂/ p^+ -WSe₂ heterostructure on h -BN. The position of the heterostructure is clearly identified. Figure 2b shows the pinpoint core-level spectra for W $4f$ $5/2$ and $4f$ $7/2$ peaks recorded at points of (i) p^+ -WSe₂/ h -BN and (ii) 3L- n -MoS₂/ p^+ -WSe₂/ h -BN. W $4f$ peaks for (ii) p^+ -WSe₂ in contact with 3L- n -MoS₂ shifts to the higher binding energy side than that for (i) p^+ -WSe₂ directly on h -BN. When p^+ -WSe₂ is doped with electron, E_F in p^+ -WSe₂ increases, resulting in the higher binding energy of W $4f$ peaks. Therefore, this data supports the p -doping reduction in WSe₂[2]. The mapping of the E_F modulation in p^+ -WSe₂ by the top gate is obtained by high-throughput peak fitting analysis using machine learning techniques[3].

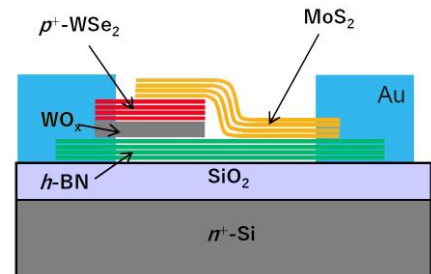


Fig. 1 Schematic image of a p^+ -WSe₂/MoS₂ TFET device structure

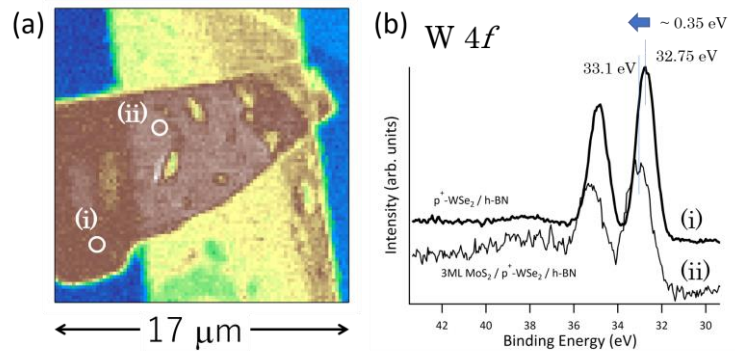


Fig. 2 (a) Photoelectron intensity mapping image for the Mo $3d$ $5/2$ peak for the 3L- n -MoS₂/ p^+ -WSe₂ heterostructure on h -BN. (b) Pinpoint core-level spectra for W $4f$ $5/2$ and $4f$ $7/2$ peaks recorded at points (i) and (ii).

We also worked on chemical characterization of monolayer tin monosulfide (SnS), a two-dimensional group IV monochalcogenides[4]. The special distribution of different phases, SnS, Sn₂S₃, and SnS₂, around the SnS single crystal nanosheet grown by the physical vapor deposition on a mica substrate has been clarified[5].

REFERENCES

- [1] J. He *et al.* Adv. Electron. Mater. **4**, 1800207 (2018).
- [2] K. Nakamura *et al.*, submitted.
- [3] T. Matsumura *et al.* Sci. Technol. Adv. Mater. **20**, 733 (2019).
- [4] N. Higashitarumi *et al.* Nature Commun. **11**, 2428 (2020).
- [5] H. Kawamoto *et al.*, submitted.

SOFT X-RAY ADSORPTION AND EMISSION SPECTROSCOPY OF THE INTERMEDIATE WATER IN BIOCOMPATIBLE POLYMERS

Shin-nosuke Nishimura¹, Keishi Akada³, Daiki Murakami^{1,2}, Kosuke Yamazoe³, Tomoya Ueda², Jun Miyawaki³, Yoshihisa Harada³, Masaru Tanaka^{1,2}

¹*Institute of Materials Chemistry and Engineering, Kyushu University,*

²*Graduate School of Engineering, Kyushu University,*

³*Institute for Solid State Physics, The University of Tokyo*

INTRODUCTION

Recently, significant efforts have been applied toward the design of polymer biomaterials which have central roles in regenerative medicine and tissue engineering application. Water definitely exists on an interface between material and biotissue, of which hydration state essentially affects for biocompatibility [1]. Hydrated water around polymer, as represented by poly(2-methoxyethyl acrylate) (PMEA), is classified into three types, non-freezing water (*NFW*), intermediate water (*IW*), free water (*FW*) in ascending order of the intensity of interaction with polymer chain [2]. Among them, the *IW* has a key role on the affinity of polymer with an organism. However, it has not been clarified what it is in a chemical structure of polymer that works on formation of the *IW*. As the first step to systematize relationship between the *IW* and polymer structure, we evaluated a hydration process on the PMEA brush depending on humidity and succeeded to detect the *IW* by soft x-ray absorption/emission spectroscopy (XAS/XES), whereas origin of the *IW* is still unclear [3, 4]. In this study, we designed and prepared the cyclic PMEA and linear poly(ethylene glycol) monomethyl ether (mPEG) brushes to examine effect of a polymer end and polymer species, respectively (Figure 1). The hydration process on these polymer brushes was evaluated by XAS/XES measurement using the same method as our previous reports.

EXPERIMENTAL

We prepared the cyclic PMEA and linear mPEG brushes on gold-coated SiC substrate by grafting-to method using sulfur-gold interaction (Figure 1). Thiol-terminated PMEA at both end was synthesized *via* reversible addition-fragmentation chain transfer (RAFT) polymerization and subsequent aminolysis. The obtained polymer was treated with iron(III) chloride under high-diluted condition, resulting in an objective cyclic PMEA. The number average molecular weight (M_n) and polydispersity index (\mathcal{D}) of cyclic PMEA were estimated to be 76000 g mol⁻¹ and 1.06 from size exclusion chromatography measurement, respectively. A commercially available product was used for thiol-terminated mPEG ($M_n = 10000$ g mol⁻¹, $\mathcal{D} = 1.13$). The gold-cated SiC substrates were soaked in methanol solutions of these polymers. The substrates were washed with methanol and dried *in vacuo* to give objective polymer brushes. Grafting density of the cyclic PMEA and linear was determined to be 0.048 and 0.11 chains nm⁻² by quartz crystal microbalance measurement, respectively.

XAS/XES measurement was performed at BL07LSU HORNET station in SPring-8. The humid air with controlled humidity was flowed on the samples to change the water contents in the brush samples

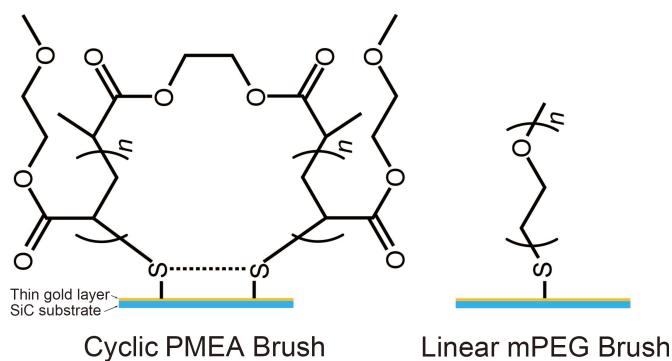


Figure 1. Chemical structure of cyclic PMEA and linear PEG brushes used in this study. These polymer brushes were prepared by grafting-to method.

RESULTS AND DISCUSSION

In the XES spectrum of bulk liquid water, two significant peaks are basically observed at ca. 525.6 eV and 526.8 eV corresponding to ordered hydrogen bonds (tetrahedral coordination) and distorted hydrogen bonds, respectively [5]. Figure 2 shows XES spectra of the cyclic PMEAs and linear mPEG brushes under the humidity control. In the low humidity range below a relative humidity of 65%, broad profiles peaked at the tetrahedrally-coordinated component dominates along with a sharp peak at ca. 527.1 eV. Above a relative humidity of 75%, increase of the peak at 526.5 eV was observed from the both spectra. We reported that *IW* was formed on the linear PMEAs brush at a relative humidity of 75% [4]. The hydration behaviors obtained from this experiment were similar to that of our previous study, indicating that the *IW* existed on the cyclic PMEAs and linear PEG brushes. Interestingly, formation of the *IW* on the cyclic PMEAs brush significantly increased compared with that on the linear PMEAs brush even though these polymer brushes had the same monomer unit and chemical component. This result suggested that the cyclic PMEAs brush formed nano-scaled space based on its loop structure and promoted adsorption of interfacial water by confinement effect. There is a possibility that the cyclic PMEAs brush shows higher biocompatibility than the linear PMEAs.

In this study, we successfully carried out to trace hydration process of the interfacial water including *IW* onto the cyclic PMEAs and linear mPEG brushes by XAS/XES measurement with humidity control. State of polymer chain on the outermost of surface might have a great effect on structure of the interfacial water. Although this challenging experiment make it increasingly clear that the origin of *IW* and the relationship of chemical structure with *IW* formation, the knowledge still is not enough to accomplish the ultimate design of biomaterial. Further investigation will be performed in our future work in order to clarify the essential feature of *IW* and the role on biocompatibility.

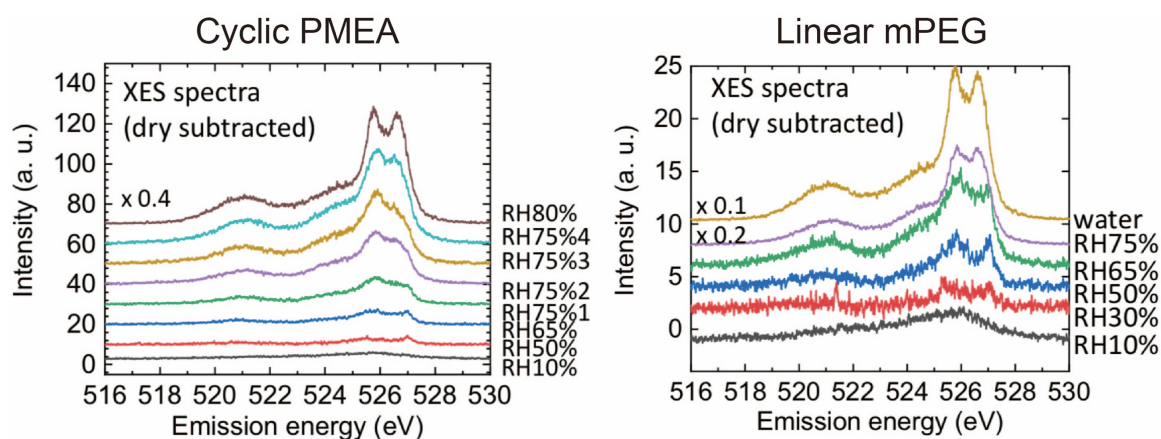


Figure 2. XES spectra of cyclic PMEAs and linear mPEG brushes under the humidity control.

REFERENCES

- [1] T. Tsuruta, *J. Biomater. Sci. Polym. Ed.*, **2010**, *21*, 1831-1848.
- [2] M. Tanaka *et al.*, *Polym. Int.*, **2000**, *49*, 1709-1713.
- [3] D. Murakami *et al.*, *Activity Report of Synchrotron Radiation Laboratory 2018*, **2019**, 68-69.
- [4] D. Murakami *et al.*, *Activity Report of Synchrotron Radiation Laboratory 2018*, **2019**, 70-71.
- [5] T. Tokushima *et al.*, *Chem. Phys. Lett.*, **2008**, *460*, 387-400.

DEVELOPMENT OF TIME-RESOLVED X-RAY PHOTOELECTRON DIFFRACTION FOR THE OBSERVATION OF THE STRUCTURAL DYNAMICS OF EPITAXIAL SILICENE

Kouichi Hayashi^{1,2}, Artoni Kevin R. Ang¹, Koji Kimura¹, Yuichiro Fukatsu¹,
Susumu Yamamoto³, Iwao Matsuda³, Takahiro Yonezawa⁴, Antoine Florence⁴,
Yukiko Yamada-Takamura⁴

¹Department of Physical Science and Engineering, Nagoya Institute of Technology, Nagoya, Japan

²Frontier Research Institute for Materials Science, Nagoya Institute of Technology, Nagoya, Japan

³Institute of Solid State Physics, The University of Tokyo, Kashiwanoha, Chiba, Japan

⁴School of Materials Science, Japan Advanced Institute of Science and Technology, Ishikawa, Japan

Introduction

Over the past half-century, photoelectron spectroscopy (PES) has become one of the most important experiments in physics, chemistry and material science. Among the related techniques, X-ray photoelectron diffraction (XPD) has grown into a powerful technique in studying surface structures. Since the first reported XPD experiments by Siegbahn and Fadley in the 1970's, XPD has been used to investigate the structures of surface reconstructions, adsorbates, interfaces and thin films.

Through the years, PES has evolved significantly alongside the rapid developments in electron spectrometers, synchrotron radiation facilities, laser light sources, and other related technologies. Typical PES experiments can now resolve nm-resolution spatial information, time-resolved and even spin-resolved information. Taking advantage of these developments, new dimensions of space-, time- and spin- can be incorporated into XPD experiments.

In this work, we demonstrate, for the first time, time-resolved X-ray photoelectron diffraction (trXPD) of an epitaxial silicene layer using a time-resolved two-dimensional angle-resolved time-of-flight (2DARTOF) system. The evolution of the diffraction rings (DR) and the forward focusing peaks (FFP) after laser irradiation can be used to extract atomic resolution structural information about the surface structure (Fig. 1). The 2DARTOF system in BL07LSU is well suited for this experiment because of its high energy and angular resolutions, and most importantly, its simultaneous recording of the photoemission intensity as a function of θ_x , θ_y , and E .

Experiment and data processing

The experiments were performed using an epitaxial silicene sample grown on a ZrB₂ thin film [1]. It has been shown that this epitaxial silicene layer has minimal electronic interactions with the substrate, and that the silicene layer buckled easily, resulting in a mixed sp²/sp³ hybridization that can be tuned to control its electronic properties [2,3]. XPS studies have shown that the Si atoms occupy at least 3 chemically different sites, and that the surface structure consists of a planar surface structure with an adatom [3,4]. This sample was chosen because of its relatively simple surface structure, and the current interest in silicene for next generation electronic device applications.

The sample was prepared *in situ* by the spontaneous segregation during the annealing of the ZrB₂/Si(111) substrate at 800°C [1]. LEED and the Si 2p core-level spectra confirm the formation of a well-defined silicene layer.

The photoemission experiments were done using a photon energy of $h\nu = 300$ eV. The ARTOF detector was set to simultaneously measure the photoemission intensity with an acceptance angle of $\pm 13^\circ$, within the energy range 97-103 eV. To obtain a larger section of the hologram pattern, the sample's orientation was scanned along the [1120] direction. For the time-resolved experiments, a 1.5 eV, 208 kHz laser was used.

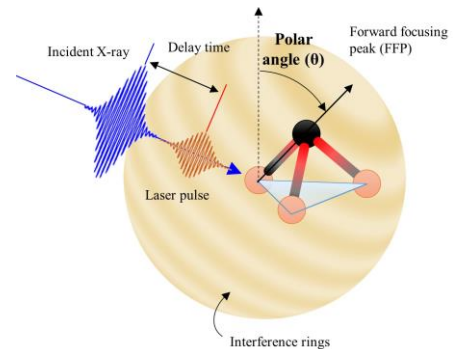


Fig. 1. Schematic diagram of the time-resolved XPD experiment.

Compared to other electron detector systems used in XPD, the 2DARTOF system has a major advantage in that it can simultaneously measure $I(\theta_x, \theta_y, E)$ (Fig. 2a). To extract the angle-integrated Si 2p spectra, the raw data is integrated along both the θ_x and θ_y directions. To get the XPD spectra, the raw data is integrated within a small energy region centred around the Si 2p binding energy (Fig. 2c). However, this will contain XPD signal from Si atoms at all sites. To separate the XPD patterns from the Si atoms occupying different sites, peak fitting of the spectra at each (θ_x, θ_y) pixel is done [5].

The extracted XPD patterns are then normalized by a background image obtained by integrating the raw 3D data within a narrow energy region in the low binding energy side.

Results

Figure 3a shows the “planar” structural model of epitaxial silicene showing the 3 distinct sites occupied by Si atoms. From the peak fitting of the angle integrated Si 2p spectra (Fig. 3b), the 2 main peak components corresponding to the Si atom at the Si_A and Si_B sites were resolved. The simulated and experimental XPD patterns extracted for these peak components are shown in Fig. 3c) and 3d), where the DR and FFPs in the simulation are well resolved in the experiment.

Epitaxial silicene consists mostly of in-plane scatterers, and thus the XPD patterns are dominated by these DRs. In XPD pattern of Si_B, a strong FFP at $\theta \sim 48^\circ$ is observed, which corresponds to the direction of the Si_C atom from the Si_B emitter. This confirms that the 2DARTOF system can be a viable system for XPD measurements.

Conclusion

In this work, we have demonstrated for the first time that the 2DARTOF system is well-suited in XPD experiments. The simultaneous measurement of $I(\theta_x, \theta_y, E)$, makes acquisition of XPD patterns faster, opening up the possibility of time-resolved XPD measurements. In our future work, we will obtain the trXPD patterns of epitaxial silicene in the pump-probe scheme.

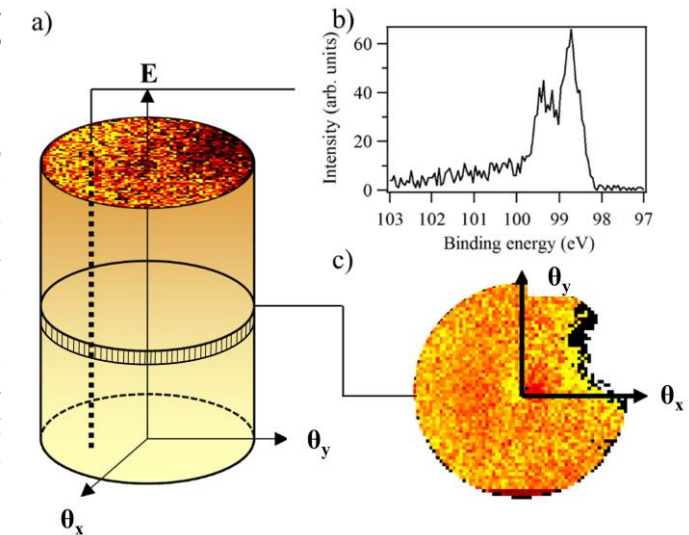


Fig. 2. a) Schematic diagram of the raw data obtained by the 2DARTOF system, b) a typical Si 2p spectra from a (θ_x, θ_y) pixel, and c) a raw 2D cut taken at the Si 2p binding energy.

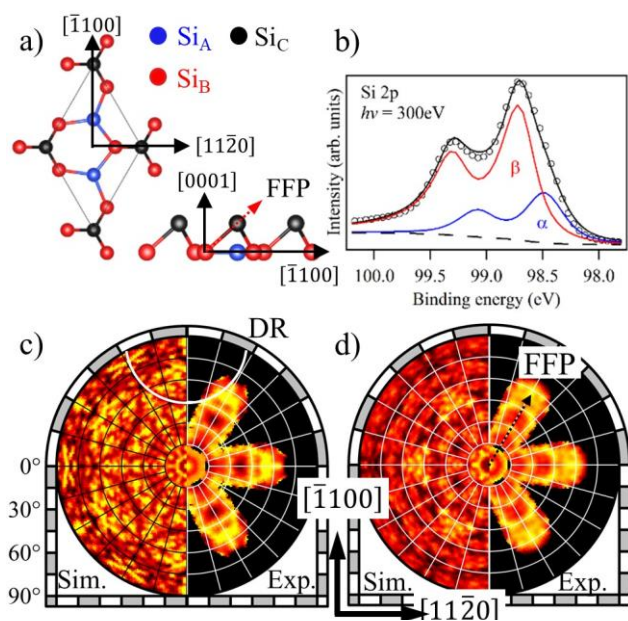


Fig. 3. a) “Planar” model for epitaxial silicene, b) the Si 2p core level spectra measured from the sample, and simulated and experimental XPD patterns from the c) Si_A and d) Si_B component.

REFERENCES

- [1] A. Fleurence, et al., Phys. Rev. Lett. **108**, 245501 (2012).
- [2] R. Friedlein and Y. Yamada-Takamura. J. Phys. Condens. Matter **27**, 203201 (2015).
- [3] C.C. Lee, et al., Phys. Rev. B, **90**, 075422 (2014).
- [4] R. Friedlein, et al., J. Chem. Phys. **140**, 184704 (2014).
- [5] K. Tsutsui, et al., Nano Lett. **17**, 7533 (2017).

TIME-RESOLVED X-RAY PHOTOELECTRON DIFFRACTION STUDY OF EPITAXIAL SILICENE

Kouichi Hayashi^{1,2}, Artoni Kevin R. Ang¹, Koji Kimura¹, Yuichiro Fukatsu¹,
Susumu Yamamoto³, Iwao Matsuda³, Takahiro Yonezawa⁴, Antoine Fleurence⁴,
Yukiko Yamada-Takamura⁴

¹Department of Physical Science and Engineering, Nagoya Institute of Technology, Nagoya, Japan

²Frontier Research Institute for Materials Science, Nagoya Institute of Technology, Nagoya, Japan

³Institute of Solid State Physics, The University of Tokyo, Kashiwanoha, Chiba, Japan

⁴School of Materials Science, Japan Advanced Institute of Science and Technology, Ishikawa, Japan

Introduction

Silicene is a monolayer of Si atoms arranged in a honeycomb lattice that exhibits massless Dirac fermions, similar to its carbon based counterpart in graphene. The development of silicene based devices has seen significant interest recently because of the expected remarkable electronic properties, stronger spin-orbit coupling of Si, and the ease of adapting such technologies into the already Si-based manufacturing infrastructure. Until recently, silicene could only be synthesized on conductive substrates, resulting in electronic interactions with the substrate. It was recently demonstrated that silicene with minimal substrate interactions can be grown on a ZrB₂/Si(111) substrate through the surface segregation of Si atoms[1]. This silicene layer was found to buckle easily, resulting in sp²/sp³ hybridization that can be tailored to tune its electronic properties [1,2]. Photoemission studies have shown that the Si atoms occupy at least 3 chemically different sites on the silicene layer (Fig. 1a) [1,3]. In this study, we investigate the local structures of epitaxial silicene and the structural dynamics induced by laser irradiation.

Experiment

The sample was prepared *in situ* by the spontaneous segregation during the annealing of the ZrB₂/Si(111) substrate at 800°C [1]. The ZrB₂/Si(111) substrate was prepared elsewhere, and degassed in the prior to sample preparation. The silicene surface was confirmed by LEED and the core-level spectra.

The photoemission experiments were done using a photon energy of $h\nu = 300$ eV. The ARTOF detector was set to simultaneously measure the photoemission intensity with an acceptance angle of $\pm 13^\circ$, within the energy range 97-103 eV. To obtain a larger section of the hologram pattern, the sample's orientation was scanned along the [11 $\bar{2}$ 0] direction. For the time-resolved experiments, a 1.5 eV, 208 kHz laser was used.

Results

The LEED and Si 2p spectra confirmed the formation of a well-defined silicene layer. From the peak fitting of the Si 2p spectra (Fig. 1b), the 2 main peak components of silicene were resolved. These 2 peaks correspond to the Si atoms occupying the Si_A and Si_B sites in Fig. 1a [2,3]. The XPD patterns of these 2 peak components were extracted by peak fitting [5], and are shown in the right hemispheres of Fig. 1c and 1d. The corresponding simulations are shown in the left hemispheres of Fig. 1c and 1d. Some diffraction rings (DR) and forward focusing peaks (FFP) in the simulations are well reproduced in the experiment.

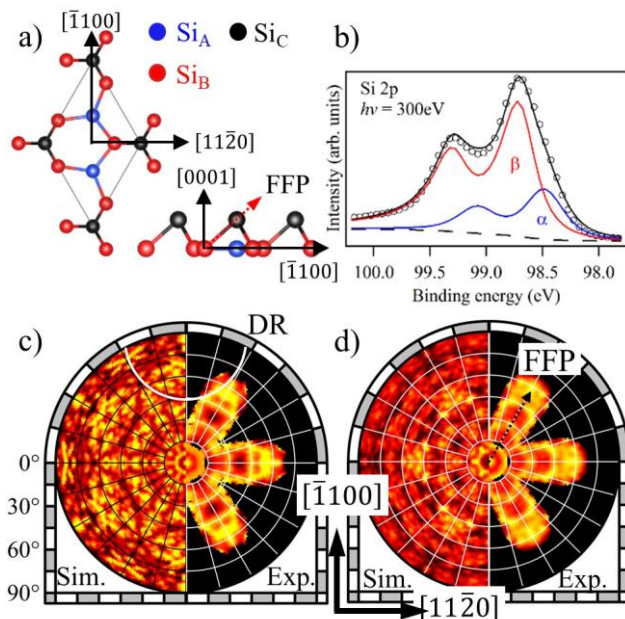


Fig. 1. a) “Planar” model for epitaxial silicene, b) the Si 2p core level spectra measured from the sample, and simulated and experimental XPD patterns from the c) Si_A and d) Si_B component.

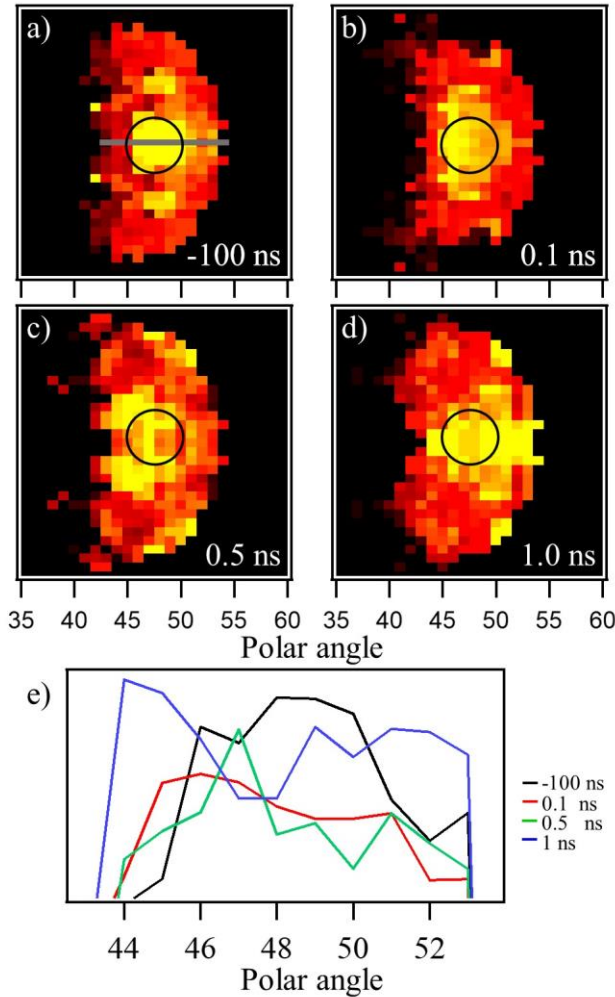


Fig. 2. The time-resolved XPD patterns of the SiB component taken at various delay times: a) -100ns, b) 0.1 ns, c) 0.5 ns and d) 1.0 ns, and e) the line profiles taken across the FFP.

to probe the structural dynamics of surfaces. Analysis of the evolution of the diffraction rings and forward focusing peaks in the XPD patterns can provide element sensitive, atomic resolution structure information about surfaces. Further experiments and first principles calculations are needed to completely understand the evolution of the epitaxial silicene structure after laser-induced heating.

REFERENCES

- [1] A. Fleurence, et al., Phys. Rev. Lett. **108**, 245501 (2012).
- [2] R. Friedlein and Y. Yamada-Takamura. J. Phys. Condens. Matter **27**, 203201 (2015).
- [3] C.C. Lee, et al., Phys. Rev. B, **90**, 075422 (2014).
- [4] R. Friedlein, et al., J. Chem. Phys. **140**, 184704 (2014).
- [5] K. Tsutsui, et al., Nano Lett. **17**, 7533 (2017).
- [6] K.J. Gaffney, et al., Phys. Rev. Lett. **95**, 125701 (2005).
- [7] M. Harb et al. Phys. Rev. Lett., **100**, 155504 (2008).

In this sample, most of the neighboring scatterers are in-plane, thus the XPD patterns are dominated by these DRs. Meanwhile, the XPD pattern of Si_B shows a strong FFP at $\theta \sim 48^\circ$, which corresponds to the direction of the Si atom at the Si_C site from the emitter at Si_B.

In the time-resolved experiments, we focused on this FFP at $\theta \sim 48^\circ$ to observe any changes in the surface structure. At -100 ns, the FFP is observed as a strong peak (marked with the black circle in Fig. 2a). At later delay times (Figs. 2b, 2c, 2d), the FFP is first seen decreasing in peak intensity and shifting to lower θ (0.1 and 0.5 ns), before shifting to higher θ and recovering its intensity (1.0 ns). At 1.0 ns, the shift to higher polar angles corresponds to an in-plane expansion of the silicene layer, which could be explained by laser-induced thermal expansion.

Meanwhile, at 0.1 and 0.5 ns, the decrease in FFP peak intensity suggests an intermediate structure that occurs before the onset of thermal equilibrium between the photoexcited electrons and phonons. This could be due to bond softening due to the increased anti-bonding character of the excited charge distribution. At higher laser fluence, it has been reported that this can even result in bond breaking and the formation of disordered state, a non-thermal melting of the surface [6,7].

While the details of the structural changes observed in silicene is still not clear, this work has demonstrated that time-resolved XPD experiments are now feasible and can be used

ELECTRIC STRUCTURE OF WATER IN THE VICINITY OF MODEL ORGANIC SURFACES BY X-RAY EMISSION SPECTROSCOPY

Tomohiro Hayashi

Department of Materials Science and Engineering, School of Materials and Chemical Technology

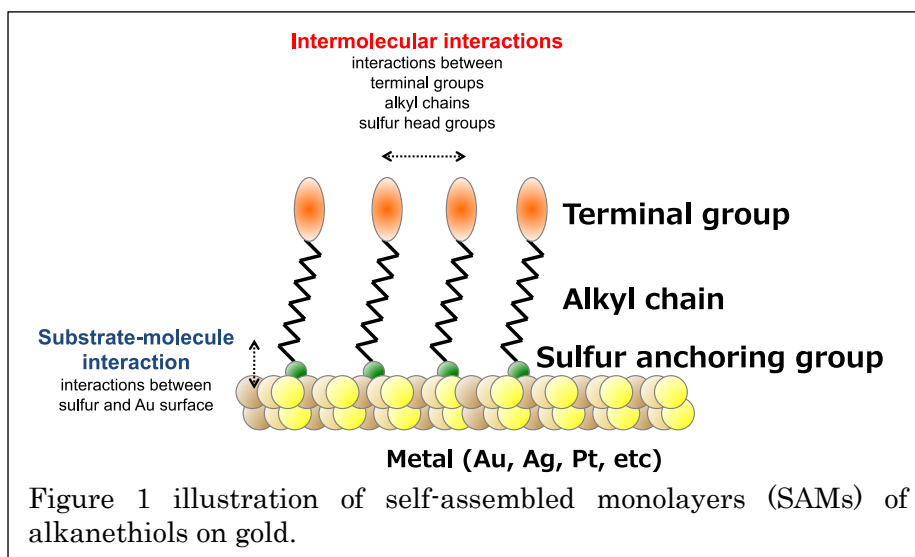
Tokyo Institute of Technology

JST-PRESTO

Introduction

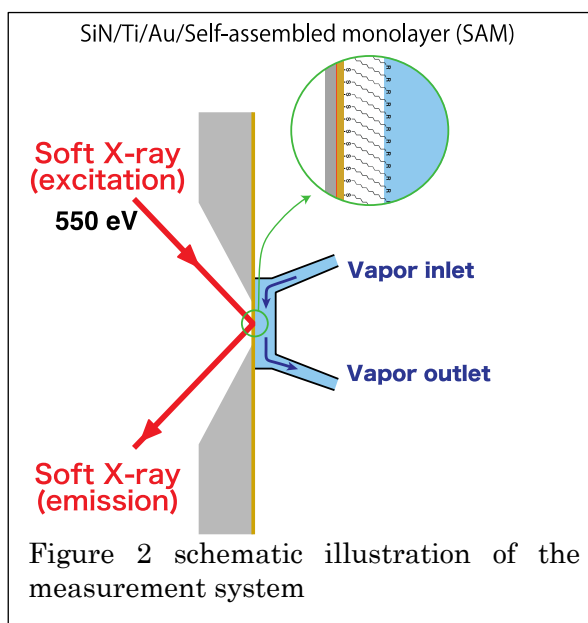
Self-assembled monolayers (SAMs) have been employed as model organic surfaces since the 1980s (Figure 1). Just by changing the terminal groups of the molecules, we can easily control the physicochemical properties of the surfaces. In a field of biomaterial and biosensing, SAMs are

often employed as scaffolding layers for protein and cells or passivating layer preventing non-specific adsorption of non-target molecules.¹ Recently, water-mediated force has been found to play an important role to govern the interaction of materials with protein molecules and cells.²⁻⁵ However, the properties of the interfacial water, in particular, hydrogen bonding state and the mechanism underlying the water-mediated force are still matters of intense debate.¹ In this work, we attempt to answer these questions by using X-ray emission spectroscopy (XES), which provides a detailed picture of the hydrogen bonding state of water.



Experimental

In this work, we employed a measurement setup shown in Fig. 2. SAMs were formed on the backside of the window. In this work, we used 8 types of SAMs. They are hydrophobic (methyl-terminated: C8), hydrophilic (hydroxy-terminated: OH), positively charged (trimethylamine-terminated: TMA), negatively charged (sulfuric acid-terminated: SA), and non-fouling [oligoethylene glycol: EG and sulfobetaine: SB]. The humidity is changed to vary the amount of water condensed on the SAMs. The energy of the incident X-ray was fixed at 550 eV.



Results and discussion

We confirmed that the thickness of the water strongly depended on the humidity in the chamber. From the quartz crystal microbalance (QCM), the thickness of water at relative humidity at 28 degree in Celcius is about 0.5 to 1 nm.

Figure 3 shows XE spectra of water adsorbed on the SAMs. For water molecules in the vicinity of OH- and C8-SAMs, the tetrahedral-coordinated water (ice-like water) is concentrated only near the interface (with a film thickness of less than 0.5 nm) and steeply changes to the structure of bulk water. In contrast, it was found that water molecules with hydrogen bonding in the distorted tetrahedral coordination was dominant for non-fouling SAMs (Fig. 3). Therefore, the distorted tetrahedral-coordinated water layer is key to the anti-adhesion properties, in agreement with our previous findings.

REFERENCES

- (1) Hayashi, T.; Hara, M., Nonfouling self-assembled monolayers: mechanisms underlying protein and cell resistance. *Current Physical Chemistry* **2011**, *1*, 90-98.
- (2) Chang, R.; Asatyas, S.; Lkhamsuren, G.; Hirohara, M.; Mondarte, E. A. Q.; Suthiwanich, K.; Sekine, T.; Hayashi, T., Water near bioinert self-assembled monolayers. *Polym. J. (Tokyo, Jpn.)* **2018**, *50*, 563-571.
- (3) Kanayama, N.; Sekine, T.; Ozasa, K.; Kishi, S.; Nyu, T.; Hayashi, T.; Maeda, M., Terminal-Specific Interaction between Double-Stranded DNA Layers: Colloidal Dispersion Behavior and Surface Force. *Langmuir* **2016**, *32*, 13296-13304.
- (4) Sekine, T.; Tanaka, Y.; Sato, C.; Tanaka, M.; Hayashi, T., Evaluation of Factors To Determine Platelet Compatibility by Using Self-Assembled Monolayers with a Chemical Gradient. *Langmuir* **2015**, *31*, 7100-5.
- (5) Tanaka, M.; Hayashi, T.; Morita, S., The roles of water molecules at the biointerface of medical polymers. *Polym. J. (Tokyo, Jpn.)* **2013**, *45*, 701-710.

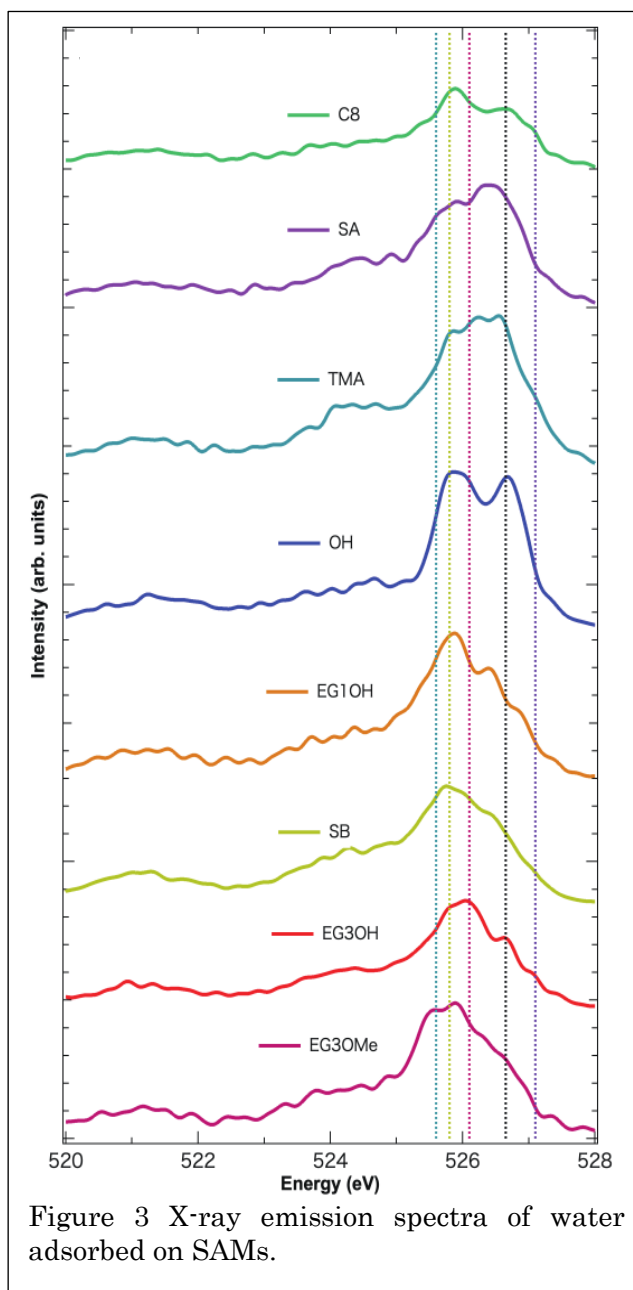


Figure 3 X-ray emission spectra of water adsorbed on SAMs.

MEASUREMENT OF THE THICKNESS DEPENDENCE OF THE MAGNET-OPTICAL CONSTANTS OF METAL FE USING FAST POLARIZATION SWITCHING

Yasuyuki Hirata¹, Keisuke Ikeda¹, Kohei Yamagami¹, Yujun Zhang², Hiroki Wadati²,
Souliman El Moussaoui¹, Iwao Matsuda¹

¹*Synchrotron Radiation Laboratory, Institute for Solid State Physics, University of Tokyo*

²*Graduate School of Material Science, University of Hyogo*

Magneto-optical effect is quite important not only for its use in devices such as magneto-optical storage devices, but also as a probe for unraveling the spin and orbital states of electrons in magnetic materials, therefore researchers of magnetism have measured magneto-optical spectrum at various wavelengths. In particular, the measurement of resonant X-ray magnetic circular dichroism (R-XMCD) and resonant X-ray magneto-optical Kerr effect (R-XMOKE) using soft X-ray are powerful measurement methods that can selectively observe the magnetic behavior of each 3d-transition-metal element, which is a main player of magnetism. However, despite the fact that the fine structure of the spectrum is important for analysis, R-XMCD for materials with a small magnetic signal has a difficulty on improving accuracy because it requires subtraction between two absorption/reflection spectra for the incident light with different polarizations. R-MOKE measurement is free from this problem, but it has an experimental limitation that it takes a long time for measurement because it requires an ellipsometry scan for each measurement point.

Taking advantage of the characteristics of the BL07LSU light source where high-speed polarization switching is available [1,2], from the 2016A period we have performed the R-MOKE measurement using the optical delay modulation method [3], and measured the magneto-optical constant of the Fe thin film (30 nm thickness) [4]. With this method, the real part (corresponding to Kerr rotation angle) and the imaginary part (corresponding to ellipticity) of the off-diagonal component of the permittivity can be simultaneously measured independently in a short time, without Kramers-Kronig transformation analysis. Although the obtained permittivity of Fe thin film was generally in good agreement with the result of the first-principles calculation, a dip structure at Fe L_3 absorption edge in the measured spectrum could not be reproduced from the calculation. It is very important to distinguish experimentally whether the dip structure is intrinsic in Fe metal, comes from interference with the thin film [5], or has another origin. In this study, we performed an R-MOKE measurement on Fe thin films with different film thickness by the optical delay modulation method using polarization switching, and clarified the film thickness dependence of the magneto-optical spectrum. The dip structure was hardly reproduced, which indicates it is not intrinsic in the magneto-optical spectrum of Fe metal. No systematic film thickness dependence was observed in the permittivity spectrum.

We prepared two Fe thin films with different thickness (30 nm thick and 15 nm thick) on MgO substrate, and capped with Ru layer (5 nm thick) to prevent surface oxidization. The reflection spectroscopy measurement with grazing geometry (incident angle of 80 degree) was performed at Fe L_3 and L_2 edge under the in-plane magnetic field of 0.3 T applied by superconducting coil magnet. The polarization of the incident light was continuously modulated between left circular polarization and right circular polarization with the frequency of 13 Hz. The reflected light was analyzed with ellipsometer at both p -polarization and s -polarization geometry. The 13 Hz component of analyzed signal corresponded to ellipticity, and the 26 Hz component of analyzed signal corresponded to Kerr rotation angle.

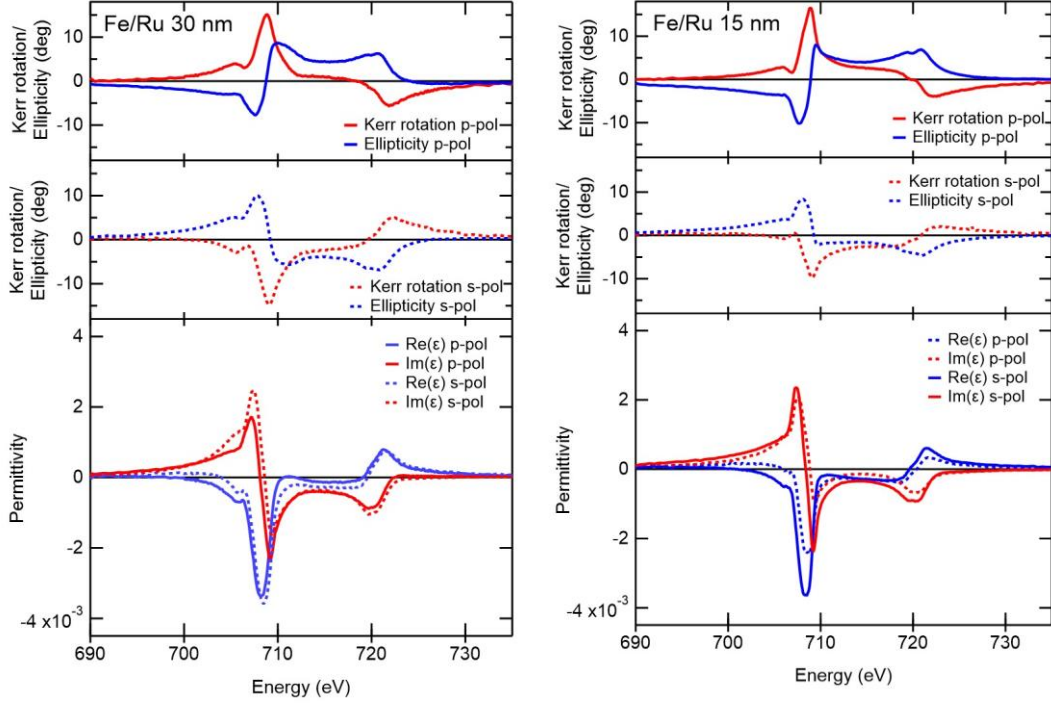


Fig. 1: Kerr rotation angle, ellipticity, and off-diagonal permittivity ε of Fe film with 30 nm thick (left panel) and Fe film with 15 nm thick (right panel). Solid line (dashed line) is obtained from p -polarization (s -polarization) reflection measurement, respectively.

Figure 1 shows the measured spectra of Kerr rotation angle, ellipticity, and off-diagonal permittivity of Fe film (30 nm thick) and Fe film (15 nm thick). Off-diagonal permittivity was derived from Kerr rotation angle, ellipticity, and refractive index of Fe [6]. Under both p -polarization and s -polarization reflection geometry, obtained off-diagonal permittivity spectra show good agreement with theoretical calculation. We cannot find any systematic dependency on thickness in the spectra of the 30 nm thick film and the 15 nm thick film, and a large dip structure observed in previous experiment has almost disappeared. Our result clearly shows the dip structure is neither real magnetic signal of Fe nor originating from an optical interference within the film. The capping layers of the samples are different between previous measurement (Cu 2 nm thick and Ta 2 nm thick) and ours (Ru 5 nm thick), but it is less likely that the dip structure comes from the capping layer because Cu and Ta do not have any optical structure at the energy around Fe L -edge. One possible origin of the dip structure is surface oxidization of the sample which may be caused by x-ray radiation.

In conclusion, we have observed the thickness dependence of off-diagonal permittivity of Fe thin film at Fe L -edge by the optical delay modulation method. No systematic dependency on thickness was found out, and the dip structure in spectrum observed in previous experiment was shown not to be intrinsic.

REFERENCES

- [1] S. Yamamoto *et al.*, J. Synchrotron Radiat. **21**, 352 (2014).
- [2] I. Matsuda *et al.*, Nucl. Instrum. Methods Phys. Res., **767**, 296 (2014).
- [3] K. Sato, Jpn. J. Appl. Phys. **20**, 2403 (1981).
- [4] Y. Kubota *et al.*, Phys. Rev. B **96**, 214417 (2017).
- [5] S. Valencia *et al.*, Physica B **345**, 189 (2004).
- [6] H.-C. Mertins *et al.*, J. Magn. Magn. Mater. **240**, 451 (2002).

Creation of multi-dimensional operando photoelectron spectroscopy (I) Selection of industry-government-academia collaborative model sample

Hirokazu Fukidome¹, Takamasa Kamogawa¹, Naoka Nagamura^{2,3}, Masaharu Oshima⁴,
Masato Kotsugi⁵, and Issei Watanabe⁶

¹Research Institute of Electrical Communication, Tohoku University, Sendai, Miyagi, Japan.

²National Institute for Materials Science (NIMS), Tsukuba, Ibaraki, Japan.

³PRESTO, Japan Science and Technology Agency, Honcho, Saitama, Japan.

⁴Institute for Solid State Physics, The University of Tokyo, Kashiwa, Chiba, Japan.

⁵Tokyo University of Science, Katsushika, Tokyo, Japan.

⁶National Institute of Information and Communications Technology (NICT), Koganei, Tokyo, Japan.

Virus and environmental issues threaten the sustainability of mankind. To balance the suppression of virus infection and active socio-economic activities, we should develop information technologies enabling a high telepresence communications. For this purpose, the wireless communication using THz frequencies is needed, indicating 100 times speeding up, compared to the current wireless communication, so-called 5G.

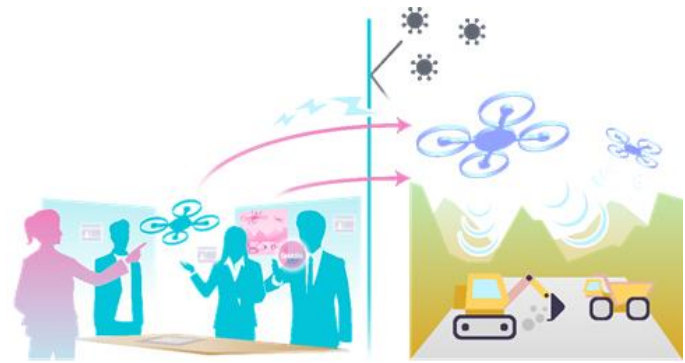


Fig. 1 A schematic view of the high telepresence communication

Two-dimensional (2D) materials such as graphene and ultrathin semiconductor devices using AlGaIn/GaN [1] and InGaAs heterointerfaces is promising for THz devices for high speed wireless communication, 6G and more. This due to excellent electronic properties, such as giant carrier mobility and ultrahigh saturation velocity, and suppression of so-called short-channel effects arising from the ultrathinness of the channels. With the advance of miniaturization and integration of devices, the importance of interfaces further increases. Especially, 2D materials are sensitive to interface environment, so many environmental parameters drive the electronic and chemical properties of 2D materials. Moreover, better spatial and time resolution is required for the advanced device analysis. Then, we attempt to realize multi-dimensional operando photoelectron spectroscopy using machine learning analysis techniques in the viewpoint of Measurement Informatic.

At first, we performed depth profiling of III-V compound semiconductor heteroepitaxial layers by ARPES measurements. Maximum Entropy Method is applied to enable sub nm order analysis (Fig. 2)[2].

In-plane 2D spectral mapping is also carried out for InP high electron mobility transistor (HEMT) device structures. Present in-plane spatial resolution of 3D nano-ESCA is ~70 nm,

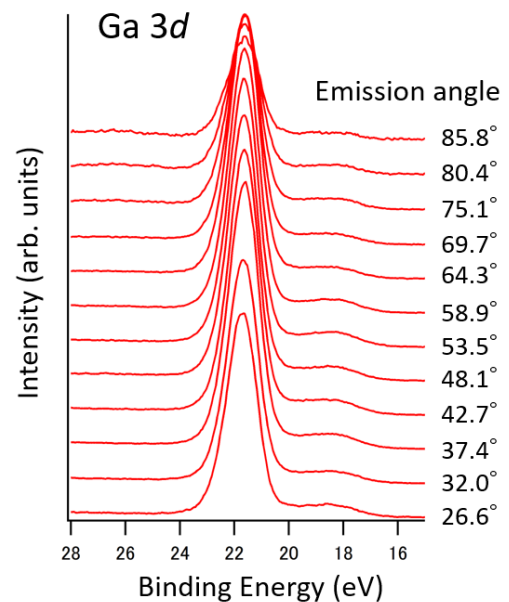


Fig. 2 Angle resolved Photoelectron spectroscopy of Ga 3d peak for the GaAs heteroepitaxial layers.

which is deteriorated by mechanical vibrations, thermal drift, charging effect, and so on. To overcome the limit of spatial resolution and make it possible to observe objects in the size of several nms, we adopt sparse modelling approach for the spectral intensity mapping datasets. Fig. 3(a) is a low-resolution image taken by coarse steps in short measurement time. Using this kind of down-sampling mappings, super-resolution image processing by sparse modelling [3] was performed as shown in Fig. 2(b). Effective spatial resolution seems to be improved by this machine learning approach.

Our final goal is to achieve below 10 nm-resolution with the aid of machine learning, such as super-resolution. Then, we will plan to execute industry-government-academia collaboration that utilize operando 3D nano-ESCA to develop novel next-generation communication devices necessary for balancing the suppression of virus infection and active socio-economic activities.

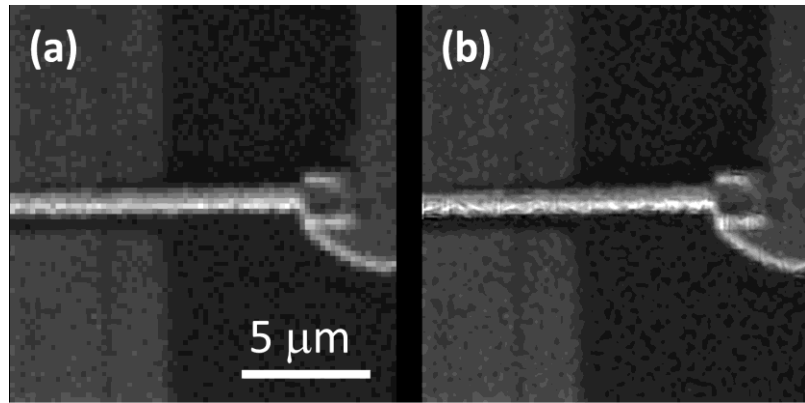


Fig. 3 (a) Photoelectron intensity mapping image for the Au 4*f* peak for the InP-HEMT device structure. Low-resolution image by down sampling. (b) Super-resolution image using sparse modeling.

REFERENCES

- [1] H. Fukidome et al. *Sci. Rep.*8, 13268 (2018).
- [2] K. Horiba et al. *Rev. Sci. Instrum.* 82, 113701 (2011).
- [3] T. Kato et al. *Neurocomputing* 240, 115 (2017).

OPERAND MEASUREMENT OF ALL SOLID-STATE LI-ION BATTERYS BY PHOTOELECTRON MICROSCOPY

Eiji Hosono^{a,b,c}, Wenxiong Zhang^d, Daisuke Asakura^{b,c}, Naoka Nagamura^e,
Masaharu Oshima^f, Yoshihisa Harada^{c,d,f}

- ^a National Institute of Advanced Industrial Science and Technology (AIST), Global Zero Emission Research Center, 1-1-1 Umezono, Tsukuba, Ibaraki 305-8568, Japan
- ^b National Institute of Advanced Industrial Science and Technology (AIST), Research Institute for Energy Conservation, 1-1-1 Umezono, Tsukuba, Ibaraki 305-8568, Japan
- ^c AIST-UTokyo Advanced Operando-Measurement Technology Open Innovation Laboratory, 5-1-5 Kashiwanoha, Kashiwa, Chiba 277-8565, Japan
- ^d Institute for Solid State Physics (ISSP), The University of Tokyo, 5-1-5 Kashiwanoha, Kashiwa, Chiba 277-8581, Japan
- ^e National Institute for Materials Science, Research Center for Advanced Measurement and Characterization, 1-2-1 Sengen, Tsukuba, Ibaraki 305-0047, Japan
- ^f Synchrotron Radiation Research Organization, The University of Tokyo, 7-3-1 Hongo, Bunkyo-ku, Tokyo, 113-8656, Japan

Development of high-performance lithium-ion battery (LIB) for stationary type and vehicle is an important research topic. The total development of LIB is very difficult, because performances such as energy density, power performance, cycle performance, and safety property are in the trade-off relationships. Thus, comprehensive researches and developments are highly important to development of LIB. Detailed understanding of the redox reactions by Li-insertion/extraction, structural change, electronic state change for the materials in LIBs is important to develop innovative materials for LIBs. In these days, cutting-edge analyses methods are necessary in addition to the innovative materials development.

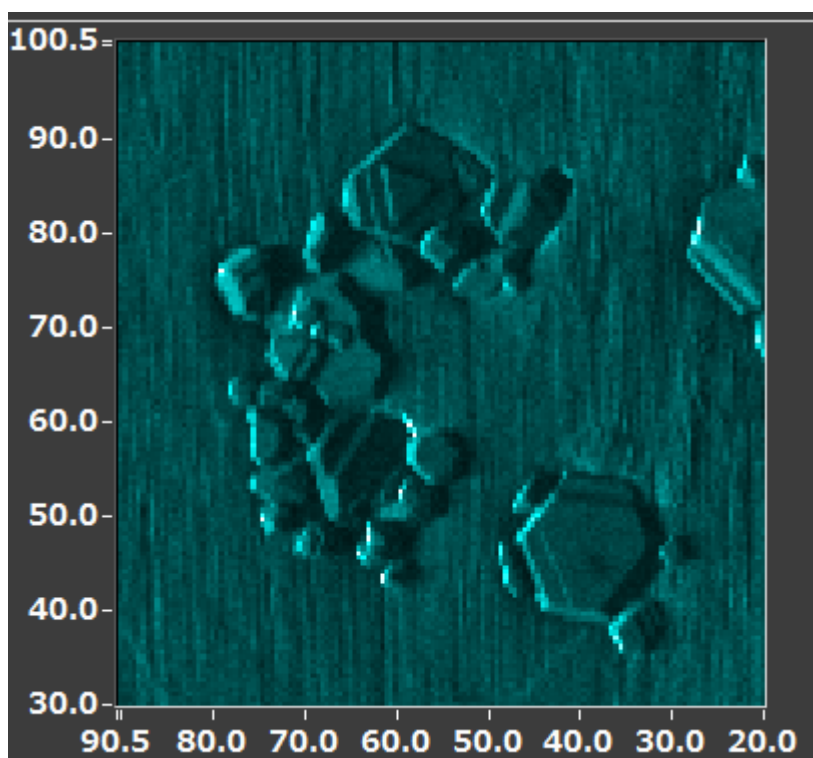


Figure 1 XPS images of LiCoO₂

To truly understand LIBs, synchrotron radiation soft X-ray spectroscopy is a useful technique with elemental selectivity, valence selectivity and orbital selectivity. We have been studying the charge-discharge mechanisms of LIBs based on the electronic-structure analysis by soft X-ray spectroscopy. In addition, *operando* measurement is very important because LIB is a high voltage device. Even deconstruction of LIB in the glovebox filled by inert Ar gas, the potential control of active material is difficult. *Operando* measurement system in soft X-ray beamline is our core-technique. We reported the *operando* soft x-ray emission spectroscopy under the charge-discharge operation [1,2].

Furthermore, microspectroscopy is another important point because the redox reaction by charge-discharge reaction influenced by the position like a facet of an electrode material and the interfaces between the electrode materials and electrolytes. Spectroscopy with spatial resolution is of particular importance.

We reported *operando* photoemission spectromicroscopy of single crystalline $\text{Li}_4\text{Ti}_5\text{O}_{12}$ (an anode material) [2] and LiCoO_2 (an cathode materials) [3] by 3DnanoESCA [4] with all-solid-state LIB. The soft X-ray photoemission spectromicroscopy experiments have been conducted at BL07LSU of SPring-8.

Here, we measured single crystalline LiCoO_2 cathode material with clear facet. Figure 1 shows images of XPS mapping image of single crystalline LiCoO_2 . From the clear image of each facet, resonant XPS was conducted.

ACKNOWLEDGEMENT

This work was conducted under the international joint research program for innovative energy technology by METI, Japan.

REFERENCES

- [1] D. Asakura, E. Hosono, H. Niwa, H. Kiuchi, J. Miyawaki, Y. Nanba, M. Okubo, H. Matsuda, H.S. Zhou, M. Oshima, and Y. Harada, “Operando Soft X-ray Emission Spectroscopy of LiMn_2O_4 Thin Film Involving Li-ion Extraction/insertion Reaction”, *Electrochem. Commun.*, 50, 93 (2015).
- [2] D. Asakura, Y. Nanba, M. Okubo, H. Niwa, H. Kiuchi, J.Miyawaki, M. Oshima, E. Hosono, Y. Harada, “Operando soft X-ray emission spectroscopy of the Fe_2O_3 anode to observe the conversion reaction”, *Physical Chemistry Chemical Physics*, 21, 26351 (2019).
- [3] K. Akada, T. Sudayama, D. Asakura, H. Kitaura, N. Nagamura, K. Horiba, M. Oshima, E. Hosono, Y. Harada, “Operando measurement of single crystalline $\text{Li}_4\text{Ti}_5\text{O}_{12}$ with octahedral-like morphology by microscopic X-ray photoelectron spectroscopy”, *J. Electron Spectrosc. Relat. Phenom.*, 233, 64 (2019).
- [4] K. Akada, T. Sudayama, D. Asakura, H. Kitaura, N. Nagamura, K. Horiba, M. Oshima, E. Hosono, Y. Harada, “Microscopic photoelectron analysis of single crystalline LiCoO_2 particles during the charge-discharge in an all solid-state lithium ion battery”, *Scientific Reports*, 9, 12452 (2019).
- [5] K. Horiba, Y. Nakamura, N. Nagamura, S. Toyoda, H. Kumigashira, M. Oshima, K. Amemiya, Y. Senba, H. Ohashi, Scanning photoelectron microscope for nanoscale three-dimensional spatial-resolved electron spectroscopy for chemical analysis. *Rev. Sci. Instrum.* 82, 113701 (2011).

MAPPING MEASUREMENT OF SINGLE CRYSTALLINE LITHIUM METAL OXIDE BY ALL SOLID-STATE LI-ION BATTERYS

Eiji Hosono^{a,b,c}, Wenxiong Zhang^d, Daisuke Asakura^{b,c}, Naoka Nagamura^e,
Masaharu Oshima^f, Yoshihisa Harada^{c,d,f}

- ^a National Institute of Advanced Industrial Science and Technology (AIST), Global Zero Emission Research Center, 1-1-1 Umezono, Tsukuba, Ibaraki 305-8568, Japan
- ^b National Institute of Advanced Industrial Science and Technology (AIST), Research Institute for Energy Conservation, 1-1-1 Umezono, Tsukuba, Ibaraki 305-8568, Japan
- ^c AIST-UTokyo Advanced Operando-Measurement Technology Open Innovation Laboratory, 5-1-5 Kashiwanoha, Kashiwa, Chiba 277-8565, Japan
- ^d Institute for Solid State Physics (ISSP), The University of Tokyo, 5-1-5 Kashiwanoha, Kashiwa, Chiba 277-8581, Japan
- ^e National Institute for Materials Science, Research Center for Advanced Measurement and Characterization, 1-2-1 Sengen, Tsukuba, Ibaraki 305-0047, Japan
- ^f Synchrotron Radiation Research Organization, The University of Tokyo, 7-3-1 Hongo, Bunkyo-ku, Tokyo, 113-8656, Japan

Many researchers have studied development of clean energy devices for the realization of a low-carbon society. There is a great need to develop innovative clean energy devices. In particular, high performance LIBs are important not only for electric vehicles, but also for power source of next-generation semiconductor devices for "Beyond 5G", which will enable high-speed, high-capacity data communication in the IoT society.

In response to these high societal needs, LIBs with higher performance than the current state are required. In recent years, research and development of all-solid-state LIBs have been focused for innovative improvement of the performances of LIBs. It is necessary to establish design guidelines based on fundamental science because a lot of technical issues remain unresolved in the all-solid-state LIBs. Thus, understanding the charge-discharge mechanism of LIBs is important to improve their properties.

In addition, *operando* measurement under the control of potential is important for detail and precise understanding because LIBs are high voltage device. Even deconstruction of LIB in the glovebox filled by inert Ar gas, the potential maintaining of active material is difficult. Recently Akada and Hosono *et al.* have successfully introduced *operando* soft X-ray photoelectron spectroscopy as a novel method to understand the LIBs during Li-intercalation/deintercalation process in LIB cathode and anode materials [1, 2]. These are results of photoelectron microscopy with spatially resolved information by 3D nanoESCA station at BL07LSU of SPring-8 [3]. Microspectroscopy is another important point in addition to *operando* measurement because the redox reaction by charge-discharge reaction affected by the position like a facet of an electrode material and the interfaces between the electrode materials and solid-state electrolytes. Spectroscopy with spatial resolution is important techniques.

Figure 1 shows the intensity mapping of Ni 3p and Mn 3s of $\text{Li}_x\text{Ni}_{0.5}\text{Mn}_{1.5}\text{O}_4$. Here, lithium ratio is controlled by the cell using liquid electrolyte. We obtained intensity mapping. The next step is *operando* measurement by all-solid-state LIBs. We will create *operando* measurement system and conduct XPS mapping measurement.

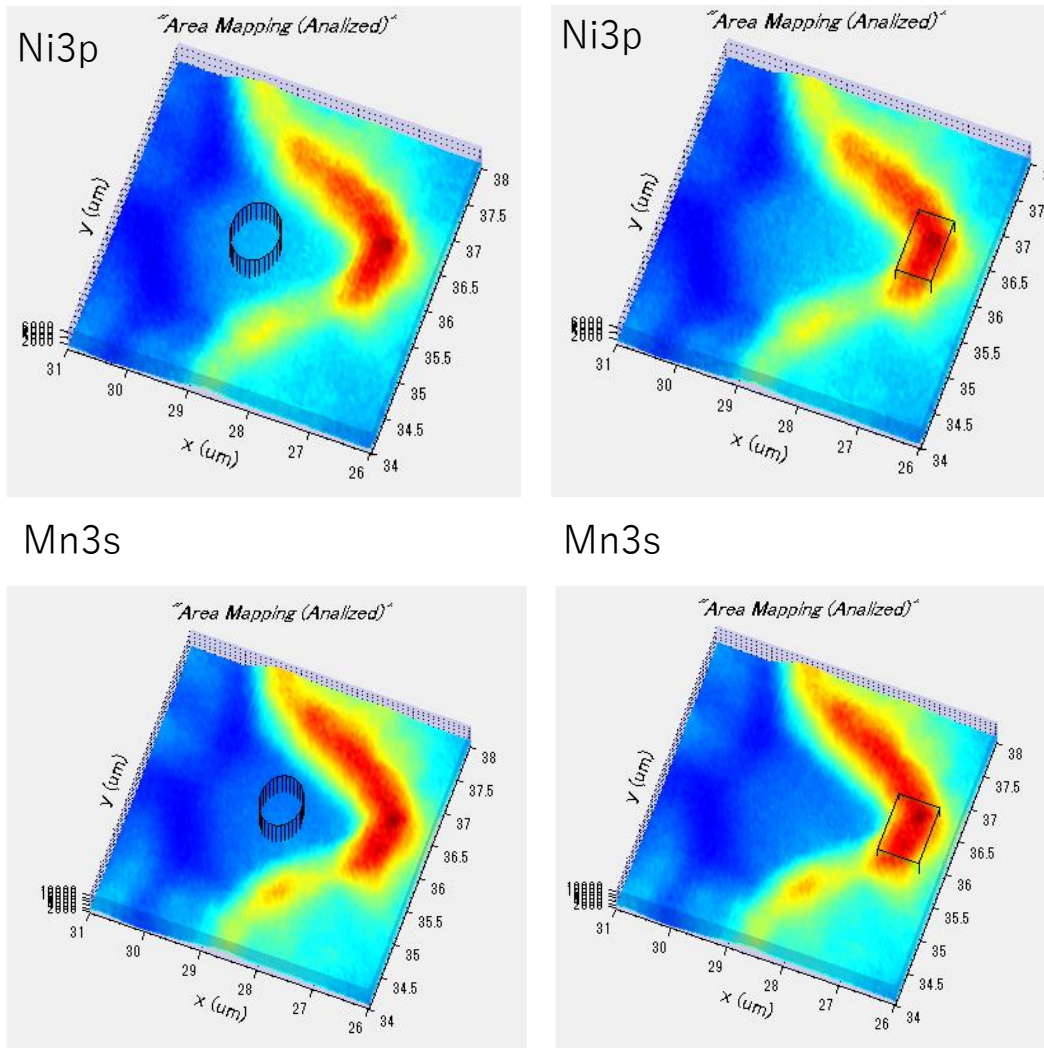


Figure 1 Intensity mapping of Ni 3p and Mn 3s of $\text{Li}_x\text{Ni}_{0.5}\text{Mn}_{1.5}\text{O}_4$.

ACKNOWLEDGEMENT

This work is partially conducted on the basis of the International joint research program for innovative energy technology by Ministry of Economy, Trade and Industry, Japan.

REFERENCES

- [1] K. Akada, T. Sudayama, D. Asakura, H. Kitaura, N. Nagamura, K. Horiba, M. Oshima, E. Hosono, Y. Harada, "Operando measurement of single crystalline $\text{Li}_4\text{Ti}_5\text{O}_{12}$ with octahedral-like morphology by microscopic X-ray photoelectron spectroscopy", *J. Electron Spectrosc. Relat. Phenom.*, 233, 64 (2019).
- [2] K. Akada, T. Sudayama, D. Asakura, H. Kitaura, N. Nagamura, K. Horiba, M. Oshima, E. Hosono, Y. Harada, "Microscopic photoelectron analysis of single crystalline LiCoO_2 particles during the charge-discharge in an all solid-state lithium ion battery", *Scientific Reports*, 9, 12452 (2019).
- [3] K. Horiba, Y. Nakamura, N. Nagamura, S. Toyoda, H. Kumigashira, M. Oshima, K. Amemiya, Y. Senba, H. Ohashi, Scanning photoelectron microscope for nanoscale three-dimensional spatial-resolved electron spectroscopy for chemical analysis. *Rev. Sci. Instrum.* 82, 113701 (2011).

Resonant inelastic soft x-ray diffraction of nanoparticles

J. Miyawaki¹, T. Yachi², S. Maki², K. Kanie² and Y. Harada¹

¹*Institute for Solid State Physics, The University of Tokyo*

²*Institute of Multidisciplinary Research for Advanced Materials, Tohoku University*

The excitation energy dependence of soft X-ray emission spectra (XES) was first measured for TiN in 1988 [1]. Four years later, Ma *et al.* proposed that the excitation energy dependence could be interpreted by the theory of resonant inelastic X-ray scattering (RIXS), and band dispersions of electronic state were observed [2]. This indicates that the absorption- and emission-processes are described by a single scattering theory, and the momentum is conserved during that process. In other words, when a core electron with momentum \mathbf{k} is excited to the conduction band and an electron at the valence band is decayed to the core hole, the emissions from the different cores could interfere with each other, and Bragg-like diffraction results in the emissions of the same momentum \mathbf{k} . These facts suggest that a more general Bragg's law, $\mathbf{q}_{\text{in}} = \mathbf{q}_{\text{out}} + \mathbf{k}_h - \mathbf{k}_e + \mathbf{G}$ is valid, in addition to the energy conservation law in RIXS, $h\nu_{\text{in}} = h\nu_{\text{out}} + E_h - E_e$, where $h\nu_{\text{in}}$ (\mathbf{q}_{in}) and $h\nu_{\text{out}}$ (\mathbf{q}_{out}) are the energy (momentum) of the incident and scattered X-ray, E_h (\mathbf{k}_h) and E_e (\mathbf{k}_e) are the energy (momentum) of the hole in the valence band and the electron in the conduction band at the final state, and \mathbf{G} is the reciprocal vector of the crystal. When the excitation and scattered energies are the same, the momentum conservation law gives $\mathbf{q}_{\text{in}} = \mathbf{q}_{\text{out}} + \mathbf{G}$, which is widely accepted as Bragg's law. The more general Bragg's law $\mathbf{q}_{\text{in}} = \mathbf{q}_{\text{out}} + \mathbf{k}_h - \mathbf{k}_e + \mathbf{G}$ (the momentum conservation law in RIXS) has been validated by the RIXS studies of the band dispersions in SiC [3], graphite, diamond [4], Si [5], and LiBC [6]. Recent observations of the dispersions of orbitons, magnons, and phonons also confirmed the validity of the principle [7].

In the above discussion, the Bragg diffraction and RIXS were treated as independent processes. However, if the Bragg diffraction and RIXS occur simultaneously, the intensity of RIXS is expected to increase assisted by the Bragg diffraction. We named this method resonant inelastic X-ray diffraction (RIXD). In the case of nanoparticles, the momentum dispersion of the elementary excitations is small, and the diffraction from the nanoparticles, that is, small angle X-ray scattering (SAXS), is expected to increase the intensity of RIXS. Therefore, we measured soft X-ray SAXS of FePt nanoparticles by a RIXS spectrometer and discussed the feasibility of RIXD by comparing the SAXS profile obtained by the elastic scattering and the momentum dependence of RIXS.

The measurement of SAXS and RIXD were conducted at HORNET end-station of SPring-8 BL07LUS using θ - 2θ scan system. In this scan system, RIXS spectra can be measured at an arbitrary scattering angle 2θ in the range between 45° and 135° , and SAXS and RIXD profiles can be obtained from momentum dependence of the intensity of the elastic and inelastic peaks, respectively. The measured sample was FePt nanoparticles. The average particle size and standard deviation were 2.7 nm and 0.37 nm, respectively.

Figure 1 shows the RIXS spectra of the FePt nanoparticle measured at 708.1 eV, which is the peak top of Fe L_3 -edge X-ray absorption spectra. A SAXS profile was obtained by integrating the intensity of the elastic peak (Fig. 2). A peak was observed in the SAXS profile at around $\theta=31^\circ$. In the hard X-ray SAXS, the SAXS profile is observed at small angles (typically 0.1 – 10°), but in the case of soft X-ray SAXS, SAXS profile is observed at larger angle, since the wave length of the soft X-ray is longer than that of hard X-ray. The obtained profile is well reproduced by a simulation with the particle size of 2.73 nm and standard deviation of 0.37 nm, and thus the obtained \mathbf{q} -dependence of the elastic peak was confirmed to be SAXS. Furthermore, the momentum dependence of the inelastic scattering indicated by a1, a2, a3, and a123 in Fig. 1 was calculated, and the increase of the intensity of

a3 peak was found at the same scattering angle of the SAXS peak, indicating the observation of RIXD. In the future, we will measure the particle size and incident energy dependences of various samples to further establish RIXD and elucidate its mechanism.

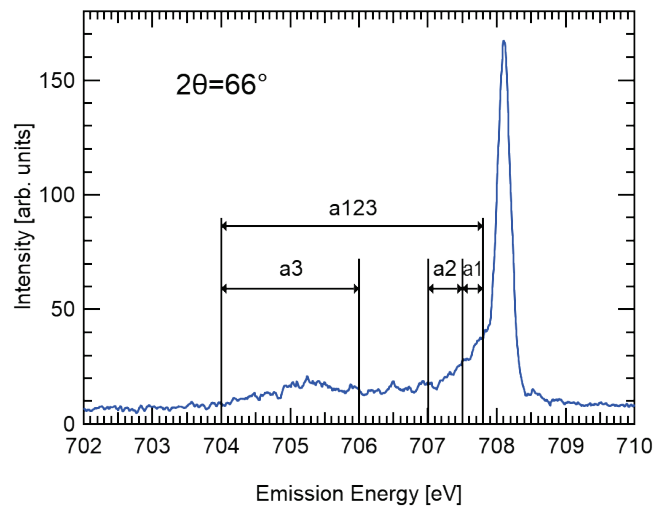


Fig. 1 RIXS spectra of FePt nanoparticle measured at 708.1 eV and $2\theta=66^\circ$.

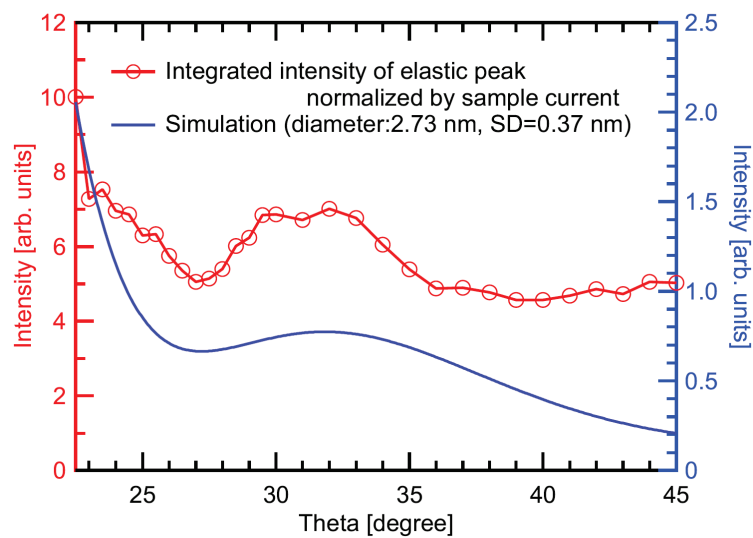


Fig. 2 The momentum dependence of the elastic peak intensity in RIXS spectra of FePt nanoparticle. Red circle and blue line correspond to the experimental result and simulation, respectively.

REFERENCES

- [1] J. E. Rubensson, *et al.*, Phys. Rev. Lett. **60**, 1759 (1988).
- [2] Y. Ma, *et al.*, Phys. Rev. Lett. **69**, 2598 (1992).
- [3] J. Luning, *et al.*, Phys. Rev. B **56**, 13147 (1997).
- [4] A. V. Sokolov, *et al.*, J. Phys. Condes. Matter **15**, 2081 (2003).
- [5] A. V. Sokolov, *et al.*, J. Electron Spectrosc. **137**, 591 (2004).
- [6] P. F. Karimov, *et al.*, J. Phys. Condes. Matter **16**, 5137 (2004).
- [7] L. J. P. Ament, *et al.*, Rev. Mod. Phys. **83**, 705 (2011).

Development of X-ray Polarization Precession Spectroscopy

J. Miyawaki, Y. Hirata[†], K. Yamagami[‡], I. Matsuda, and Y. Harada

Institute for Solid State Physics, The University of Tokyo

Magnonics is a next-generation technology, that utilizes a collective excitation of electron spin (magnon or spin wave), and is an alternative technology to electronics, which utilizes electrons for information transfer and computation. Compared with electron- and spin-based electronics and spintronics, magnonics does not suffer from Joule heat. Magnon has longer mean free path, which is advantageous for long-distance information transfer. Magnon has a wave nature, which offers a possibility of quantum computation. Thus, researchers are trying to use high-frequency terahertz magnons to speed up magnonic devices and observe magnons injected to magnonics materials to understand the operating mechanism of devices [1–6].

For the magnon observation, ferromagnetic resonance (FMR), Brillouin light scattering (BLS), inelastic neutron scattering (INS), spin-polarized electron energy loss spectroscopy (SPEELS), and time-resolved spectroscopy have mainly been used. FMR and BLS observe magnons only at $q \approx 0 \text{ nm}^{-1}$ and cannot observe propagating magnons at $q \neq 0 \text{ nm}^{-1}$. INS and SPEELS can observe at larger q , but INS cannot observe higher energy magnons and require large sample volume, and SPEELS is surface sensitive. Therefore, INS and SPEELS is not suitable for *operando* experiments. Thus, a new technique to observe propagating magnons in *operando* condition has been explored. In this study, we developed X-ray polarization precession spectroscopy (XPPS), which is a new method to observe dispersion of magnons by X-ray with high energy resolution to understand the properties of magnon in devices.

XPPS was proposed as a new technique to measure the frequency of spin waves by observing a rotational/angular Doppler effect in the polarization of scattered X-ray induced by spin waves in the sample via magnetic linear dichroism [7]. Since magnetic linear dichroism is employed in XPPS, resonant condition is required to measure XPPS signal. The measurement principle and experimental setup are shown in Fig. 1(a). The scattered X-ray is irradiated to a multilayer polarizer, the intensity of the reflected X-ray is spatially resolved by CCD, and the period of the rotation of the polarization can be detected. The energy resolution of XPPS reaches 50 GHz (0.2 meV), which is very high energy resolution for X-ray based spectroscopy to obtain the energy of magnons. Thus, XPPS has a promising technique for *operando* experiment of magnonic devices.

XPPS experiments were conducted at free-port end-station of SPring-8 BL07LSU using superconducting magnet chamber equipped with a polarization analyser (Fig. 2). The linear vertical polarization was used for the incident X-ray, and the multilayer polarizer of the polarization analyser was positioned orthogonal to the electronic vector of the incident X-ray. The position dependence of the reflected X-ray intensity was measured by CCD.

Figure 3 shows a XPPS result of $\text{Y}_3\text{Fe}_5\text{O}_{12}$ (YIG) and Pt. 705.0 eV and 709.6 eV correspond pre-edge and the peak-top of Fe L_3 -edge X-ray absorption spectra of YIG. YIG showed the difference between pre- and post-edge of Fe L_3 -edge, while Pt, which is non-magnetic, showed no difference. In YIG, the difference spectra showed the intensity modulation with a period of $\sim 100 \mu\text{m}$. This period corresponds the magnon energy of $\sim 5.5 \text{ meV}$, which matches the energy obtained by inelastic neutron scatterings [8]. Thus, we succeeded in detecting XPPS signal and extracting the energy of magnon.

[†]Present Address: *Department of Applied Physics, National Defense Academy*

[‡]Present Address: *Quantum Materials Science Unit, Okinawa Institute of Science and Technology Graduate University*

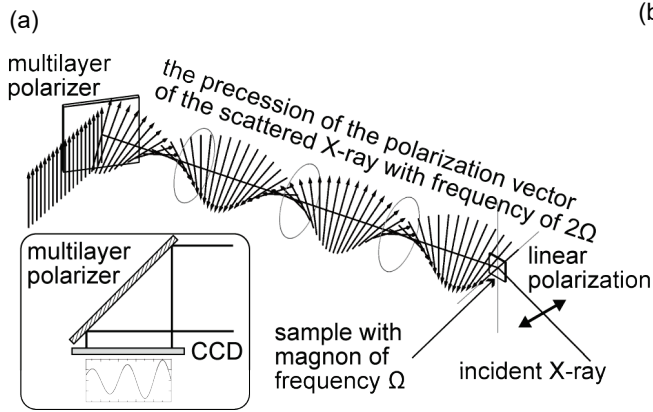


FIG. 1. (a) The measurement principle and (b) experimental setup of XPPS. Linearly polarized X-ray of a resonant energy is irradiated to a sample that possesses a spin wave of frequency Ω , and the precessional motion of frequency 2Ω is induced to the polarization vector of the scattered X-ray. The multilayer polarizer reflects the vertically polarized component of the scattered X-ray, and thus spatially resolved reflection intensity gives the intensity modulation due to the precession in the scattered X-ray.

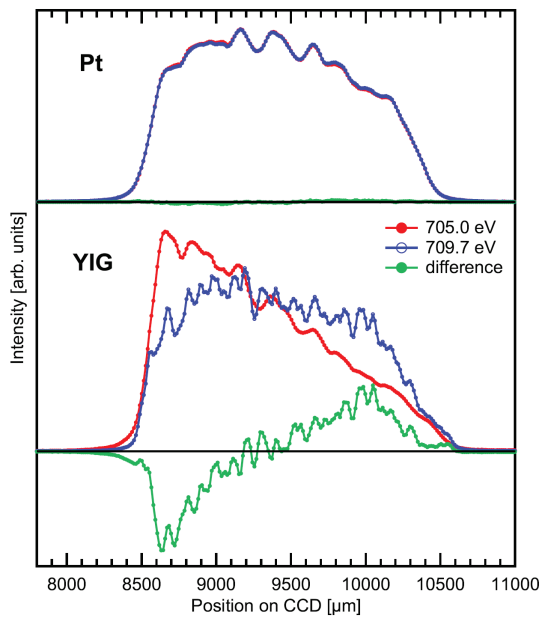
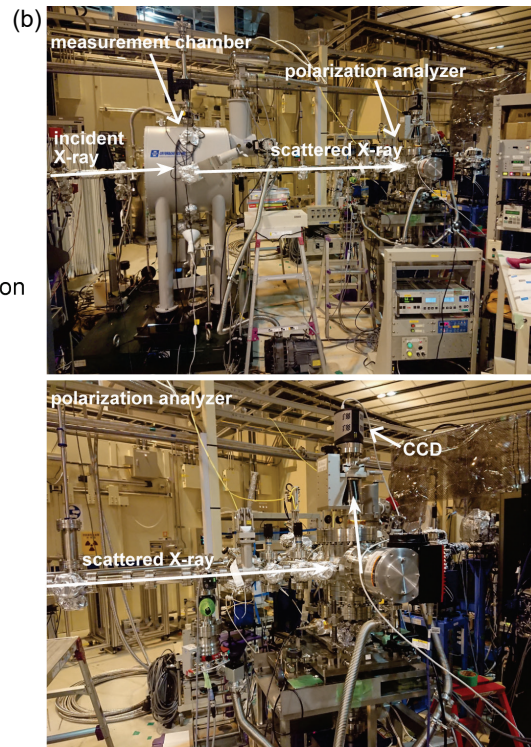


FIG. 2. XPPS of Pt and YIG at Fe L_3 -edge. Spatially resolved reflection intensity of the scattered X-ray from the multilayer polarizer was measured at pre- (red) and post-edge (blue) of Fe L_3 -edge. Since the intensity profiles by the pre-edge excitation has no resonant effect, the signal can be regarded as a background affected by the surface of the sample and the polarizer.

REFERENCES

- [1] S. Neusser *et al.*, Adv. Mater. **21**, 2927 (2009).
- [2] Y. Kajiwara *et al.*, Nature **464**, 262 (2010).
- [3] V. V. Kruglyak *et al.*, J. Phys. D: Appl. Phys. **43**, 264001 (2010).
- [4] A. V. Chumak *et al.*, Nat. Phys. **11**, 453 (2015).
- [5] H. Yu *et al.*, Nat. Comm. **7**, 11255 (2016).
- [6] C. Du *et al.*, Science **357**, 195 (2017).
- [7] R. Röhlsberger, Phys. Rev. Lett. **112**, 117205 (2014).
- [8] J. S. Plant, J. Phys. C: solid State Phys. **10** 4805 (1977).

Resonant Inelastic Soft X-ray Scattering of $\text{Y}_3\text{Fe}_5\text{O}_{12}$

J. Miyawaki and Y. Harada

Institute for Solid State Physics, The University of Tokyo

Further development of the information society requires innovation in information technology, and faster, compact, and low energy-consumption devices have been pursued. One of the next generation technologies to realize this goal is magnonics, which utilizes magnons (spin waves), that is, a collective excitation of spins instead of electrons for the transmission and processing of information. Since no electronic current is induced when the magnon propagates through the magnetic material, there is no energy dissipation due to Joule heating. There is a very wide frequency of magnons known, and if higher frequency magnons can be used, ultra-fast devices could be created. Currently, fundamental research is in progress to realize actual devices. Higher-frequency terahertz magnons have been investigated to speed up the devices, and the magnons injected in the magnonic materials has been investigated to understand the behaviour of the magnons in the device and efficiently utilize magnons. Magnons have been observed by using ferromagnetic resonance, Brillouin light scattering, inelastic neutron scattering, spin-polarized electron energy loss spectroscopy, and time-resolved spectroscopy. However, these experimental methods are not suitable for observing high-energy magnons at larger q , and the development of a new method to observe a propagating magnons is urgently needed. In this study, we focus on X-ray spectroscopy for the observation of the high-frequency propagating magnons and apply resonant inelastic soft X-ray scattering (SX-RIXS) to magnonic materials to elucidate the behaviour of the high-energy magnon.

A $\text{Y}_3\text{Fe}_5\text{O}_{12}$ (YIG)(111) single crystal was measured, which is very promising for magnonics due to its very low damping and long mean free path of magnon. X-ray absorption spectra (XAS) and RIXS were measured at HORNET end-station of SPring-8 BL07LSU. All the measurements were performed at room temperature. XAS was measured in partial fluorescence yield mode using a silicon drift detector, and Fe L_3 -edge inverse partial fluorescence yield (IPFY) XAS was obtained from O K emission. The energy resolution of RIXS at Fe L -edge was set at 175 meV. A momentum-resolved RIXS was obtained by θ - 2θ scan of $2\theta=45$ – 135° and 9° step. During the θ - 2θ scan, an elastic peak was measured at each 2θ from Au with σ polarization. For RIXS of YIG, π polarization was used.

Fe L_3 -edge XAS of YIG is shown in Fig. 1(a). The spectral shape of XAS is good agreement of YIG, having two characters of Fe^{3+} in octahedral (O_h) and tetrahedral (T_d) symmetry [1,2]. Figure 1(b) shows the incident photon energy dependence of RIXS spectra of YIG at $\theta=45^\circ$ and $2\theta=90^\circ$. In addition to dd excitations at ~ 1.3 eV and ~ 1.8 eV, which mainly originate from $O_h \text{Fe}^{3+}$, dd excitations around 2.5 eV were observed, which would be assigned for $T_d \text{Fe}^{3+}$. The peak width at around loss energy of 0 eV is clearly larger than the energy resolution, indicating that there is a contribution of inelastic scattering. For the momentum-resolved RIXS, #7 (710.1 eV) was chosen since the contribution of inelastic scattering was largest among the measured energies. Figure 2 shows RIXS spectra near the elastic peak obtained by θ - 2θ scan. The peak at each 2θ was analyzed by a peak fitting of two gaussian profiles: One is the elastic peak, and the other is for inelastic scattering. The experimental results (red circles) were well reproduced by the two gaussian profiles. Since the energy resolution was set at 175 meV, it was difficult to identify low energy magnons below 100 meV. The inelastic peaks (green lines) at ~ 110 meV showed a weak dispersion. The energy scale of the inelastic peaks ranges from ~ 110 meV to ~ 130 meV. Inelastic neutron scattering measurements and a theoretical calculation revealed that YIG possessed magnon dispersions up to 100 meV [3,4]. The energy scale of the observed dispersion is higher than

that of magnons of YIG, indicating that the observed inelastic scattering would be assigned to bimagnon. The identification of the bimagnon requires a complete picture of the magnetic excitations in YIG. Further analysis will be conducted to understand RIXS spectra and the dispersion of the inelastic peak near the elastic peak.

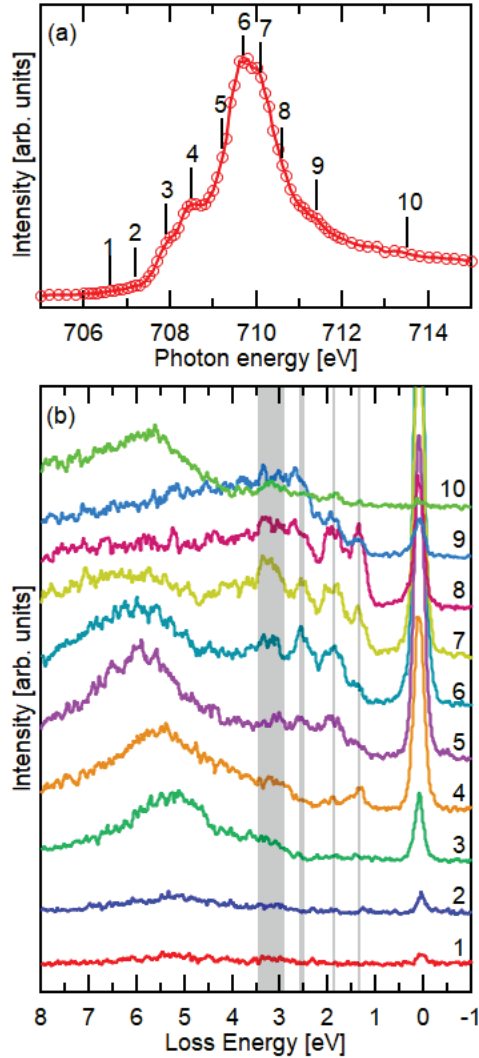


FIG. 1. Fe L_3 -edge (a) XAS and (b) RIXS spectra of YIG(111) single crystal. The numbers labeled in (a) indicate the incident photon energies used to measure RIXS spectra in (b).

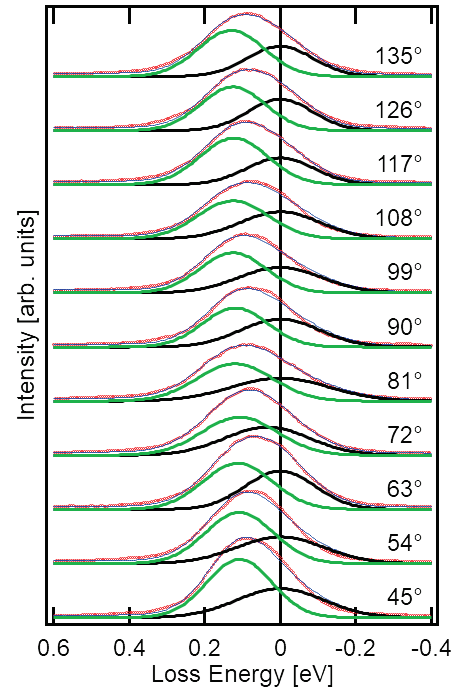


FIG. 2. Fe L_3 -edge RIXS spectra of YIG measured at different θ - 2θ angles. Red circles are experimental results, and black, green, and blue lines correspond to the fitting results of elastic peaks, inelastic peaks, and sum of two peaks and background. Angles labeled on the spectra indicate 2θ angle.

REFERENCES

- [1] F. M. F. de Groot *et al.*, J. Phys. Chem. B **109**, 20761 (2005).
- [2] H. B. Vasili *et al.*, Phys. Rev. B **96**, 014433 (2017).
- [3] J. S. Plant, J. Phys. C: Solid State Phys. **10**, 4805 (1977).
- [4] A. J. Princep *et al.*, npj Quantum Materials **2**, 63 (2017).

Development of Coherent Soft X-ray Diffraction Imaging Technique for Observation of Ultra-fast Magnetic Dynamics

Yuichi Yamasaki^{1,2,3}, Kohei Yamamoto^{4,5}, Yuichi Yokoyama^{1,6}, Yasuyuki Hirata⁴, Hiroki Wadati^{4,7}, and Taka-hisa Arima^{3,8}

¹*Research and Services Division of Materials Data and Integrated System (MaDIS), National Institute for Materials Science (NIMS)*

²*PRESTO, Japan Science and Technology Agency (JST)*

³*RIKEN Center for Emergent Matter Science (CEMS)*

⁴*The Institute for Solid State Physics, University of Tokyo*

⁵*Department of Materials Molecular Science, Institute for Molecular Science*

⁶*Japan Synchrotron Radiation Institute (JASRI)*

⁷*Graduate School of Material Science, University of Hyogo*

⁸*Department of Advanced Materials Science, University of Tokyo*

Introduction:

In recent years, topological magnetic structures, such as magnetic skyrmions, have been actively studied. Magnetic skyrmions, nanometer-scale vortex-like magnetic structures, can be controlled by external stimuli, such as electric field and pressure, and thus are expected to be a promising candidate for next-generation spintronics device materials. To understand the dynamics of magnetic skyrmions, it is important to observe them at high spatial and temporal resolutions. Resonant soft X-ray scattering is also known to be a suitable technique for observing such magnetic skyrmion dynamics because of its high sensitivity in detecting spin polarization [1-3]. Therefore, in the present study, we have developed a diffractometer of small-angle resonant soft x-ray magnetic scattering to observe topological magnetic textures in the undulator beamline BL07LSU, SPring-8. The apparatus is equipped with a vacuum chamber having a background pressure of $< 1 \times 10^{-5}$ Pa, a CCD camera (2048x2048 pixel, Princeton Instrument), a direct beam catcher, and a sample holder. To observe transmitted soft X-ray scattering, we prepared thin plate sample thinned by FIB method or magnetic thin films fabricated on Si_3N_4 substrates.

Results:

We tried to measure resonant soft X-ray small-angle scattering from magnetic multilayer films and multiferroic BiFeO_3 lamellas. The magnetic films were fabricated with thickness of several tens nano-meters and with different compositions, $\text{Ta}_5[\text{Pt}_3\text{CoTa}_2]_{10}$, $\text{Ta}_5[\text{Pt}_3\text{Co}_{1.2}\text{Ta}_2]_{10}$, $[\text{Co}/\text{Pt}]_{15}$, and $[\text{Co}/\text{Pt}]_6$. The thickness of the samples were sufficiently thin for soft X-rays to penetrate, and absorption measurements confirmed the presence of the sample. A pinhole with a diameter of several micro-meters was placed on the thin film sample to irradiate a circularly shaped soft X-ray to the sample. Figure 1 shows resonant soft x-ray diffraction image

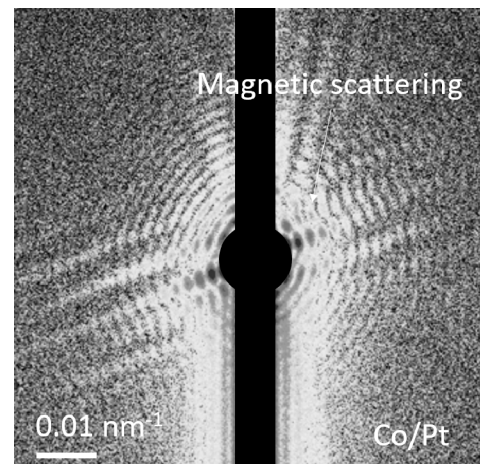


Figure 1: Diffraction pattern from Co/Pt multilayer thin film.

from [Co/Pt]₆ observed at the Co *L*-edge resonance energy. However, the scattering intensity was weak and the diffraction pattern was not sufficiently accurate to reconstruct the real space image from the obtained coherent diffraction pattern. This is probably due to the small perpendicular magnetization component in the magnetic multilayer film. The other samples were damaged during the experiment and no significant data could be obtained.

The multiferroic iron oxide BiFeO₃ is known to have a ferroelectric polarization, which gives rise a long-period cycloidal magnetic structure with a wave-length of 62 nm. The competition between ferromagnetic interaction and the Dzyaloshinskii-Moriya interactions between the Fe ions results in the non-collinear magnetic structure. We performed small-angle scattering experiments at the *L*-absorption edge of Fe on the lamella samples to observe the magnetic scattering derived from the cycloid magnetic structure. Figure 2 shows diffraction patterns from the lamella sample of BiFeO₃. Magnetic scattering was observed with superimposing on the concentric diffraction pattern from pinhole. In the previous study, six magnetic scatters were observed for the (110) surface sample, whereas in the present experiment, magnetic scattering was found to be broad in the azimuthal direction. It is assumed that the magnetic structure may be different due to the influence of FIB processing. To confirm whether the magnetic scattering observed in the lamella sample is intrinsic or not, a follow-up experiment comparing with other FIB processed samples is required in the future.

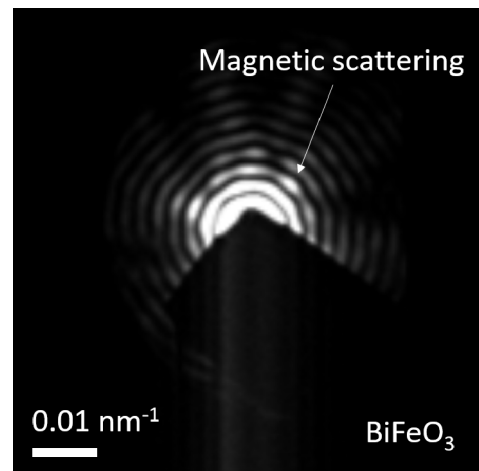


Figure 2: Diffraction pattern from BiFeO₃ lamella sample.

Conclusion:

In this study, we developed the equipment for resonant soft x-ray small angle scattering and succeeded in observing the magnetic scattering from the magnetic thin films and multiferroic BiFeO₃ lamella sample. As a next step, we aim to observe temporal variations of the magnetic structure in real space by combining the coherent soft x-ray diffraction imaging technique with time-resolved pump-probe measurement.

References

- [1] “Dynamical Process of Skyrmion-Helical Magnetic Transformation in Chiral-Lattice Magnet FeGe as Probed by Small-Angle Resonant Soft X-ray Scattering”, Y. Yamasaki, D. Morikawa, T. Honda, H. Nakao, Y. Murakami, N. Kanazawa, M. Kawasaki, T. Arima, and Y. Tokura, *Phys. Rev. B* 92, 220421(R) (2015)
- [2] “Coherent Resonant Soft X-ray Scattering Study of Magnetic Textures in FeGe”, Victor Ukleev, Y. Yamasaki, Daisuke Morikawa, Naoya Kanazawa, Yoshihiro Okamura, Hironori Nakao, Yoshinori Tokura, Taka-hisa Arima, *Quantum Beam Science*. 2 [1] 3 (2018)
- [3] “Element-specific soft x-ray spectroscopy, scattering, and imaging studies of the skyrmion-hosting compound Co₃Zn₈Mn₄”, V. Ukleev, Y. Yamasaki, D. Morikawa, K. Karube, K. Shibata, Y. Tokunaga, Y. Okamura, K. Amemiya, M. Valdivares, H. Nakao, Y. Taguchi, Y. Tokura, T. Arima, *Physical Review B*. 99 [14] 144408 (2019)

REVERSIBLE AND IRREVERSIBLE ANIONIC REDOX FOR HIGH-CAPACITY BATTERY MATERIALS

Naoaki Yabuuchi¹ and Daisuke Asakura²

¹Department of Chemistry and Life Science, Yokohama National University

²Research Institute for Energy Conservation, National Institute of Advanced Industrial Science and Technology

To realize the sustainable energy development, the electrification of automobiles has progressed in the past several years. This movement reduces the dependence on fossil fuels used for internal combustion engine technology together with accelerating the use of renewable energy, including solar, wind, and biomass. In the past three decades, technology of rechargeable lithium batteries, *i.e.*, lithium-ion batteries, has been highly sophisticated, and currently Ni-based layered materials dominate the market of lithium-ion batteries for electric vehicles. However, further increase in energy density of lithium-ion batteries is required to extend cruising distances of electric vehicles. In the past few years, many lithium-excess metal oxides with layered and disordered rocksalt structures, Li_2MnO_3 -based electrode materials have been studied as potential high capacity electrode materials. However, Mn ions in Li_2MnO_3 ($\text{Li}_{1.33}\text{Mn}_{0.67}\text{O}_2$) cannot be oxidized beyond the tetravalent limit, and therefore, anionic species, oxide ions, donate electrons on Li extraction. Nevertheless, low reversibility of anionic redox for pure Li_2MnO_3 is experimentally observed, leading to insufficient reversibility as electrode materials. To increase in the reversibility of anionic redox, the substitution of metal ions with higher ionic characters with oxide ions, for instance, Nb^{5+} (Li_3NbO_4) and Ti^{4+} (Li_2TiO_3), has been proposed. For the Li-excess metal oxides, the charge compensation process on Li extraction is achieved by electron donation from oxide ions, but detailed reaction mechanisms remain as a debatable subject, *e.g.*, dimerization of oxygen and formation of holes in oxygen.

In this study, a binary system of Li_2TiO_3 – LiMnO_2 is examined as electrode materials for Li storage applications, and its reaction mechanism is studied by resonant inelastic X-ray scattering (RIXS) study. In this binary system, nanosized $\text{Li}_{7/6}\text{Ti}_{1/3}\text{Mn}_{1/2}\text{O}_2$ has been prepared by mechanical milling from a mixture of Li_2TiO_3 and LiMnO_2 . [1] TEM observation reveals that particle size is reduced to 5 – 20 nm, and these nanosize particles are agglomerated for each other, forming secondary particles with diameters of 50 – 200 nm after milling. Nanosize $\text{Li}_{7/6}\text{Ti}_{1/3}\text{Mn}_{1/2}\text{O}_2$ delivers large reversible capacities in Li cells, and an initial discharge capacity reaches 295 mA h g^{-1} even at room temperature (Figure 1). Charge compensation processes for nanosize $\text{Li}_{7/6-y}\text{Ti}_{1/3}\text{Mn}_{1/2}\text{O}_2$ were further examined by O K-edge RIXS study (Figure 2a). From the data of Mn K-edge and L-edge XAS study, Mn oxidation from a trivalent to tetravalent state is evidenced on charge for the slope region of 3 – 4 V [1], but no oxidation of Mn ions is

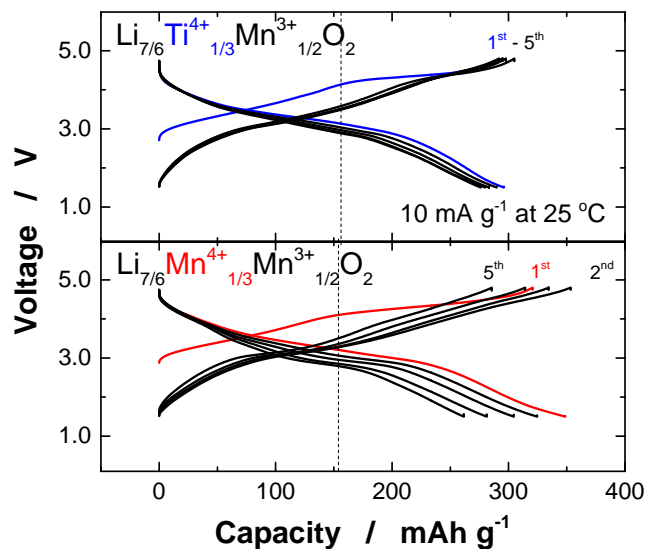


Fig. 1. Charge/discharge curves of nanosize $\text{Li}_{7/6}\text{Ti}_{1/3}\text{Mn}_{1/2}\text{O}_2$ at room temperature. The data of $\text{Li}_{7/6}\text{Mn}^{4+}_{1/3}\text{Mn}^{3+}_{1/2}\text{O}_2$ is also shown for comparison.

found at the plateau region. O K-edge RIXS spectra clearly reveals that a new peak is observed after charge at 8 eV, which suggests that charge compensation is achieved by the donation of electron from oxide ions at the plateau region, and the formation of holes by electrochemical oxidation.[2]

To further clarify the role of Ti ions on anionic redox reversibility, a binary system of $\text{Li}_2\text{MnO}_3\text{-LiMnO}_2$ is also prepared and tested as electrode materials. $\text{Li}_{7/6}\text{Mn}^{4+}_{1/3}\text{Mn}^{3+}_{1/2}\text{O}_2$ was also successfully prepared by mechanical milling from the mixture of Li_2MnO_3 and LiMnO_2 . This phase is metastable containing Mn^{4+} and Mn^{3+} ions and cannot be obtained by a conventional calcination process. Charge/discharge curves of nanosize $\text{Li}_{7/6}\text{Mn}^{4+}_{1/3}\text{Mn}^{3+}_{1/2}\text{O}_2$ in a Li cell are also shown in Figure 1. An observed initial discharge capacity reaches 350 mA h g^{-1} , which is larger than that of $\text{Li}_{7/6}\text{Ti}_{1/3}\text{Mn}_{1/2}\text{O}_2$. Nevertheless, cyclability is insufficient as electrode materials, and a reversible capacity of *ca.* 100 mA h g^{-1} is lost on initial five cycles. Much better capacity retention is achieved for $\text{Li}_{7/6}\text{Ti}_{1/3}\text{Mn}_{1/2}\text{O}_2$. Reversibility of anionic redox for $\text{Li}_{7/6}\text{Mn}^{4+}_{1/3}\text{Mn}^{3+}_{1/2}\text{O}_2$ has been also examined by RIXS study as shown in Figure 2b. A similar peak with $\text{Li}_{7/6}\text{Ti}_{1/3}\text{Mn}_{1/2}\text{O}_2$ at 8 eV is observed for $\text{Li}_{7/6}\text{Mn}^{4+}_{1/3}\text{Mn}^{3+}_{1/2}\text{O}_2$ after charge. However, intensity of the peak is much higher for the $\text{Li}_{7/6}\text{Ti}_{1/3}\text{Mn}_{1/2}\text{O}_2$, indicating that oxygen redox chemistry is clearly stable for the Ti-substituted sample. This result directly supports the role of Ti^{4+} ions, which are effective to stabilize anionic redox associated with the high ionic character and donation of electron to oxide ions.

These findings open a new direction to design high-capacity positive electrode materials with highly reversible electrochemistry on the basis of anionic redox. Further optimization of chemistries, compositions, and particle sizes on these electrode materials contributes the development of advanced high-energy rechargeable Li batteries in the future.

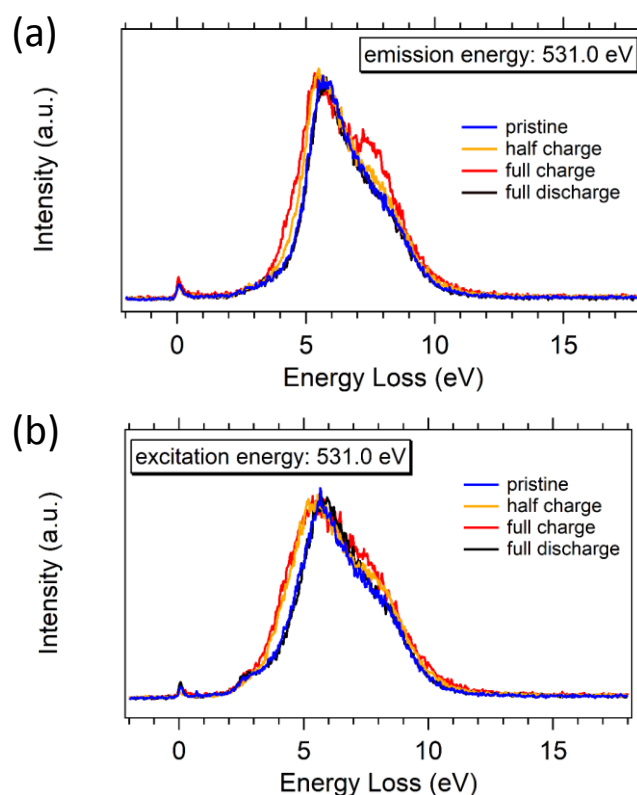


Fig. 2. Comparison of changes in RIXS spectra for nanosize $\text{Li}_{7/6}\text{Ti}_{1/3}\text{Mn}_{1/2}\text{O}_2$ and $\text{Li}_{7/6}\text{Mn}^{4+}_{1/3}\text{Mn}^{3+}_{1/2}\text{O}_2$ on charge/discharge processes.

REFERENCES

- [1] Y. Kobayashi, M. Sawamura, S. Kondo, M. Harada, Y. Noda, M. Nakayama, S. Kobayakawa, W. Zhao 1, A. Nakao, A. Yasui, H. B. Rajendra, K. Yamanaka, T. Ohta, and chi, *Materials Today*, in-press
- [2] T. Sudayama, K. Uehara, T. Mukai, D. Asakura, X.-M. Shi, A. Tsuchimoto, B. Mortemard de Boisse, T. Shimada, E. Watanabe, Y. Harada, M. Nakayama, M. Okubo and A. Yamada, *Energy & Environmental Sciences*, in-press

ELECTRONIC STATE OF INTERMEDIATE WATER IN BIOCOMPATIBLE POLYMERS INVESTIGATED BY XAS AND XES

Koichi Ozaki¹, Jumpei Yahiro¹, Masaru Nakada¹, Masahiro Kunisu¹,
Kosuke Yamazoe², Jun Miyawaki² and Yoshihisa Harada²

¹Toray Research Center, Inc.,

²The Institute for Solid State Physics, The University of Tokyo

Introduction

Poly (vinyl-pyrrolidone) (PVP) and Poly (ethylene-glycol) (PEG) have been widely used for various biomedical applications because of their excellent biocompatibility. Biocompatibility is one of the important factors for polymers used for biomedical applications. It is considered that adsorbed water on the polymer surface contributes to expression of biocompatibility. Water molecules existing near the biocompatible polymer could be classified into three types; free water, intermediate water and non-freezing water [1]. In particular, the intermediate water has an important role to control the biocompatibility of polymers. However, the local structural and dynamical properties of intermediate water are not well understood yet. It has been reported that water molecules confined in a polyelectrolyte brush form characteristic local hydrogen-bonded structure [2]. Based on this result, water molecules in the close vicinity of a biocompatible polymer are expected to form a specific hydrogen-bonded structure to express biocompatibility. In order to reveal the role of hydrogen-bonded structure of water on biocompatibility, it is necessary to obtain accurate information about the hydrogen-bonded structure of those water molecules. In this study, we examine the hydrogen-bonded structure of water molecules hydrating PVP and PEG molecules in detail using X-ray absorption spectroscopy (XAS) and X-ray emission spectroscopy (XES).

Experimental

The PVP ($M_w=4000-5000$) and PEG ($M_w=3350$ and 20000) were purchased from Sigma-Aldrich. PVP and PEG aqueous solutions at different concentrations were prepared as measurement samples. Absolutely dry PVP (dry-PVP) and PEG (dry-PEG) were also measured. O 1s XAS and XES measurements were performed at the BL07LSU HORNET station in SPring-8. The measurement of the polymer aqueous solution was performed using a solution cell under ambient pressure by circulating the aqueous solution. The dry samples were mounted on a Cu sample plate and measured in a high vacuum condition.

Results and Discussion

Figure 1 shows the O 1s XES spectra of dry-PEG ($M_w=20000$) measured at various scan rates of the Cu plate. XES measurements were performed at the excitation energy of 537 eV. A broad peak around 527 eV was observed for the XES spectra with the scan rate of 0.16 and 0 $\mu\text{m/s}$. The shape of the XES spectra changed gradually with increasing the scan rate, indicating the presence of X-ray induced degradation of the polymer during the XES measurement at lower scan rate. Since the shapes of the XES spectra above the 5.0 $\mu\text{m/s}$ scan rate were almost the same, we set the scan rate of 5.0 $\mu\text{m/s}$ to obtain the XES spectra of the dry-PVP and dry-PEG samples.

Figure 2(a) depicts O 1s XES spectra of PVP aqueous solution at the excitation energy of 550 eV. XES measurements were performed with a flow rate of 5.0 ml/s to avoid the accumulation of radiation damage.

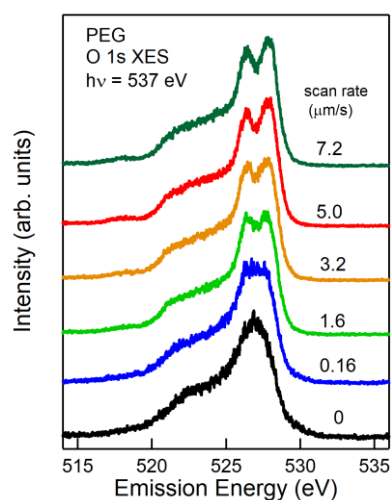


Figure 1. O 1s XES spectra of dry-PEG with various scan rate: 7.2, 5.0, 3.2, 1.6, 0.16 and 0 ($\mu\text{m/s}$).

Two $1b_1$ -derived peaks ($1b_1'$ and $1b_1''$) were observed in the XES spectra of pure water [3]. The raw XES spectra for aqueous solutions contain X-ray emission signals from oxygens both in water molecules and in PVP. Subtracting the polymer component, we can obtain the signal from water molecules. In order to remove the PVP polymer contribution from the raw XES spectra, we focused on the energy range below 522 eV. In this region, the spectral intensity seems to well reflect the relative contributions of water and polymer. Thus each contribution was estimated by performing least-squares fit of the XES spectrum of dry-PVP and pure water in the energy range below 522 eV. The results after subtraction of the polymer contribution are shown in the bottom of Figure 2(a). It was found that the $1b_1'$ peak is dominant in the extracted spectra. The $1b_1'$ -dominant peak profile with a clear shoulder structure around 524.5 eV (possibly assigned as $3a_1$ derived peak) obtained for the 65 wt% PVP solution is quite similar to the previously obtained spectrum for water molecules confined in a polyelectrolyte brush [2]. Therefore water molecules in the 65 wt% PVP solution may exist almost in the form of non-freezing and intermediate water hydrating the PVP polymer. Water molecules in the 30 wt% PVP solution consist of strong $1b_1'$ and weak $1b_1''$ profiles, which can be reproduced by the mixture of bulk liquid water as well as non-freezing and intermediate water hydrating the PVP polymer. Detailed analysis of the XES fraction for the water hydrating PVP may have rich information about the hydrogen-bonded structure of intermediate water and its relation to the biocompatibility of PVP.

Figure 2(b) shows the O 1s XES spectra of PEG ($M_w=3350$) aqueous solutions. Broad peaks at ~ 526.5 eV and ~ 528.0 eV were observed for the XES spectra of dry-PEG. In this case, in addition to the energy range below 522 eV, the energy range above 526 eV was also used for the fitting to estimate the PEG contribution. The results after removal of the polymer contribution are shown in the bottom of Figure 2(b). It

should be noted that the extracted XES profiles are close to the spectrum of pure water, in contrast to the PVP results. The present study raises the possibility that a *static* hydrogen-bonded structure of intermediate water is different between PVP and PEG aqueous solutions. In contrast, *dynamical* hydrogen-bonded structure of intermediate water hydrating PVP and PEG aqueous solutions is similar [4, 5]. Consequently, to understand the behavior of intermediate water, it is important to understand both the *dynamical* and the *static* hydrogen-bonded structures. Several questions remain unanswered at present yet. Future studies on the current topic are recommended.

References

- [1] T. Tsuruta, *J. Biomater. Sci.* **21** (2010) 1831.
- [2] K. Yamazoe *et al.*, *Langmuir* **33** (2017) 3954.
- [3] T. Tokushima *et al.*, *Chem. Phys. Lett.* **460** (2008) 387.
- [4] T. Takei *et al.*, *Anal. Sci.* **26** (2010) 337.
- [5] M. Nakada *et al.*, *Materialia* **12** (2020) 100743.

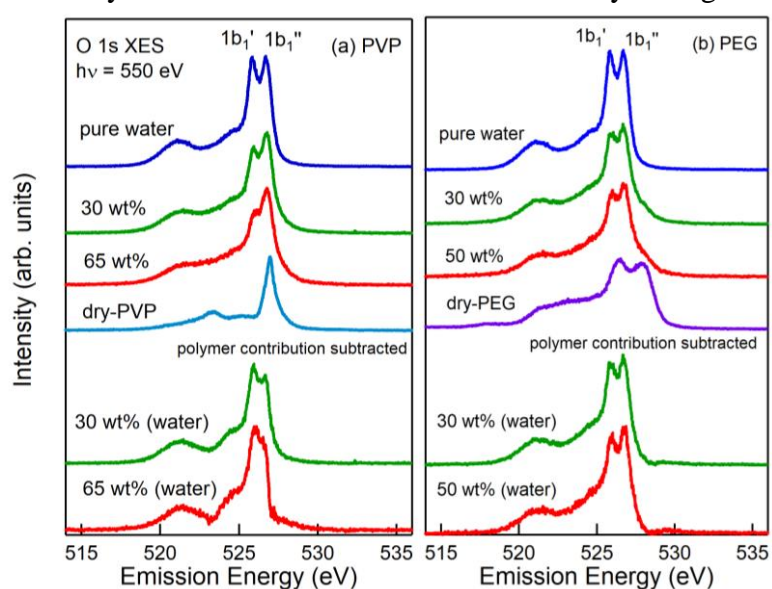


Figure 2. O 1s XES spectra of (a) PVP and (b) PEG aqueous solutions. The spectra of pure water and dried polymer powder were also shown for comparison. Bottom: Spectra with the polymer contribution subtracted.

Present status of the development of time-resolved ambient pressure

X-ray photoelectron spectroscopy system at SPring-8 BL07LSU

Susumu Yamamoto* and Iwao Matsuda

The Institute for Solid State Physics, The University of Tokyo

** Present affiliation: Institute of Multidisciplinary Research for Advanced Materials,
Tohoku University*

Introduction

Operando spectroscopy, observation of working catalysts under reaction conditions, is essential for our understanding of reaction mechanisms as well as the rational development guidelines for novel catalysts. Ambient pressure X-ray photoelectron spectroscopy (AP-XPS) is one of the most powerful *operando* spectroscopies, which permits the investigation of the electronic and chemical states of adsorbates and catalysts under gas atmospheres at near-ambient pressure. However, the typical temporal resolution of AP-XPS has been limited to ms, and thus the dynamic processes faster than ms could not be studied. A pump-probe measurement can overcome the limitation of the temporal resolution, in which a sample is pumped by ultrafast optical laser and probed by X-ray. At SPring-8 BL07LSU, we developed time-resolved X-ray photoelectron spectroscopy (tr-XPS) in ultrahigh vacuum in a pump-probe fashion [1, 2]. The temporal resolution of tr-XPS is ~50 ps, which is determined by the pulse width of probe X-ray.

In this study, we aimed to develop a time-resolved ambient pressure X-ray photoelectron spectroscopy (tr-APXPS) by combining AP-XPS with tr-XPS. tr-APXPS permits monitoring the time evolution of photocatalytic reactions in real time and under reaction conditions; all the players in photocatalytic reactions such as photo-excited carriers, adsorbates, substrates can be investigated by tr-APXPS.

Experimental

The experiments were performed at the soft X-ray undulator beamline BL07LSU at SPring-8 [3]. AP-XPS experiments were carried out using an AP-XPS apparatus that combines a differentially pumped electron analyzer (SPECS, PHOIBOS 150 NAP) with an ambient-pressure gas cell [4]. A one-dimensional delay-line detector (DLD) is adopted as a detector of the electron analyzer.

Femtosecond (fs) laser systems were installed at SPring-8 BL07LSU. The fs laser pulses were synchronized to synchrotron radiation X-ray pulses, and the delay time of fs laser pump pulse relative to X-ray probe pulse can be controlled. There were two different fs laser systems; high pulse energy and low repetition rate (mJ, 1 kHz) and low pulse energy and high

repetition rate (μJ , 208 kHz). Optical parametric amplifier (OPA) was installed in both laser systems, which can change the wavelength of fs laser. In the present study, high pulse energy and low repetition rate (mJ, 1 kHz) laser system was used.

Results and discussion

In the development of tr-APXPS, we reported the installation of a soft X-ray chopper at SPring-8 BL07LSU. The soft X-ray chopper was operated at 1 kHz, and reduced the repetition rate of probe X-ray (208 kHz in the H-mode operation of SPring-8) to 1 kHz to match that of pump laser. Consequently, time-resolved XPS measurements became possible with the same experimental setup as in conventional static XPS measurements. In addition, soft X-ray chopper blocks all the X-ray pulses that are not used in pump-probe measurements. This decreases unnecessary burden on the sample and the detector. Thus, the photon flux can be increased by opening slits in X-ray beamline to improve measurement efficiency.

Test tr-APXPS measurements were performed on the naturally oxidized *p*-type Si(111) ($\text{SiO}_2/p\text{-Si}(111)$) surface in 1 mbar CO_2 . The wavelength of pump laser was changed from 800 nm to 400 nm. This was because the small pre-pulses in 800 nm can induce the surface photovoltage effect of Si. The amplitude of the pre-pulses was much decreased by frequency doubling to 400 nm. In addition to the energy shift of Si $2p$ core level due to surface photovoltage effect, we could detect the energy shift of CO_2 gas phase peak in O $1s$ core level. The energy shift of gas phase peak in AP-XPS reflects the change of the sample work function. Notably, the energy shift was different between Si $2p$ and O $1s$ core levels. The present results demonstrate that of tr-APXPS can provide a wealth of information in photo-excited systems and will be very suited to study various light-induced reactions including photocatalysts and plasmonic chemical reactions.

REFERENCES

- [1] K. Ozawa, S. Yamamoto, *et al.*, e-J. Surf. Sci. Nanotechnol. **17**, 130-147 (2019).
- [2] M. Ogawa, S. Yamamoto, *et al.*, Rev. Sci. Instrum. **83**, 023109 (2012).
- [3] S. Yamamoto *et al.*, J. Synchrotron Rad. **21**, 352-365 (2014).
- [4] T. Koitaya, S. Yamamoto, *et al.*, e-J. Surf. Sci. Nanotechnol. **17**, 169-178 (2019).

Development of time-resolved X-ray absorption and photoelectron spectroscopy system using time-of-flight electron analyzer

Susumu Yamamoto^{1,*}, Rei Hobara², Kenichi Ozawa³, and Iwao Matsuda¹

¹ *The Institute for Solid State Physics, The University of Tokyo*

² *Department of Physics, The University of Tokyo*

³ *Department of Chemistry, Tokyo Institute of Technology*

** Present affiliation: Institute of Multidisciplinary Research for Advanced Materials,
Tohoku University*

Introduction

Understanding the dynamics of photoexcited carriers is essential for improving the efficiency of light-energy conversion materials such as photocatalysts and solar cells. Photoexcited carriers (electrons/holes) generated by light absorption move between an occupied state and an unoccupied state. Therefore, it is important to observe both occupied and unoccupied states in order to get the whole picture of the photoexcited carriers dynamics. However, there has been no experimental method that allows the observation of both occupied and unoccupied states dynamics.

In this study, we aim to develop a picosecond time-resolved X-ray absorption/photoelectron spectroscopy (XPS/XAS) system using a time-of-flight (TOF) electron analyzer, and track the temporal changes of electronic structures in both occupied and unoccupied states. In addition, the TOF electron analyzer has a unique feature that all kinetic energy electrons can be detected and energy-resolved by the detector. In the case of a hemispherical electron analyzer, only electrons with the fixed kinetic energy determined by electrostatic lenses are detected by the detector. Taking advantage of this unique feature of TOF electron analyzer, we can measure XAS spectra with different probing depths at once. The time-resolved XAS spectra using TOF analyzer will allow the temporal evolution of excited electronic states along the depth direction.

Experimental

The experiments were performed using a TOF electron analyzer (VG Scienta, ARTOF 10k) at the soft X-ray undulator beamline BL07LSU at SPring-8 [1]. We developed a picosecond time-resolved XPS system using the TOF electron analyzer, and studied the relaxation dynamics of photoexcited carriers on various surfaces and interfaces [2]. In the present study, thus, we aim to extend the application of the TOF electron analyzer to XAS measurements. We developed the software program that can control both TOF electron analyzer and the soft X-ray beamline (undulator and monochromator) to measure XAS spectra. The sample studied in this research was the rutile TiO₂(110) surface. The sample surface was cleaned by Ar ion sputtering (1.0 kV, 1x10⁻⁴ Pa Ar, 10 min), and annealing in an oxygen atmosphere (920 K in 1x10⁻⁴ Pa O₂). The surface order was confirmed by low energy electron diffraction (LEED).

Results and discussion

Figure 1 shows the Ti L-edge XAS spectrum of the clean TiO₂(110) surface measured using TOF electron analyzer. The XAS spectrum in total electron yield (TEY) was obtained by integrating the whole TOF region indicated by the blue lines in Fig. 1(a). The obtained XAS spectrum in Fig. 1(b) is in good agreement with the TEY-XAS spectrum measured with the sample current. This confirms the successful measurement of XAS spectra using TOF electron analyzer. By changing the TOF window for the integration, we can change the probing depth. For example, we could obtain the surface sensitive XAS spectra if the TOF window is tuned to Auger electrons. Now we plan to perform XAS experiments on the sample that has a distribution of chemical states in the depth direction (e.g., ice H₂O thin films adsorbed on the TiO₂ surface).

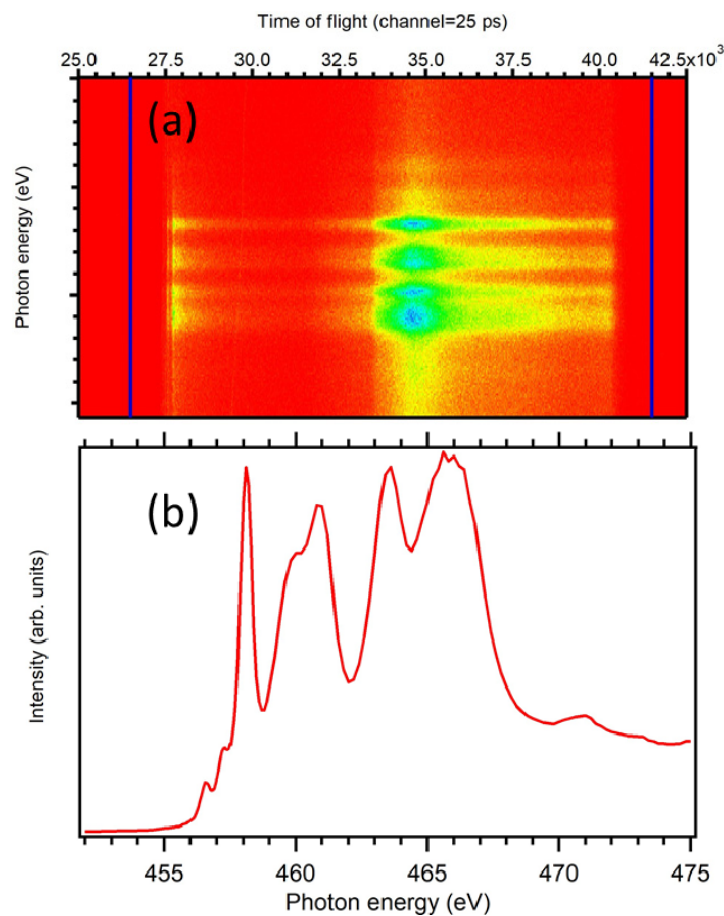


Figure 1. Ti L-edge XAS spectrum of the clean TiO₂(110) surface measured using TOF electron analyzer. (a) TOF spectra as a function of photon energy (b) XAS spectrum obtained by integrating the TOF region indicated by the blue lines in the panel (a).

REFERENCES

- [1] S. Yamamoto *et al.*, J. Synchrotron Rad. **21**, 352-365 (2014).
- [2] S. Yamamoto *et al.*, J. Phys. Soc. Jpn. **82**, 021003 (2013).

SOFT X-RAY ABSORPTION SPECTROSCOPY OF Ca_2RuO_4 UNDER ELECTRIC FIELD

Daiki Ootsuki¹, Yukie Takasuka¹, Ayuko Hishikawa¹,
Tatsuhiko Ishida¹, Teppei Yoshida¹, Kosuke Yamazoe², Tomoyuki Tsukada²,
Jun Miyawaki², Yoshihisa Harada²,

Chanchal Sow³, Shingo Yonezawa³, Yoshiteru Maeno³, and Fumihiko Nakamura⁴

¹Graduate School of Human and Environmental studies, Kyoto University,

²Synchrotron Radiation Laboratory, The Institute for Solid State Physics, The University of Tokyo,

³Department of Physics, Kyoto University,

⁴Department of Education and Creation Engineering, Kurume Institute of Technology

The exploration of non-equilibrium phase transition and non-linear conductivity in strongly correlated electron systems is one of the frontier of condensed matter physics. By applying electric fields, Mott insulators exhibit the insulator to metal transition with a non-linear conductivity [1-2], which is so called ‘‘Mott breakdown’’ analogous to dielectric breakdown [3]. Recently, Nakamura *et al.* have discovered an electric-field induced insulator to metal transition of Ca_2RuO_4 with nonlinear conductivity. The threshold electric field E_{th} of ~ 40 V/cm is weakest among the Mott insulators [4]. It would be desirable to understand how the electronic structure is changed by applying electric field and to clarify the origin of the non-linear conductivity of Ca_2RuO_4 .

The various stimuli such as temperature, chemical substitution, and applied pressure induce the metal to insulator transition of Ca_2RuO_4 with a structural phase transition [5-7]. The structural phase transition affects the orbital configuration of this system through RuO_6 octahedra [5]. Actually, the insulating state of Ca_2RuO_4 is characterized by the crystal field splitting as well as on-site Coulomb interaction. The recent polarization-dependence of angle-resolved photoemission spectroscopy combined with dynamical mean-field theory (DMFT) revealed the coexistence of the band insulating state of d_{xy} orbitals originating from the crystal-field splitting and the Mott insulating states of half-filled $d_{xz/yz}$ orbitals [8].

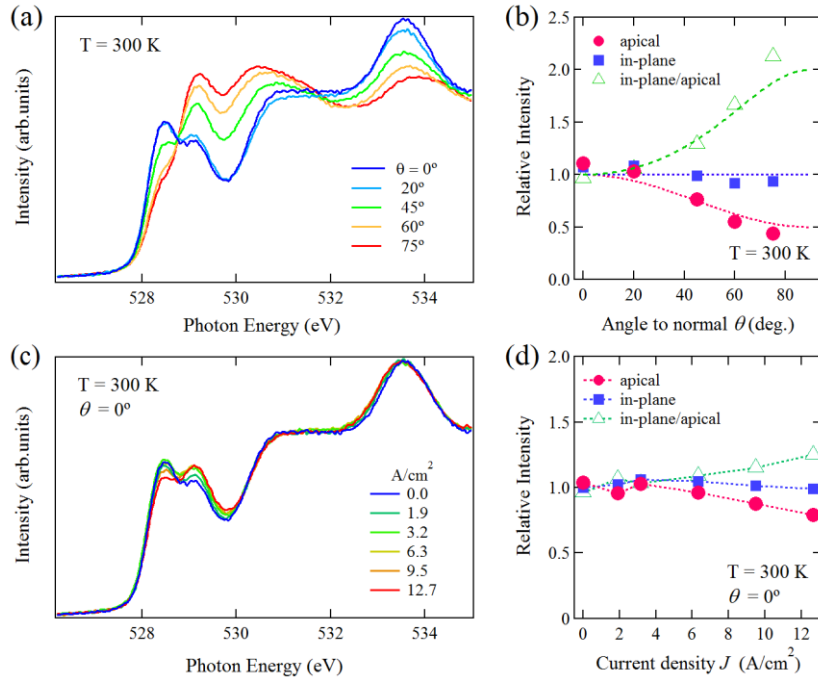


Figure 1. O 1s XAS spectra of Ca_2RuO_4 as a function of (a) angle θ and (c) current density J . Intensities of apical and in-plane components as a function of (b) angle θ and (d) current density J .

In this study, we have investigated the electric-field dependence of the electronic structure for Ca_2RuO_4 by means of soft x-ray absorption spectroscopy (XAS) under electric field at SPring-8 BL07LSU. High quality single crystals of Ca_2RuO_4 were grown by floating-zone method. In order to apply the electric field, the gold wires were attached to the terminals both ends of the sample using silver epoxy. The electric field was applied parallel to the ab -plane and the voltage-current characteristics were measured *in situ* during the XAS measurements. The sample temperature is monitored by the directly attached Pt thermometer and controlled by liquid helium. Although the current flow gives rise to the joule heating effect, the sample heating kept less than 3 K during all measurements.

Figure 1 (a) shows the angle dependence of the O $1s$ x-ray XAS spectra take at $T = 300$ K. The XAS spectrum strongly depends on the angle θ . We focus on the intensities at ~ 528.3 eV and ~ 529.1 eV derived from the apical and in-plane oxygen, respectively. To quantify the intensities of the apical and in-plane components, we fitted the intensities derived from apical and in-plane oxygen with a Gaussian as shown in Fig. 1 (b). The angle dependence of XAS spectra is basically consistent with the previous XAS study reported by Mizokawa *et al* [9]. This indicates that the carrier concentration between the Ru $4d_{xy}$ and $4d_{yz/zx}$ orbitals is close to 1:1 at $T = 300$ K. Figures 1 (c) and (d) show the electric field dependence of the XAS spectra at $T = 300$ K. Here, we obtained the electric-field dependence of XAS spectra at the normal incidence. By increasing current density J , the apical intensity decreases, while the in-plane intensity increases. As shown in Fig. 1 (d), the intensity ratio of the apical and in-plane components gradually increases with current density J .

Figure 2 shows the relationship between the crystal-field splitting Δ , spin-orbit coupling λ_{so} , and the intensity ratio of the apical and in-plane components of XAS spectra. The solid curve indicate the theoretical estimation on the basis of the simple Hamiltonian of Ref. 10. From the theoretical curve, we obtained the crystal-field splitting Δ and spin-orbit coupling λ_{so} . With increasing current density, the crystal field splitting energy increases from the compressed RuO_6 octahedra to the elongated RuO_6 octahedra. These results suggest that the electric field induces the elongation of the RuO_6 octahedra.

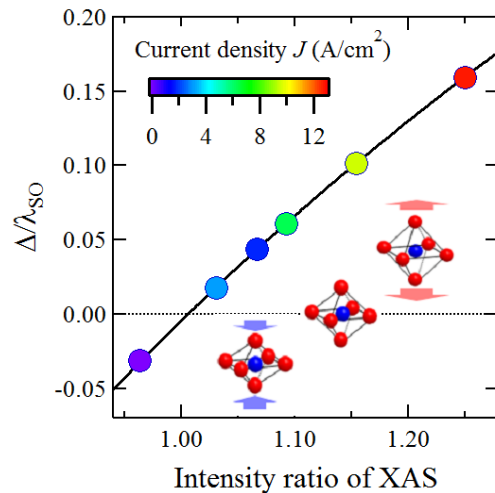


Figure 2. XAS intensity ratio between the apical and in-plane components. The solid line is the model expectation of the Hamiltonian of Ref. 10.

REFERENCES

- [1] Y. Taguchi *et al.*, Phys. Rev. B **62**, 7015 (2000).
- [2] K. Inagaki *et al.*, J. Phys. Soc. Jpn. **73**, 3364-3369 (2004).
- [3] T. Oka, Phys. Rev. B **86**, 075148 (2012).
- [4] F. Nakamura *et al.*, Sci. Rep. **3**, 2536 (2013).
- [5] O. Friedt *et al.*, Phys. Rev. B **63**, 174432 (2001).
- [6] F. Nakamura *et al.*, Phys. Rev. B **65**, 220402 (2002).
- [7] S. Nakatsuji and Y. Maeno, Phys. Rev. Lett. **84**, 2666-2669 (2000).
- [8] D. Sutter *et al.*, Nat. Commun. **8**, 15176 (2017).
- [9] T. Mizokawa *et al.*, Phys. Rev. Lett. **87**, 07702 (2001).
- [10] G. Fatuzzo *et al.*, Phys. Rev. B **91**, 155104 (2015).

OPERANDO XPS STUDY OF CO₂ HYDROGENATION ON A SINGLE-ATOM ALLOY Pd-Cu MODEL CATALYST

J. Yoshinobu, S. Tanaka, K. Mukai, W. Osada, T. Matsuda, S. Nakano, Y. Choi,
S. Yamamoto, and I. Matsuda

The Institute for Solid State Physics, The University of Tokyo

Introduction

Single-atom alloy catalyst (SAAC) is an alloy in which a small amount of functional metal atoms are deposited and embedded in the surface of a metal substrate. The deposited atoms give a new specific function to the substrate, where the main catalytic activity of the substrate is still active [1]. When high-resolution XPS measurement is performed using high-intensity synchrotron radiation, a very small amount (a few percent or less) of embedded atoms on the substrate surface can be detected, and their chemical states can be clearly identified. Furthermore, it is possible to observe the changes in the electronic and chemical states of the adsorbed atoms/molecules as well as the catalyst surface in ambient conditions using NAP-XPS. *Operando* measurements using mass spectrometry and NAP-XPS can elucidate the catalytic function of SAAC during the reaction.

In this study, we prepared a single-atom alloy catalyst (SAAC) Pd-Cu(111) and investigated the hydrogenation of carbon dioxide (CO₂) using NAP-XPS. CO₂ is one of the greenhouse effect gases. At present, methanol synthesis from CO₂ is performed at high temperature (~500K) and under high pressure using Cu/ZnO catalysts. This reaction is an exothermic reaction, in which the molar number decreases for the forward direction. Thus, more active and efficient catalysts which can be operated at lower temperature are highly demanded.

Recently, we found the desorptions of hydrogenated species after a large amount of hydrogen exposure to formate species (HCOO) on a Pd-Cu(111) surface using temperature programmed desorption. In the present study, we aimed to clarify the hydrogenation reaction process of CO₂ on a single-atom alloy catalyst Pd-Cu(111) by NAP-XPS.

Experimental

Experiments were carried out using NAP-XPS system at SPring-8 BL07LSU. The clean Cu(111) was prepared in a UHV preparation chamber of NAP-XPS system. A small amount of Pd was vapor-deposited on the surface to prepare a single atom alloy model catalyst Pd-Cu(111). The amount of Pd deposited was estimated to be 0.02 ML (monolayer). In a NAP cell, CO₂ (0.9 mbar) and H₂ (0.5 mbar) were introduced under isothermal conditions near room temperature. During this process, the model catalyst surface was observed by NAP-XPS. Next, the substrate temperature was raised stepwise by heating under constant pressure of CO₂ (0.9 mbar) and H₂ (0.5 mbar).

Results and discussion

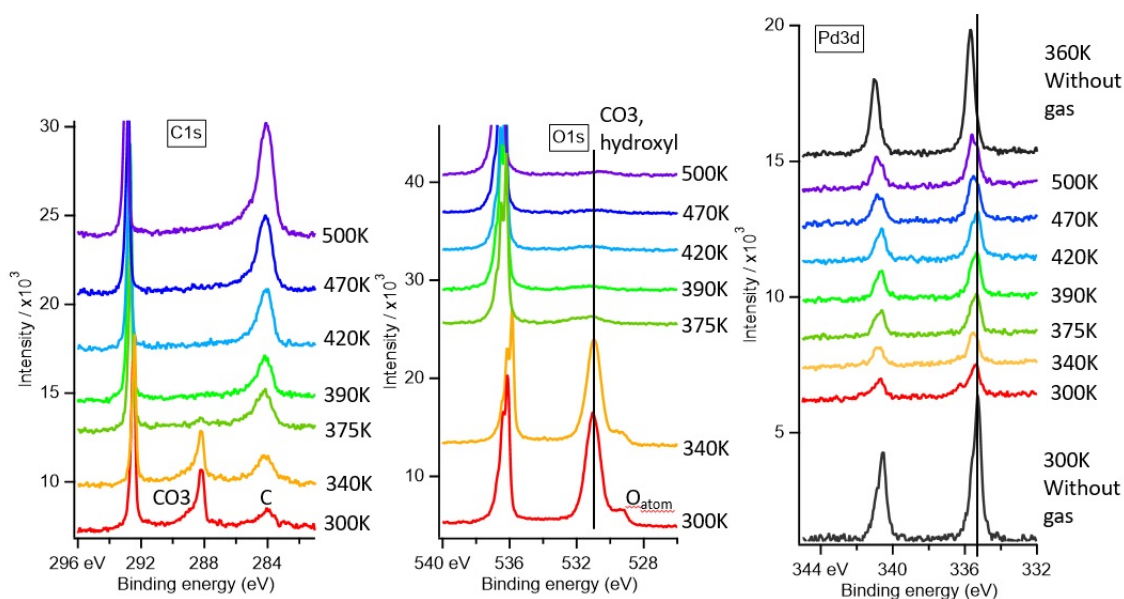
Before the introduction of mixed gases (CO₂ + H₂), only H₂ was gradually introduced in the NAP cell at 300 K up to 3.0 mbar, and the model catalyst surface was investigated by NAP-XPS; the core-level spectra of Cu 2p, Cu LVV Auger, Cu 3p, and Pd 3d were measured. However, any peak shifts due to hydrogen adsorption and an appearance of new peaks were not

observed under the present conditions. Even if the dissociative adsorption of hydrogen occurs, hydrogen is thermally desorbed at room temperature, i.e., a sufficient amount of hydrogen is not adsorbed on the surface.

CO₂ (0.9 mbar) and H₂ (0.5 mbar) were introduced into the NAP cell at 300 K, and Pd3d, C1s, and O1s were observed by AP-XPS (see Fig. 1). Based on our previous study [2], major surface species were attributed to CO₃ species; a small amount of atomic oxygen were also observed. In the case of Pd3d, a small peak was newly observed on the high binding energy side. This may be assigned to the Pd atoms bonded to atomic oxygen species.

When heating the sample from 300K to 500K, the C1s and O1s peaks originating from CO₃ species were observed up to 375K but almost disappeared above 390K. The O1s peak attributed to atomic oxygen almost disappeared above 375K. On the other hand, the peak derived from carbon species (~284 eV) gradually increased with heating.

The present study suggests that the dissociation of CO₂ and the formation of CO₃ and O species occur at 300 K (disproportionation). However, no experimental evidence was detected to indicate hydrogenation of CO₂ at the present experimental conditions. Therefore, in order to achieve a sufficient amount of adsorbed hydrogen atoms at the surface to induce hydrogenation, lower temperature and/or higher H₂ pressure may be needed.



- Figure 1 A series of XPS spectra of C 1s, O 1s and Pd 3d of the Pd-Cu(111) surface under CO₂ (0.9 mbar) and H₂ (0.5 mbar) at 300 K and subsequent heating.

REFERENCES

- [1] G. Giannakakis et al., Accounts of Chemical Research, **52**, 237 (2018).
- [2] T. Koitaya et al., Topics in Catalysis, **59**, 526 (2016).

AP-XPS STUDY OF ELECTRONIC STATES OF METAL NANO PARTICLES AND METAL HYDRIDE COMPLEX

J. Yoshinobu¹, W. Osada¹, Y. Choi¹, S. Tanaka¹, K. Mukai¹,
T. Koitaya², S. Yamamoto³, and I. Matsuda¹

¹*The Institute for Solid State Physics, The University of Tokyo*

²*Institute for Molecular Science*

³*Institute of Multidisciplinary Research for Advanced Materials, Tohoku University*

Introduction

When a hydrogen atom is bonded to metal, the chemical state of hydrogen can be classified into atomic hydrogen (H), proton (H⁺) or hydride (H⁻), or an intermediate state between them; it can easily change, depending on its surrounding environment. The chemical state of metal which is bonded to hydrogen also changes accordingly. By utilizing various hydrogen species on a metal surface, a new reaction path can be developed for "highly selective", "very difficult" and/or "highly efficient" processes. One might think that a metal is "reduced" when it is bonded to hydrogen. However, when neutral hydrogen takes an electron from metal and it becomes hydride (H⁻), the metal is now "oxidized". Using high-resolution X-ray photoelectron spectroscopy (XPS), the chemical state of metal can be elucidated at each site, based on the chemical shift of its core level peak. In the case of surface chemistry, we can trace the chemical states of surface and bulk during the processes including hydrogen adsorption, absorption and desorption. Although the formal charges of hydrogen and metal have been estimated based on valency in a hydrogen-containing metal complex, one can experimentally elucidate the chemical state of a metal atom using XPS. In this study, we planned to perform ambient pressure (AP) XPS measurements of metal-alloy nanoparticles and multinuclear metal complexes in the presence of hydrogen.

Experimental

In this beam time, we carried out XPS measurements of Pt nano particles and Pt₇₅Pd₂₅ nano particles synthesized by Yamauchi group at Kyushu University, and multinuclear Ti complexes including Ti₄N₄ [C₅Me₄SiMe₃]₄ synthesized by Shima group at RIKEN (hereafter abbreviated as Ti₄N₄ complex).

(A) In the case of Pt and Pt₇₅Pd₂₅ nano particles, these nano particles were deposited on a Au foil. First, we measured Pt 4f and Pd 3d XPS in vacuum at room temperature. Next, the sample was heated to 250 °C in vacuum, and Pt 4f and Pd 3d XPS spectra were measured in vacuum at room temperature. Finally, the sample was heated under H₂ (20 mbar) at 250 °C for 20 minutes, and XPS of Pt 4f and Pd 3d measurements were performed at room temperature.

(B) In the case of Ti₄N₄ complex, a small amount of Ti₄N₄ complex was dissolved in degassed n-hexane in an Ar glove box and 5 μL of this solution was dropped on a PdCu alloy substrate. After evaporating and drying the sample solvent, the sample was carefully moved from the glove box to the load-lock chamber of the AP-XPS system using a vacuum transfer device. First, we measured XPS spectra of Ti 2p, C 1s, O 1s and N 1s in vacuum at room temperature. Next, H₂ gas (5 mbar) was introduced and subsequently evacuated; during this process AP-XPS measurement was carried out for Ti 2p, C 1s, O 1s and N 1s.

Results and discussion

(A) XPS spectra of Pt nano particles and Pt₇₅Pd₂₅ nano particles during the above processes were obtained. When comparing the XPS spectra of the as-installed sample and the heated

sample at 250°C, we confirmed that the O 1s intensity was decreased after heating, but a remarkable change in the spectral shapes of Pt 4f and Pd 3d was not observed. Even after heating at 250°C under H₂ pressure (20 mbar) for 20 minutes, no significant change was observed in Pt 4f and Pd 3d XPS in vacuum. Thus, the significant surface segregation of Pd atoms in the alloy nano particle was not observed under the present hydrogen pressure and heating conditions.

(B) Our previous experiments suggested that the present Ti₄N₄ complex reacts with oxygen and water, and it is easily oxidized. In this experiment, we carefully prepared the sample and transferred it to the AP-XPS chamber as described above. Figure 1 shows Ti 2p, C 1s, O 1s and N 1s XPS spectra of Ti₄N₄ complex on a PdCu substrate. Ti 2p_{3/2} and N 1s peaks were observed at 456.8 eV and 397.2 eV, respectively, indicating that Ti takes a tetravalent state and N atoms are bonded to the metal. Next, we also carried out AP-XPS measurements during the H₂ exposure and pumping processes. Upon H₂ exposure, we found the disappearance of N 1s peak, the increase of O 1s and the peak shift of Ti 2p_{3/2} to 459.6eV. These results indicate that there is no nitrogen in the complex and it was oxidized. We assume that upon H₂ exposure the partial pressure of water vapor was increased in the AP cell by some reactions between hydrogen and the inner wall of a stainless-steel AP cell, and thus produced water reacts with the complex.

For future work, we need to control the gases in the AP cell to eliminate the possibility of oxidation of metal complex.

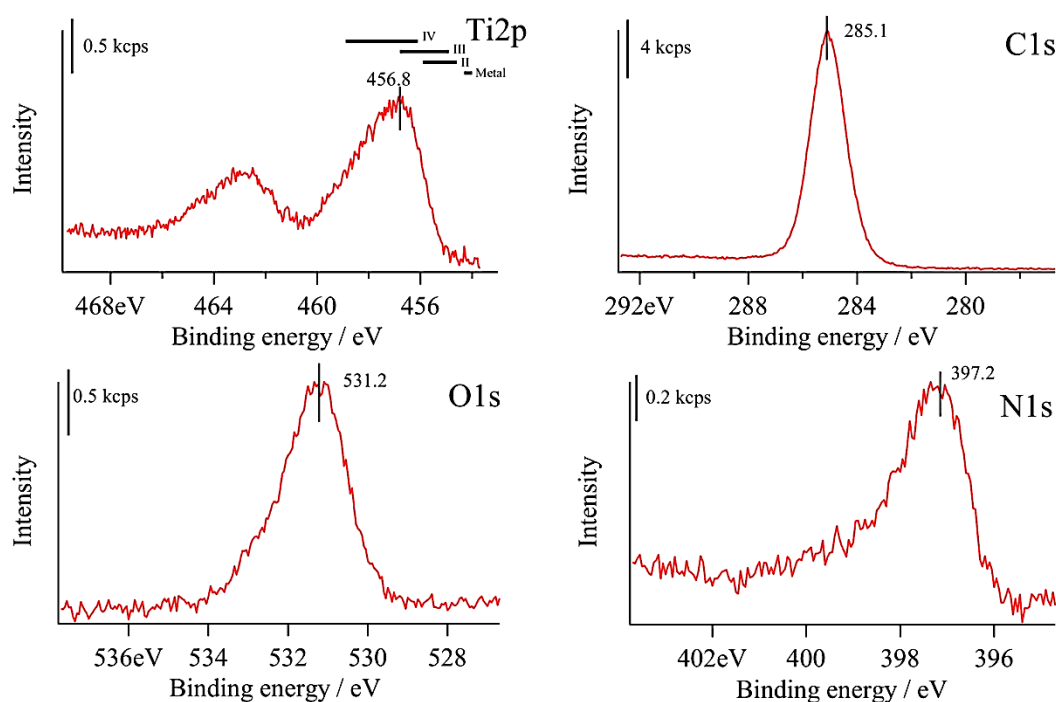


Figure 1 Ti 2p, C 1s, O 1s and N 1s XPS spectra of Ti₄N₄ complex deposited on a PdCu substrate. XPS measurements were carried out in vacuum at room temperature ($h\nu = 680$ eV).

DYNAMICS OF PHOTOCATALYTIC MATERIALS FOR WATER SPLITTING REACTION STUDIED BY TRANSIENT X-RAY ABSORPTION SPECTROSCOPY

Yohei Uemura,¹ Ahmed Ismail,¹ Hebatalla Elnaggar,¹ Federica Frati,¹ Hiroki Wadati,^{2,3} Yasuyuki Hirata,² Yujun Zhang,² Kohei Yamagami,² Susumu Yamamoto,² Iwao Matsuda,² Frank de Groot¹

¹*Inorganic Chemistry and Catalysis, Debye Institute for Nanomaterials Science, Utrecht University, Universiteitslaan 99, 3584 CG Utrecht, The Netherlands*

²*Institute for Solid State Physics, University of Tokyo, Kashiwa, Chiba 277-8581, Japan*

³*Graduate School of Material Science, University of Hyogo, Kamigori, Hyogo 678-1297, Japan*

Introduction

From the viewpoint of building a sustainable society, developing a renewable energy resource is an important subject in the modern science and technologies. Water splitting reaction where water molecules (H_2O) are decomposed into hydrogen (H_2) and oxygen (O_2) is expected to be a key reaction to achieve a renewable energy process. Photocatalysts and photoelectrodes play a central role in the water splitting reaction utilizing sunlight. Semiconductors such as TiO_2 , $\alpha\text{-Fe}_2\text{O}_3$ is typical photocatalysts/photoelectrodes. They have been developed for several decades and new materials are still explored to enhance its catalytic efficiency for our daily use. Fundamental studies on the mechanisms of photocatalysts/photoelectrodes have been based on theoretical calculations, electrochemical methods and spectroscopic studies. X-ray absorption spectroscopy (XAS) is a new trend to study the excited states of photocatalytic materials. XAS can address local symmetries and electronic states of a specific element in the material under investigation and give complementary information which is not provided from optical spectroscopies. In order to understand dynamics of excited states of photocatalysts and photoelectrodes, we measured thin films of hematite ($\alpha\text{-Fe}_2\text{O}_3$) and copper tungstate (CuWO_4). $\alpha\text{-Fe}_2\text{O}_3$ and CuWO_4 are have been studied as photoelectrodes for solar-assisted water splitting reaction. We have already measured fast carrier dynamics of both the samples based on femtosecond XAS measurements in PAL-XFEL.¹ We focused on how the photoexcited states are progressed in hundreds of picoseconds. Here, we will present the result of the transient XAS study on the photoexcited state of $\alpha\text{-Fe}_2\text{O}_3$, which has been recently published in ref. 1.

Experimental details

Pump probe XAS experiments were performed at BL07LSU, SPring-8. An illustration of the setup employed in this study is displayed in Figure 1 (a) and the details of the setup is described in ref. 2. The repetition of the excitation laser was ~ 1 kHz and its wavelength was ~ 400 nm which was generated by doubling the fundamental wavelength of a Ti:Sapphire laser (~ 800 nm) using a BBO crystal. The samples were thin films of $\alpha\text{-Fe}_2\text{O}_3$ and CuWO_4 deposited on an Indium-Tin-oxide-coated glass substrate. The thickness of the samples was ~ 50 nm.

Results

Transient XAS measurements by the sample current: In our experiments, an x-ray chopper developed in SPring-8 was employed in order to select x-ray synchronised with an excitation laser.³ In the previous experiments², the signals from the x-ray pulses synchronised with an excitation laser were accumulated by using electric gates. Although the x-ray signals can be efficiently by this method, a fast-response detector (response time: nanoseconds) is needed to be employed. The x-ray chopper can isolate the x-rays synchronised with the laser and only the selected x-rays hit a sample. As the consequence, a relatively slow-response detector (\sim milliseconds) could be employed. In our beamtime, we tried to measure transient XAS by measuring the sample current in addition to counting photoelectrons from the sample. transient XAS of the $\alpha\text{-Fe}_2\text{O}_3$ sample was measured by the sample current.

Although XAS spectra with a good signal-to-noise ratio (S/N) was obtained by measuring the sample current, we did not confirm transient signals measured by the sample current. It would be because the excitation laser affected the sample current signals, which could be smeared out transient signals. However, the synchronization of the x-ray pulses was achieved and obtained XAS spectra with a good S/N. It would be possible to measure XAS with a transmitting geometry by employing the x-ray chopper, which should extend the choice of the samples to be measured. It would be possible to distinguish transient signals from bulk and from surface of a sample when the sample current and PEY are employed at the same time.

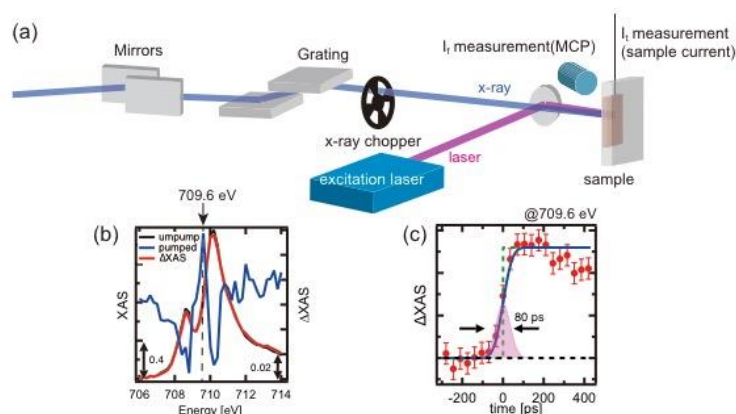


Figure 1 (a) an illustration of the experimental setup at BL07LSU, (b) the transient Fe L_{III} edge XAS spectra of hematite (c) the kinetic trace at 709.6 eV

The transient XAS of $\alpha\text{-Fe}_2\text{O}_3$: Transient Fe L_{III} XAS of hematite was measured by a partial electron yield (PEY) detection. The fluence of the excitation laser was set to 10 mJ/cm^2 , which is below the damage threshold of the sample. The transient XAS at a delay time of 80 ps is shown in the central panel of Figure 1. There are three distinctive transient features found around 708.6, 709.6 and 710.2 eV. The transient feature around 709.6 eV was also observed by the transient experiments in PAL-XFEL, which appeared just after the sample was excited by the laser.¹ The transient feature originates from the creation of Fe(II) species compared by the theoretical calculations. The transient features seen around 708.6 eV and 710.2 eV were not observed at faster delay time ($< 10 \text{ ps}$) in PAL-XFEL. These new features could come from local structural changes which happens between 10 ps and 80 ps after the photoexcitation. Small polaron creation in a hematite thin film was observed around a delay time of 1 ps after photoexcitation by femtosecond transient extreme ultraviolet spectroscopic experiments⁴. Further local structural changes could happen in later delay time. Considering the time range of water splitting reaction, the excited state of hematite should be important to understand the driving force of the water splitting reaction. We have also measured transient XUV spectra of several hematite samples by a delay time of 1 ns. We would like to combine the transient Fe L_{III} XAS data with the XUV data to understand more details of photoexcited states of hematite.

REFERENCES

1. Ismail, A. S. M., et al., Direct Observation of the Electronic States of Photoexcited Hematite with Ultrafast 2p3d X-Ray Absorption Spectroscopy and Resonant Inelastic X-Ray Scattering. *Phys. Chem. Chem. Phys.* **2020**, *22*, 2685-2692.
2. Takubo, K., et al., Capturing Ultrafast Magnetic Dynamics by Time-Resolved Soft X-Ray Magnetic Circular Dichroism. *Appl. Phys. Lett.* **2017**, *110*, 162401.
3. Osawa, H.; Ohkochi, T.; Fujisawa, M.; Kimura, S.; Kinoshita, T., Development of Optical Choppers for Time-Resolved Measurements at Soft X-Ray Synchrotron Radiation Beamlines. *Journal of Synchrotron Radiation* **2017**, *24*, 560-565.
4. Carneiro, L. M.; Cushing, S. K.; Liu, C.; Su, Y.; Yang, P.; Alivisatos, A. P.; Leone, S. R., Excitation-Wavelength-Dependent Small Polaron Trapping of Photoexcited Carriers in $\alpha\text{-Fe}_2\text{O}_3$. *Nat. Mater.* **2017**, *16*, 819-825.

INVESTIGATION OF THE ELECTRONIC STRUCTURE OF COBALT OXIDE SPINEL ON ELECTRODES FOR WATER OXIDATION CATALYSTS USING CO 2P3D RIXS

Minmin Chen,^a Kosuke Yamazoe,^{b,c} Jun Miyawaki,^{b,c} Yoshihisa Harada,^{b,c} Serena DeBeer,^a Olaf Rüdiger^a

^aMax Planck Institute for Chemical Energy Conversion, Mülheim an der Ruhr, Germany

^bInstitute for Solid State Physics, The University of Tokyo, Kashiwa, Chiba 277-8581, Japan

^cSynchrotron Radiation Research Organization, The University of Tokyo, 7-3-1 Hongo, Bunkyo-ku, Tokyo 113-8656, Japan

Development of new anode materials based on earth abundant transition metals for water splitting is strategically important for industrial and large-scale applications. Water splitting has been considered one of the most promising strategies for energy conversion and storage.¹ Here, we study Co₃O₄ spinel on electrode surfaces by spectroelectrochemistry. The spinels are synthesized as nanoparticles of around 10 nm that form aggregates of 100-300 nm diameter. The materials are drop cast on the electrode surface, in this case a gold-coated SiN window. In order to stabilize the small catalyst particles (particle size 300 nm) on the electrode surface, Nafion is used as a binder. Unfortunately, Nafion showed extreme X-ray sensitivity during our experiments. Being a fluorine-rich polymer, the F K-edge at 690 eV absorbed the X-rays and damaged the polymer structure, which resulted in a simultaneous decrease of the Co intensity.

The use of Fumion as a binder solves this problem. Fumion does not contain any F atoms in its structure and showed no detectable photodegradation during the spectroelectrochemical experiments. Nevertheless, we did not detect any significant changes on the 2p3d RIXS or at the Co L-edge XAS with the applied potential (Figure 1).

In order to understand the 2p3d RIXS of the spinel system, we also measured spectra from Al₂CoO₄, Co₂ZnO₄ and CoO as powder samples. The Al₂CoO₄ is a spinel, where the Co³⁺ at the O_h sites has been substituted

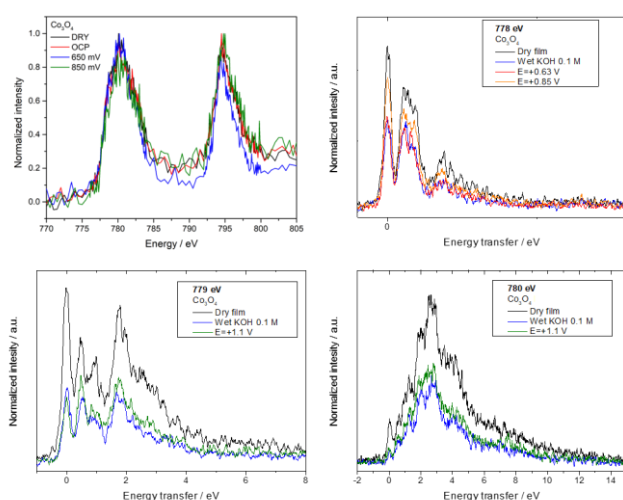


Figure 1. Co L-edge XAS (top-left) and 2p3d RIXS spectra of an electrode prepared by drop casting Co₃O₄ nanoparticles and Fumion as a binder. The conditions are indicated on the figure, the electrolyte was KOH 0.1 M.

with Al³⁺ atoms. Similarly, on the Co₂ZnO₄, the T_d Co²⁺ has been substituted with Zn²⁺ ions. CoO has a NaCl-like structure with all the Co²⁺ ions in a O_h geometry. The total electron yield Co L-edge XAS shown in Figure 2 (left), correspond to what would be expected for a Co³⁺ HS in the case of the Co₂ZnO₄. The lower L₃ edge position for the CoO and Al₂CoO₄ is also in agreement with a lower oxidation state of the cobalt and the different fine structure may reflect the different multiplet structure resulting from a T_d vs an O_h coordination geometry. The Al₂CoO₄ L₃ edge shows a broad peak around 785 eV that at this point we suspect is an artefact. The RIXS spectra of the CoO show a well-defined feature at 0.9 eV and a second feature that appears at higher excitation energies at 2 eV. The Al₂CoO₄ has 2 features at 0.5 and 0.9 eV. At higher incident energy an additional band appears at 2 eV. The Co₂ZnO₄ does

not show any well-defined bands, only a peak at 1.8 eV and at higher excitation energies (780-784 eV, not shown) a broad band was observed. The 2p3d RIXS spectra have been compared to the powder Co_3O_4 measured at Sextants (Figure 2, right). The spectra have been normalized to the elastic peak, except for the spectra at 779 where the elastic peak was quite weak. At low excitation energies there is a band at 0.75 eV, most likely resulting from the Co^{2+} sites on the spinel, while as the excitation energy is increased the most prominent features at around 2 eV could be assigned to the Co^{3+} sites, demonstrating the potential of 2p3d RIXS to study such materials. Multiplet calculations are planned for the near future to analyse these results in detail.

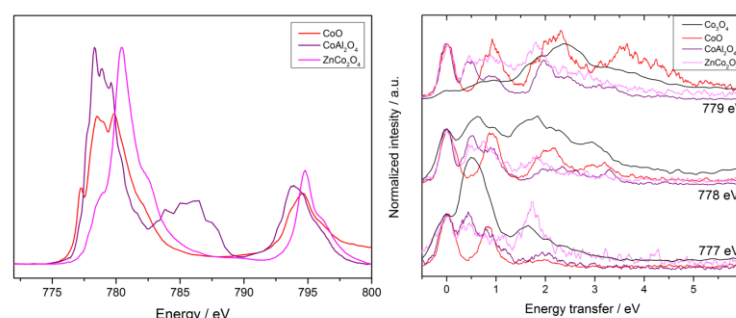


Figure 2. Co L-edge XAS (TEY) from powder samples (left) and 2p3d RIXS (right) of the same samples at three different incident energies. The spectra of Co_3O_4 powder measured at SOLEIL Sextants beamline was added to the figure as a comparison.

No significant changes were observed for the Co_3O_4 particles under different applied electrode potentials. This could be a limitation of the experimental setup used in soft X-ray measurements. Electrochemistry takes place at the interface with the electrolyte. If particle films are too thick and the changes with the applied potential take place far from the electrode surface, the X-ray beam may not penetrate enough on the film to observe any changes. Another possibility is that the particle conductivity is too small, as a result, only a minor fraction of the film may be under potential control. Consequently, we may be measuring all the time the bulk of the particles, which remain unresponsive to the applied potential (see

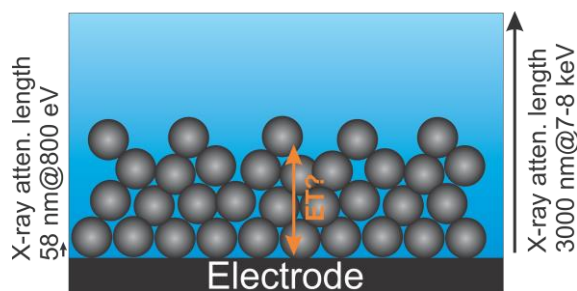


Figure 3. Schematic representation of the particles on an electrode and the attenuation lengths at different energies for X-ray. The arrows on the side of the figure are scaled to the represented particle size (assuming particles of around 150 nm in diameter).

Figure 3). We have repeated these measurements at the Co K-edge. When using hard X-rays, we probe the whole film.² Similarly to what we have observed on the soft X-ray regime, we could not detect significant changes on the spectral signatures with the applied potential. This suggests, that the particles may be isolating, and that only a minor fraction is responding to the potential. We are currently investigating how to produce homogeneous Co_3O_4 spinel-structured films with controlled thicknesses on electrodes to see if we can overcome this limitation in future experiments.

References

1. T. Grewe, M. Meggouh and H. Tuysuz, *Chem.-Asian J.*, 2016, **11**, 22-42.
2. H. J. King, M. Fournier, S. A. Bonke, E. Seeman, M. Chatti, A. N. Jumabekov, B. Johannessen, P. Kappen, A. N. Simonov and R. K. Hocking, *The Journal of Physical Chemistry C*, 2019, **123**, 28533-28549.

INVESTIGATION OF THE ELECTRONIC STRUCTURE OF ELECTRODEPOSITED COBALT OXIDE FILMS ON ELECTRODES FOR WATER OXIDATION CATALYSTS USING CO 2P3D RIXS

Minmin Chen,^a Kosuke Yamazoe,^{b,c} Jun Miyawaki,^{b,c} Yoshihisa Harada,^{b,c} Serena DeBeer,^a Olaf Rüdiger^a

^aMax Planck Institute for Chemical Energy Conversion, Mülheim an der Ruhr, Germany

^bInstitute for Solid State Physics, The University of Tokyo, Kashiwa, Chiba 277-8581, Japan

^cSynchrotron Radiation Research Organization, The University of Tokyo, 7-3-1 Hongo, Bunkyo-ku, Tokyo 113-8656, Japan

Development of new anode materials based on earth abundant transition metals for water splitting is strategically important for industrial and large-scale applications. Water splitting has been considered one of the most promising strategies for energy conversion and storage.¹ Cobalt oxide films electrodeposited from Co^{2+} salts in neutral pH buffered solutions show high catalytic activity at low overpotential in mild environments, combined with extended stability as a result of a self-healing mechanism.² Although this catalyst has been studied over the last years using different spectroscopic techniques (including operando Co K-edge XAS) and EPR, most of the studies presented so far, did not employ ultra-pure electrolytes and it has recently been shown that trace amounts of iron dramatically improve the catalytic performance of such materials.³ At this point, the role of iron in catalyst activation is still not fully understood.

We measured the Co L-edge XAS while we were electrodepositing Co oxide on the electrode from a solution of $\text{Co}(\text{NO}_3)_2$ 0.5 mM in phosphate buffer solution (PBS) at pH 7.0. In Figure 1, one can see that the electrode did not contain any Co. Once the cell was filled with the $\text{Co}(\text{NO}_3)_2$ solution, but kept at open circuit potential (OCP), we can already detect a cobalt signal from the Co in solution. As we apply a potential of 0.9 V (vs Ag/AgCl), the intensity of the Co L-edge increases. After the second 60 s potential pulse, the intensity does not increase any further, indicating that either the film does not grow anymore, or that the film is too thick and the growth goes beyond the penetration limit of the X-rays. After the electrodeposition, the electrolyte was switched to PBS without cobalt. Unfortunately, the Co signal rapidly disappears upon changing the electrolyte. Even if the potential was kept high to stabilize higher oxidation states on the film. If the electrolyte was switched to KOH 0.1 M, the films were more stable so that we could measure spectra at different applied potentials as a result of the lower solubility of Co at high pH.

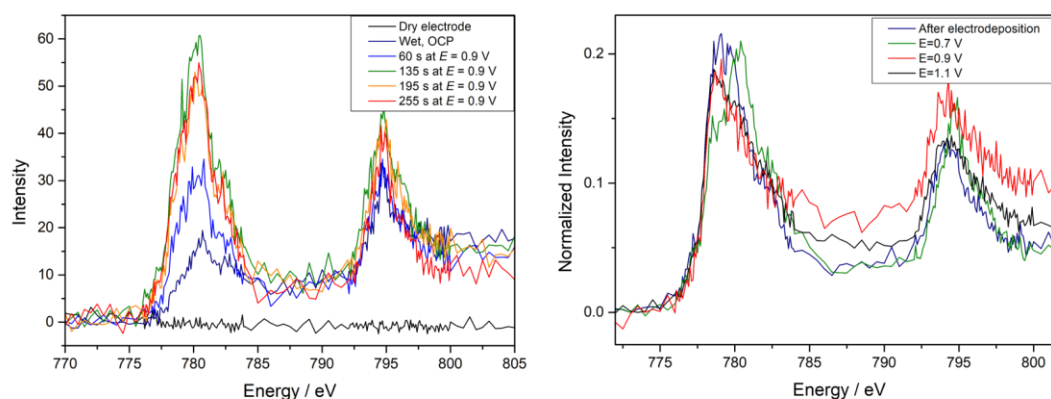


Figure 1. Co L-edge XAS of an electrode where Co was electrodeposited. On the left, the spectra measured during electrodeposition are shown. Measured in PBS pH 7.0 and in the presence of $\text{Co}(\text{NO}_3)_2$ 0.5 mM in solution. On the right figure, the L-edges measured at different applied electrode potentials in KOH 0.1 M.

Interestingly, the Co L-edge shifts to higher energy at 0.7 V (vs Ag/AgCl), with a maximum intensity for the L₃ at 782 eV, similar to what was measured for Co₂ZnO₄ (see our 2019 activity report on spinel Co₃O₄), suggesting that the cobalt has been oxidized to Co³⁺. On the other hand, when the potential was increased and the catalyst started doing water oxidation the L-edge maximum shifts to lower energy (Figure 1).

The 2p3d RIXS spectra of these electrodeposited Co oxides is less structured than that measured for the spinel systems. The operando measurements showed just a small change at 779 eV excitation energy, where the spectra recorded at the highest potential did not show a separate feature at 1 eV (Figure 2).

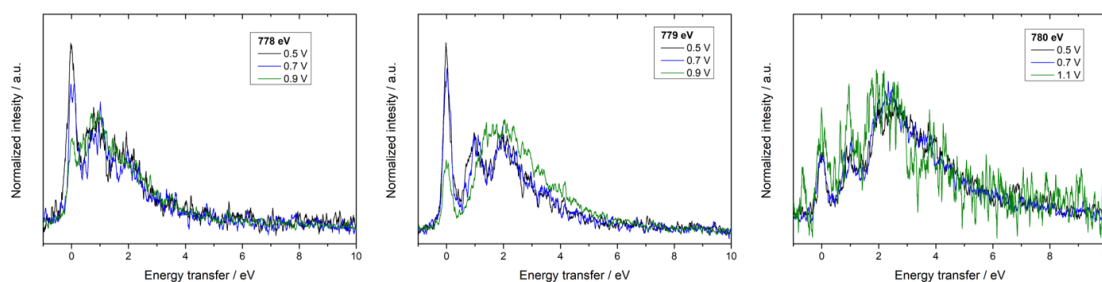


Figure 2. Corresponding 2p3d RIXS spectra measured for the electrodeposited Co oxide film shown in figure 6 at 3 different incident energies as indicated on the figure. Measured in KOH 0.1 M.

Operando studies in the soft X-ray regime are extremely challenging. On one hand, the experimental setup requires a vacuum environment, which makes the design of the spectroelectrochemical cell challenging. Nevertheless, we have successfully designed a cell that operates on a three-electrode configuration. The cell did not leak during the measurements.

The electrodeposited films showed a small response to the applied potential. We could monitor the film growth by following the Co L-edge XAS. Under basic pH conditions, the measured spectra suggest the formation of Co³⁺ at applied potentials just before the catalytic wave starts. Under turnover conditions, the L₃ edge shifts to lower energy, suggesting a Co²⁺ configuration. This may be because the rate-limiting step is the oxidation of Co²⁺, and once this state is formed, water oxidation takes place at a fast rate, and the higher valence states cannot be observed on the time scale of the experiment. This contrasts with what we have measured using in situ EPR for the same catalyst, where a Co⁴⁺ signal was detected.⁴ Nevertheless, EPR measurements are not real operando experiments, since the measurement requires low temperatures (10K). The freezing process may slow down the catalytic cycle and allow the detection of Co⁴⁺.

REFERENCES

1. T. Grewe, M. Meggouh and H. Tuysuz, *Chem.-Asian J.*, 2016, **11**, 22-42.
2. C. Costentin and D. G. Nocera, *Proceedings of the National Academy of Sciences*, 2017, **114**, 13380-13384.
3. F. Song, L. Bai, A. Moysiadou, S. Lee, C. Hu, L. Liardet and X. Hu, *J. Am. Chem. Soc.*, 2018, **140**, 7748-7759.
4. Y. Kutin, N. Cox, W. Lubitz, A. Schnegg and O. Rüdiger, *catalysts*, 2019, **9**, 926.

SPIN-POLARIZED SURFACE STATES ON MAX PHASE COMPOUND V₂AlC

Takahiro Ito^{1,2}, Masashi Ikemoto², Damir Pinek³, Koichiro Yaji⁴,

Shik Shin⁴, and Thierry Ouisse³

¹*Nagoya University Synchrotron radiation Research center (NUSR), Nagoya University, Nagoya
464-8603, Japan*

²*Graduate School of Engineering, Nagoya University, Nagoya 464-8603, Japan*

³*Grenoble Alpes, CNRS, Grenoble INP, LMGP, F-38000 Grenoble, France*

⁴*Institute for Solid State Physics, The University of Tokyo, 5-1-5 Kashiwanoha, Kashiwa, Chiba
277-8581, Japan*

MAX phases ($M_{n+1}AX_n$, where M is an early transition metal, A belongs to groups 13-15 and X is either C or N, $n = 1 - 3$) have recently attracted much attention due to their possible application to the production of a new class of two-dimensional (2D) systems called MXenes [1]. However, the bulk electronic structure of MAX phases has been studied mostly through *ab initio*, DFT calculations, mainly due to a lack of single crystalline samples. We have performed angle-resolved photoemission spectroscopy (ARPES) on several MAX phase single crystals to directly investigate the electronic structure of these systems [2,3]. Among the MAX phases, V₂AlC has been expected to be categorized as a high-symmetry point semi-metal with crossing point with some Dirac-like properties referred as “Dirac point (DP)” at the Fermi level (E_F) along ΓM line together with “nodal-line (NL)” around 0.2 eV from DFT calculation [3, 4]. From the recent SARPES study of V₂AlC with using a quasi - continuous - wave laser [5], the existence of the spin-polarized states has been elucidated [6]. Since the observed spin states show the anti-parallel spin splitting along the tangential axis to the larger electron pocket around the Γ point, Rashba effect [7] or the formation of the spin-polarized “drum-head surface states” have been expected to be possible origins of the spin states. To pursue the origin of the observed spin-states as well as the other spin-states if exists on V₂AlC, we have performed SARPES study with using He I light source, which is available for the spin mapping at the wide momentum space.

Figures 1(a) and (b) show the band structure near E_F and the constant energy ARPES image at 0.2 eV, comparing with the DFT band structure along the ΓM (AL) line and the DFT Fermi surface of ΓKM (AHL) plane, respectively. While the large (small) electron pocket e_L (e_s) seems to be in consistent with the previous ARPES studies [3,6], we have found an apparent dispersive feature (SS) appears between e_L and e_s bands. Since the observed SS has not been reproduced by the bulk DFT calculation, and SS dispersive feature shows similarity with the e_s band with higher binding energy shift, we expect that the origin of SS to be a “surface state”. It should be noted that the observed SS has never been observed on the previous ARPES studies with using UV synchrotron from $h\nu = 40 \sim 140$ eV [4] or laser-source of $h\nu \sim 7$ eV [6]. We expect possible origin of SS might be so called surface termination effect at the cleaved surface, which could be different from the other previous studies.

In Fig. 1(c), the SARPES spectra at the momentum cut- $m1$ to $m6$ and $p1$ to $p6$ are shown with the spin polarization along y-axis (S_y). Here, y-axis corresponds to the tangential direction to the electron pockets around the Γ point as shown in Fig. 1(b). Around the e_L pocket, S_y^- (S_y^+) polarization around 50 - 200 meV following a relatively small anti-parallel spin feature at the lower binding energy has clearly been observed around $k_x \sim \pm 0.5 \text{ \AA}^{-1}$. The

observed spin-states around the e_L pocket show a good consistency with the previous laser-SARPES study [6]. On the other hand, we have found a sizable spin polarization around SS. At the cut-m1 and m2 in Fig. 1(c), S_y^- polarization has been observed. Though the strong polarization around NL (0.2 eV at the cut-m4) might be expected to affect to the polarization in the wide momentum/energy range, appearance of S_y^- polarization below 0.1 eV at the cut-p1 and p2 should ensure the different origin of the spin-states around SS from the ones around NL (and/or e_L pocket). From the detail comparison of the relative peak position of SS between S_y^+ and S_y^- SARPES spectra, S_y^+ appears at the lower binding energy side at the cut m1(m2), while it appears at the higher side at p1(p2). Therefore it has been expected that the SS spin-polarized states might have spin-splitting which is inverted with respect to the Γ point. This result suggests that the size of spin-splitting at SS will be much smaller than one around e_L . To understand whether the mechanisms of the formation of spin-states around e_L pocket and SS are the same or not, further ARPES study choosing surface termination as well as DFT calculation of spin-texture will be performed in our future work.

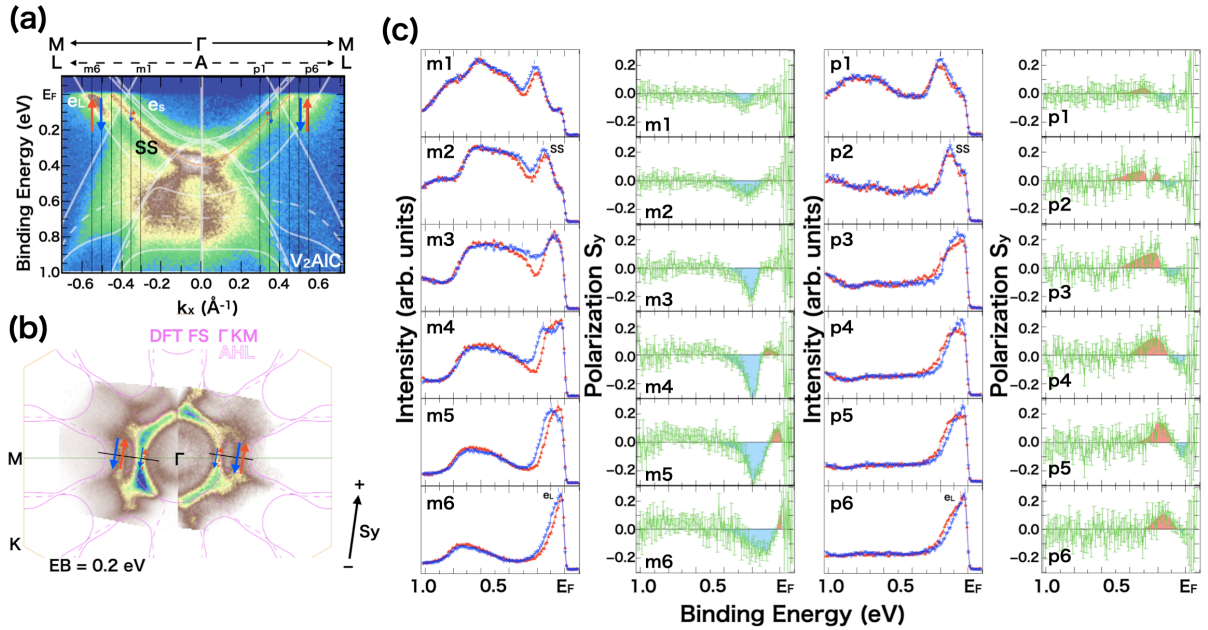


Fig. 1: (a) Band structure along ΓM line of V_2AlC . White solid (dashed) lines are obtained from DFT calculation along the ΓM (AL) line. (b) Constant energy ARPES image at 0.2 eV of V_2AlC . Purple solid (dashed) lines are Fermi surface on the ΓKM (AHL) plane obtained by the DFT calculation. The definition of spin polarization axis (S_y) is indicated by black arrow. (c) SARPES spectra (S_y^+ : \triangle ; S_y^- : \blacktriangledown) (left) and spin-polarization (right) of V_2AlC at the momentum cut from m1 (p1) to m8 (p6) in Fig. 1 (a).

REFERENCES

- [1] M. Barsoum, MAX phases (Wiley, Weinheim 2013).
- [2] T. Ito *et al.*, Phys. Rev. B **96**, 195168 (2017).
- [3] D. Pinek *et al.*, Phys. Rev. B **98**, 035120 (2018).
- [4] T. Zhang *et al.*, Nature **566**, 475 (2019).
- [5] K. Yaji *et al.*, Rev. Sci. Instrum. **87**, 053111 (2016).
- [6] T. Ito *et al.*, ACTIVITY REPORT OF SYMCHROTRON RADIATION LABORATORY 2018, 90 (2019).
- [7] V. Sunko *et al.*, Nature **549**, 492 (2017).

ABSENCE OF HYBRIDIZATION BETWEEN SPIN-POLARIZED BANDS IN QUASI-ONE-DIMENSIONAL GIANT RASHBA SYSTEM BI/INAS(110)-(2×1)

Takuto Nakamura¹, Yoshiyuki Ohtsubo^{2,1}, Ayumi Harasawa³, Koichiro Yaji³,
Shik Shin³, Fumio Komori³, Shin-ichi Kimura^{2,1}

¹*Department of Physics, graduate School of Science, Osaka University*

²*Graduate School of Frontier Bioscience, Osaka University*

³*The Institute for Solid State Physics, The University of Tokyo*

Surface electronic structure with helical-spin texture thanks to spin-orbit interaction (SOI) have been extensively studied not only for basic physics but also for applications to spintronic devices [1-3]. In order to describe such system, a simple spin texture, one band has only one spin polarization orientation and orbital character, has been widely used in the earlier studies. However, recent spin and angle-resolved photoelectron spectroscopy (SARPES) and first principles calculation studies have been revealed that the spin texture of these systems are actually not so simple, but strongly entangled with the orbital components of the surface band structure [4-6]. Spin inversion and gap opening due to hybridization between spin-polarized bands has also been reported about 2D Rashba system such as Bi/Ag quantum well [6, 7]. Although such studies have been carried out extensively for 2D systems, its extension to one-dimensional (1D) or quasi-1D (Q1D) systems were not achieved yet. In this project, we observed spin-orbital texture on a giant Rashba-type spin-splitting Q1D system Bi/InAs(110)-(2×1) [8] by using laser-based SARPES equipment [9].

Figure 1 (a) shows spin-integrated ARPES band mapping of the Bi/InAs(110)-(2×1) surface along Q1D chain direction with *p*- polarized photons. Two parabolic bands, S1 and S2, with a top away from the center of the surface Brillouin zone ($k = 0 \text{ \AA}^{-1}$) were observed near the Fermi level. ARPES constant energy contour (not shown) indicated the anisotropic, Q1D character of both S1 and S2. From the in-plane spin-resolved measurement as shown in figure 1 (b), both parabolic bands show clear spin polarization, and the signs of the spin polarizations are the opposite to each other. These results are consistent with our previous data [7], suggests the spin splitting due to Rashba-type SOI.

In order to clarify the hybridization effect of the two spin-polarized bands, we extracted the energy distribution curves (EDCs) from figure 1 (a) and show the results in figure 1 (d). The peak positions of the S1 (S2) band are indicated by a filled (open) triangles. Although the two bands are crossing each other at $k = 0.21 \text{ \AA}^{-1}$, no energy gap was observed. Moreover, spin-resolved EDCs as shown in figure 1 (e) indicated no spin-inversion nor interference at the crossing point ($k = 0.21 \text{ \AA}^{-1}$). These results suggest that there is no band modulation in Bi/InAs(110)-(2×1) surface, such as spin flipping or spin gaps opening, due to the hybridization between the spin-polarized bands. This behaviour is different from that of the known 2D Rashba systems such as Bi/Ag quantum wells [6,7].

We are currently tracking the detailed changes in orbital components and spin polarization at the initial state in combination with the density-functional-theory calculation, in order to understand this lack of hybridization between Rashba-type spin-polarized surface bands.

REFERENCES

- [1] É. I. Rashba, Sov. Phys.-Solid State **2**, 1109 (1960).
 [2] M. Z. Hasan and C. L. Kane, Rev. Mod. Phys. **82**, 3045 (2010).
 [3] A. Manchon *et al.*, Nature Mat. **14**, 871 (2015).
 [4] K. Yaji *et al.*, Nat. Commun. **8**, 14588 (2017).
 [5] K. Kuroda *et al.*, Phys. Rev. B **94**, 165162 (2016).
 [6] R. Noguchi *et al.*, Phys. Rev. B **95**, 041111(R) (2017).
 [7] H. Bentmann *et al.*, Phys. Rev. Lett. **108**, 196801 (2012).
 [8] T. Nakamura *et al.*, Phys. Rev. B **98**, 075431 (2018).
 [9] K. Yaji *et al.*, Rev. Sci. Instrum. **87**, 053111 (2016).

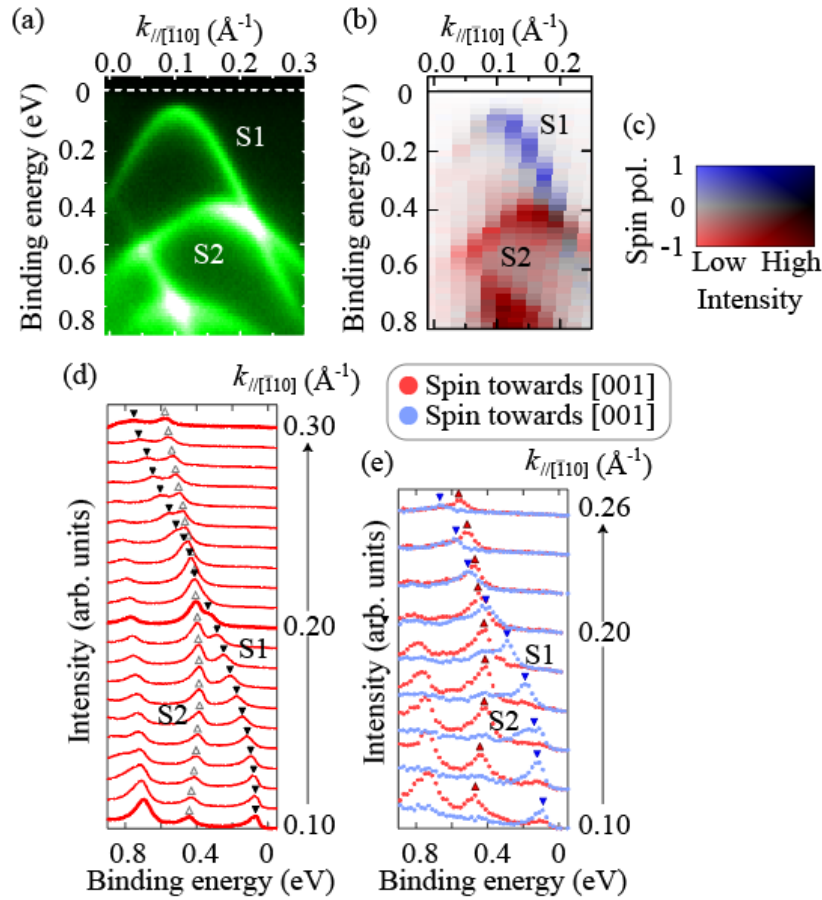


Figure1. Surface electronic structure of Bi/InAs(110)-(2x1) surface. (a) Spin-integrated and (b) spin-resolved ARPES band mapping along Bi chain direction. Spin-direction was set to in-plane chain normal ($k_{//[001]}$) direction. (c) The 2D color code for (b). blue-red color corresponds to spin polarization and the contrast of the color to the intensity of photoelectrons. (d) Spin-integrated and (e) spin-resolved EDCs. All data were measured at 45K.

TOPOLOGICAL SURFACE STATE MODIFIED BY ADSORPTION OF ORGANIC DONOR MOLECULE

Tatsuya Kitazawa¹, Koichiro Yaji², Kosuke Shimozawa¹, Hiroshi Kondo¹, Takayoshi Yamanaka¹, Hiroshi Yaguchi¹, Yukiaki Ishida², Kenta Kuroda², Ayumi Harasawa², Takashi Iwahashi³, Yukio Ouchi³, Fumio Komori², Shik Shin², and Kaname Kanai¹

¹*Department of Physics, Faculty of Science and Technology, Tokyo University of Science*

²*Institute for Solid State Physics, The University of Tokyo*

³*Department of Materials Science and Engineering, Tokyo Institute of Technology*

Topological insulators (TIs) have attracted much attention in quantum matter physics. Topological surface states (TSS) have a helical-spin texture, in which the spin-locked electrons are topologically protected against the backscattering from nonmagnetic impurities due to time reversal symmetry¹. This property of TSS will be important in next-generation spintronic devices because it will allow lower-energy electronic transport. Thus, controlling the TSS by creating topological interfaces with other materials is vital for using TIs in spintronic devices. In 2016, Tu *et al.* reported a topological p-n junction on the surface of $\text{Bi}_{2-x}\text{Sb}_x\text{Te}_{3-y}\text{Se}_y$, a three-dimensional TI fabricated by using electron-accepting organic molecule F_4 -tetracyanoquinodimethane (TCNQ), and they achieved on-off switching of charge current flow originating from TSS², suggesting that electronic functional organic molecules are suitable for TI spintronic devices. Recently, there have been several studies of the TI interface with organic molecules toward using TIs in spintronic devices. Caputo *et al.* examined the cobalt phthalocyanine (CoPc)/ Bi_2Se_3 interface³ and observed a slight shift in the Dirac point (DP) to higher binding energy by angle-resolved photoemission spectroscopy (ARPES) experiments, indicating charge transfer from CoPc to Bi_2Se_3 . This means that the CoPc/ Bi_2Se_3 interface is a chemisorption system. However, a negligible shift in the Bi 4f core levels was observed by X-ray photoemission spectroscopy (XPS), indicating little charge transfer at the interface. These experimental results contradict each other. The interface between TCNQ, a typical electron acceptor, and Bi_2Se_3 was studied by Pia *et al.*⁴ They observed a DP shift to higher binding energy by ARPES and a shift of the Bi 4f core level toward lower binding energy accompanied by TCNQ deposition by XPS measurements. These results indicate that there is a chemical interaction between adsorbed TCNQ and Bi_2Se_3 . Therefore, studies of the interfacial electronic structure of the TCNQ/ Bi_2Se_3 interface should consider chemical interactions, such as charge transfer.

These earlier experimental studies of the interface between the organic molecules and the TI surface have led to contradictory interpretations of the interactions at the organic molecule/TI interfaces. Little attention has been paid to the electronic structure of molecular layers, although this is essential for properly evaluating the interfacial electronic structure. Also, it can be pointed out that there are few reports on the electron donating molecules (n-type dopant) although some researches on the electron-accepting molecules (p-type dopant) like TCNQ and its derivatives have been reported.

In the present work, we directly observed the electronic structure both of the molecular layers and the TI surface to fully understand the influences on the TSS upon the adsorption of the molecules. We focused on the interface between tetrathianaphthacene (TTN) and Bi_2Se_3 .

Bi_2Se_3 has been extensively investigated as a prototypical TI. A Bi_2Se_3 single crystal comprises five-atom layers (Se-Bi-Se-Bi-Se) stacked along the [111] direction, which are known as quintuple layers (QLs). The QLs are attached to each other by weak van der Waals (vdW) forces and the interlayer gap between QLs is called the vdW gap. We chose Bi_2Se_3 because it has a single Dirac cone at the Γ point in the (111) surface Brillouin zone and a wide band gap of ~ 0.3 eV. This simple electronic structure allows us to trace the DP shift accompanied by the molecular deposition easily. To create the organic molecular layer/TI interface, we vacuum deposited TTN onto Bi_2Se_3 . TTN is a π -conjugated molecule containing

four electron rich sulfur atoms and has a strong donor nature by a small ionization energy of ~ 4.4 eV. TTN functions as a strong n-type dopant for Bi_2Se_3 because the Fermi level of Bi_2Se_3 is lower than the highest occupied molecular orbital of TTN. The role of donor organic molecules on the TI surface has not been investigated thoroughly, in contrast to acceptor organic molecules or n-type dopants, like alkali metals and other inorganic materials. Organic molecules have the advantages of requiring lower-cost methods for creating the interface with TI and having a lower risk of intercalation into the bulk. Thus, organic molecules are good candidates for manipulating the TSS.

In this work, we observed the entire electronic structure of the TTN/ Bi_2Se_3 interface by examining the TTN thickness dependence of the interfacial electronic state using UPS, XPS, and ARPES.

Figure 1 shows the Fermi surfaces and the energy band dispersions measured at the TTN/ Bi_2Se_3 interface for various TTN thicknesses by ARPES. For the 5Å-thick TTN, the Dirac point (DP) shifted toward higher binding energy ($E-E_F = -0.42 \pm 0.02$ eV) and the Fermi surface area of TSS increased. The hexagonal warping of the Fermi surface was also observed. We also observed the emergence of a new state just below the Fermi level with a parabolic band dispersion and hexagonal Fermi surface upon TTN deposition. This new state was identified as the two-dimensional electron gas state (2DEG) originating from the bulk conduction band, which is induced by the band-bending derived from the increase in the number of TSS electrons.

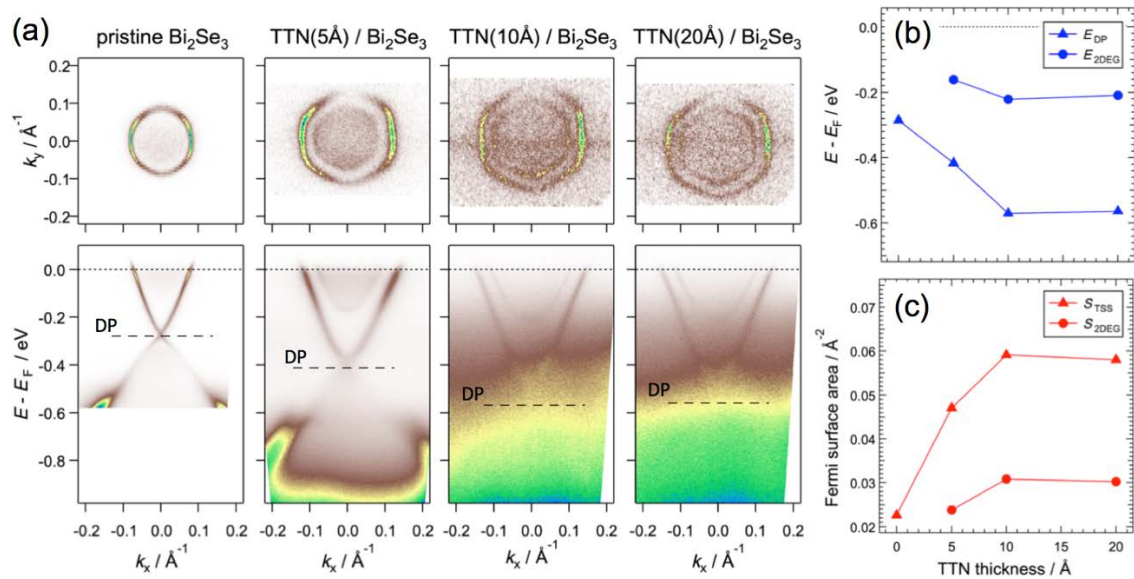


Fig. 1: Development of the electronic structure at the TTN/ Bi_2Se_3 interface. a) ARPES spectra of Bi_2Se_3 and a TTN molecular layer of various thicknesses, showing the Fermi surface and the energy band dispersion of photoemission intensity. The dashed lines labeled DP represent the energy of DPs. These ARPES spectra are acquired along the momentum line slightly off the Γ K line in the surface Brillouin zone. b) Positions of the DP (E_{DP}) and the bottom of 2DEG band dispersion (E_{2DEG}) and c) the Fermi surface area of TSS (S_{TSS}) and 2DEG (S_{2DEG}).

REFERENCES

- [1] P. Roushan *et al.*, Nature **460**, 1106 (2009).
- [2] N. H. Tu *et al.*, Nat. Comm. **7**, 13763 (2016).
- [4] M. Caputo *et al.*, Nano Lett. **16**, 3409 (2016).
- [5] A. D. Pia *et al.*, Chem. Phys. Chem. **19**, 2405 (2018).

INVESTIGATION OF TOPOLOGICAL PROPERTIES IN SUPERCONDUCTING TASE₃

Chun Lin¹, Ryo Noguchi¹, Kenta Kuroda¹, Koichiro Yaji¹, Ayumi Harasawa¹, Shik Shin¹,
Atsushi Nomura², Masahito Sakoda³, Masakatsu Tsubota⁴, Satoshi Tanda³,

and Takeshi Kondo¹

¹*The Institute for Solid State Physics, The University of Tokyo*

²*Department of Physics, Tokyo University of Science*

³*Department of Applied Physics, Hokkaido University*

⁴*Department of Physics, Gakushuin University*

In recent years, a great deal of research activities are associated with the quantum materials characterized by either the low dimensionality [1] or the electronic topology [2]. TaSe₃ is known as a quasi-1D semimetal with layered chain-like structure [Fig. 1 (a)] and has been extensively discussed in the early ages for its superconducting properties and the absence of charge density wave (CDW) [3]. These characteristics make it distinct from other transition-metal trichalcogenides, which typically undergo multiple CDW transitions [3]. As shown in Fig. 1 (b), it is considered that the absence of CDW stems from the relatively poor nesting conditions in TaSe₃ due to its more 3D-like electronic structure and CDW may be induced by Cu intercalation [4,5] or in mesowires [6], both of which are expected to reduce the dimensionality. A recent first-principle calculation indicate that TaSe₃ actually belongs to a strong topological insulator (TI) phase and moreover predict intriguing topological phase transitions among strong TI, weak TI, Dirac semimetal, and normal insulator phases through a slight change of lattice parameters, as demonstrated in the topological phase diagram of Fig. 1 (c) [7]. Therefore, TaSe₃ offers a simple system to study the interplay between superconductivity and topological phases, and the possibility of selecting different topological phase by changing physical parameters (temperature, element substitution etc.).

A direct investigation of the electronic structure of TaSe₃ via angle-resolved photoemission spectroscopy (ARPES) is consequently indispensable to elucidate its novel topological properties. We have conducted laser-based spin-resolved ARPES (SARPES) measurements at the Institute for Solid State Physics, the University of Tokyo last year and reported the first unambiguously observation of the electronic structure of TaSe₃ and the possible topological surface states (TSSs) [8]. In present study, we show the high-resolution band structure of the possible TSSs and confirm that these surface states are indeed spin-momentum locked. Therefore, our results reveal a well-established TI phase in quasi-1D TaSe₃.

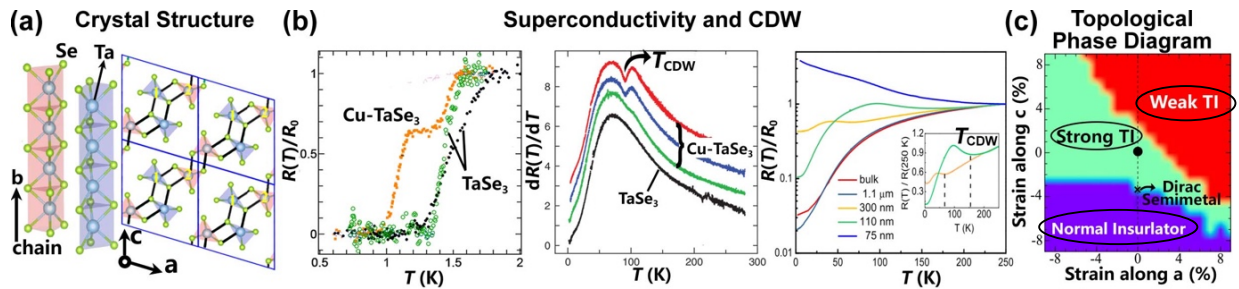


Fig. 1 (a) Crystal structure and unit cell of TaSe₃ [7]. (b) Superconductivity in pure and Cu-doped TaSe₃ (left) [4], CDW signature in Cu-doped TaSe₃ (middle) [5], and direct observation of CDW in mesowire TaSe₃ with

hundreds of nano-meters in width (right) [6]. (c) Topological phase diagram of TaSe₃ including strong topological insulator (TI), weak TI, Dirac semimetal, and normal insulator phases [7].

Figures 2 (a,b) show the 3D Brillouin zone [7] and our recently calculated TSSs at the X point on (-101) surface. Figure 2 (c) is the schematic of the experimental ARPES setup and the typical sample size. In Figs. 2 (d,e), we present the high-resolution Fermi surface and the band dispersion at the X point. The observed sharp and high-intense features near E_F are nicely consistent with our calculations in Fig. 2 (b). To further confirm whether the sharp electronic states are spin-polarized, Fig. 2 (f) shows one typical spin-revolved energy distribution curves and the corresponding spin polarization at a momentum position indicated by the dash line in Fig. 2 (e). Taking advantage of our high-resolution SARPES, the spin splitting is clearly observed for the spin up and spin down states, uncovering a spin polarization of $\sim 20\%$. We confirmed a reversal of the spin polarization for an opposite momentum position. Therefore, our results elucidate the spin-momentum locked TSSs in TaSe₃.

To sum up, we performed high-resolution SARPES measurements on TaSe₃ focusing on the surface states, the results confirm the spin-momentum locked TSSs and hence a TI state.

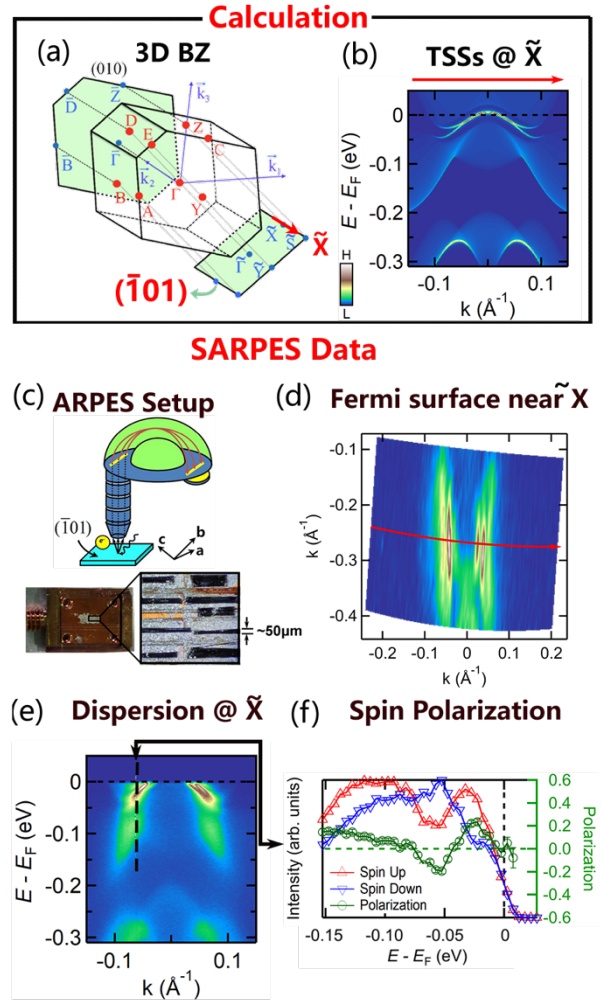


Fig. 2 (a) 3D Brillouin zone (BZ) of TaSe₃ [7]. (b) Calculated topological surface states (TSSs) at the X points on (-101) surface [7]. (c) ARPES setup. Typical samples size is $\sim 1 \times 0.05 \times 0.01$ mm³. (d) Observed surface-state Fermi surface on (-101) surface near the X point at 10 K. (e) The corresponding high-resolution dispersion at the X point with momentum position indicated by the red arrow in (d). (f) Spin polarization at the momentum position indicated by a dash line in (e). Red and blue curves are energy distribution curves of spin up and spin down states, respectively.

REFERENCES

- [1] Y. Liu, et al., Nat. Rev. Mater. 1, 1 (2016).
- [2] X.-L. Qi, S.-C. Zhang, Rev. Mod. Phys. **83**, 1057–1110 (2011).
- [3] P. Monceau, Adv. Phys. **61**, 325 (2012).
- [4] A. Nomura, et al., EPL. **124**, 67001 (2019).
- [5] A. Nomura et al., EPL. **119**, 17005 (2017).
- [6] J. Yang et al., ArXiv190609527 (2019).
- [7] S. Nie et al., Phys. Rev. B **98**, 125143 (2018).
- [8] C. Lin et al., ISSP Activity Report of Synchrotron Radiation Laboratory (2018).

ANGLE- AND SPIN-RESOLVED PHOTOEMISSION SPECTROSCOPY RESEARCH ON TYPE-II WEYL SEMIMETAL WTe₂

Yuxuan Wan^{1,2}, Lihai Wang³, Keisuke Koshiishi¹, Masahiro Suzuki¹, Peng Zhang²,
Jaewook Kim⁴, Kenta Kuroda², Koichiro Yaji², Ryo Noguchi², Ayumi Harasawa², Shik Shin²,
Atsushi Fujimori¹, Sang-Wook Cheong³, Takeshi Kondo²

¹*Department of Physics, The School of Science, The University of Tokyo*

²*The Institute for Solid State Physics, The University of Tokyo*

³*The Center for Quantum Materials Synthesis, Rutgers University*

Introduction

So far, no example of Weyl fermions has been observed in particle physics research. On the other hand, some topological materials are expected to host electrons behaving as Weyl fermions. These materials, called Weyl semimetals, have spin-polarized bands with cone-like linear dispersions with zero-mass near Weyl points, which are generated when either time-reversal or space-inversion symmetry is broken. The Weyl points are topologically protected, and intriguingly, topological surface states connect a pair of Weyl points with opposite chirality, forming arc-like Fermi surface (Fermi arc).

In some Weyl semimetals, the hole- and electron-like pockets touch each other at several Weyl points. These kinds of Weyl semimetals are called type-II Weyl semimetals, and WTe₂ we study here is one of such candidates. In WTe₂, the space inversion symmetry along *c*-axis is broken, thus the top and bottom surfaces should be different [1-3]. Theoretical calculations predict distinct Fermi arc states for these two surfaces [4], which require detailed experimental investigation.

Experiment

The single crystals of WTe₂ with large domains were grown via the iodine vapor transport method [4]. Comparing with previous studies, the single crystals have a much larger domain size. We developed a new method to obtain a pair of samples with opposite polar surfaces as shown in Fig. 1, namely “sandwich method”. A single crystal of sample was fixed on a metal substrate with silver paste as usual ARPES experiment. Then we applied silver paste on the top surface of the sample and covered it with another metal substrate. After heating the sample until the silver paste was hardened, we separated the two substrates to cleave the sample. The two pieces of sample would expose different surfaces.

The experiment was carried out with the spin-resolved laser ARPES (SARPES) at ISSP, the University of Tokyo. The light source is 7 eV laser from KBBF crystal. We measured two kinds of

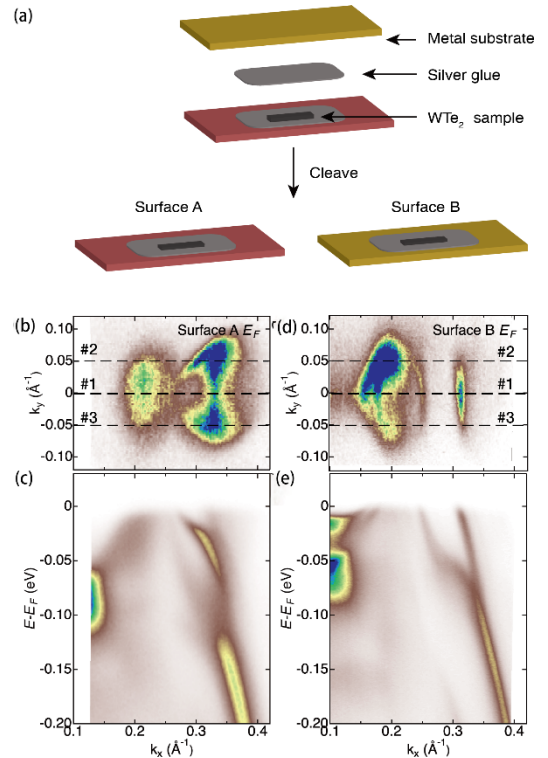


Fig.1 (a) The method to get a pair of samples with polar surfaces. (b) and (c) The Fermi surfaces on both the polar surfaces by laser ARPES. (d) and (e) Band dispersions along high symmetry cuts.

surfaces of WTe_2 : surface A and B. We used the 7 eV laser ARPES to map the energy contours and measured the band structures. We found two kinds of ARPES results on the polar surfaces. SARPES measurements on candidate topological surface states were taken after the ARPES measurements. We distinguished surface states from bulk states.

Results

We measured two kinds of surfaces of WTe_2 : surfaces A and B with 7 eV laser-ARPES. In Fig. 1 (b)-(e), we can see the arc-like surface states on both surface A and B. The surface states of the opposite surfaces are different because of the lack of inversion symmetry as expected.

Figure 2 shows the SARPES results of the candidate topological surface states. The spin polarization of bulk bands inverted on the polar surfaces, while surface states keep the same direction. We also found a surface resonance state generated by the mixture of the surface state and the hole pocket, suggesting that the hole and electron pocket also connect below the Fermi level, which is not predicted by theoretical studies. The band structures are linear near the contact point with a Dirac-like cone.

We observed two kinds of surfaces of type-II Weyl semimetal WTe_2 with laser-ARPES. Clear surface states which connect the bulk hole- and electron-like pockets could be seen. By SARPES measurements, we found that the surface states are all spin-polarized, which are compatible with topological Fermi arcs.

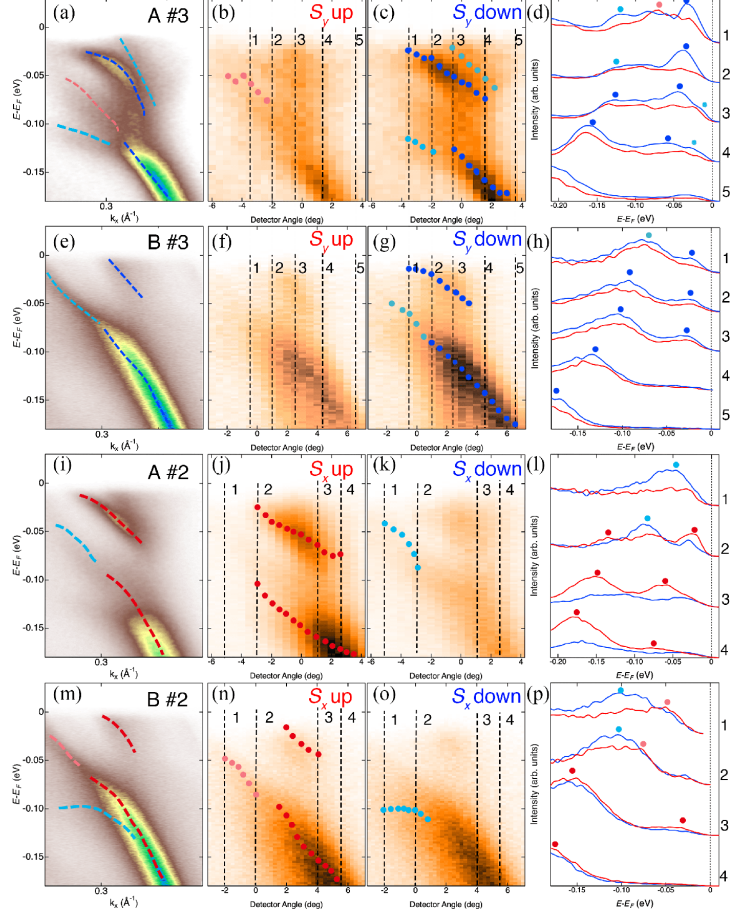


Fig.2 (a) and (e) The ARPES images of cut 3 on surface A and B, respectively. The red (pink)/blue (light-blue) dashed lines indicate the band dispersions with s_y -up/down polarization. (b),(c),(f) and (g) Laser-SARPES images for s_y -up and down.(d) and (h) Energy distribution curves (EDCs) for up (red) and down(blue) along dashed line in (b), (c), (f), and (g). The marks indicated the positions of the peaks: light-blue and pink rounds for bulk states and blue and red for surfaces, which are also plotted on (b), (c), (f), and (g) . (i)-(p) Similar set for spin x component along cut 2 on surface A and B.

REFERENCES

- [1] A.Soluyanov *et al.* *Nature* 527.7579 (2015).
- [2] Y.Wu *et al.*, *Phy. Rev. B* 94, 121113(R) (2016).
- [3] F.Y.Bruno *et al.*, *Phy. Rev. B* 94, 121112(R) (2016)
- [4] W.Zhang *et al.*, *Phy. Rev. B* 96, 165125 (2017)

DEVELOPMENT OF TIME-, SPIN- AND ANGLE-RESOLVED PHOTOEMISSION SPECTROSCOPY MACHINE AT ISSP

K. Kawaguchi, K. Kuroda, Z. Zhao, A. Harasawa, K. Yaji, R. Noguchi, S. Tani,
M. Fujisawa, S. Shin, F. Komori, Y. Kobayashi, T. Kondo
The Institute for Solid State Physics (ISSP), The University of Tokyo

Spin- and angle-resolved photoemission spectroscopy (SARPES) is a powerful technique to directly access spin-polarized electronic structures [1]. In 2014, We have newly built the laser-SARPES machine at ISSP, which is based on the 6.994-eV laser generated by KBBF non-linear crystal and the double VLEED-type spin detector [2]. Thanks to the high-flux light source as well as the high-efficiency of the detectors, our SARPES machine enables us to reveal the various spin-polarized states and the related phenomena.

Recently, we have started to a project to upgrade our laser-SAPRES machine by combining femtosecond laser pulses to perform pump-probe time-resolved SARPES (tr-SARPES). In contrast to the standard SARPES, this technique allows us to investigate the non-equilibrium spin-polarized electronic states and its spin dynamics disentangled from the charge dynamics. We have installed a new 10.7 eV-laser pulse developed by Kobayashi group of ISSP [3], which is based on the Yb-doped fiber with the high repetition rate (1 MHz). The 10.7 eV laser is generated by the third harmonic generation of the 347-nm driver in Xe gas. The high-energy probe pulse will cover the entire first Brillouin Zone (BZ), which is a great advantage compared to the conventional 6 eV-lasers based on Ti:sapphire laser.

In this activity report, we report the status of the machine development. At this stage, we have detected the SARPES signals probed by 10.7 eV laser. We here will show its demonstrations on polycrystalline-Au, and Bi/Si (111) films.

We characterize energy resolution by measuring polycrystalline gold plate (Fig. 1). By fitting analysis of the energy distribution curves (EDCs) by a Fermi-Dirac function convoluted by Gaussian, we estimate the energy broadening of the laser itself to be 20 meV. This value is reasonable if we consider the band width of the fundamental laser generated by the Yb-doped fiber. We also find that there is no significant space charging effect, which is the best advantage of the high-repetition laser.

Next, we mapped the band dispersions of Bi/Si (111) film. Fig. 2(a) shows the observed Fermi-surfaces covering the

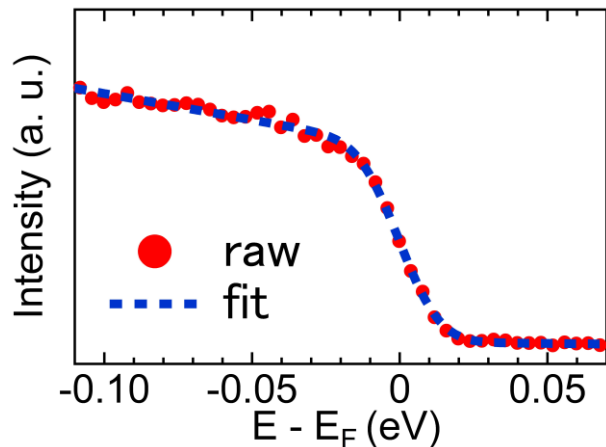


Fig. 1: EDCs recorded by 10.7 eV laser on the polycrystalline gold plate at 17 K. Dashed curve is a fitting function to deduce the energy resolution of the laser pulse itself.

BZ. We also measured the clear band dispersions of Bi/Si (111) in wide energy-momentum windows [Fig. 2(b)]. This guarantees that our laser system is stable for SARPES and ability to investigate the spin-polarized band structure for entire first BZ. We are now installing the pump pulses to perform the pump-probe tr-SARPES measurement.

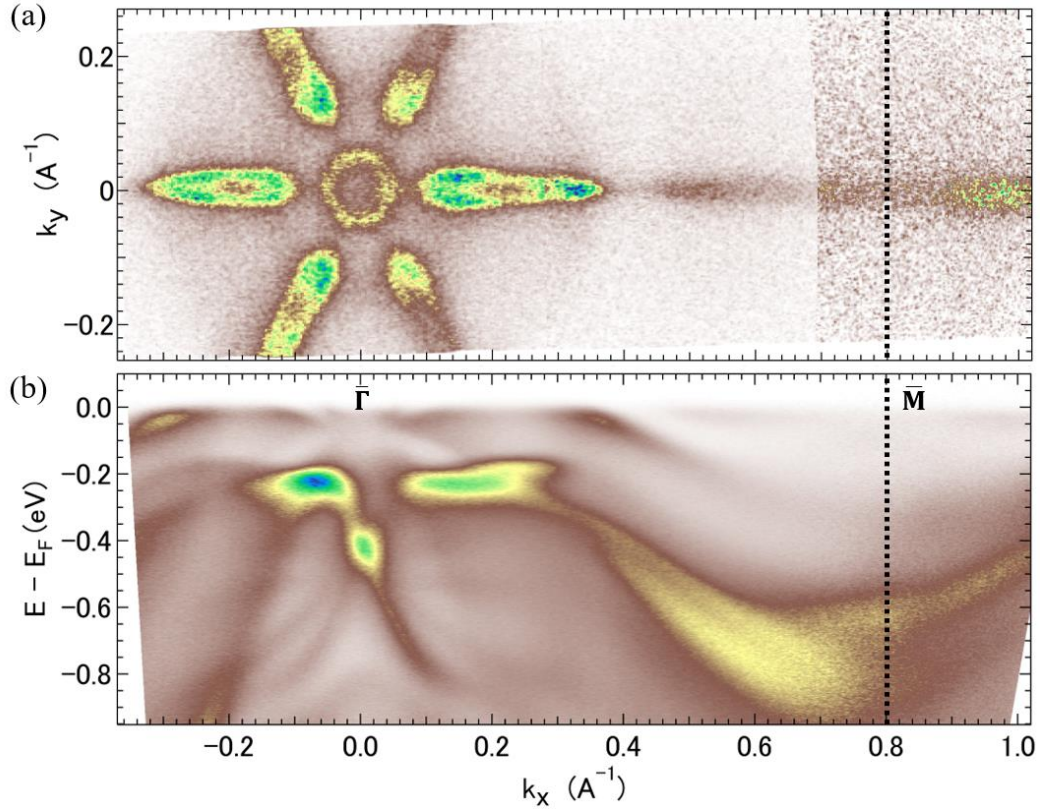


Fig. 2: (a) The Fermi surface of Bi/Si (111) films. 10.7 eV laser is p-polarization set up, and analyzer slit is along Γ M line. (b) Band dispersion image along Γ -M direction.

References:

- [1] J. H. Dil, *Electron. Struct.* **1**, 023001 (2019).
- [2] K. Yaji *et al.*, *Rev. Sci. Instrum.*, **87**, 053111 (2016).
- [3] Z. Zhao *et al.*, *Opt. Exp.* **25**, 13517 (2017).

THE WEAK TOPOLOGICAL INSULATOR STATE IN ZRTE₅

Peng Zhang¹, Ryo Noguchi¹, Kenta Kuroda¹, Chun Lin¹, Kaishu Kawaguchi¹, Koichiro Yaji², Ayumi Harasawa¹, Simin Nie³, Hongming Weng⁴, V. Kandyba⁵, A. Giampietri⁵, A. Barinov⁵, Qiang Li⁶, G.D. Gu⁶, Shik Shin^{7,1}, and Takeshi Kondo¹

¹*Institute for Solid State Physics, University of Tokyo, Kashiwa, Chiba 277-8581, Japan.* ²*Research Center for Advanced Measurement and Characterization, National Institute for Materials Science, Tsukuba, Ibaraki 305-0003, Japan.* ³*Department of Materials Science and Engineering, Stanford University, Stanford, California 94305, USA.* ⁴*Beijing National Laboratory for Condensed Matter Physics and Institute of Physics, Chinese Academy of Sciences, Beijing 100190, China.* ⁵*Elettra - Sincrotrone Trieste, Basovizza, Italy.* ⁶*Condensed Matter Physics and Materials Science Department, Brookhaven National Laboratory, Upton, NY, USA.* ⁷*Office of University Professor, University of Tokyo, Kashiwa, Chiba 277-8581, Japan*

Two distinct topological insulators exist in three dimensions: strong topological insulator (STI) and weak topological insulator (WTI). Among them, STI have been widely studied in the past decades both in theories and experiments. There are 2D spin-momentum locked Dirac cones on all the surfaces, in which the perfect backscattering is prohibited, while general scattering away from 180 degree still exists. On other hand, there are many theory studies on WTI but experiments are still rare. WTI host surface states only on the side surfaces. They are thought to be weak since two adjacent layers in even-layer WTI may couple with each other, leading to a topologically trivial phase. However, it is found that WTI surface states are actually robust as a results of delocalization. Furthermore, surface bands of WTI generally have a quasi-1D dispersion. Similar to the quantum spin Hall edge states, there are less scattering channels than STI, and smaller scattering at the side surface is expected. However, experiments on surface states of WTI are rare, due to the difficulty to prepare a large and uniform side surface of layered materials. Cleavage is generally useful for top surface, and such techniques proved its power on STI. In nature, most materials can only be cleaved from top surface, and it is difficult to prepare a side surface. The only example is Bi₄I₄, which has two cleaved surface at the same time (specially) [1]. ZrTe₅ is another candidate of WTI [2]. Although there are some spectroscopic studies on the top surface, there is no study on the side surface. The key evidence for WTI of ZrTe₅, the results from side surface, is missing, and the properties of the surface band is absent.

ZrTe₅ has a quasi-1D crystal structure. The layer distance for the top surface is ~ 7.3 Å, and it is ~ 6.9 Å for the side surface. As a result of the large layer distances, in principle, it should be possible to cleave both surfaces. However, Te-Te bonding exists between adjacent layers for the side surface, making it much more difficulty to cleave than the top surface stacked by van der Waals forces. We successfully cleaved the side surface of WTe₅, and measured its band structure with laser ARPES. We resolved a Fermi surface only dispersing along the chain direction (a), as displayed in Fig. 1a. The ARPES intensity plot along k_a shows a hole-like band. By comparing with the calculations [2], we found this band should be the surface band. The spin polarization is expected for the surface band.

We measured two pairs of EDCs (Fig. 1a) by spin-resolved ARPES from three different samples. The k_a locations are also shown in Fig. 1b. The spin polarization curves along the b , a and c directions are displayed in Fig. 1c - e. In each panel of Fig. 1c - e, the five curves with the same color (blue or red) are taken at two different k_b ($k_b \sim 0$ and 10 , indicated in Fig. 1a)

from three samples (one sample at only $k_b \sim 0$, in total $6 - 1 = 5$ curves). These five curves show no obvious difference, confirming the repeatability of the measurements. We notice that the spin polarization curves in the background range (< -0.15 eV) are not zero but have offsets. Such constant polarization in the background may come from the asymmetry of the spin + and spin - channels, or may come from the matrix-element effect in the photoemission process, which is often observed in spin-resolved ARPES. We averaged the five polarization curves with the same color in Fig.1c - e, and subtracted the resulting curves by a constant to remove the background polarization. The results are displayed in Fig.1f - h. It is clear that the spin is polarized along b direction, tangent with the Fermi surface, forming the quasi-1D spin-momentum locking pattern. Our results prove the existence of topological surface states on the side surface, and the weak topological insulator nature of ZrTe₅.

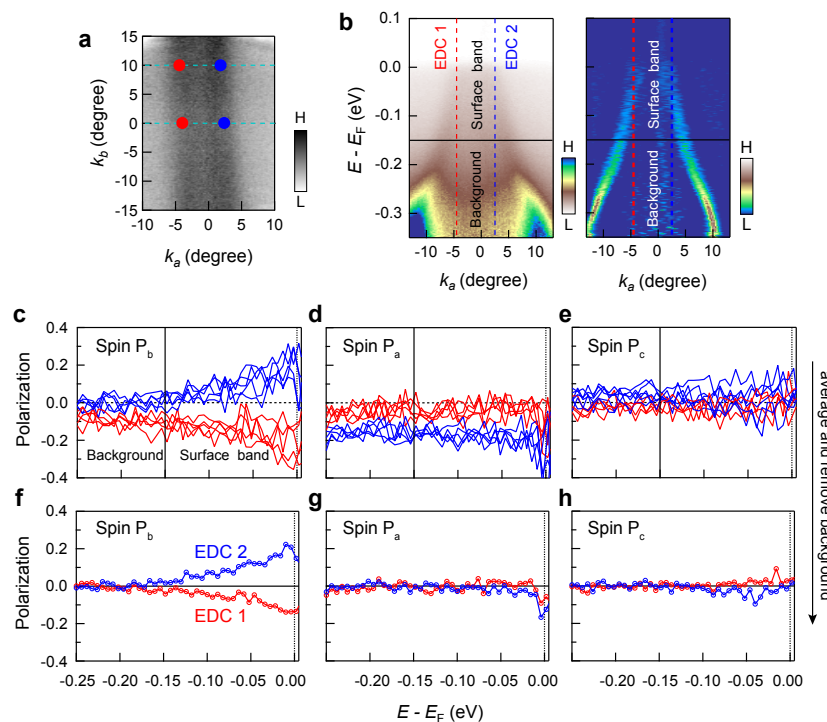


Figure 1. Spin polarization calibration. (a) Fermi surface of the side surface. The red and blue dots indicate the locations in k -space of the spin-polarized EDCs in (c - h). (b) Intensity plot of the band structure along k_a and its MDC curvature plot. The red and blue lines indicate the k_a locations of the spin-polarized EDCs. Due to the quasi-1D feature of the Fermi surface, the band structure at $k_b \sim 0$ and $k_b \sim 10$ in (a) are basically the same. (c - e) Raw spin polarization curves along b , a and c directions measured at the indicated locations in (a) and from different samples. The polarization curves at the same k_a are almost the same (independent of k_b locations or samples). So the curves are just distinguished by their k_a values with red and blue colors. (f - h) Spin polarization curves along b , a and c directions, obtained by averaging the same-color curves in (c - e), respectively. Since the background part (< -0.15 eV) should show no spin polarization, we subtracted a constant for all the curves to remove the background spin polarization.

References:

- [1] R. Noguchi, et al. Nature 566, 518 (2019).
- [2] H. Weng, Dai, X. & Fang, Z. Phys. Rev. X 4, 011002 (2014).

Observation of spin polarized surface states in polar Weyl semimetal T_d -MoTe₂

M. Sakano¹, Y. Tanaka¹, M. S. Bahramy^{1,2}, H. Takahashi^{1,3}, K. Kuroda⁴, A. Harasawa⁴, K. Yaji⁴, S. Shin⁴, S. Ishiwata^{1,3}, K. Ishizaka^{1,2}

¹*Quantum-Phase Electronics Center (QPEC) and Department of Applied Physics, The University of Tokyo*

²*RIKEN Center for Emergent Matter Science (CEMS)*

³*Graduate School of Engineering Science, Osaka University*

⁴*Institute for Solid State Physics, The University of Tokyo*

The electronic structure in the low temperature phase of T_d -MoTe₂, which is theoretically predicted as a type-II Weyl semimetal, has been intensively investigated by angle-resolved photoelectron spectroscopy [1-6]. Until now, some segment-like band features resembling Fermi arcs are experimentally observed, which are indicative of the topological surface states connecting the bulk Weyl nodes [5,6]. However, since the complicated electronic structure near the Fermi level makes it difficult to be observed, the interpretations of ARPES results on the observed Fermi-arc-like bands are still controversial. Here we investigate the spin polarizations of the Fermi arc features for both polar terminations by utilizing the high-resolution spin and angle-resolved photoelectron spectroscopy (SARPES) [7].

T_d -MoTe₂ has the noncentrosymmetric crystal structure with polarization along the stacking direction (c -axis), so it has the “top” and “bottom” polar domains. The top surface is denoted by (001) and the bottom surface is denoted by (00-1). According to the band calculations, there are eight Weyl points in the first Brillouin zone of T_d -MoTe₂. Their energy levels and coordinates are predicted to be $(E, k_x, k_y, k_z) = (E_F + 6.7 \text{ meV}, \pm 0.185, \pm 0.013, 0)$ (W1s : near the Γ -X line) and $(E_F + 59 \text{ meV}, \pm 0.181, \pm 0.053, 0)$ (W2s : the far from Γ -X line) by the theoretical research[21]. Fig. 1(a) and (b) show the energy contours at $E_F + 6.7 \text{ meV}$ for the (001) and (00-1) surfaces respectively. On the (001) surface, an arc-like surface state dispersing from the W1 can be seen between the hole pocket and the electron pocket. In addition, there is another surface state that crosses the Γ -X line near the electron pocket, indicated by “SS”. On the (00-1) surface, there is a sharp surface state that connects the pair of W1s with different chirality, indicated by the white arrow in Fig. 1(b).

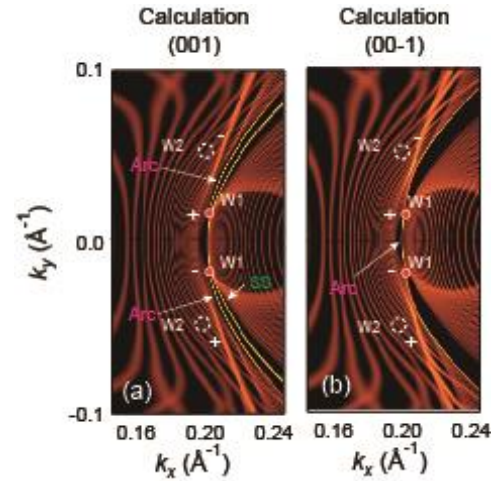


Fig. 1 The calculated energy contour at $E_F + 6.7 \text{ meV}$ for (001) (a) and (00-1) (b) surfaces.

Fig. 2(a) shows the energy contour at E_F on the (001) surface obtained by ARPES at 20 K. The two types of sharp photoelectron intensities are observed indicated by the pink solid brackets and the green curve. The pair of segments is the possible Fermi arcs connecting W1 and W2 from the comparison with the calculation shown in Fig. 1(a). The state indicated by the green curve is also a surface state but can be distinguished from the Fermi arc.

Next, looking at the energy contours at $E_F + 20 \text{ meV}$ for the (00-1) surface shown in Fig. 2(b), a short segment of the photoelectron intensity can be observed at $k_x \sim 0.20 \text{ \AA}^{-1}$ along the Γ -X line, as indicated by the pink marker. This segment is the possible Fermi arc connecting the pair of W1 across the Γ -X line, as shown in the calculation for the (00-1) surface (Fig. 1(b)).

To investigate the spin structures of the topological surface states, we perform SARPES along Fermi arcs and the SS. On the (001) surface, the SARPES measurements were performed along the orange lines (#0~#7) shown in Fig 2(a). Figs. 2(c)~(e) show the spin-resolved spectrums along #0 ~ #7 for the S_x , S_y and S_z respectively. The measurement position (#0 ~ #7) in momentum space is calculated from

the detector angle shown on the horizontal axis of Figs. 2(c)-(e). The red and blue curves represent the photoelectron intensities of the up spins and down spins, respectively. From the ARPES results shown in Fig. 2(a), there are the Fermi arc and the SS, on #0, #2~#7. The peak positions shown in the spin resolved momentum distribution curves (MDCs) are the Fermi arc and SS peak positions obtained by fitting the MDCs by the normal ARPES measurement shown in Fig 2(a). In the spin-resolved spectrums for S_x shown in Fig. 2(c), the only one peak is observed on the #1, whereas two peak structures are observed on the #2 reflecting the two different surface states, so we can say that the Arc and the SS can be measured by SARPES. The spin resolved MDCs for S_y (Fig. 2(d)) shows that the SS has S_y up polarization on the Γ -X line, the up-spin spectrums have the two-peak structure in the region slightly off the Γ -X line (#2-#5), so we can see that the S_y of the Fermi arc near W1 is up on the (001) surface. For S_z , the Arc and SS seem to have the opposite polarization near the Γ -X line, but they have large S_z -up polarization far from the Γ -X line. Next, we move on to the results of the (00-1) surface. Fig. 2(b) shows the energy contour at $E_F + 20$ meV on the (00-1) surface. SARPES is performed along the orange line in Fig. 2(b), so the peak in the 3D spin-resolved MDCs shown in Fig. 2(f)-(h) corresponds to the peak of the Arc. There seem to be no difference in the photoelectron intensities of the up and down of S_x , but the MDC of S_y -down ARPES intensities shown in Fig. 2(g) has a sharp peak which is consistent with the peak position of the Arc observed by the normal ARPES. Finally, the MDC of S_z -up ARPES intensities shown in Fig. 2(h) has a peak structure at the same position with the result of the normal ARPES, so we can see the Arc have the small S_z -down polarization.

We focus on the spin components along y of the Arc in the vicinity of the Γ -X line. The Arc of the (001) surface has S_y -up polarization ($P_y \sim 0.4$) just outside of the pair of W1 at $k_y \sim \pm 0.01 \text{ \AA}^{-1}$. On the other hand, the Arc on the (00-1) surface at $k_y = 0$ has S_y -down polarization ($P_y \sim -0.6$). In other words, the sign of the spin polarizations of the Fermi arcs on the top and bottom surface reverse at the W1s, the junction point between the Arcs. This feature seems to reflect the Berry flux emerging from the Weyl points, as the source and sink of Berry flux in momentum space.

REFERENCES

- [1] A. A. Soluyanov, *et al.*, Nature **527**, 495(2015).
- [2] Y. Sun, *et al.*, Phys. Rev. B **92** 161107 (2015).
- [3] Z. Wang, *et al.*, Phys. Rev. Lett. **117**, 056805(2015).
- [4] L. Huang, *et al.*, Nat. Mater. **15**, 1155 (2016).
- [5] A. Tamai, *et al.*, Phys. Rev. X **6**, 031032 (2016).
- [6] M. Sakano, *et al.*, Phys. Rev. B **95**, 121101 (2017).
- [7] K. Yaji *et al.*, Rev. Sci. Instrum. **87**, 053111 (2016).

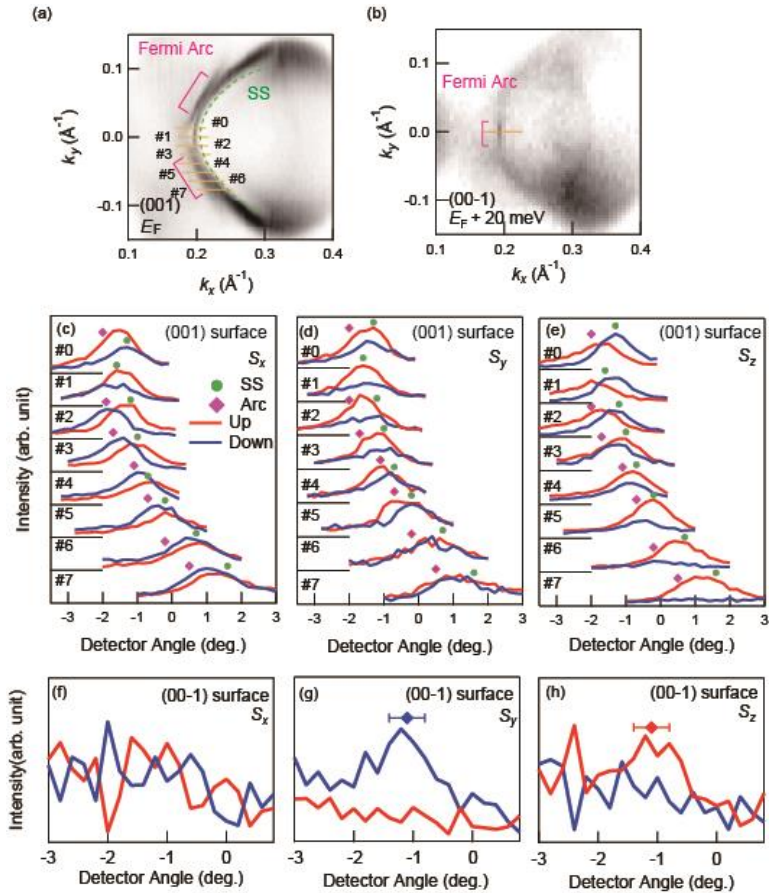


Fig.2 ARPES energy contour at E_F for (001) (a) and at $E_F + 20$ meV for (00-1) (b). (c)-(e) 3D SARPES momentum distribution curves along the orange lines in (a). (f)-(h) 3D SARPES momentum distribution curves corresponding to the orange line in (b).

SARPES STUDY OF A PB ATOMIC LAYER ON GE(111)

Koichiro Yaji¹ and Fumio Komori²

¹Research Center for Advanced Measurement and Characterization,
National Institute for Materials Science

²Division of Nanoscale Science, Institute for Solid State Physics, The University of Tokyo

Strongly spin-orbit coupled materials, such as topological insulators and Rashba systems, are placed at a central research field in condensed matter physics not only because of fundamental interests but also spintronic applications. In the standard model of the strongly spin-orbit coupled systems, the spin direction is perpendicular to both the direction of surface normal and the momentum of an electron. Recently, in contrast to the scenario of the spin-momentum locking, the spin-orbital locking model was reported in several papers [1]. Also, in our previous studies [2,3], we demonstrated the spin-orbit coupling of surface states on Bi(111) and Bi₂Se₃ with spin- and angle-resolved photoemission spectroscopy using a vacuum ultraviolet laser (laser-SARPES). Here we show the spin-orbit coupling of surface states of a monolayer Pb film on Ge(111) (Pb/Ge(111)- β) investigated by laser-SARPES. Moreover, we demonstrate the incident-light-angle dependence of SARPES.

SARPES measurements were performed at E-building in the Institute for Solid State Physics [4]. The Pb/Ge(111) sample was *in-situ* prepared in a molecular beam epitaxy chamber which was directly connected to the analysis chamber. We used an *n*-type Ge(111) substrate. The clean surface was obtained with the several cycles of Ar⁺ ion sputtering with the ion energy of 0.5 kV and subsequent annealing at 600 °C. Pb was evaporated from an aluminum crucible. The thickness of Pb and the orderliness of the monolayer film was judged from low-energy-electron-diffraction pattern. The photoelectrons were excited by 6.994-eV photons and were analyzed with a ScientaOmicron DA30-L analyzer equipped with very-low-energy-electron-diffraction type spin detectors. The electron deflector function is useful for studying the light-incident-angle dependence of SARPES. The effective Sherman function was 0.28. The sample temperature was kept at 40K during the measurements.

Figure 1 shows an ARPES image recorded along Γ K in the surface Brillion zone of Pb/Ge(111)- β , being parallel to the mirror plane of the surface. We find several bands around Γ , which are ascribed to the subsurface states of Ge(111) [5]. The bands crossing the Fermi level (E_F) around $k \sim 0.40$ - 0.45 \AA^{-1} are Pb-derived states, where the splitting is due to the Rashba effect [6]. The bands lying in the energy range of 0.3-0.8 eV below E_F around $k > 0.3 \text{ \AA}^{-1}$ are also Pb-derived states and show semiconducting behavior. The overall shapes of the bands observed with $h\nu = 6.994 \text{ eV}$ well agree with those with $h\nu = 21 \text{ eV}$ reported in our previous study [7].

The SARPES measurements were performed with p- and s-polarized lights [Fig. 2], which could be regarded as orbital-selective SARPES. Here, the light incident angles were set to 20° and 40°. We used the spin detector for resolving the *y*-spin component, which was perpendicular

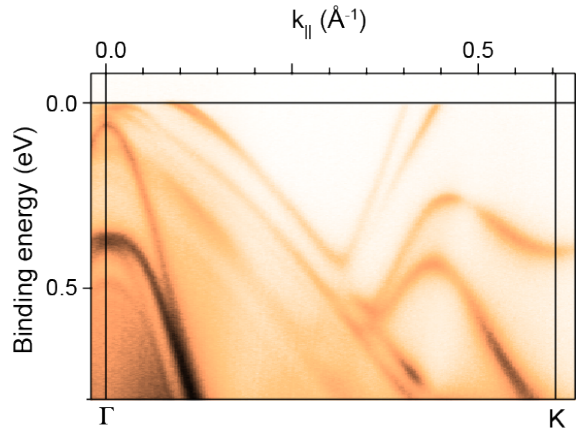


Fig. 1 The ARPES image of Pb/Ge(111)- β along Γ K recorded with the photon energy of 6.994 eV. The color arrangement gives the information of the photoelectron intensity.

to the mirror plane of the surface. As shown in Fig. 2, we clearly demonstrate that the observed spin polarizations are inverted upon switching the light polarizations. This indicates that the symmetric and anti-symmetric orbitals are independently coupled to mutually opposite spins as in other spin-orbit coupled systems such as Bi(111) and Bi₂Se₃. The total spin polarization is obtained from the integrations of the orbital-selective spin polarizations with p- and s-polarized lights. For the light incident angle of 20°, the spin-polarized branches show opposite spin directions each other, which is in agreement with the scenario of the Rashba effect. On the other hand, for the 40° incidence, the total spin polarizations are in the same directions, which is against the Rashba scenario and violates the time reversal symmetry. Besides, the theoretical calculation suggests that these branches exhibit the Rashba-type spin texture [7]. Therefore, we conclude that the spin polarization observed with SARPES with the incident angle of 40° is largely influenced by the final-state effect in photoemission process. It is likely that the photoionization cross sections between the p- and s-polarizations are different. We have to mind that the total spin polarization is not always derived from the integrations of the orbital-resolved ones.

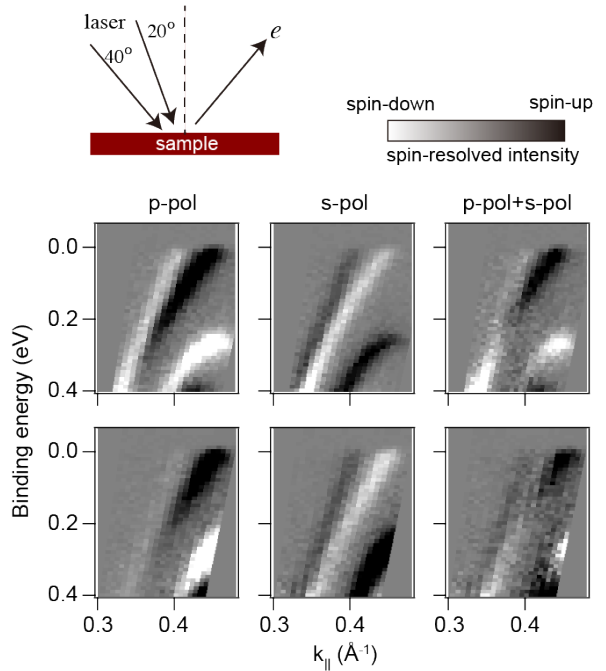


Fig. 2 Laser-SARPES images for the Pb-derived surface states along ΓK recorded with the light incident angles of 20° (upper panels) and 40° (lower panels) with the p-polarized light (left panels) and the s-polarized light (center panels). The right panels represent the orbital-integrated SARPES image. White and black colors give the information of the negative-positive spin polarizations. The left-upper panel is a schematic drawing of the experimental geometry.

REFERENCES

- [1] Z.-H. Zhu et al., Phys. Rev. Lett. **110**, 216401 (2013), Y. Cao et al., Nat. Phys. **9**, 499 (2013), H. Zhang et al., Phys. Rev. Lett. **111**, 066801 (2013), Z. Xie et al., Nat. Commun. **5**, 3382 (2014).
- [2] K. Kuroda et al., Phys. Rev. B **94**, 165162 (2016).
- [3] K. Yaji et al., Nat. Commun. **8**, 14588 (2017).
- [4] K. Yaji et al., Rev. Sci. Instrum. **87**, 053111 (2016).
- [5] K. Yaji et al., J. Electron Spect. Rel. Phenom. **201**, 92 (2015).
- [6] K. Yaji et al., Nat. Commun. **1**, 17 (2010).
- [7] K. Yaji et al., Phys. Rev. B **86**, 235317 (2012).

HIGH-RESOLUTION SPIN-RESOLVED ELECTRONIC STRUCTURE OF TOPOLOGICAL HEAVY-FERMION MATERIALS

Andrés F. Santander-Syro, Franck Fortuna, Maximilian Thees

Institut des Sciences Moléculaires d'Orsay (ISMO), Université Paris-Saclay and CNRS, France

Cris Adriano

Instituto de Física “Gleb Wataghin”, UNICAMP, Campinas-SP, 13083-859, Brazil

Ce-based intermetallic compounds have interesting physical properties that arise from the interplay between Ruderman-Kittel-Kasuya-Yoshida (RKKY) magnetic interaction, crystalline electric field and Fermi surface (FS) effects in connection to d_{xy} strong hybridization between the Ce^{3+} $4f$ electrons and the conduction electrons. Ce-based materials often present non-trivial ground states, such as heavy fermion, unconventional superconductivity and non-Fermi-liquid behavior, which frequently appear in the vicinity of a magnetically ordered state. Interestingly, some of these properties, seem to be favored to occur in low symmetry systems such as tetragonal structure, well-known examples are the families of $CeMIn_5$, Ce_2MIn_8 ($M = Co, Rh, Ir, Pd$), $CePt_2In_7$ and $CeCuSi_2$.

In this context, recent attention was given to the $CeTX_2$ family ($T =$ transition metal; $X =$ pnictogen), which hosts both ferromagnetic (FM) and antiferromagnetic (AFM) members with complex magnetic behavior [1]. In particular, in this project we investigated, using laser-excited spin- and angle-resolved photoemission spectroscopy (Laser-SARPES), the compound $CeCuBi_2$ that crystallizes in the tetragonal $ZrCuSi_2$ -type structure (P4/nmm [1]). Previous studies show that $CeCuBi_2$ has an AFM ordering at $T_N = 16$ K with a large magnetic anisotropy [1].

As shown in Figure 1, in the AFM phase we detected a dispersive hole-like state with a finite spin polarization. This state may arise from unpaired or incompletely paired moments near the material surface, as also observed in other AFM heavy-fermion systems [2]. Further data analyses and complementary spin-integrated ARPES measurements are currently being performed to clarify its origin.

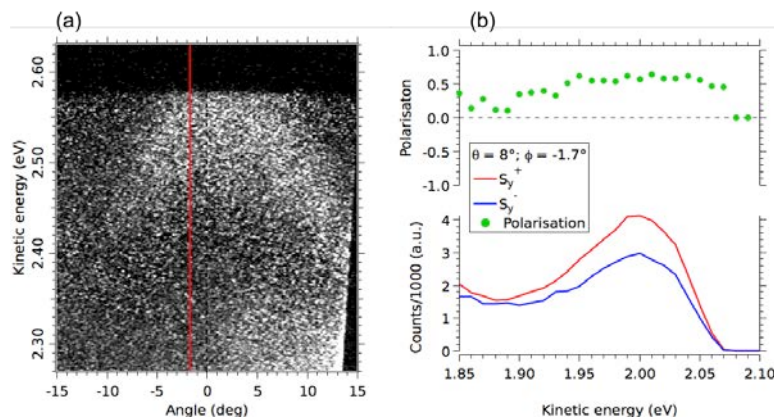


Figure 1. (a) laser-ARPES energy-momentum map showing a hole-like state right below the Fermi level in $CeCuBi_2$. (b) Bottom panel: spin-resolved energy distribution curves along the momentum marked by the red line in (a); top panel: net spin polarization.

REFERENCES

[1] Cris Adriano et al., Phys. Rev. B **90**, 235120 (2014).

[2] A. Chikina et al., Nat. Commun. **5**, 1-7 (2014).

Study of spin structure in domain-regulated alloy of atomic layer

Ting-Yu Chen¹, Li-Cheun Yang², Santosh Chiniwar¹, H. -T. Jeng¹, Woei Wu Pai³, S. -J. Tang^{1,2},

1. *Department of Physics, National Tsing Hua University, Hsinchu 30013, Taiwan*

2. *National Synchrotron Radiation Research Center (NSRRC), Hsinchu 30076, Taiwan*

3. *Center for Condensed Matter Sciences, National Taiwan University, Taipei 106, Taiwan*

The enhanced Rashba effect of a 2-dimensional (2D) surface alloy has been a center of interest in surface-science community. A typical Rashba effect in a 2D system is mainly contributed by the out-of-plane electric field caused by the inversion–symmetry breaking perpendicular to the surface plane. Consequently, the k momentum of degenerate surface-state bands locked with opposite in-plane spin polarizations shift in positive and negative directions, respectively, forming a concentric 2D constant-energy contour (CEC). However, previous studies on 2D surface alloys revealed the enhanced Rashba effect correlated with possible in-plane electric field and thus out-of-plane spin polarizations. Such effect was attributed to the second-order warping term of spin-orbit interaction in addition to the first-order term for the typical Rashba effect.

Our group found that the surface-state bands of GeAg₂ surface alloy formed on Ag(111) exhibits anomalous splitting centered at surface zone center $\bar{\Gamma}$ as shown in Fig. 1. The splitting is obvious in one symmetry direction $\bar{\Gamma}\bar{M}_{Ag_2Ge}$ but negligible in another $\bar{\Gamma}\bar{K}_{Ag_2Ge}$. The corresponding 2D CECs centered at $\bar{\Gamma}$ is displayed in Fig. 2(a), exhibiting an entangled configuration of inner hexagon and outward snowflakes that rotate 30° with each other.

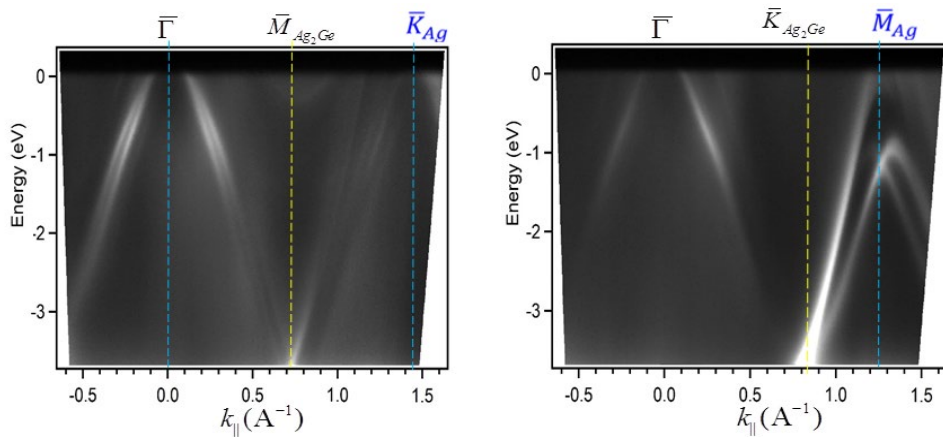


Fig. 1: The measured energy band dispersions for Ag₂Ge on Ag(111) in two symmetry directions

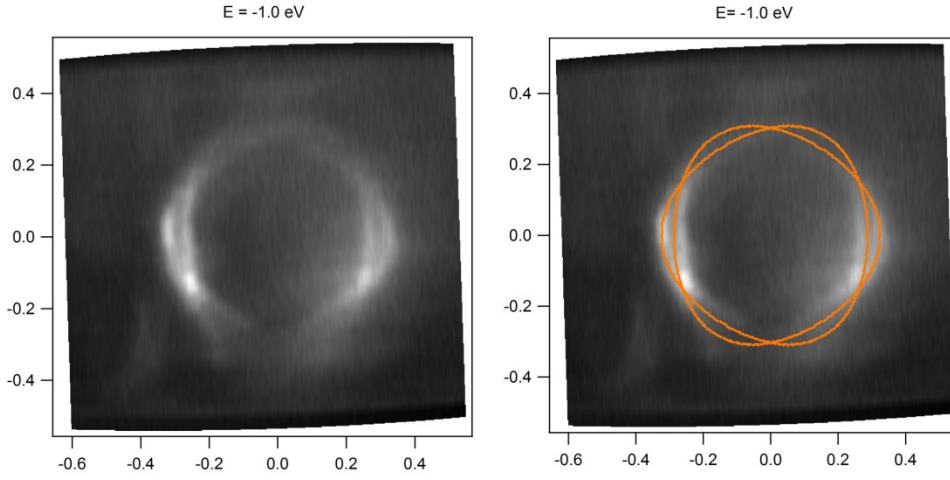


Fig. 2: (a) The measured 2D constant energy contours at -1.0 eV for surface-state bands of Ag_2Ge surface alloy on $\text{Ag}(111)$ centered at $\bar{\Gamma}$ and (b) the corresponding fitting result.

We employed the spin-orbit interacting model of the first-order Rashba term and the second-order Warping term to simulate the measured CECs in Fig. 2(a); the match is very agreeable as shown by the orange fitting curve in Fig. 2(b). Moreover, the fitting result shows that the contribution to the splitting is dominantly from the Warping term, being in complete contrast to the behaviors in most surface alloys where the first-order Rashba term dominates. If it is the case, the spin polarizations of the surface-state bands of Ag_2Ge surface alloy centered at $\bar{\Gamma}$ would be dominantly out-of-plane. This motivated us to come to the Synchrotron Radiation Laboratory in the Institute for Solid State Physics, The University of Tokyo, Japan to use the spin- and angle-resolved photoelectron spectroscopy (SARPES) to measure the spin texture of surface state bands of Ag_2Ge surface alloy. Figure 3 shows the scanning-tunneling-microscopy (STM) image of Ag_2Ge surface alloy coexisting with striped-phase germanene which form triangle arrays enclosing the Ag_2Ge surface alloy. We believe the triangle arrays break the in-plane symmetry to cause the in-plane electric field.

Figure 4 shows the preliminary results of our spin-resolved photoemission measurement carried out in SARPES machine time in Nov 2019. The applied magnetic field was along the out-of-plane direction (z direction). Indeed one can see the energy distribution curves (EDCs), taken at off-normal 8° , corresponding to two opposite directions ($\pm z$) of magnetic fields reveal difference in intensities for the two peaks of the split surface-state bands. However, it is a bit abnormal that the two peaks of red EDC are both higher than those of blue EDC. I think the surface normal of our sample was not completely aligned with the detector axis during measurement. In our next SARPES machine, we will be much more careful in those measurement details.

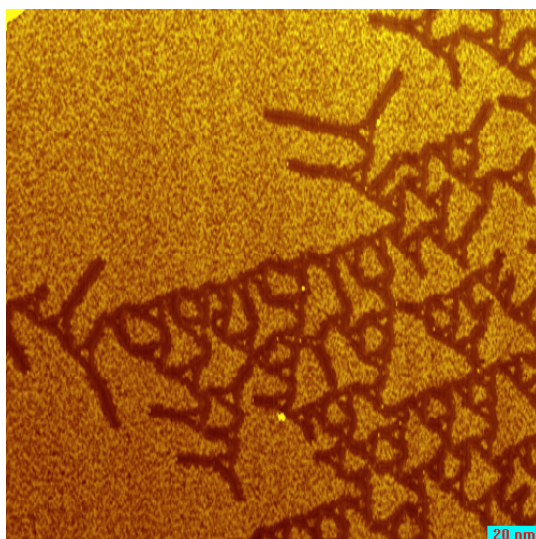


Fig. 3: The STM image of Ag_2Ge surface alloy coexisting with striped-phase germanene in the form of triangle arrays.

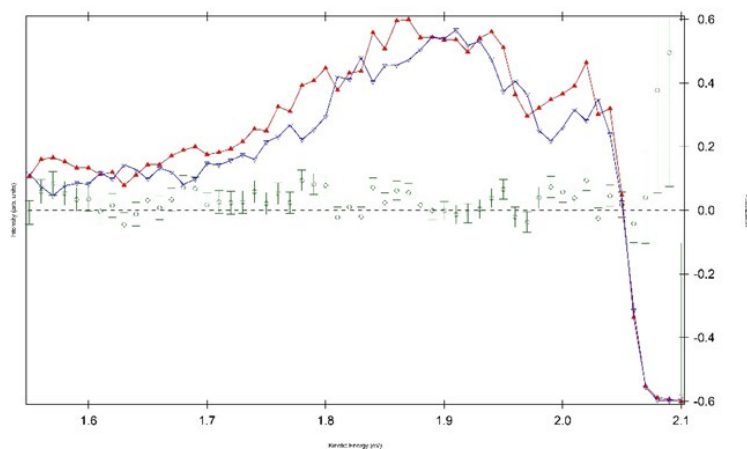


Fig. 4: The preliminary result of spin-resolved photoemission measurement on the split surface-state bands of Ag_2Ge surface alloy. Red and blue EDCs correspond to opposite directions ($\pm z$) of magnetic fields.

Spin resolved ARPES on interfacial electronic states of Bi/NbSe₂

R. Stania¹, H. Jung^{1,2}, H.W. Yeom^{1,2}

¹*Center for Artificial Low Dimensional Electronic Systems, Institute for Basic Science (IBS),
Pohang 37673, Republic of Korea*

²*Department of Physics, Pohang University of Science and Technology (POSTECH), Pohang
37673, Republic of Korea*

Introduction

Bulk, as well as low-dimensional, bismuth (Bi) have provided extremely rich platforms to advance our knowledge in condensed matter physics, ranging from high thermoelectric properties[1] to giant Rashba effect with highly spin-polarized electrons [2][3]. Moreover, there have recently been much interest in the topological classification of Bi, and it has been reported that pure Bi is topologically non-trivial in bulk [4][5], as well as in thin film[6]. More recently, it has also been reported that due to the higher-order topology, Bi also possesses topologically protected hinge (edge) states even in bulk form [7]. Such new identifications of Bi are expected to open up further possibilities for Bi-based structures, particularly when combined with other novel materials.

In order to utilize the rich properties of Bi-based structures, both to explore further fundamental aspects and for future device applications, it is essential to understand the electronic interactions of low-dimensional Bi on various substrates, particularly at their interfaces (e.g., topological quantum computations when combined with superconductors [7]). Of special interest are two-dimensional (2D) layered van-der-Waals materials (vdW) which are known to host exceptional spin-related properties and have strong potential for spintronic applications [8].

Thus, in our experiments, we aimed to investigate the electronic structures of ultra-thin Bi and its interfacial electronic states on a transition metal dichalcogenide (TMDC). In particular, 2H-NbSe₂ not only shows a phase transition from metallic state to charge density wave (CDW) state [9], but also towards superconducting state at one of the highest transition temperatures amongst the TMDCs [10]. In addition, NbSe₂ was recently predicted to be topologically non-trivial [11]. Thus, Bi/NbSe₂ is an ideal playground to explore such interactions and an important step towards the investigation of topological superconductivity and Majorana fermions.

Experimental details

The NbSe₂ samples were cleaved under UHV conditions and the surface quality was confirmed using LEED and He II α . The Bi layers were grown in a separate chamber and coverage was determined using He II α excitation. The high resolution ARPES and SARPES measurements were performed using a laser light source with a photon energy of 6.994 eV at the laser-SARPES machine developed at ISSP [12]. All photoemission experiments were carried out at sample temperatures below 35 K under UHV condition (about 1×10^{-8} Pa).

Results and discussion

By using high resolution ARPES we were able to distinguish the bands around the Γ point which not only shows the expected bands for freestanding few-layer Bi(111) but also additional bands that could not be clearly allocated and may resemble interface states (Figure 1a). Spin dependent measurements reveal a strong spin texture (Figure 1b) for the TSS around $E_B=0.7$ eV and especially for the surface state near the Fermi level, which was expected to be less strong polarized for few BL Bi films. More structural investigation and theoretical calculation will be required in order to determine the origins of the sub-bands.

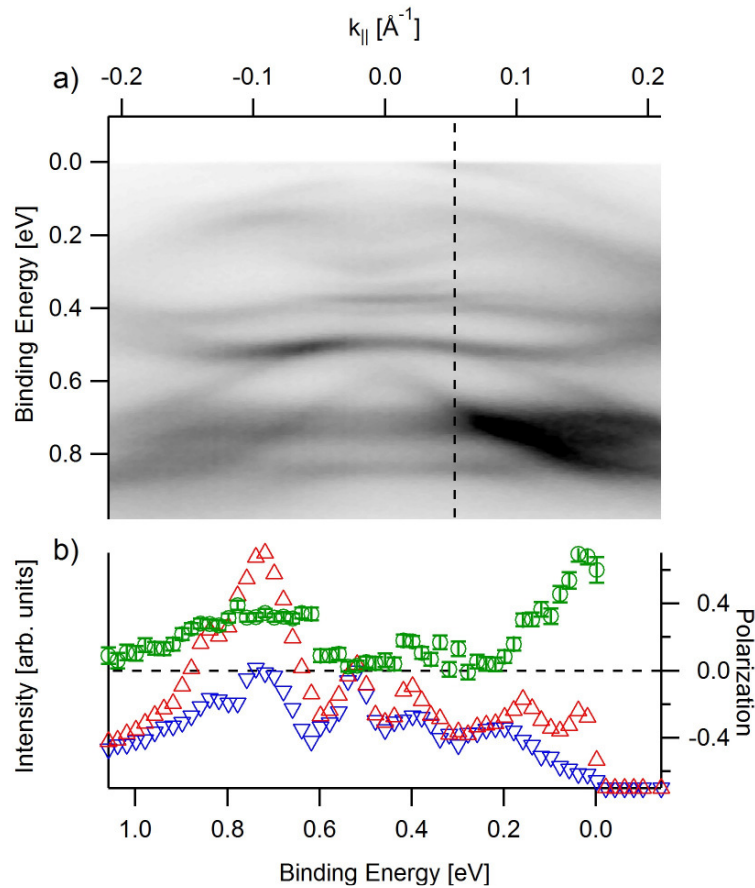


Fig. 1 a) Spin integrated measurement of Bi/NbSe₂ along the Γ K direction; b) spin dependent EDC along the dashed line in a) with red (blue) corresponding to out of plane spin up (down) measurements and green the polarization

References

- [1] B. Poudel, *et al.*, Science, **320**, 634 (2008)
- [2] Y. Koroteev, *et al.*, Phys. Rev. Lett., **93**, 046403 (2004)
- [3] T. Hirahara, *et al.*, Phys. Rev. B, **76**, 153305 (2007)
- [4] S. Ito, *et al.*, Phys. Rev. Lett., **117**, 35 (2016)
- [5] Y. Ohtsubo, *et al.*, New J. Phys., **18**, 123015 (2016)
- [6] I.K. Drozdov, *et al.*, Nat. Phys., **10**, 664 (2014)
- [7] F. Schindler, *et al.*, Nat. Phys., **14**, 918 (2018)
- [8] D. Pensin, A.H. MacDonald Nature Mater., **11**, 409 (2012)
- [9] D.E. Moncton, *et al.*, Phys. Rev. Lett., **34**, 734 (1975)
- [10] R. F. Frindt Phys. Rev. Lett., **28**, 299 (1972)
- [11] M. S. Bahramy, *et al.*, Nature Mater., **17**, 21 (2017)
- [12] K. Yaji, *et al.*, Rev. Sci. Instrum., **87**, 053111 (2016)

HIGH-RESOLUTION SPIN- AND ANGLE-RESOLVED PHOTOEMISSION SPECTROSCOPY ON DOPED MAGNETIC TOPOLOGICAL INSULATORS

Keisuke Fukutani^{1,2}, Chandan De¹, Roland Stania^{1,2}, Koichiro Yaji³, Kenta Kuroda³,
Jaeyoung Kim^{1,2}, and Han-Woong Yeom^{1,4}

¹*Center for Artificial Low dimensional Electronic Systems, Institute for Basic Science (IBS), Republic of Korea*

²*Pohang Accelerator Laboratory, Pohang University of Science and Technology (POSTECH), Republic of Korea*

³*The Institute for Solid State Physics, The University of Tokyo, Japan*

⁴*Department of Physics, Pohang University of Science and Technology (POSTECH), Republic of Korea*

The topological classifications in condensed matter physics have led to a paradigm shift in our understanding of the properties of solids, where the fundamental characteristics of matters can be determined not only by their symmetries and many-body interactions but also by their topological orders [1]. Such new classification schemes, have allowed for the predictions and discoveries of various new types of materials, leading to the realizations of intriguing electronic properties [2-7]. Among them, the interplay between the topological order and magnetism (broken time-reversal symmetry) has garnered much attentions as it is expected to lead to various exotic phenomena, such as quantum anomalous Hall effect [8] and topological magnetoelectric effect [9], and have been extensively studied to date [10].

Recently, a discovery of an intrinsic antiferromagnetic topological insulator MnBi_2Te_4 has been reported [11-13], followed by extensive investigations by various experimental and theoretical means on this material as well as its hetero-structural cousins $(\text{MnBi}_2\text{Te}_4)_n(\text{Bi}_2\text{Te}_3)_m$ [14-17]. On the other hand, despite the expected broken time-reversal symmetry, the electronic band structures of these materials are variously reported with regard to the presence of the band gap in the Dirac cone [18-23], which is at the heart of topological electronic properties. While there are several proposed hypotheses to explain such discrepancies [20,22,23], the general consensus has not been reached.

The keys to resolve such issue can be provided by high-resolution spin- and angle-resolved photoemission spectroscopy (SARPES), which allows us to simultaneously probe the topological surface Dirac band and their momentum-dependent spin textures. Since it is known for these materials that the microscopic domain sizes and the presence of bulk band projections, pronounced above the photon energies of $h\nu \sim 10$ eV [11], can obscure the unambiguous observation of the Dirac bands, utilizations of the micro-spot-sized, laser-based ($h\nu = 7$ eV) SARPES available at the Institute for Solid State Physics (ISSP) at the University of Tokyo would be an ideal experimental probe to tackle the present issue.

In our experiments, we have performed laser-SARPES measurements on the pristine as well as Sb-doped $(\text{MnBi}_2\text{Te}_4)_n(\text{Bi}_2\text{Te}_3)_m$ at the temperatures above and below the magnetic phase transition temperatures and have revealed their electronic structures as well as the corresponding spin textures near the Γ point in the surface Brillouin zone. Fig. 1 shows the ARPES intensity plots and the corresponding Fermi surface mapping for the pristine MnBi_2Te_4 and MnBi_4Te_7 . It can be clearly seen that the both materials possess *gapless* Dirac cones centered at the Γ point with the Dirac point (E_D) located at the binding energy of ~ 2.7 eV with no clearly identifiable band gap. These observations are consistent with some of the earlier ARPES studies [20-23], and likely point to the possibility that near the surface, the magnetic configurations are different from that of the bulk (i.e., possible surface magnetic

reconstructions), so as to provide the effective protection from gap-opening even in the absence of the time-reversal symmetry [15]. In order to identify the magnetic configurations near the surface and to identify the possible origin of the gapless Dirac cones, we have further obtained the spin-resolved ARPES data for the pristine as well as the Sb-doped samples. The spin-resolved data show unconventional spin textures for topological surface states and are currently under further investigation in conjunction with theoretical calculations as well as transport measurements.

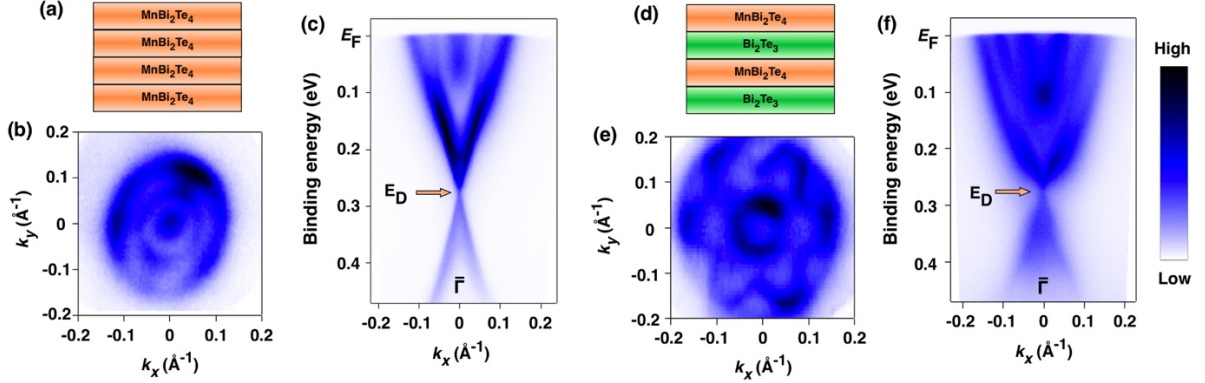


Figure 1: ARPES intensity maps for (a-c) MnBi_2Te_4 and (d-f) MnBi_4Te_7 . (a) and (b) schematically show the layer-stacking sequences for each of the materials, where the topmost layers are determined to be both MnBi_2Te_4 . (b) and (e) show the Fermi surface mappings and (c) and (f) show the band dispersions around the Γ point. The Dirac point E_D , where the upper and lower Dirac cones meet in the gapless dispersions are indicated by the arrows for both materials. The data were obtained with the s -polarized 7-eV laser at the temperature of $T = 10$ K.

REFERENCES

- [1] M. Z. Hasan and C. L. Kane, *Rev. Mod. Phys.* **82**, 3045 (2010).
- [2] C.-Z. Chang *et al.*, *Science* **340**, 167 (2013).
- [3] C.-K. Chiu *et al.*, *Rev. Mod. Phys.* **88**, 035005 (2016).
- [4] P. Zhang *et al.*, *Science* **360**, 182 (2018).
- [5] C.X. Trang *et al.*, *Nat. Commun.* **11**, 159 (2020).
- [6] L. Fu *et al.*, *Phys. Rev. Lett.* **100**, 096407 (2008).
- [7] A. Das *et al.*, *Nat. Phys.* **8**, 887 (2012).
- [8] F. D. M. Haldane, *Phys. Rev. Lett.* **61**, 2015 (1988).
- [9] X.-L. Qi *et al.*, *Phys. Rev. B* **78**, 195424 (2008).
- [10] Y. Tokura *et al.*, *Nat. Rev. Phys.* **1**, 126 (2019).
- [11] M. M. Otrokov *et al.*, *Nature* **576**, 416 (2019).
- [12] E. D. L. Rienks *et al.*, *Nature* **576**, 423 (2019).
- [13] Y. Gong *et al.*, *Chinese Phys. Lett.* **36**, 076801 (2019).
- [14] R. C. Vidal *et al.*, *Phys. Rev. X* **9**, 041065 (2019).
- [15] Y.-J. Hao *et al.*, *Phys. Rev. X* **9**, 041038 (2019).
- [16] L. Ding, *et al.*, *Phys. Rev. B* **101**, 020412(R) (2020).
- [17] R. C. Vidal *et al.*, *Phys. Rev. B* **100**, 121104 (2019).
- [18] J. Wu *et al.*, *Science Advances* **5**, eaax9989 (2019).
- [19] K. N. Gordon *et al.*, arXiv:1910.13943 (2019).
- [20] P. Swatek *et al.*, *Phys. Rev. B* **101**, 161109(R) (2020).
- [21] B. Chen *et al.*, *Nat. Commun.* **10**, 4469 (2019).
- [22] Y.J. Chen *et al.*, *Phys. Rev. X* **9**, 041040 (2019).
- [23] Y. Fu *et al.*, *Phys. Rev. B* **101**, 161113(R) (2020).

Half-metallicity of the ferrimagnet Mn_2VAI revealed by resonant inelastic soft x-ray scattering in a magnetic field

R.Y. Umetsu,^{1,*} H. Fujiwara,² K. Nagai,² Y. Nakatani,² M. Kawada,² A. Sekiyama,^{2,3} F. Kuroda,^{4,5} H. Fujii,^{4,5} T. Oguchi,^{3,4,5} Y. Harada,⁶ J. Miyawaki,⁶ and S. Suga^{4,7}

¹*Institute for Materials Research and Center for Spintronics Research Network, Tohoku University, 2-1-1 Katahira, Sendai 980-8577, Japan*

²*Division of Materials Physics, Graduate School of Engineering Science, Osaka University, 1-3 Machikaneyama, Toyonaka, Osaka 560-8531, Japan*

³*Center for Spintronics Research Network, Osaka University, 1-3 Machikaneyama, Toyonaka, Osaka 560-8531, Japan*

⁴*Institute of Scientific and Industrial Research, Osaka University, 8-1 Mihogaoka, Ibaraki 567-0047, Japan*

⁵*CM²-MaDIS, National Institute for Materials Science, 1-2-1 Sengen, Tsukuba, Ibaraki 305-0047, Japan*

⁶*Institute for Solid State Physics, The University of Tokyo, 5-1-5 Kashiwanoha, Kashiwa, Chiba 277-8581, Japan and Synchrotron Radiation Research Organization, The University of Tokyo, 1-1-1 Koto, Sayo-cho, Sayo, Hyogo 679-5148, Japan*

⁷*Forschungszentrum Jülich, PGI-6, 52425 Jülich, Germany*



(Received 22 October 2018; published 9 April 2019)

Detailed information on the electronic states of both V and Mn $3d$ electrons in the ferrimagnet Mn_2VAI is obtained by bulk sensitive resonant inelastic soft x-ray scattering (SX-RIXS) excited with circularly polarized light under an external magnetic field. The results under the V L -edge excitation have revealed the negligible partial density of states (PDOS) of the V $3d$ states around the Fermi energy as well as their rather localized character. Under the Mn L -edge excitation, on the other hand, the spectra are dominated by fluorescence with clear magnetic circular dichroism with noticeable excitation photon energy dependence. Compared with the theoretical prediction of the RIXS spectra based on the density-functional-theory band structure calculation, an itinerant, spin-dependent character of the Mn $3d$ states and decays of the Mn $2p$ core states are confirmed in consistency with the half-metallicity of the Mn $3d$ states.

DOI: [10.1103/PhysRevB.99.134414](https://doi.org/10.1103/PhysRevB.99.134414)

I. INTRODUCTION

Since the half-metallic electronic structure was predicted in the half-Heusler alloys of NiMnSb and PtMnSb [1] and in full-Heusler alloys such as Co-based Heusler alloys [2,3], a large number of investigations have been carried out from the interest in the field of spintronics. When electrons around the Fermi energy (E_F) are completely spin polarized, a system must be very useful as a ferromagnetic electrode for the spin injection and tunnel magnetoresistance as well as various spin utilizable devices [4]. For example, magnetoresistance of the magnetic tunneling junction with using complete half-metal ferromagnets would ideally be infinite [5]. Very recently, other types of Heusler alloys such as Mn-based Heusler alloys and their quasiternary alloys have also been pointed out to show the half-metallic electronic states [6–12]. Among them Mn_2VAI is one of the most attractive materials for device application. Its magnetic properties and theoretically predicted electronic structures were reported in the early 1980's [13–15].

If the Mn_2VAI orders completely, atoms of Mn, V, and Al occupy the Wyckoff positions $8c$, $4b$, and $4a$, respectively, with the space group $Fm\bar{3}m$. (See the Supplemental Material [16] for more details.) The spontaneous magnetization per

formula unit of $1.9 \mu_B/\text{f.u.}$ at 4.2 K is close to $2 \mu_B/\text{f.u.}$ [13] predicted by the generalized Slater-Pauling rule [17] and is much smaller than those in Co-based Heusler alloys. The magnetic critical Curie temperature T_C of this ferrimagnet Mn_2VAI is quite high, about 760 K, with antiferromagnetically coupled V and Mn spins below T_C [13,14]. This material is thought to be very promising for spintronic devices at room temperature because the expected current to switch its spin would be rather low. To investigate the magnetic properties of Mn_2VAI , extensive studies have recently been carried out by using x-ray absorption magnetic circular dichroism (XAS-MCD) for bulk [18] and film [19–21] specimens. The electronic structures have also been discussed by analyzing the XAS-MCD spectra for bulk single crystals, showing the itinerant character of the Mn $3d$ states, whereas the V $3d$ states are essentially localized [18]. On the other hand, the spin-polarized *unoccupied* electronic structures have been predicted by the analysis of XAS-MCD spectra for the film samples [19].

For the fundamental investigations of half-metallic materials, researchers should pay attention to how to provide convincing evidence of the half-metallic electronic states. To date fundamental magnetic properties reflecting the specific character of the half-metallic electronic states have been investigated. For example, rather small high-field magnetic susceptibility [22] and the negligibly small pressure dependence of the magnetization in some Co-based Heusler alloys have been reported. These results are understood as reflecting the

*rieume@imr.tohoku.ac.jp

fact that the electronic state near E_F is insensitive to applied external fields in the case of half-metallic ferromagnets [23]. Recently, anisotropic magnetoresistance is also predicted to serve as one of the practical screening tests of the half-metallic ferromagnets from both theoretical and experimental aspects [24,25].

We report here a method to probe the spin-polarized electronic structures of the half-metallic ferrimagnet Mn_2VAl Heusler alloy with highly ordered $L2_1$ -type structure by means of resonant inelastic soft x-ray scattering (SX-RIXS) measurements of the V and Mn $2p$ core excitation with use of right- and left-helicity circularly polarized light under an external magnetic field. RIXS is a bulk sensitive photon-in and photon-out spectroscopy, and very powerful for investigating, for example, the d - d excitations for open shell $3d$ orbitals and magnetic excitations for spin systems [26–29] as well as $2p$ - $3d$ transitions in element- and symmetry-specific ways. These excitations and decays are sensitive to spin, electron correlation, crystalline symmetry, in addition to the strength of hybridization with the ligand band. Furthermore, RIXS is insensitive to the surface conditions because of its long probing depth (>100 nm) in contrast to any kind of photoelectron spectroscopy (PES). Since the emitted light is probed, RIXS is not affected by any external perturbation such as magnetic field in contrast to PES for electrons. In the present study, the photon energy ($h\nu_{\text{in}}$) dependence of the magnetic circular dichroism (MCD) of RIXS was measured in detail in order to obtain the spin-dependent information. The results obtained in the present experiments and theoretical analyses confirmed the half-metallicity of Mn_2VAl , demonstrating that the RIXS and RIXS-MCD are very powerful for the study of the electronic structures of the half-metallic ferromagnetic or ferrimagnetic materials.

II. EXPERIMENT

A. Sample preparation

A mother ingot of polycrystalline Mn_2VAl was fabricated by induction melting in an argon atmosphere. Since the vapor pressure of Mn is high during the melting, excess Mn elements are contained in the mother ingot. A single crystal was grown by the Bridgman method with a size of 12 mm in diameter and about 30 mm in length. The obtained ingot was annealed at 1473 K to grow the crystal grains. Furthermore, a two-step annealing process at 1123 and then 873 K was employed in order to control the microstructures and to heighten the degree of order. These sample preparation processes resulted in a rather high degree of order as $S = 0.84$ in our sample compared with $S = 0.5$ by Kubota *et al.* [20] and $S = 0.4$ by Meinert *et al.* [19] in their samples. Crystal orientation was checked by the back Laue method and the specimen was cut in a strip form in the direction parallel to $\langle 100 \rangle$. The sample composition was confirmed to be Mn: 50.5, V: 26.9, Al: 22.6 (at. %) with an electron probe microanalyzer. Sample magnetization was measured with a superconducting quantum interference device (SQUID) magnetometer. The magnetization (M - H) curve measured at 5 K for Mn_2VAl showed that more than 90% of saturation magnetization is realized already at 0.2 T of the external magnetic field. The

expected value of the magnetic moment for Mn_2VAl by the Slater-Pauling rule, which is predicted by Galanakis *et al.* [17], is $2 \mu_B/\text{f.u.}$ A slight deviation of the saturation magnetic moment $1.82 \mu_B/\text{f.u.}$ of our sample from $2 \mu_B/\text{f.u.}$ might be caused by a small amount of the off-stoichiometric composition. Although the atomic content of Mn is well controlled in the present specimen, the atomic content of V is slightly increased compared to that of Al. The half-metallic electronic structures are, however, robust for the slight off-stoichiometric effect in the present case, which is simulated by the density functional theory (DFT) [18].

B. Measurements

Resonant inelastic soft x-ray scattering (SX-RIXS) for V and Mn $2p$ core excitation was measured at room temperature at the HORNET end station installed at the end of the long undulator beam line BL07LSU of SPring-8, Japan [30,31]. Measurement was performed with an external magnetic field of 0.25 T, which was applied by a permanent magnet with two poles for passing the excitation light [32,33]. The direction of the magnetic field was repeatedly reversed by the rotatable feed through supporting the magnet. (See the Supplemental Material [16] for more details on the experimental geometry.) Right- and left-helicity circularly polarized lights (RCP and LCP) parallel to the magnetic field were incident at 45° onto the $\langle 100 \rangle$ plane for excitation. Light emitted at 45° from this surface was dispersed by a grating and detected by a two-dimensional detector. The $\langle 100 \rangle$ axis was contained in the scattering plane. The direction of the magnetic field was reversed to confirm the genuine magnetic circular dichroism in this RIXS experiment. The total energy resolution was set to ~ 140 (170) meV at the V (Mn) $2p_{3/2}$ edge. RIXS measurements were performed on a surface of the sample obtained by fracturing in an Ar globe box in advance and transferred to a RIXS chamber with a vacuum of 1×10^{-5} Pa without any exposure to atmosphere.

III. RESULTS AND DISCUSSION

A. RIXS and RIXS-MCD experimental spectra

Figures 1(a) and 1(b) show the x-ray absorption spectra (XAS) of V and Mn L_3 edges, respectively, by means of the total electron yield recorded at 20 K [18]. The numbers above the vertical bars on the XAS indicate the incidence photon energy $h\nu_{\text{in}}$ for RIXS spectra. Figures 1(c) and 1(d) show the RIXS spectra for the V and the Mn L_3 edges at room temperature, respectively, measured by parallel (μ^+ : blue) and antiparallel (μ^- : red) configurations between the light helicity and the direction of the magnetic field as a function of the energy loss given by the horizontal axis. In the figures, strong intensity peaks without any energy loss are always observed and they are called the elastic component. In the larger energy loss region, the so-called fluorescence peaks are observed with their energy loss increasing linearly with $h\nu_{\text{in}}$. The relative height of the fluorescence peak is noticeably smaller than that of the elastic peak in the case of V L_3 -edge excitation and the difference of fluorescence between μ^+ and μ^- is not prominent, whereas its difference is clearly observed in the Mn L_3 -edge excitation.

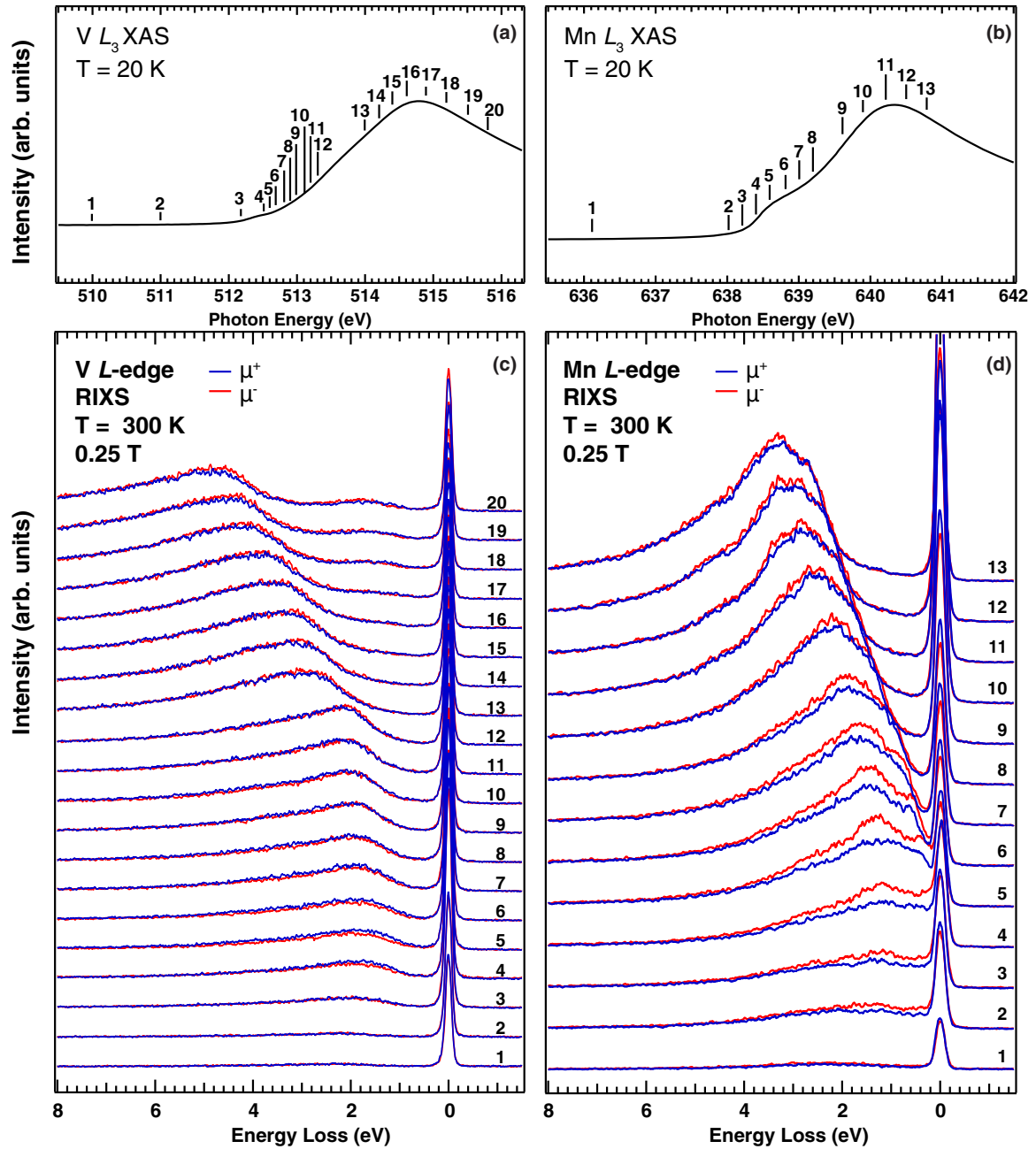


FIG. 1. XAS and RIXS spectra for V and Mn L_3 edges. (a), (b) are XAS for the V and the Mn L_3 edges, respectively, at 20 K and 2 T magnetic field [18]. (c), (d) are the RIXS spectra for the V and the Mn L_3 edges, respectively, obtained at room temperature. In (c), (d), the RIXS spectra were measured by parallel (μ^+) and antiparallel (μ^-) configurations between the light helicity and the direction of the magnetic field. The numbers above the vertical bars on the XAS indicate the excitation photon energy $h\nu_{in}$ for the RIXS spectra.

Figures 2(a) and 2(b) show the detailed intensity maps of the RIXS spectra for the V L_3 edge obtained by the circularly polarized light excitation. The horizontal axis shows the energy loss from the incident photon energy $h\nu_{in}$. The spectral differences of the RIXS between the parallel and antiparallel configurations, RIXS-MCD, are shown in Fig. 2(c). The corresponding results for the Mn L_3 edge are shown in Figs. 2(d)–2(f), respectively. From the comparison of these spectra between the V and the Mn L_3 edges, several significant features are recognized as have been only partly discussed by the polarization averaged RIXS spectra [18]. The most

characteristic feature is that the fluorescence peak associated with the V L_3 edge does not branch off from the elastic peak. On the other hand, there is almost no gap in the energy loss between the elastic peak and the appearance of the fluorescence peak for the Mn L_3 edge. In addition, weak structure is observed around the constant energy loss ~ 2 eV for a wide excitation region above $h\nu_{in} \sim 515$ eV for the V L_3 edge. This inelastic energy loss feature is considered to be associated with the d - d excitation because the existence of any feature at a constant energy loss cannot be due to any fluorescence feature. When we compare the fluorescence MCD for the V

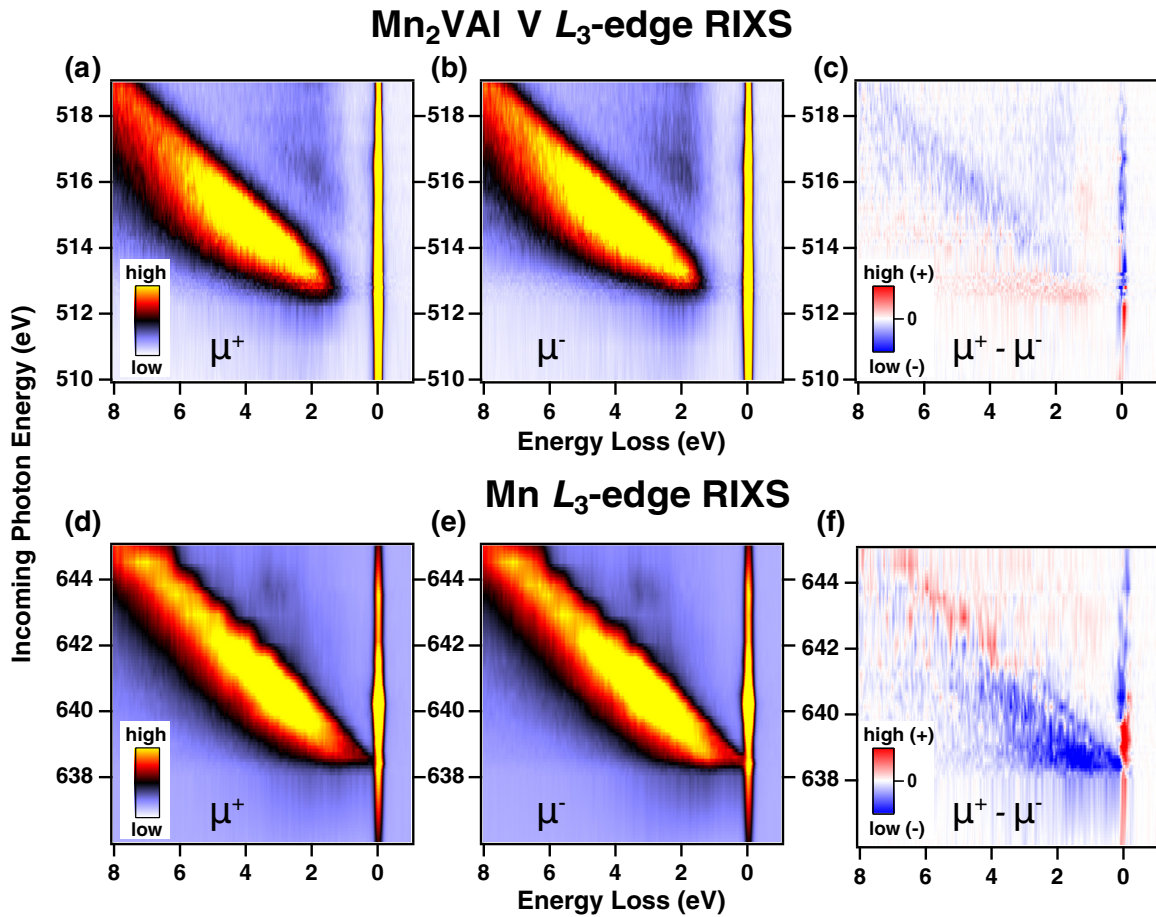


FIG. 2. Intensity maps of $h\nu_{\text{in}}$ -dependent RIXS and MCD at V and Mn L_3 edges in Mn_2VAI . (a), (b) are the intensity maps of the RIXS of V as a function of $h\nu_{\text{in}}$ obtained at room temperature in a magnetic field of 0.25 T for μ^+ and μ^- configurations. RIXS-MCD is given by $\mu^+ - \mu^-$ in (c). (d)–(f) show the corresponding results for the Mn L_3 edge.

and Mn L_3 edges in Figs. 2(c) and 2(f), it is clearly recognized as the negative Mn fluorescence MCD is spread in the photon energy range in $h\nu_{\text{in}} = 638\text{--}639$ eV, while very weak positive V fluorescence MCD is observed around $h\nu_{\text{in}} = 513$ eV.

Typical RIXS spectra and their MCD at $h\nu_{\text{in}} = 512.5$ eV for the V L_3 edge and $h\nu_{\text{in}} = 638.6$ eV for the Mn L_3 edge are reproduced in Figs. 3(a) and 3(b), respectively, by solid lines. The RIXS-MCD features are observed in both cases of V and Mn L_3 -edge excitations, and the sign of the MCD of the major fluorescence feature is found to be opposite between the cases of V and Mn in agreement with the ferrimagnetic character of this material, Mn_2VAI . Here, one notices that a broad peak is observed in the V L_3 -edge excitation, while double-peak features split by 1.0–1.2 eV are observed in Fig. 3(b) in the case of the Mn L_3 -edge excitation beside the elastic peak. Detailed RIXS-MCD for the Mn L_3 threshold excitation with changing $h\nu_{\text{in}}$ is shown later in Figs. 4(a1)–4(a6). These characteristic features must be closely correlated with the electronic structures of V and Mn.

B. Theoretical basis

For interpreting the observed RIXS and MCD spectra, theoretical calculations were performed by means of DFT [18]. Based on the DFT, spin-resolved partial density of states

(PDOS) of the V, Mn, and Al are calculated as shown in Fig. 3(c) together with the total density of states (DOS). The e_g and t_{2g} derived components are separately shown in Figs. 3(d) and 3(e) for V and Mn, respectively. First of all, the PDOS of Al is almost negligible near E_F . In the case of the V $3d$ states, the PDOS are found to be very small in the region of $E_F \pm 0.6$ eV. High PDOS of V of the t_{2g} occupied states are around -1.5 eV and those of the unoccupied t_{2g} and e_g states are located at around $+1.6$ eV.

In the case of the Mn $3d$ states, however, rather complex electronic structures strongly dependent on the spin are predicted. Although the occupied valence bands below -0.4 eV are composed of both t_{2g} and e_g states with both spin-up and -down states, clear differences are recognized above this energy. Namely, spin-down t_{2g} states are crossing E_F with high PDOS but the spin-up t_{2g} states have negligible PDOS between -0.5 eV and $+0.7$ eV. In the case of the e_g states of Mn, up-spin states have negligible PDOS between -0.4 and $+0.4$ eV, though down-spin states have a certain PDOS between -0.4 and $+1$ eV before showing high PDOS around $+1.4$ eV. Thus half-metallic PDOS behavior so far predicted is reconfirmed in Fig. 3(e).

As already pointed out in Figs. 2(a) and 2(b), the fluorescence component of RIXS in the V L_3 edge does not branch off from the elastic peak. The absence of any additional

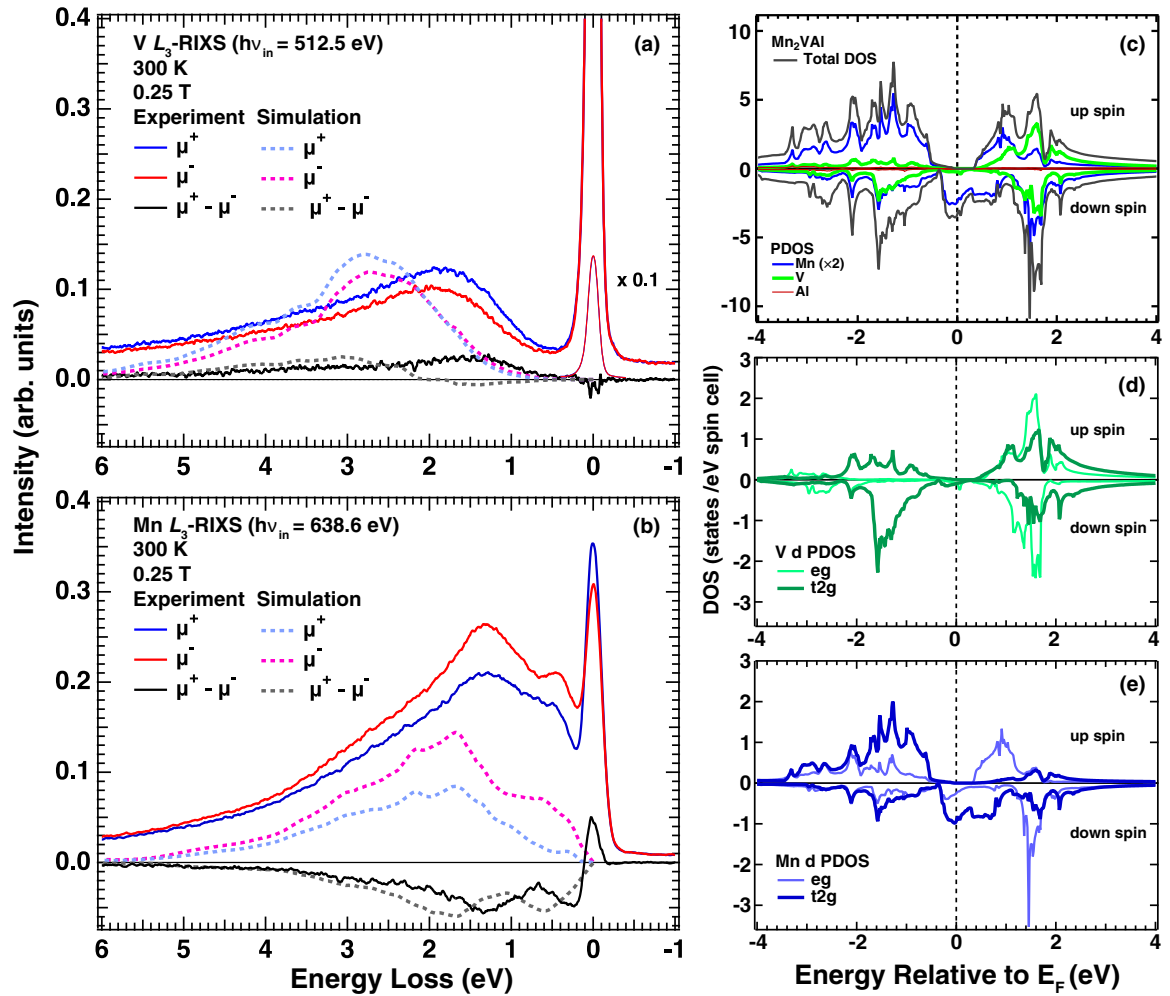


FIG. 3. Representative RIXS spectra for V and Mn L_3 edges, and theoretically predicted PDOSs of Mn, V, and Al in Mn_2VAI . RIXS spectra recorded for μ^+ and μ^- configurations at incoming photon energy $h\nu_{in}$ of 512.5 eV (a) and 638.6 eV (b) at the V and Mn L_3 edges, respectively, together with the MCD. (a), (b) include simulated spectra based on the DFT for V and Mn L_3 edges, respectively. (c) shows the theoretical prediction of the spin-dependent total DOS as well as PDOSs of Mn, V, and Al [18]. (d), (e) correspond to the e_g and t_{2g} components of the partial DOSs of V and Mn, respectively [18].

fluorescence peak between the elastic peak and the peak around ~ 2 eV for the L_3 threshold excitation is consistent with the weakness or negligible PDOSs of the V $3d$ states around E_F for both spin-up and spin-down V $3d$ states. The energy splitting between the V unoccupied $e_g + t_{2g}$ states PDOS and the occupied t_{2g} PDOS ranges from 2 to 4 eV [Fig. 3(d)]. Although this predicted $d-d$ splitting energy is slightly larger than the experimental $d-d$ splitting energy roughly estimated as 2–3 eV in the RIXS energy loss peak in Figs. 2(a) and 2(b), this constant loss energy feature in Figs. 2(a) and 2(b) can be unambiguously ascribable to the genuine RIXS feature due to the $d-d$ excitation. On the other hand, the RIXS feature for the Mn L_3 -edge excitation branches off really from the elastic peak and moves linearly with $h\nu_{in}$ revealing its fluorescence origin, suggesting the finite PDOS at E_F of the Mn $3d$ states. In the PDOS for the Mn shown in Fig. 3(e), finite PDOS exists around the E_F in the down-spin state, supporting the experimental results.

The RIXS-fluorescence spectra were simulated based on the Kramers-Heisenberg formula as shown in Eq. (A8) in the

Appendix, where details of the calculations are explained. Since the correlation between the fluorescence RIXS-MCD and the band structures must be discussed, more detailed calculation with taking the magnetization into account must be performed. Under the external magnetic field of 0.25 T, magnetization is almost saturated with the magnetic moment along the magnetic field [13,18]. Simulated RIXS-fluorescence spectra and the MCD based on the DFT for V and Mn L_3 edges are shown by dotted lines in Figs. 3(a) and 3(b), respectively, in addition to the experimental spectra. It is seen that the simulated RIXS-MCD qualitatively reproduces the experimental feature, for example, such as the double-peak feature of the fluorescence in the Mn L_3 edge. If we compare the spectra of theoretically predicted fluorescence and its MCD with corresponding experimental results, one notices that the predicted spectra are more widely energy spread than the experimental results. This may be due to the larger electron correlation energy between the Mn $3d$ electrons beyond that employed in the ordinary DFT calculation.

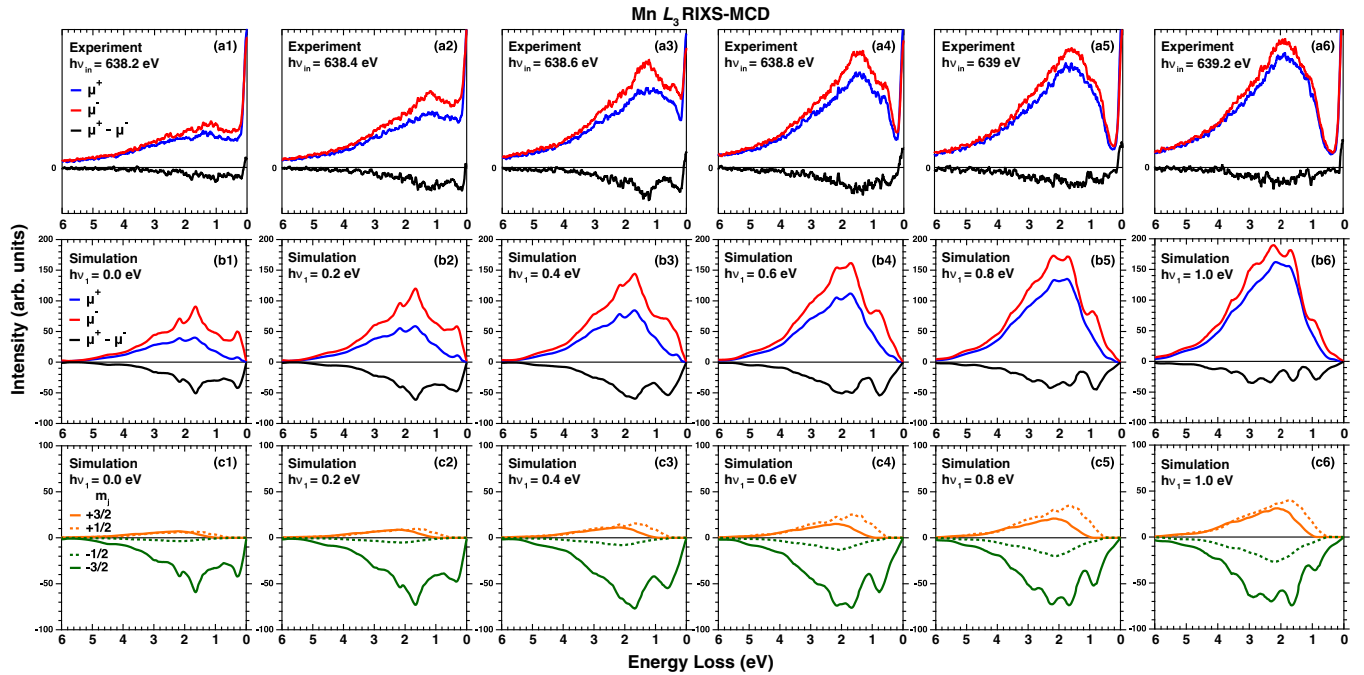


FIG. 4. RIXS and RIXS-MCD spectra for Mn L_3 edges. (a1)–(a6) show the experimental RIXS results for the μ^+ and μ^- configurations and their MCD spectra for the Mn L_3 edge as a function of the energy loss. Theoretically calculated RIXS and RIXS-MCD spectra based on DFT calculation are in (b1)–(b6). The definition of $h\nu_1$ is given in the text. (c1)–(c6) show m_j resolved RIXS-MCD spectra for the Mn L_3 edge, and the summation of the whole components of these spectra corresponds to the RIXS-MCD spectra in (b1)–(b6).

C. Detection of the spin-polarized Mn 3d electronic states

In order to further discuss the Mn 3d states around E_F , RIXS and the MCD were systematically investigated in the Mn L_3 -edge threshold excitation region. Figures 4(a1)–4(a6) show the experimental RIXS spectra for μ^+ and μ^- configurations and their MCD with changing the $h\nu_{in}$ ($638.2 \leq h\nu_{in} \leq 639.2$ eV). Before performing detailed calculations to simulate the experimental spectra, PDOS as well as excitation and deexcitation processes must be considered. Figure 5 shows schematic views of the Mn L_3 RIXS-MCD processes by considering the PDOS for the half-metallic magnetic system. The difference of the photon energy $h\nu_{in}$ from the energy E_{2p0} between the E_F and the $m_j = -3/2$ Mn $2p$ core state is defined hereafter by $h\nu_1$. PDOS of the up- (down-) spin state is schematically shown on the left- (right-) hand side of the energy axis (vertical axis) in each figure. The Zeeman splitting of the Mn $2p$ core level states of around 0.5 eV due to the effective magnetic field induced by the spin-polarized 3d states is taken into account in the present simulation. The excitation to the empty conduction band states is shown in Fig. 5 by the upward arrows with the filled circles. The gap of 0.3 eV from the E_F to the bottom of the DOS in the majority up-spin state of the Mn 3d states is taken into account.

Five energy ranges of $h\nu_1 = h\nu_{in} - E_{2p0}$ can be considered for the excitation as (1) below 0.16 eV, (2) 0.16–0.46 eV, (3) 0.46–0.63 eV, (4) 0.63–0.8 eV, and (5) above 0.8 eV. Since the experimental results were obtained at 300 K, one should note that the energy broadening of around 0.1 eV cannot be neglected in the comparison between the experimental results and theoretical prediction. In both the $2p$ core excitation and the $3d$ - $2p$ fluorescence decay processes, the spin is conserved

in the dipole transition. However, the hole spin can be relaxed before the fluorescence decays into the core hole with $m_j = -1/2$ and $+1/2$ states which are composed of both spin-up and -down states due to the spin-orbit coupling, so even when the $m_j = -1/2$ state with spin-down state is excited to the empty conduction band, the core hole spin can be partially relaxed to the spin-up state before the fluorescence takes place. This means that one should take into account the fluorescence in both spin-down and -up channels with the fixed relative weight given in the initial core hole states when the fluorescence decays to the core holes with $m_j = -1/2$ or $+1/2$ states are calculated. In Fig. 5, the width of the arrows corresponds to the transition probability.

The fluorescence spectra for the Mn L_3 -edge excitation are calculated as shown in Figs. 4(b1)–4(b6). In the experimental MCD spectra in Figs. 4(a1)–4(a6), the intensity increases with increasing $h\nu_{in}$ showing the double-peak feature, which becomes less clear above $h\nu_{in} = 638.8$ eV. Such a tendency is qualitatively reproduced by the calculated spectra. Figures 4(c1)–4(c6) show the predicted MCD spectra of fluorescence to the Mn $2p$ $m_j = -3/2$, $-1/2$, $+1/2$, and $+3/2$ states. That is, the summation of the total four components in these spectra [(c1)–(c6)] corresponds to the MCD spectra shown by the black lines in Figs. 4(b1)–4(b6). It is clear that the fluorescence decay to the $m_j = -3/2$ state is dominating at the low $h\nu$ threshold. Since the down-spin t_{2g} states have substantial PDOS of the unoccupied states from E_F to $+0.8$ eV, and the down-spin e_g states have high PDOS around $+1.4$ eV, the pure down-spin $m_j = -3/2$ states can be continuously excited at least up to $h\nu_1 \sim 0.8$ eV in addition to the region in $+1.2$ – 1.6 eV inducing the remarkable negative

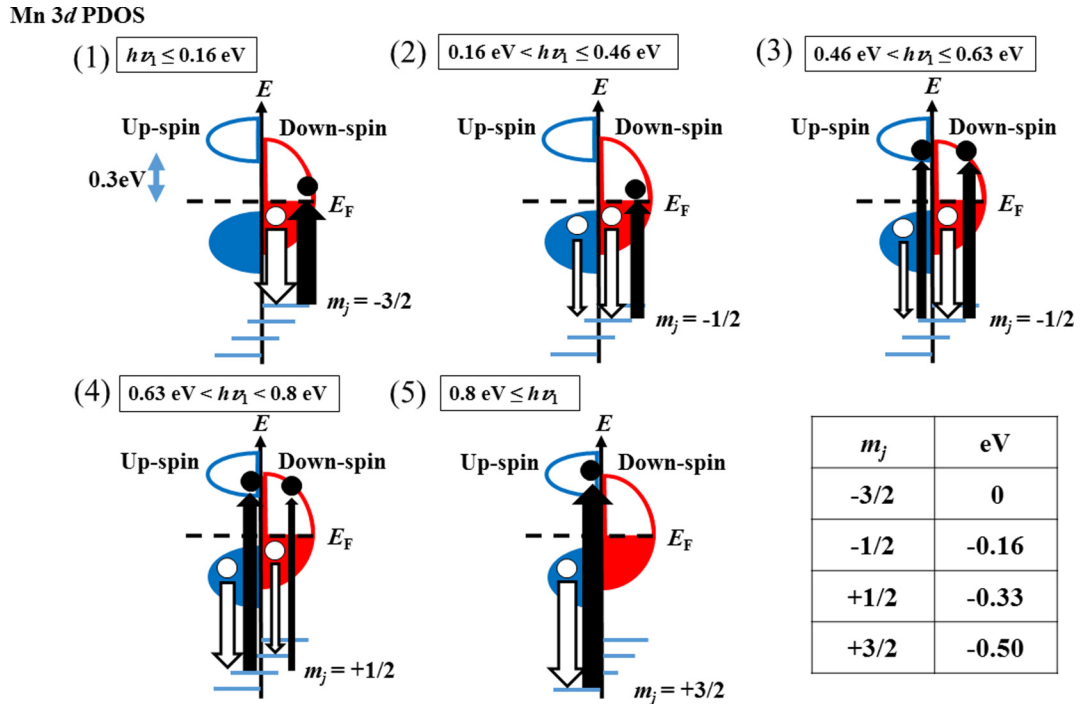


FIG. 5. Schematic views of the RIXS-MCD processes in the case of half-metallic density of states. Excitation from the Zeeman split $2p$ m_j core states is considered in the present simulation as indicated in the table and the Zeeman splitting is around 0.5 eV due to the effective magnetic field. The difference of the photon energy ($h\nu_{in}$) from the energy E_{2p0} between the Fermi energy (E_F) and the Mn $2p$ $m_j = -3/2$ state is given here by $h\nu_1$. PDOS of the up- (down-) spin states is schematically shown on the left- (right-) hand side of the energy axis (vertical axis) in each panel. A gap of 0.3 eV from the E_F to the bottom of the DOS in the majority up-spin state is also employed. The spin is thought to be fully down and up in the $m_j = -3/2$ and $+3/2$ states, respectively. On the other hand, the spin at $m_j = -1/2$ and $+1/2$ states is composed of both spin-up and -down states due to the spin-orbit coupling. The width of the arrows corresponds to the transition probability.

fluorescence MCD in Figs. 4(c1)–4(c6). Since the PDOS of the occupied Mn 3d states in the region from E_F down to -0.4 eV for the down-spin state is rather high, noticeable fluorescence and its clear MCD is predicted just from the energy loss of 0 eV as clearly seen in Figs. 4(b1) and 4(c1), and 4(b2) and 4(c2). The fluorescence feature with an energy loss peak near 0.3 eV in Figs. 4(b1) and 4(b2) is thought to reflect the high PDOS of the down-spin occupied t_{2g} states in the above-mentioned region.

With increasing $h\nu_1$ up to ~ 0.46 eV, excitation from the $m_j = -1/2$ state becomes gradually feasible in addition to the excitation from the $m_j = -3/2$ state, providing negative but small MCD of the fluorescence to the $m_j = -1/2$ state as shown in Figs. 4(c2) and 4(c3). The origin of the doublet feature of the fluorescence and its MCD separated by ~ 1 eV [Figs. 4(a2)–4(a4)] is relatively well predicted by the calculation as shown in Figs. 4(b1)–4(b4) and 4(c1)–4(c4). Both of the doublet features must be due to the fluorescence transition into the down-spin $m_j = -3/2$ core hole state.

For 0.46 eV $< h\nu_1 < 0.63$ eV, both down- and up-spin states are excited from the $m_j = -1/2$ core states. For 0.63 eV $< h\nu_1 < 0.8$ eV, a similar situation takes place for the $m_j = +1/2$ core states. In each case, both spin-down and -up states are excited and fluorescence takes place after the relaxation of the core hole spin. With the increase in the $h\nu_1$, the relative weight of the transition to the $m_j = -1/2$, $+1/2$, and $+3/2$ states increases gradually with the increase

of the magnitude of the individual fluorescence MCD. As a result, the total magnitude of the predicted fluorescence MCD decreases relatively as seen in the series of Figs. 4(b1)–4(b6) in consistency with the experimental results in Fig. 4(a3)–4(a6).

In the present study, detailed $h\nu_{in}$ dependence of RIXS-MCD was clearly observed, providing the spin-dependent information on the bulk electronic structures with the single magnetic domain. This technique has a great advantage to investigate the half-metallic bulk electronic structures compared to various other investigations, which have been performed up to now. Ultraviolet-photoemission spectroscopy (UPS) [34] and hard x-ray angle-resolved photoelectron spectroscopy (HAXARPES) [35,36] are such examples. In the case of UPS, it is known that the surface electronic structure accessible by UPS is noticeably different from that in the bulk. The HAXARPES is much more bulk sensitive. However, its orders-of-magnitude reduced photoionization cross sections for the valence band electronic states, compared with the UPS, strongly hinder the usefulness of HAXARPES studies. Moreover the possible recoil shift effects for the valence electron states spoil reliable discussions on the most important electronic structures near the E_F in Mn_2VAl [37,38]. Although spin-polarized and angle-resolved photoelectron spectroscopy (SP-ARPES) will be desired to detect the half-metallicity, its low detection efficiency (orders of 10^{-4} or less) makes it almost impossible to make a reliable

experiment. Therefore, the electronic structure, especially the half-metallicity of the bulk Heusler alloys, has not yet been fully clarified. The qualitative agreement obtained in the present experiments and theoretical analyses confirmed the half-metallicity of Mn_2VAI , demonstrating that the RIXS and RIXS-MCD are powerful for the study of the electronic structures of the half-metallic ferromagnetic or ferrimagnetic materials.

IV. CONCLUSION

RIXS and its MCD measurements in magnetic field were performed on the single-crystal half-metallic Heusler alloy, Mn_2VAI , in order to obtain reliable information on the bulk electronic state of the $3d$ electrons. The d - d excitation due to the t_{2g} - e_g splitting is clearly observed for V in Mn_2VAI under the L_3 -edge excitation. The loss energy of the V d - d RIXS maximum is found to be about 2 eV, being comparable to the splitting energy between the theoretically predicted e_g and t_{2g} states. The delayed branching off in the V $3d$ - $2p$ fluorescence peak from the elastic peak demonstrates the nearly absent V $3d$ PDOS around E_F . The clear appearance of the t_{2g} - e_g RIXS of V reflect the rather localized character of the V $3d$ states. The RIXS-MCD of the fluorescence peaks of the Mn $3d$ - $2p$ transition under the L_3 -edge excitation shows a negative sign with clear $h\nu_{\text{in}}$ dependence. The sign and the shape of the RIXS-MCD are qualitatively reproduced in consistence with the DFT calculations and confirmed the absence of the up-spin Mn $3d$ PDOS at the E_F , demonstrating the half-metallicity of the Mn_2VAI Heusler alloy. Thus the bulk sensitive RIXS studies under external magnetic field are confirmed to be essential to study the detailed electronic structures of various Heusler alloys and family materials.

ACKNOWLEDGMENTS

We sincerely thank K. Yubuta, T. Sugawara, and Y. Murakami for their help in making single crystals and EPMA experiments, and Professor T. Kanomata for valuable discussions. This research was supported by Precursory Research for Embryonic Science and Technology (PRESTO), Japan Science and Technology Agency (JST), and Grant-in-Aid for Scientific Research Grants No. JP18K03512, No. JP18H01690, No. JP16H03851, No. JP16H02267, and No. JP17H06154 from the Ministry of Education, Culture, Sports, Science and Technology Japan. This work was carried out under the approval of BL07LSU at SPring-8 Synchrotron Radiation Research Organization and the Institute for Solid State Physics, The University of Tokyo (Proposals No. 2013A7447, No. 2013B7459, No. 2014B7478, No. 2016B7512, and No. 2017B7552). F.K., H.F., and T.O. acknowledge a support by the ‘‘Materials research by Information Integration’’ Initiative project from JST.

APPENDIX: SIMULATION BASED ON THE DENSITY FUNCTIONAL THEORY

The electronic structure calculation based on DFT has been performed using the HILAPW code, which is based on the

all-electron full-potential augmented plane-wave (FLAPW) method [39]. The generalized gradient approximation (GGA) using the Perdew-Burke-Ernzerhof scheme has been used for the exchange-correlation potential [40,41]. The relativistic effects are considered for the $2p$ core states including the spin-orbit coupling. On the other hand, the spin-orbit coupling for the $3d$ states is negligible compared with the $2p$ states, since the orbital magnetic moments of Mn and V were estimated as $0.026 \mu_B/\text{Mn}$ and $0.037 \mu_B/\text{V}$ by XAS-MCD measurements, respectively [18]. Plane-wave expansion cutoffs were set to 20 Ry for the wave functions and 80 Ry for the charge density and potential functions. The muffin-tin sphere radius was chosen as 1.1 Å for all elements. For the Brillouin-zone integration, a $16 \times 16 \times 16$ uniform mesh was used with the tetrahedron integration technique. The atoms were placed on the general form X_2YZ of the $L2_1$ structure with X at the $8c$ site in the Wyckoff position, Y at the $4b$ site, and Z at the $4a$ site. The lattice constant was set to 5.875 Å [7].

The RIXS spectra were simulated by using the Kramers-Heisenberg formula [29,42], described as

$$\sigma(v_{\text{in}}, v_{\text{out}}) \propto \sum_f \left| \sum_i \frac{\langle b | \hat{F}_2^{(\mu_2)} | i \rangle \langle i | \hat{F}_1^{(\mu_1)} | a \rangle}{E_i - E_a - h\nu_{\text{in}} - i\Gamma_i} \right|^2 \times \delta[(h\nu_{\text{in}} - h\nu_{\text{out}}) - (E_b - E_a)], \quad (\text{A1})$$

where a , b , and i denote the initial, final, and intermediate states having the energy of E_a , E_b , and E_i , respectively. The incoming and outgoing photon energies are described as $h\nu_{\text{in}}$ and $h\nu_{\text{out}}$, respectively. Lifetime broadening of a core hole is given by Γ_i of 0.36 (0.28) eV for Mn (V) [43], and the dipole transition operator is described as $\hat{F}^{(\mu)}$ for the photon helicity (μ) of the circularly polarized light. The electron configurations of the initial, intermediate, and final states with $|a\rangle = |2p^6v\rangle$, $|i\rangle = |2p^5ve\rangle$, and $|b\rangle = |2p^6v^{-1}e'\rangle$ are taken into account with the relative energy of $E_a = 0$, $E_i = \varepsilon_e - E_{2p}$, and $E_b = \varepsilon_{e'} - \varepsilon_{v^{-1}}$. Here v and e represent the valence electrons and the electron in the empty conduction band, and v^{-1} and $\varepsilon_{v^{-1}}$ stand for the valence electron state with one hole induced by the decay into the $2p$ core hole state and the energy of valence electrons with one hole. Then the denominator of Eq. (A1) can be expressed by considering these energies and the content of the δ function as

$$E_i - E_a - h\nu_{\text{in}} - i\Gamma_i = \varepsilon_{v^{-1}} + \varepsilon_e - \varepsilon_{e'} - E_{2p} - h\nu_{\text{out}} - i\Gamma_i.$$

If we assume $\varepsilon_e = \varepsilon_{e'}$, where no change is considered for the electron excited into the empty conduction band on the fluorescence decay, the denominator of Eq. (A1) is further approximated as

$$E_i - E_a - h\nu_{\text{in}} - i\Gamma_i = \varepsilon_{v^{-1}} - E_{2p} - h\nu_{\text{out}} - i\Gamma_i. \quad (\text{A2})$$

On the same assumption the transition matrix elements are transformed as

$$\langle i | \hat{F}_1^{(\mu_1)} | a \rangle = \langle e | \hat{F}_1^{(\mu_1)} | 2p \rangle, \quad (\text{A3})$$

$$\langle b | \hat{F}_2^{(\mu_2)} | i \rangle = \langle v^{-1} | \hat{F}_2^{(\mu_2)} | 2p^{-1} \rangle \delta(e' - e). \quad (\text{A4})$$

The summation for the intermediate states $|i\rangle$ can be expressed by the two integrals as follows, and the RIXS intensity

can be described as

$$\sigma(v_{\text{in}}, v_{\text{out}}) \propto \sum_f \int d\varepsilon_{v-1} \int d\varepsilon_e \frac{|\langle v^{-1} | \hat{F}_2^{(\mu_2)} | 2p^{-1} \rangle|^2 \cdot |\langle e | \hat{F}_1^{(\mu_1)} | 2p \rangle|^2}{(\varepsilon_{v-1} - E_{2p} - hv_{\text{out}})^2 + \Gamma_i^2} \delta[(hv_{\text{in}} - hv_{\text{out}}) - (\varepsilon_e - \varepsilon_{v-1})]. \quad (\text{A5})$$

If we assume that the square of the matrix element in the numerator is proportional to the partial density of states of the occupied (unoccupied) states denoted as D^{occ} (D^{unocc}) at the energy of ε_{v-1} (ε_e) of occupied (unoccupied) valence states multiplied by the transition probability $w_{jm_j m_s}^{(\mu)}$ between the $2p$ and $3d$ states depending on the helicity (μ) [44–46], we obtain

$$|\langle e | \hat{F}_1^{(\mu_1)} | 2p \rangle|^2 \propto \sum_{jm_j m_s} w_{jm_j m_s}^{(\mu_1)} D_{(m+\mu_1)m_s}^{\text{unocc}}(\varepsilon_e), \quad (\text{A6})$$

$$|\langle v^{-1} | \hat{F}_2^{(\mu_2)} | 2p^{-1} \rangle|^2 \propto \sum_{j'm'_j m'_s} w_{j'm'_j m'_s}^{(\mu_2)} D_{(m'+\mu_2)m'_s}^{\text{occ}}(\varepsilon_{v-1}). \quad (\text{A7})$$

Here j , m_j , m_s , and those with a prime ($'$) stand for the total angular momentum of the $2p$ core states, their z component and its spin, while m and m_s , as well as those with a prime denote the magnetic quantum number and the spin of the $3d$ states under consideration. Here $m = m_j - m_s$ is assumed for the $2p$ states. In the present calculation, the relativistic effects are considered for the $2p_{j=3/2}$ core states including the spin-orbit interaction for the states with $m_j = \pm 3/2$ and $\pm 1/2$, while the $3d$ spin is well defined by m_s . Furthermore, we take into account the Zeeman splitting of the $2p$ states due to the effective magnetic field of the $3d$ states. The weight coefficient $w_{jm_j m_s}^{(\mu)}$ is given by multiplication of the Clebsch-Gordan coefficient and the Gaunt coefficient.

Finally we obtained the RIXS intensity as

$$\begin{aligned} \sigma^{\mu_1, \mu_2}(v_{\text{in}}, v_{\text{out}}) &\propto \sum_{jm_j} \sum_{m_s m'_s} \int d\varepsilon_{v-1} \frac{w_{jm_j m'_s}^{(\mu_2)} w_{jm_j m_s}^{(\mu_1)} D_{(m'+\mu_2)m'_s}^{\text{occ}}(\varepsilon_{v-1}) D_{(m+\mu_1)m_s}^{\text{unocc}}(\varepsilon_e)}{(\varepsilon_{v-1} - E_{2p_{jm_j}} - hv_{\text{out}})^2 + \Gamma_i^2} \\ &= \sum_{jm_j} \sum_{m_s m'_s} \int d\varepsilon_{v-1} \frac{w_{jm_j m'_s}^{(\mu_2)} w_{jm_j m_s}^{(\mu_1)} D_{(m'+\mu_2)m'_s}^{\text{occ}}(\varepsilon_{v-1}) D_{(m+\mu_1)m_s}^{\text{unocc}}[\varepsilon_{v-1} + (hv_{\text{in}} - hv_{\text{out}})]}{(\varepsilon_{v-1} - E_{2p_{jm_j}} - hv_{\text{out}})^2 + \Gamma_i^2}. \end{aligned} \quad (\text{A8})$$

In the simulation, we practically give the energy of unoccupied valence states ε_e using the energy offset (hv_1) from Fermi energy (E_F) as $\varepsilon_e = E_F + hv_1$. Then, we further transform Eq. (A8) as

$$\sigma^{\mu_1, \mu_2}(v_1, v_{\text{out}}) \propto \sum_{jm_j} \sum_{m_s m'_s} \int d\varepsilon_{v-1} \frac{w_{jm_j m'_s}^{(\mu_2)} w_{jm_j m_s}^{(\mu_1)} D_{(m'+\mu_2)m'_s}^{\text{occ}}(\varepsilon_{v-1}) D_{(m+\mu_1)m_s}^{\text{unocc}}(hv_1 + E_F)}{(\varepsilon_{v-1} - E_{2p_{jm_j}} - hv_{\text{out}})^2 + \Gamma_i^2}. \quad (\text{A9})$$

In this model, the magnitude of the RIXS-MCD is proportional to the D^{unocc} or the quantity of the core holes and the line shape reflects the energy distribution of the D^{occ} . Moreover, the spin polarization of the $2p$ core hole plays an essential role in the spin selective transition with dipole selection rule. Thus, the RIXS-MCD is clearly observed at the pre-edge of the L_3 XAS since the excitation from the spin-polarized $m_j = -3/2$ states is dominant. In the case of the $m_j = \pm 1/2$, however, the spins of the core hole are mixed, and the core hole spins can be relaxed between spin up and down before the fluorescence takes place. This allows the optical path in which the spins in the absorption process and emission process are different. The fluorescence spectra thus obtained are shown in Figs. 4(b) and 4(c). Note that the transition probability for the circularly polarized photon was taken into account in the absorption process only, but it was averaged in the emission process since the polarization of the outgoing photon was not measured in the experiment.

-
- | | |
|--|---|
| <p>[1] R. A. de Groot, F. M. Mueller, P. G. van Engen, and K. H. J. Buschow, <i>Phys. Rev. Lett.</i> 50, 2024 (1983).</p> <p>[2] J. J. Kübler, A. R. Williams, and C. B. Sommers, <i>Phys. Rev. B</i> 28, 1745 (1983).</p> <p>[3] S. Ishida, S. Akazawa, Y. Kubo, and J. Ishida, <i>J. Phys. F</i> 12, 1111 (1982).</p> <p>[4] G. Schmidt, D. Ferrand, L. W. Molenkamp, A. T. Filip, and B. J. van Wees, <i>Phys. Rev. B</i> 62, 4790(R) (2000).</p> <p>[5] M. Jullere, <i>Phys. Lett. A</i> 54, 225 (1975).</p> <p>[6] S. Ishida, S. Asano, and J. Ishida, <i>J. Phys. Soc. Jpn.</i> 53, 2718 (1984).</p> | <p>[7] R. Weht and W. E. Pickett, <i>Phys. Rev. B</i> 60, 13006 (1999).</p> <p>[8] K. Özdogañ, I. Galanakis, E. Şaşıođlu, and B. Aktaş, <i>J. Phys.: Condens. Matter</i> 18, 2905 (2006).</p> <p>[9] G. D. Liu, X. F. Dai, H. Y. Liu, J. L. Chen, Y. X. Li, G. Xiao, and G. H. Wu, <i>Phys. Rev. B</i> 77, 014424 (2008).</p> <p>[10] V. Alijani, J. Winterlik, G. H. Fecher, S. S. Naghavi, and C. Felser, <i>Phys. Rev. B</i> 83, 184428 (2011).</p> <p>[11] K. Özdogañ, E. Şaşıođlu, and I. Galanakis, <i>J. Appl. Phys.</i> 113, 193903 (2013).</p> <p>[12] Y. C. Gao and X. Gao, <i>AIP Adv.</i> 5, 057157 (2015).</p> |
|--|---|

- [13] Y. Yoshida, M. Kawakami, and T. Nakamichi, *J. Phys. Soc. Jpn.* **50**, 2203 (1981).
- [14] H. Itoh, T. Nakamichi, Y. Yamaguchi, and N. Kazama, *Trans. Jpn. Inst. Metals* **24**, 265 (1983).
- [15] T. Nakamichi and C. V. Stager, *J. Magn. Magn. Mater.* **31–34**, 85 (1983).
- [16] See Supplemental Material at <http://link.aps.org/supplemental/10.1103/PhysRevB.99.134414> for details on the crystal structure of Mn₂VAl Heusler alloy with L₂₁ type (see Refs. [13,14,47]), and for details on the scattering geometry in SX-RIXS measurements. The single crystal of the Mn₂VAl specimen was tilted 45° from the direction of the incident x-ray. The right- and left-helicity circularly polarized incident photon is used for RIXS excitation.
- [17] I. Galanakis, P. H. Dederichs, and N. Papanikolaou, *Phys. Rev. B* **66**, 174429 (2002).
- [18] K. Nagai, H. Fujiwara, H. Aratani, S. Fujioka, H. Yomosa, Y. Nakatani, T. Kiss, A. Sekiyama, F. Kuroda, H. Fujii, T. Oguchi, A. Tanaka, J. Miyawaki, Y. Harada, Y. Takeda, Y. Saitoh, S. Suga, and R.Y. Umetsu, *Phys. Rev. B* **97**, 035143 (2018).
- [19] M. Meinert, J.-M. Schmalhorst, G. Reiss, and E. Arenholz, *J. Phys. D: Appl. Phys.* **44**, 215003 (2011).
- [20] T. Kubota, K. Kodama, T. Nakamura, Y. Sakuraba, M. Oogane, K. Takanashi, and Y. Ando, *Appl. Phys. Lett.* **95**, 222503 (2009).
- [21] P. Klaer, E. Arbelo Jorge, M. Jourdan, W. H. Wang, H. Sukegawa, K. Inomata, and H. J. Elmers, *Phys. Rev. B* **82**, 024418 (2010).
- [22] R.Y. Umetsu, N. Endo, A. Fujita, R. Kainuma, A. Sakuma, K. Fukamichi, and K. Ishida, *J. Phys.: Conf. Ser.* **200**, 062036 (2010).
- [23] T. Kanomata, Y. Chieda, K. Endo, H. Okada, M. Nagasako, K. Kobayashi, R. Kainuma, R.Y. Umetsu, H. Takahashi, Y. Furutani, H. Nishihara, K. Abe, Y. Miura, and M. Shirai, *Phys. Rev. B* **82**, 144415 (2010).
- [24] F. J. Yang, Y. Sakuraba, S. Kokado, Y. Kota, A. Sakuma, and K. Takanashi, *Phys. Rev. B* **86**, 020409(R) (2012).
- [25] S. Kokado, M. Tsunoda, K. Harigaya, and A. Sakuma, *J. Phys. Soc. Jpn.* **81**, 024705 (2012).
- [26] C. F. Hague, J.-M. Mariota, L. Journela, J.-J. Galleta, A. Rogalev, G. Krillb, and J.-P. Kappler, *J. Electron Spectrosc. Relat. Phenom.* **110–111**, 179 (2000).
- [27] A. Kotani, *J. Phys. Chem. Solids* **66**, 2150 (2005).
- [28] S. Grenier, J. P. Hill, V. Kiryukhin, W. Ku, Y.-J. Kim, K. J. Thomas, S. W. Cheong, Y. Tokura, Y. Tomioka, D. Casa, and T. Gog, *Phys. Rev. Lett.* **94**, 047203 (2005).
- [29] L. J. P. Ament, M. van Veenendaal, T. P. Devereaux, J. P. Hill, and J. van den Brink, *Rev. Mod. Phys.* **83**, 705 (2011).
- [30] Y. Senda, S. Yamamoto, H. Ohashi, I. Matsuda, M. Fujisawa, A. Harasawa, T. Okuda, S. Takahashi, N. Nariyama, T. Matsushita, T. Ohata, Y. Furukawa, T. Tanaka, K. Takeshita, S. Goto, H. Kitamura, A. Kakizaki, and M. Oshima, *Nucl. Instrum. Methods Phys. Res., Sect. A* **649**, 58 (2011).
- [31] Y. Harada, M. Kobayashi, H. Niwa, Y. Senba, H. Ohashi, T. Tokushima, Y. Horikawa, S. Shin, and M. Oshima, *Rev. Sci. Instrum.* **83**, 013116 (2012).
- [32] J. Miyawaki, S. Suga, H. Fujiwara, H. Niwa, H. Kiuchi, and Y. Harada, *J. Synchrotron Radiat.* **24**, 449 (2017).
- [33] J. Miyawaki, S. Suga, H. Fujiwara, M. Urasaki, H. Ikeno, H. Niwa, H. Kiuchi, and Y. Harada, *Phys. Rev. B* **96**, 214420 (2017).
- [34] X. Kozina, J. Karel, S. Ouardi, S. Chadov, G. H. Fecher, C. Felser, G. Stryganyuk, B. Balke, T. Ishikawa, T. Uemura, M. Yamamoto, E. Ikenaga, S. Ueda, and K. Kobayashi, *Phys. Rev. B* **89**, 125116 (2014).
- [35] M. Jourdan, J. Minár, J. Braun, A. Kronenberg, S. Chadov, B. Balke, A. Gloskovskii, M. Kolbe, H. J. Elmers, G. Schönhense, H. Ebert, C. Felser, and M. Kläui, *Nat. Commun.* **5**, 3974 (2014).
- [36] R. Fetzer, B. Stadtmüller, Y. Ohdaira, H. Naganuma, M. Oogane, Y. Ando, T. Taira, T. Uemura, M. Yamamoto, M. Aeschlimann, and M. Cinchetti, *Sci. Rep.* **5**, 8537 (2015).
- [37] S. Suga, S. Itoda, A. Sekiyama, H. Fujiwara, S. Komori, S. Imada, M. Yabashi, K. Tamasaku, A. Higashiya, T. Ishikawa, M. Shang, and T. Fujikawa, *Phys. Rev. B* **86**, 035146 (2012).
- [38] S. Suga and A. Sekiyama, *Photoelectron Spectroscopy: Bulk and Surface Electronic Structures*, Springer Series in Optical Sciences Vol. 176 (Springer, Berlin, Heidelberg, 2013).
- [39] E. Wimmer, H. Krakauer, M. Weinert, and A. J. Freeman, *Phys. Rev. B* **24**, 864 (1981).
- [40] J. P. Perdew, K. Burke, and M. Ernzerhof, *Phys. Rev. Lett.* **77**, 3865 (1996).
- [41] J. P. Perdew, K. Burke, and M. Ernzerhof, *Phys. Rev. Lett.* **78**, 1396 (1997).
- [42] F. de Groot and A. Kotani, *Core Level Spectroscopy of Solids*, Advances in Condensed Matter Sciences (CRC Press, Boca Raton, FL, 2008).
- [43] J. L. Campbell and T. Papp, *At. Data Nucl. Data Tables* **77**, 1 (2001).
- [44] J. Jiménez-Mier, J. van Ek, D. L. Ederer, T. A. Callcott, J. J. Jia, J. Carlisle, L. Terminello, A. Asfaw, and R. C. Perera, *Phys. Rev. B* **59**, 2649 (1999).
- [45] K. O. Kvashnina, Y. O. Kvashnin, J. R. Vegelius, A. Bosak, P. M. Martin, and S. M. Butorin, *Anal. Chem.* **87**, 8772 (2015).
- [46] G. van der Laan and A. I. Figueroa, *Coord. Chem. Rev.* **277–278**, 95 (2014).
- [47] K. Momma and F. Izumi, *J. Appl. Crystallogr.* **44**, 1272 (2011).



Influence of interface dipole layers on the performance of graphene field effect transistors



Naoka Nagamura ^{a, b}, Hirokazu Fukidome ^{c, *}, Kosuke Nagashio ^d, Koji Horiba ^e, Takayuki Ide ^c, Kazutoshi Funakubo ^c, Keiichiro Tashima ^c, Akira Toriumi ^d, Maki Suemitsu ^c, Karsten Horn ^f, Masaharu Oshima ^g

^a National Institute for Materials Science, 1-2-1 Sengen, Tsukuba, Ibaraki, 305-0047, Japan

^b PRESTO, Japan Science and Technology Agency, 4-1-8 Honcho, Kawaguchi, Saitama, 332-0012, Japan

^c Research Institute of Electrical Communication, Tohoku University, 2-1-1 Katahira, Aoba-ku, Sendai, 980-8577, Japan

^d Department of Materials Engineering, Graduate School of Engineering, The University of Tokyo, 7-3-1 Hongo, Bunkyo-ku, Tokyo, 113-8656, Japan

^e Photon Factory, Institute of Materials Structure Science, High Energy Accelerator Research Organization, 1-1 Oho, Tsukuba, Ibaraki, 305-0801, Japan

^f Department of Physical Chemistry, Fritz Haber Institute of the Max Plank Society, 14195, Berlin, Germany

^g Synchrotron Radiation Research Organization, The University of Tokyo, 7-3-1 Hongo, Bunkyo-ku, Tokyo, 113-8656, Japan

ARTICLE INFO

Article history:

Received 29 March 2019

Received in revised form

25 May 2019

Accepted 9 June 2019

Available online 11 June 2019

ABSTRACT

The linear band dispersion of graphene's bands near the Fermi level gives rise to its unique electronic properties, such as a giant carrier mobility, and this has triggered extensive research in applications, such as graphene field-effect transistors (GFETs). However, GFETs generally exhibit a device performance much inferior compared to the expected one. This has been attributed to a strong dependence of the electronic properties of graphene on the surrounding interfaces. Here we study the interface between a graphene channel and SiO₂, and by means of photoelectron spectromicroscopy achieve a detailed determination of the course of band alignment at the interface. Our results show that the electronic properties of graphene are modulated by a hydrophilic SiO₂ surface, but not by a hydrophobic one. By combining photoelectron spectromicroscopy with GFET transport property characterization, we demonstrate that the presence of electrical dipoles in the interface, which reflects the SiO₂ surface electrochemistry, determines the GFET device performance. A hysteresis in the resistance vs. gate voltage as a function of polarity is ascribed to a reversal of the dipole layer by the gate voltage. These data pave the way for GFET device optimization.

© 2019 Published by Elsevier Ltd.

1. Introduction

Interfaces of a graphene channel, such as those with gate oxides or contact metals, demand precise and accurate control of electronic level alignment. In graphene, the linear band dispersion near the Fermi level in principle provides excellent intrinsic electronic properties, e.g. an extremely high mobility of carriers, derived from their zero-effective mass. These intrinsic properties make graphene a promising material for next-generation electronics applications, such as graphene-based field-effect transistors (GFETs) and high-electron mobility transistors (HEMTs). At present, however, actual graphene channels used in GFETs actually exhibit transport

properties inferior to those anticipated from the intrinsic electronic properties [1–4]. This inferiority is ascribed to the high susceptibility of the electronic properties of graphene to the surrounding interfaces as well as to technological immaturity in graphene device fabrication. This high susceptibility is also in part due to the linear band dispersion. In conventional semiconductors, the average kinetic energy per electron is $E_K \sim \hbar^2 n_d^{2/d} / 2m^*$ where m^* is the effective mass and n_d is the average electron density in d spatial dimensions. The Coulomb energy per electron is of the order $E_C \sim e^2 n_d^{1/d} / \epsilon_0$ where e is the electron charge. Therefore, the effective coupling constant α_{eff} , which indicates the ratio of Coulomb over kinetic energy and is related to the strength of the electron–electron interactions, is given by $\alpha_{\text{eff}} = E_C / E_K = 2m^* e^2 n_d^{-1/d} / \hbar^2 \epsilon_0$. This depends on carrier density. On the other hand, the average kinetic energy per electron in graphene is of the order $E_K \sim \hbar v_F n^{1/2}$ where v_F is the Fermi–Dirac velocity and n is the

* Corresponding author.

E-mail address: fukidome@riec.tohoku.ac.jp (H. Fukidome).

2D electronic density, owing to its linear dispersion. So, the α_{eff} in 2D graphene is described as $\alpha_{\text{eff}} = E_C/E_K = (e^2/\epsilon_0)/\hbar v_F$. This is independent of the electronic density, but affected by the dielectric constant of the surrounding environment [5–7].

Of the various interfaces, the interface with gate oxides is of particular concern [8,9] because oxide films are the most popular materials for insulating layers in semiconductor devices. The interface between a graphene channel and a gate oxide not only acts as scattering centers for carriers but also causes drastic changes in electronic characteristics of graphene such as e-e interactions described above. Changes in the dielectric constants of gate oxides, such as SiO₂, thus influence the transport properties or in other words, the device performance [10]; for example, depositing ice on a graphene channel enhances carrier mobility in the channel [11]. This is explained by a reduction in α_{eff} by the high dielectric constant of ice. Hence the interface chemistry also influences the transport properties. This is shown by reports that a graphene channel interfaced with hydrophilic SiO₂ exhibits degraded transport properties, such as a reduced carrier mobility and hysteresis in the resistance-gate bias curve in the gate-bias sweep direction, when compared to a channel interfaced with hydrophobic SiO₂ [12,13]. The difference between hydrophobic and hydrophilic SiO₂ lies in the presence of adsorbed water molecules on the latter, which are sandwiched between graphene and hydrophilic SiO₂ [14].

The impact of interface physics and chemistry on graphene channels should thus be fully understood for further development in the GFET technology. Imaging techniques are most useful to extract interface characteristics and microstructures [15–18]. To this end, we have developed a core-level photoelectron spectromicroscopy technology, called “3D nano-ESCA,” where we can scan the sample with a high lateral spatial resolution (70 nm) [19] to record photoelectron spectra (the “third dimension”) to quantitatively analyze electronic level information, such as the Fermi level in graphene, and also chemical states, for example the oxidation valency of SiO₂ at the desired points, from core level line positions [20]. We have demonstrated in our previous reports that 3D nano-ESCA is useful for the microscopic investigation of GFETs [21,22]. In fact, microscopic spatial variations of the potential landscape in a GFET were elucidated by measuring the Fermi level using 3D nano-ESCA. Thus, 3D nano-ESCA is a most suitable tool to analyze electronic states, chemical states and, indirectly, transport properties.

This study describes how SiO₂ surface chemistry, i.e., hydrophilicity vs. hydrophobicity, modulates the electronic states of the graphene channel from a microscopic viewpoint and then compares the influence of states with the transport properties obtained from the macroscopic electrical characteristics of GFETs.

2. Methods

2.1. Sample preparation

Exfoliated graphene was transferred onto SiO₂ thin films (90 nm) on p⁺-Si(100) substrates. The color contrasts in optical images depending on the layer number were emphasized at the graphene sheets on 90 nm SiO₂/Si substrates, so the presence of a mono-layer of graphene was confirmed by the optical contrasts and Raman spectroscopy [23]. To prepare a hydrophobic SiO₂ thin film, we performed the so-called reoxidation process of the SiO₂ thin film by annealing it at 1273 K for 5 min in a 100% oxygen gas flow [13]. This process induces the desorption of H₂O molecules from the surface and produces surface siloxane groups. On the other hand, to prepare hydrophilic SiO₂ thin films, an O₂ plasma treatment with an O₂/Ar mixture (1:9) flow rate of 50 cm³/min was carried out [13].

After the exfoliation of monolayer graphene on the prepared SiO₂ thin films, Ni contact electrodes were prepared by vacuum evaporation, and structured by electron-beam lithography. The post annealing procedure was not adopted, and the measurements for sample characterization were performed on as-fabricated devices.

2.2. Sample characterization

Spatially resolved C 1s, Si 2p, and O 1s core-level photoelectron spectra measurement was carried out using the 3D nano-ESCA instrument installed at the University of Tokyo outstation beamline, BL07LSU at SPring-8 [19,24]. In this beamline, the synchrotron radiation (SR) beam has a high energy-resolving power ($E/\Delta E > 10^4$). The photon energy of the SR beam used for measurements was 1000 eV. The lateral spatial resolution, i.e., the spot size of the X-rays focused using a Fresnel zone plate, was 70 nm. The energy resolution of the spectrometer was set to 300 meV and the accuracy of the angle resolution was 0.9°. The binding energy scale was calibrated using the photoelectron peaks of a gold mesh foil (Au 4f 7/2, binding energy: 84.0 eV) at the same potential as the source electrode, and the Fermi levels detected in valence spectra on Ni electrodes. Details of the experimental setup can be found elsewhere [19,22]. The resistance-gate voltage characteristics were evaluated in ambient air conditions using a semiconductor parameter analyzer (B1500A, Keysight Technologies Inc.).

3. Results and discussion

To quantitatively analyze the impact of SiO₂ surface chemistry on band level alignment, we first demonstrate the applicability of 3D nano-ESCA; we then discuss the influence of interface chemistry between graphene and SiO₂ on the channel performance. In section 3.3, we compare the electronic states with the device performance (e.g., hysteresis), which varies with SiO₂ surface chemistry, and finally in section 3.4, we show that SiO₂ surface chemistry affects the electronic states of graphene near metal contacts as well.

3.1. 3D nano-ESCA imaging of GFET

3D nano-ESCA, as illustrated in Fig. 1(a), is used to analyze the electronic structure of a GFET and to quantitatively clarify the effect of surface chemistry of SiO₂ thin films on the graphene channel. A GFET structure on a 1 cm × 1 cm substrate is mounted on a sample holder as shown in Fig. 1(b). Electrodes, including source, drain, and gate, are connected to the chamber ground. The optical micrograph of the GFET device structure consisting of a graphene flake channel region and contact metal electrodes is shown in the upper picture in Fig. 1(c). The faint shape of the graphene flake is barely visible. On the other hand, highly spatially resolved elemental mapping of the GFET device, where the intensities of the C 1s, Si 2p, and Ni 3p core-level spectra are red, green, and pink, respectively, are shown in the lower picture of Fig. 1(c), which is the same region as the upper one. A sharp image is obtained by using the nano-focused X-ray beam (70 nm) with a Fresnel zone plate [19]. 3D nano-ESCA thus has a high enough lateral spatial resolution to reflect the GFET architecture. As discussed above, hydrophobic SiO₂ thin films deposited on Si(100) substrates were subjected to the so-called reoxidation process, which leads to the surface being covered by siloxane groups (Fig. 1(d)), while the hydrophilic one is covered with silanol groups (Fig. 1(e)) [13,22]. The cross sections of both devices are schematically shown in Fig. 1(d) and (e), respectively.

3.2. Interface chemistry of graphene with SiO₂

The electronic and chemical states at the interfaces of graphene

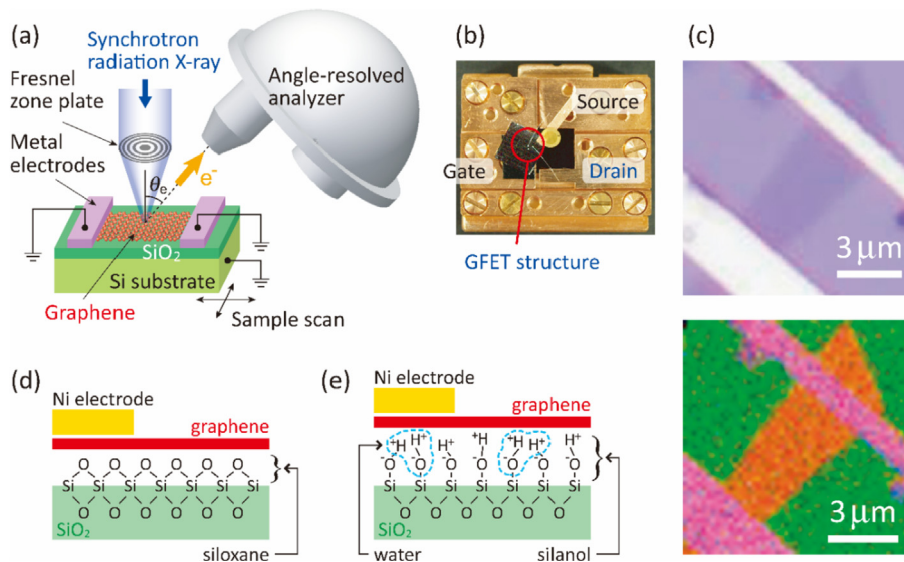


Fig. 1. Schematic of the measurements and graphene-oxide interface in GFET. (a) Schematics of the 3D nano-ESCA imaging system. (b) Photo of a sample holder upon which a GFET device structure on a substrate is mounted. (c) (upper) Optical micrograph of a GFET, barely showing the graphene flake. (lower) Elemental mapping of a GFET using 3D nano-ESCA, where green is the silicon substrate, pink are the nickel contacts, and red the graphene flake. (d, e) Schematic cross-sections of Ni electrodes and graphene on (d) hydrophobic and (e) hydrophilic SiO₂ thin films, respectively, indicative of the chemical composition. (A colour version of this figure can be viewed online.)

channels in GFETs with hydrophobic or hydrophilic SiO₂ films were examined by performing a point-for-point spectroscopic analysis of the C 1s, Si 2p, and O 1s core levels at the center of the graphene channels with 3D nano-ESCA, as shown in Figs. 2 and 3. Along the graphene channels, we used the core-level binding energies to investigate the potential level alignment of graphene on the hydrophobic (blue curves in Figs. 2 and 3) and hydrophilic (red curves in Figs. 2 and 3) SiO₂ thin films on the Si(100) substrates. The C 1s spectrum of graphene on the hydrophobic SiO₂ thin film on Si(100) has a higher binding energy, compared to that on the hydrophilic SiO₂ thin film on Si(100) (Fig. 2(a)). The C 1s spectra can be

decomposed into two components by precisely examining the binding energy, which directly reflects the Fermi level position relative to the Dirac point, of the graphene channels (Fig. 2(b)). The lower binding energy component is attributed to graphene, while the higher binding energy component, which is somewhat broader, is attributed to contaminations probably arising from lithographic processing, according to our previous angle-resolved analysis of the C 1s spectra of GFETs [22]. Although these contaminants could have an influence as p-type dopants and scattering centers in the graphene channels [25], the amount of residual carbon contaminants is almost the same between graphene channels on hydrophilic SiO₂ and hydrophobic SiO₂ according to the intensity of peak components assigned to contaminants in Fig. 2(b), so we assume that the effect of contaminants is the same on the hydrophilic and hydrophobic SiO₂. It is obvious that the peak of graphene on a hydrophilic SiO₂ thin film has a lower binding energy than that on a hydrophobic SiO₂ thin film. This result can be explained by the fact that doping induces a shift in the Fermi level, resulting in a shift in the C 1s binding energy [26], as schematically shown in Fig. 2(c). The binding energy of graphene on a hydrophobic SiO₂ thin film is 284.45 eV, which is very close to that of neutral graphene [27,28]. Graphene on a hydrophobic SiO₂ thin film on Si(100) therefore exhibits negligible doping; on the other hand, it can be inferred from the lower binding energy (284.23 eV) of the C 1s peak that graphene on a hydrophilic SiO₂ thin film is hole-doped. The difference between the spectra is about 0.22 eV. Assuming a linear band dispersion of graphene with respect to the wave vector, we use the following equation to estimate the concentration of doped holes (N_h) as follows [29,30],

$$E_{DP} - E_F = \hbar v_F \sqrt{\pi} \sqrt{N_h} \quad (1)$$

Here, E_F , E_{DP} , \hbar , and v_F are the Fermi level, Dirac point energy, reduced Planck's constant, and the Fermi velocity of electrons in graphene ($\sim 1.1 \times 10^6$ m/s), respectively. Inserting our experimental value of 0.22 eV as the value of ($E_{DP} - E_F$), the concentration of the doped holes (N_h) in graphene on hydrophilic SiO₂ thin films is estimated to be 2.4×10^{12} cm⁻². The SiO₂ surface chemistry thus has a strong influence on the Fermi level position relative to the

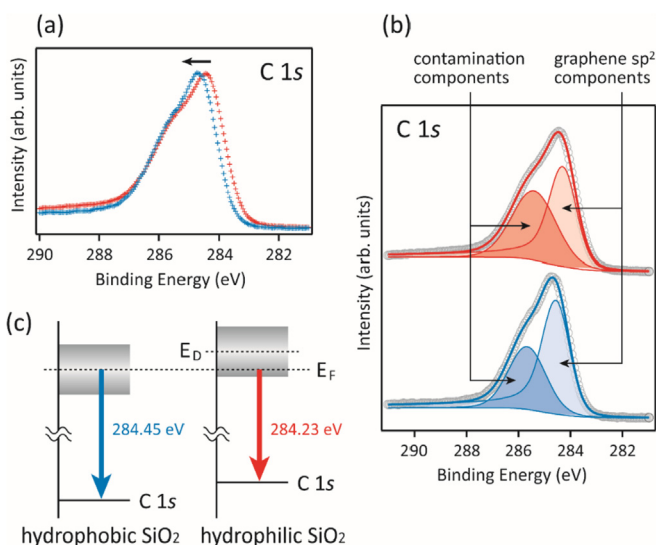


Fig. 2. Electronic states of graphene channels in contact with SiO₂ gate oxides. (a) Pinpoint C 1s core-level spectra recorded at the center of the graphene channels on hydrophobic (blue) and hydrophilic (red) SiO₂ thin films on Si(100) substrates. (b) Decomposition of the spectra displayed in (a). (c) Schematic diagram to explain the peak shift in graphene at different SiO₂ surface conditions. For comparison, the data on hydrophilic SiO₂ thin films was sourced from Ref. [22]. (A colour version of this figure can be viewed online.)

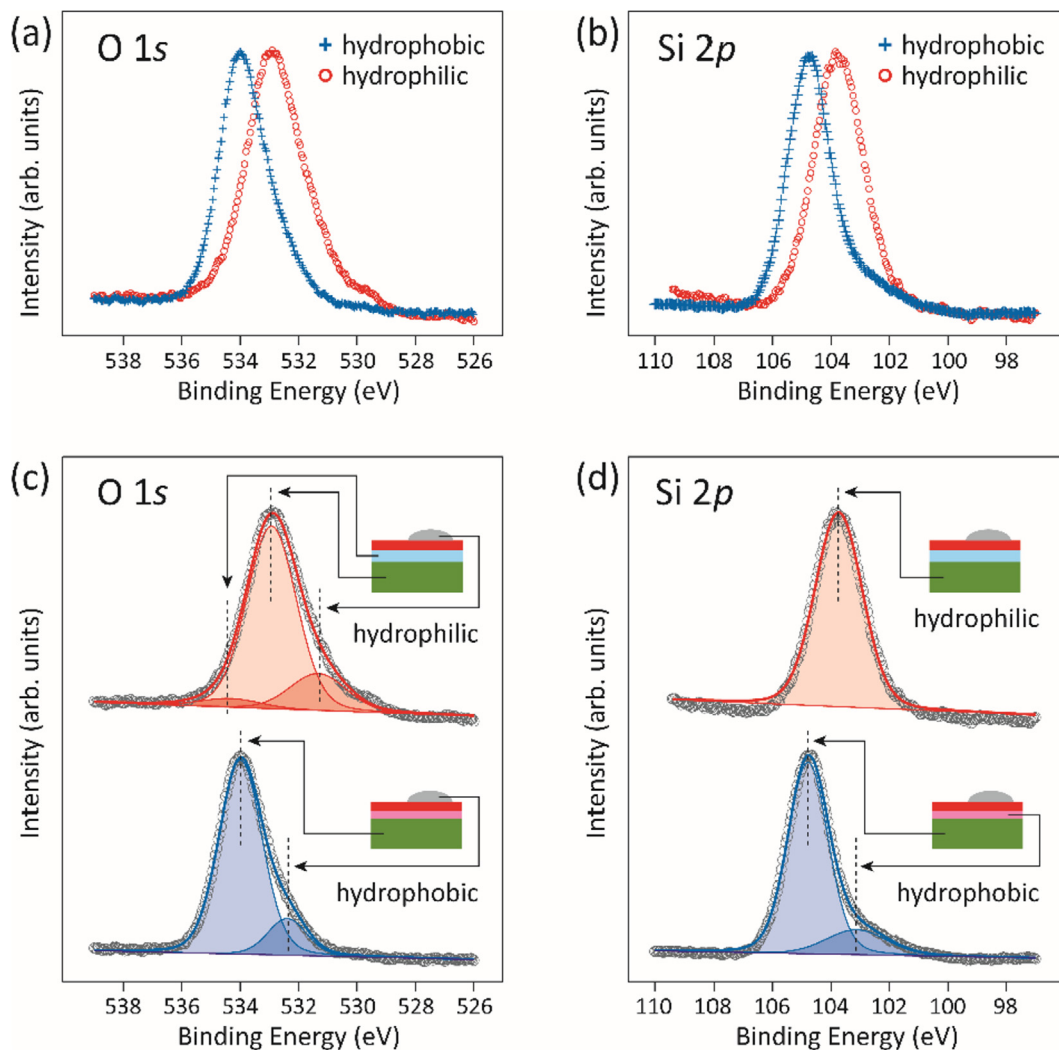


Fig. 3. Electronic and chemical states of the SiO₂-graphene channel interface. (a, b) Si 2p and O 1s core level spectra at the center of the graphene channels on hydrophobic (blue plus sign) and hydrophilic (red circle) SiO₂ thin films on Si(100) substrates, respectively. For comparison, the data of a hydrophilic SiO₂ thin films is sourced from ref. 22. (c, d) Decomposed Si 2p and O 1s spectra, respectively. (A colour version of this figure can be viewed online.)

Dirac point, i.e., the doping strength, in the graphene channel.

In order to investigate the influence of SiO₂ surface chemistry on the electronic states of graphene, pinpoint measurements of the Si 2p and O 1s core lines of the SiO₂ thin films underneath graphene were conducted at the center of the graphene channels, as shown in Fig. 3(a) and (b), respectively, with the decomposition of these core lines shown in Fig. 3(c) and (d). The Si 2p core lines of hydrophobic SiO₂ contain a small shoulder around 103 eV, which is not observed in hydrophilic SiO₂. This shoulder, which occurs at lower binding energies, is ascribed to the surface siloxane, as schematically shown in Fig. 1, which has a lower valency than stoichiometric SiO₂ [31]. This is corroborated by the angle dependence of the peak intensity ratio of the siloxane peak over the bulk SiO₂ peak (Fig. 4(a) and (b)); the results indicate that siloxane is present on the surface. Both the O 1s and Si 2p core lines of the hydrophilic SiO₂ thin film are shifted towards lower binding energies by a considerable amount (~1.2 eV) when compared to the shifts in their counterparts corresponding to the hydrophobic SiO₂ thin film. This means that there is an interfacial layer that affects the binding energies.

We interpret the shift towards lower binding energies as being not of chemical origin, they would be too large anyway, but due to the potential alignment in the GFET device. The difference in

binding energies is very similar (the width of the O 1s peak is slightly different and there is a chemical shift which reveals itself by the presence of a second component in both interfaces). The considerable shift in binding energies can be analyzed using the schematic band diagram of graphene/SiO₂/Si interfaces in GFETs (Fig. 5(a)). In our pinpoint analysis, the graphene channel, metal contacts, and back gate (Si substrate) are grounded, i.e., the applied gate bias (V_G) = 0 V, as shown in Fig. 1(b). The Fermi level then extends through all three materials as a straight line. Band alignment at the Si/SiO₂ interface can be derived from the Fermi level at the Si surface [20]. SiO₂, which has a large bandgap (~9 eV), causes a large potential drop in the Si substrate at the interface, as shown in Fig. 5(a).

A comparison of graphene/hydrophobic SiO₂ and graphene/hydrophilic SiO₂ interfaces, in terms of the binding energies of the core levels and valence band, is shown in Fig. 5(b). Here, the Fermi level of SiO₂ is again aligned with that of graphene. We could detect the graphene, the topmost layer of the SiO₂ thin film under graphene, and the graphene/SiO₂ interface because the probing depth was a few nanometers, considering the escape depth of photoelectrons with a kinetic energy of about 500 (O 1s) and 900 (Si 2p) eV [32] at the incident photon energy 1000 eV. The binding

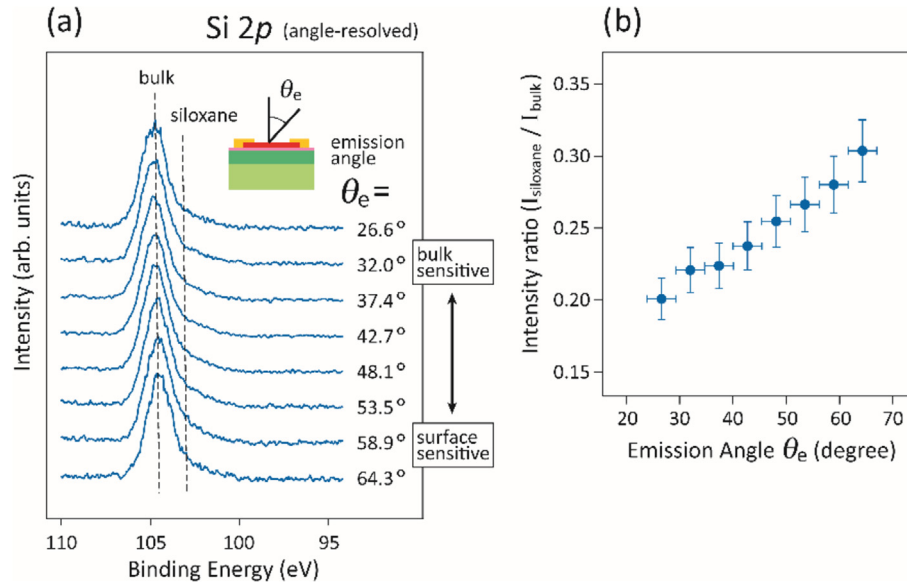


Fig. 4. Emission angle dependence of surface siloxane and bulk SiO_2 . (a) Si 2p core level spectra measured in various emission angles. Photoelectron signal from grazing angle is surface sensitive, and that from near normal angle contains information of buried bulk regions. (b) Emission angle dependence of the intensity ratio between the shoulder peak at 103 eV derived from the surface siloxane and the main peak component at 105 eV derived from the bulk SiO_2 substrate. (A colour version of this figure can be viewed online.)

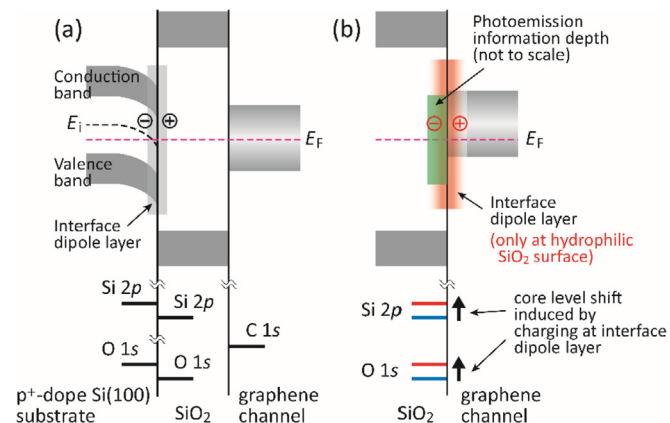


Fig. 5. Schematic band diagrams of interfaces in GFET structures. (a) Schematic band diagram across the GFET. (b) Schematic band diagram of graphene and SiO_2 thin films to demonstrate the influence of SiO_2 surface chemistry. (A colour version of this figure can be viewed online.)

energies of the Si 2p and O 1s core levels thus reflect the changes in valence band alignment with respect to the Fermi level. The point to be noted is the presence or absence of a dipole layer at the graphene/ SiO_2 interface, which depends on the SiO_2 surface chemistry. With respect to the graphene/hydrophilic SiO_2 interface, graphene and SiO_2 are charged positively and negatively, respectively, as can be inferred from the shifts in the C 1s (Fig. 2(a)), Si 2p (Fig. 3(a)), and O 1s core levels (Fig. 3(b)). We attribute the existence of silanol groups on the surface of the hydrophilic SiO_2 thin film to the negative charges on the surface. According to previous theoretical predictions, neither silanol nor siloxane groups cause doping in graphene [33]. While this prediction awaits experimental confirmation, the potential shift due to silanol groups, when in contact with water molecules, may be causing the doping in graphene. In fact, this suggestion is supported by the low value of the acid-dissociation constant (pK_a) of the SiO_2 surface (~ 4.5) [34], which indicates a negative charge by the process of giving up a proton in water, which has a higher value pK_a (pH) of 7. This has

been verified by in-situ electrochemical Fourier transform infrared spectroscopy (FTIR) in combination with quantum chemical calculations, which indicate that negatively charged silanol groups are formed when a SiO_2 surface is in contact with water [35]. Furthermore, our suggestion is supported by previous theoretical studies pointing out the role of water in the doping of graphene on substrates such as SiO_2 [36,37]. The dipole layer thus consists of positively-charged graphene and a negatively-charged hydrophilic SiO_2 thin film, resulting in a potential drop in the layer, as shown in Fig. 5(b). The potential drop shifts the energy position of the Si 2p and O 1s core lines upwards relative to the Fermi level. In the case of the hydrophobic SiO_2 thin film, no dipole layer is present at the interface, hence graphene is not doped, (see Fig. 2), when the surface of the hydrophobic SiO_2 thin film is covered with uncharged siloxane groups. A negligible dipole layer is then formed at the interface. This results in a negligible potential drop, as expressed by the straight line across the interface (Fig. 5(b)). Thus, pinpoint core level spectroscopy demonstrates that the SiO_2 surface chemistry has a great impact on the interfacial electronic level alignment between graphene and SiO_2 .

3.3. Influence of SiO_2 surface chemistry on GFET electrical characteristics

The above difference in level alignment in graphene on a hydrophilic or hydrophobic SiO_2 substrate is expected to have a strong influence on GFET electrical characteristics as well [12,13], because the electronic states of the graphene channel determine the GFET electrical characteristics. Therefore, we compared the resistance (R)-gate voltage (V_G) curves of GFETs using hydrophobic and hydrophilic SiO_2 thin films as the gate oxides, as shown in Fig. 6(a). In the GFETs, Ni thin films and $\text{p}^+\text{-Si}(100)$ substrates are used as the source/drain electrodes and back gate, respectively. The most striking feature in these curves is the large hysteresis found in the R - V_G curve of the GFET using a hydrophilic SiO_2 thin film as the gate oxide, but not in the GFET using hydrophobic SiO_2 [12,13]. The curves for forward and backward sweep on hydrophobic SiO_2 are identical and are thus not resolved in Fig. 6(a). Such hysteresis, which is reproduced over many consecutive sweeps [13], indicates

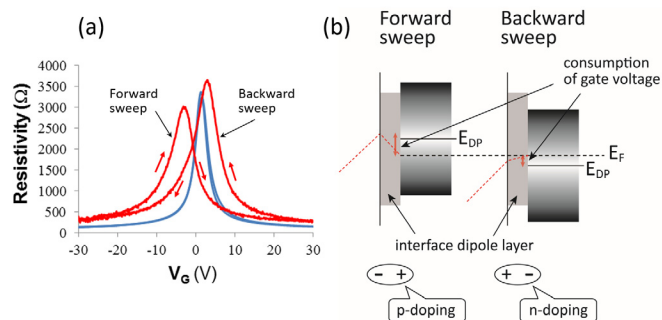


Fig. 6. Influence of SiO₂ surface chemistry on GFET electrical characteristics. (a) R - V_G curves of the GFETs using hydrophobic (blue) and hydrophilic (red) SiO₂ thin films on Si(100) substrates. (It should be explained in the Figure which of the red curves is forward and backward) No hysteresis occurs in graphene on hydrophobic SiO₂, hence the forward and backward sweep coincide. (b) Schematic diagram explaining the mechanism behind the hysteresis of the R - V_G curve; the interface dipole layer plays a crucial role. (A colour version of this figure can be viewed online.)

that the doping type changes with a change in the direction of the gate voltage sweep. Because the dipole layer induces a difference in the level alignment between the two GFETs (Fig. 5(b)), it is obvious that the dipole layer formed between graphene and the hydrophilic SiO₂ thin film affects the doping level of the graphene channel, as schematically shown in Fig. 6(b). What we observe here is that the reversal of gate voltage inverts the polarity of the dipole layer, which arises from the polarity inversion of the charging states of graphene and the hydrophilic SiO₂ surface. As an aside we note that the consumption of gate voltage by the dipole layer (Fig. 6(b)) can cause a broadening in the width of the R - V_G curve of the GFET with hydrophilic SiO₂ rather than hydrophobic SiO₂ [38]. This is because the effective gate capacitance C increases by the dipole layer in the formula [39] which represents the graphene resistance R ;

$$R = \frac{L}{w} \times \frac{1}{e\mu\sqrt{n_0^2 + (C|V_G - V_D|)^2}} + R_C \quad (2)$$

where L/w is the aspect ratio of the transistor, μ is the mobility, n_0 is the residual charge, and R_C is the constant background resistance.

The next thing to be discussed is the comparison of Dirac voltages of the GFETs, where the resistivity (R) is the highest and the Fermi level is considered to coincide with the Dirac point, by relating the results obtained by 3D nano-ESCA, as described in the previous subsection. To relate with the 3D nano-ESCA measurements, we used the R - V_G curve in the forward sweep for the GFET using a hydrophilic SiO₂ thin film. The reason for this choice is as follows. The R - V_G curves were measured by sweeping V_G from -30 V to $+30$ V (forward sweep) and later from $+30$ V to -30 V (backward sweep); it was stopped at -30 V, after which 3D nano-ESCA measurements at $V_G = 0$ V were carried out. Therefore, these measurements can be regarded to occur during a forward sweep. The Dirac voltage of the GFET using a hydrophilic SiO₂ thin film in the forward sweep is more positive than that recorded using a hydrophobic SiO₂ thin film. This indicates the graphene channel in the GFET using a hydrophilic SiO₂ thin film in the forward sweep is more hole-doped than that using a hydrophobic SiO₂ thin film. This result is consistent with the pinpoint C 1s core level spectra of the graphene channel, which indicate the binding energy shift toward lower energy on a hydrophobic SiO₂ thin film due to hole doping as shown in Fig. 2, although we must consider adsorbed molecules other than water, such as O₂, during the R - V_G measurements [12,14]. These changes in the R - V_G curves are thus explained by the modulation in the electronic states of graphene

channels in terms of their interface chemistry with SiO₂ gate oxides, which was described in the previous subsection as demonstrated through 3D nano-ESCA.

3.4. Influence of SiO₂ surface chemistry near the metal contact

Surprisingly, SiO₂ surface chemistry also exerts an influence on the electronic states near the interface with the metal contact, which is also a key component in GFET. One of the consequences of such metal-contact influence is the formation of a charge transfer region (CTR) [13,40], which can extend up to a width of 1 μ m in the GFET using hydrophilic SiO₂ as the gate oxide [22]. The CTR is supposed to be formed due to the disappearance of the density of states (DOS) near the Dirac point in graphene. Unfortunately, however, the influence of SiO₂ surface chemistry on the CTR is still unclear.

To clarify the influence of SiO₂ surface chemistry on the electronic states of the graphene channel near the interface between graphene and contact metal, we performed spatially resolved C 1s core level spectroscopy near the metal contact using 3D nano-ESCA. The spatial variation in the binding energy of graphene, which reflects the change in doping (work function), on hydrophilic and hydrophobic SiO₂ thin films is shown in Fig. 7. It can be inferred that across the entire measured range, the binding energy of graphene on a hydrophilic SiO₂ thin film is smaller than that on a hydrophobic SiO₂ thin film. This means that graphene on a hydrophilic SiO₂ thin film is more positively charged, compared to that on a hydrophobic SiO₂ thin film. The value of binding energy (~ 284.45 eV), which is very close to that of neutral graphene [27], indicates that the graphene channel is negligibly doped when a hydrophobic SiO₂ thin film was used, in agreement with the data in Fig. 2.

In sharp contrast to the hydrophobic SiO₂ thin film, the binding energy of graphene on hydrophilic SiO₂ becomes smaller near the contact metal as shown in Fig. 7. The binding energy shift originates from local charge density as shown in Fig. 2(c), so the results which display the spatial distribution of the binding energy shift in Fig. 7 can be interpreted as a direct measurement of the screening

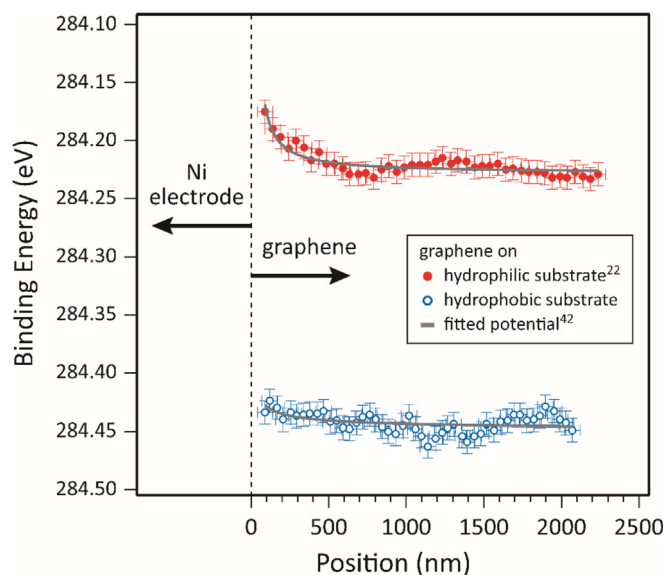


Fig. 7. Influence of SiO₂ surface chemistry on the potential variation across the graphene-contact metal interface. Change in the C1s core level of graphene peak across the graphene/Ni interface in GFETs using hydrophilic (red) and hydrophobic (blue) SiO₂ thin films as the gate oxides. For comparison, data on hydrophilic SiO₂ thin films is sourced from ref. 22. (A colour version of this figure can be viewed online.)

potential in graphene. Sub-micron CTR formation is detected in the graphene channel on the hydrophilic substrate, as reported in previous studies [22]. The determining factor in CTR formation is, in principle, supposed to be the charge transfer between materials of different work functions [13], 4.5 eV for graphene and 5.4 eV for Ni [41], which thermodynamically equilibrate the graphene/Ni system [22].

To explain the difference in the screening potential of the hydrophilic and hydrophobic substrates, we performed theoretical estimations of the screening potential according to the Thomas-Fermi approach proposed by Khomyakov et al. [42]. For a single layer of graphene, they described the screening potential in terms of the charge density in an ungated condition as follows

$$V(x) = \mu_F + \text{sign}(\sigma) \sqrt{\left| \frac{V_B |V_B|}{x/l_s} - \mu_F |\mu_F| \right|} \quad (3)$$

where x is the distance from the metal/graphene contact edge, $l_s = \hbar v / \pi \alpha |V_B|$ is a scaling length, $V_B = V_{B1} + V_{B2}$, $\hbar v = 6.05 \text{ eV} \cdot \text{\AA}$, and $\alpha = e^2 / 4\pi \epsilon_0 \kappa \hbar v = 2.38 / \kappa$ is the fine-structure constant in graphene. κ is the effective dielectric constant. V_{B1} and V_{B2} are boundary potential constants, which can be written as

$$V_{B1} = \frac{1}{4}(W - W_G), \quad V_{B2} = \frac{\pi}{4}(W_M - W_G) \quad (4)$$

where W_G is the work function of free-standing graphene (4.5 eV), W_M is the work function of the contact metal layer (5.4 eV; Ni in this case), and W is the work function of the graphene-covered metal. The parameter β depends on the contact geometry and $\beta = \pi$ when a distance x is large enough compared to d , a thickness of the contact metal ($x \gg d$), where $d \sim 25 \text{ nm}$ in this case. W was evaluated using density functional theory (DFT) calculations [43]. In the case of graphene on Ni(111), the conical dispersion in the graphene band is destroyed by strong graphene-metal bonding interactions [44]. However, in our process, the resistant residue prevents chemisorption between graphene and the Ni contact. Later, we can refer the value of an Au contact, which shows physisorption with graphene, and has a work function ($\sim 5.4 \text{ eV}$) similar to that of a Ni contact. For large graphene-metal separations due to resistant residues, $W - W_G \sim 0.4$ [43]. Subsequently, we obtained $\kappa \sim 1.8 \pm 0.9$ for graphene on a hydrophobic substrate and $\kappa \sim 77 \pm 4$ for graphene on a hydrophilic substrate¹ by curve fitting to the measured points in Fig. 7 using eq. (3) with $V_B \sim 0.325$. If we can neglect polarization effects at the graphene channel, the effective dielectric constant κ is given by the average of the dielectric constant of SiO_2 ($\sim 3.9 \text{ eV}$) and that of the vacuum due to the image effect [5], i.e., $\kappa \sim 2.5$. This value is close to the experimentally obtained value on the hydrophobic substrate. The large value of κ on the hydrophilic substrate is due to the polarization of the water layer, which has a large dielectric constant at the graphene/substrate interface. Lacking spatial resolution, the interface dipole layer, of the order of several nanometers, cannot be detected in our system. However, the screening potential changes moderately at large values of κ and we can detect spatial shifts in the screening potential by 3D nano-ESCA with a spatial resolution of $\sim 100 \text{ nm}$. Therefore, the difference in the potential variation between the hydrophilic and hydrophobic substrates is

¹ The estimated value of the effective dielectric constant, κ , is different from our previous study in ref. 22 because we adopted the undoped limit of Eq. (3) as a rough approximation. However, our argument that κ shows larger value on a hydrophilic substrate than typical value of graphene's κ (~ 2.5) is consistent. The chemical potential μ_F , in other words, the doping level of the graphene on the hydrophilic substrate is evaluated compared to the hydrophobic case in this study, so now we can use Eq. (3), which is more general fitting function than a previous study.

caused by the difference in the effective dielectric constants, rather than the presence/absence of CTR. Although further theoretical investigation with quantum chemistry is required, we believe that the positive charging of graphene due to interactions with a hydrophilic SiO_2 thin film may assist graphene-Ni interactions, which in turn increases the amount of hole-doping in graphene near Ni, assuming that charge transfer occurs through bonding between graphene and Ni in the wide region which is larger than an interfacial dipole layer region.

4. Conclusions

In summary, a combination of 3D nano-ESCA and device characteristics enabled us to quantitatively elucidate that SiO_2 surface chemistry as well as the metal contacts determine the electronic states of graphene channels and consequently, the GFET device performance. By using samples in a device geometry and layer arrangement, we observe a gate voltage induced reversal of the interface dipole orientation. The results obtained will serve as the basis for a quantitative understanding of the GFET operation mechanism, which will help in the realization of high-performance graphene-based devices.

Acknowledgments

This work was supported by Japan ministry of internal affairs and communications for SCOPE (1816-2004), the Japan Society for the Promotion of Science through its "Funding Program for World-Leading Innovative R&D on Science and Technology (FIRST Program)" and "Grant-in-Aid for Scientific Research B (Grant Number: 15H03560 and 15K17463)," "Grant-in-Aid for Scientific Research S (Grant Number: 16H06361)," "the Ministry of Education, Culture, Sports, Science and Technology through its "Grant-in-Aid for Scientific Research on Innovative Areas (Grant Number: 26107503)," Japan Science and Technology Agency through its "Core Research for Evolutional Science and Technology," and "Materials Research by Information Integration" Initiative project and PRESTO (Grant Number: JPMJPR17NB), and the Research Program for CORE lab of "Dynamic Alliance for Open Innovation Bridging Human, Environment and Materials" in "Net-work Joint Research Center for Materials and Devices." This work was performed at the Synchrotron Radiation Research Organization, University of Tokyo (Proposal Nos. 7402 for 2009–2011, 7418 for 2011, 7435 for 2012, and 7419 for 2012–2014).

References

- [1] A. Geim, K. Novoselov, The rise of graphene, *Nat. Mater.* 6 (2007) 183–191.
- [2] S. Fratini, F. Guinea, Substrate-limited electron dynamics in graphene, *Phys. Rev. B* 77 (2008), 195415(1–6).
- [3] J.H. Chen, C. Jang, S. Xiao, M. Ishigami, M.S. Fuhrer, Intrinsic and extrinsic performance limits of graphene devices on SiO_2 , *Nat. Nanotechnol.* 3 (2008) 206–209.
- [4] K. Nagashio, T. Nishimura, K. Kita, A. Toriumi, Metal/graphene contact as a performance killer of ultra-high mobility graphene - analysis of intrinsic mobility and contact resistance, in: IEEE International Electron Devices Meeting IEDM 2009, Baltimore, (Maryland, USA), 2009 p.23.2.1–4.
- [5] T. Ando, Screening effect and impurity scattering in monolayer graphene, *J. Phys. Soc. Jpn.* 75 (2006), 074716(1–7).
- [6] K. Nomura, A.H. MacDonald, Quantum Hall ferromagnetism in graphene, *Phys. Rev. Lett.* 96 (2006), 256602(1–7).
- [7] V.N. Kotov, B. Uchoa, V.M. Pereira, F. Guinea, A.C. Neto, Electron-electron interactions in graphene: current status and perspectives, *Rev. Mod. Phys.* 84 (2012) 1067–1125.
- [8] C. Hwang, D.A. Siegel, S.K. Mo, W. Regan, A. Ismach, Y. Zhange, A. Zettl, A. Lanzara, Fermi velocity engineering in graphene by substrate modification, *Sci. Rep.* 2 (2012), 590(1–4).
- [9] C.R. Dean, A.F. Young, I. Meric, C. Lee, L. Wang, S. Sorgenfrei, K. Watanabe, T. Taniguchi, P. Kim, K.L. Shepard, J. Hone, Boron nitride substrates for high-quality graphene electronics, *Nat. Nanotechnol.* 5 (2010) 722–726.

- [10] T. Ando, A.B. Fowler, F. Stern, Electronic properties of two-dimensional systems, *Rev. Mod. Phys.* 54 (1982) 437–672.
- [11] C. Jang, S. Adam, E.D. Williams, S.D. Sarma, M.S. Fuhrer, Tuning the effective fine structure constant in graphene: opposing effects of dielectric screening on short- and long-range potential scattering, *Phys. Rev. Lett.* 101 (2008), 146805(1–4).
- [12] M. Lafkioti, B. Krauss, T. Lohmann, U. Zschieschang, H. Klauk, K.V. Klitzing, J.H. Smet, Graphene on a hydrophobic substrate: doping reduction and hysteresis suppression under ambient conditions, *Nano Lett.* 10 (2010) 1149–1153.
- [13] K. Nagashio, T. Yamashita, T. Nishimura, K. Kita, A. Toriumi, Electrical transport properties of graphene on SiO₂ with specific surface structures, *J. Appl. Phys.* 110 (2011), 024513(1–6).
- [14] S. Ryu, L. Liu, S. Berciaud, Y.J. Yu, H. Liu, P. Kim, G.W. Flynn, L.E. Brus, Atmospheric oxygen binding and hole doping in deformed graphene on a SiO₂ substrate, *Nano Lett.* 10 (2010) 4944–4951.
- [15] H. Fukidome, M. Kotsugi, K. Nagashio, R. Sato, T. Ohkochi, T. Itoh, A. Toriumi, M. Suemitsu, T. Kinoshita, Orbital-specific tunability of many-body effects in bilayer graphene by gate bias and metal contact, *Sci. Rep.* 4 (2014), 3713(1–5).
- [16] E.J. Lee, K. Balasubramanian, R.T. Weitz, M. Burghard, K. Kern, Contact and edge effects in graphene devices, *Nat. Nanotechnol.* 3 (2008) 486–490.
- [17] T. Mueller, F. Xia, M. Freitag, J. Tsang, P. Avouris, Role of contacts in graphene transistors: a scanning photocurrent study, *Phys. Rev. B* 79 (2009), 245430(1–6).
- [18] R. Jalilian, L.A. Jauregui, G. Lopez, J. Tian, C. Roecker, M.M. Yazdanpanah, R.W. Cohn, I. Jovanovic, Y.P. Chen, Scanning gate microscopy on graphene: charge inhomogeneity and extrinsic doping, *Nanotechnology* 22 (2011), 295705(1–9).
- [19] K. Horiba, Y. Nakamura, N. Nagamura, S. Toyoda, H. Kumigashira, M. Oshima, K. Amemiya, Y. Senba, H. Ohashi, Scanning photoelectron microscope for nanoscale three-dimensional spatial-resolved electron spectroscopy for chemical analysis, *Rev. Sci. Instrum.* 82 (2011), 113701(1–6).
- [20] F.J. Himpsel, F.R. McFeely, A. Taleb-Ibrahimi, J.A. Yarmoff, Microscopic structure of the SiO₂/Si interface, *Phys. Rev. B* 38 (1988) 6084–6096.
- [21] H. Fukidome, K. Nagashio, N. Nagamura, K. Tashima, K. Funakubo, K. Horiba, M. Suemitsu, A. Toriumi, M. Oshima, Pinpoint operando analysis of the electronic states of a graphene transistor using photoelectron nanospectroscopy, *APEX* 7 (2014), 065101(1–4).
- [22] N. Nagamura, K. Horiba, S. Toyoda, S. Kurosumi, T. Shinohara, M. Oshima, H. Fukidome, K. Nagashio, A. Toriumi, Direct observation of charge transfer region at interfaces in graphene devices, *Appl. Phys. Lett.* 102 (2013), 241604(1–5).
- [23] K. Nagashio, T. Nishimura, K. Kita, A. Toriumi, Mobility variations in mono- and multi-layer graphene film, *APEX* 2 (2009), 025003(1–3).
- [24] S. Yamamoto, Y. Senba, T. Tanaka, H. Ohashi, T. Hirono, H. Kimura, M. Fujisawa, J. Miyawaki, A. Hasarawa, T. Seike, S. Takahashi, N. Nariyama, T. Matsushita, M. Takeuchi, T. Ohata, Y. Furukawa, K. Takeshita, S. Goto, Y. Harada, S. Shin, H. Kitamura, A. Kakizaki, M. Oshima, I. Matsuda, New soft X-ray beamline BL07LSU at SPring-8, *J. Synchrotron Radiat.* 21 (2014) 352–365.
- [25] A. Pirkle, J. Chan, A. Venugopal, D. Hinojos, C.W. Magnuson, S. McDonnell, L. Colombo, E.M. Vogel, R.S. Ruoff, R.M. Wallace, The effect of chemical residues on the physical and electrical properties of chemical vapor deposited graphene transferred to SiO₂, *Appl. Phys. Lett.* 99 (2011), 122108(1–3).
- [26] M. Copuroglu, P. Aydogan, E.O. Polat, C. Kocabas, S. Sützer, Gate-tunable photoemission from graphene transistors, *Nano Lett.* 14 (2014) 2837–2842.
- [27] M. Scardamaglia, B. Aleman, M. Amati, C. Ewels, P. Pochet, N. Reckinger, J.F. Colomer, T. Skaltsas, N. Tagmatarchis, R. Snyders, L. Gregoratti, C. Bittencourt, Nitrogen implantation of suspended graphene flakes: annealing effects and selectivity of sp² nitrogen species, *Carbon* 73 (2014) 371–381.
- [28] C. Riedi, C. Coletti, T. Iwasaki, A.A. Zakharov, U. Starke, Quasi-free-standing epitaxial graphene on SiC obtained by hydrogen intercalation, *Phys. Rev. Lett.* 103 (2009), 246804(1–4).
- [29] K.V. Novoselov, A.K. Geim, S.V. Morozov, D. Jiang, M.I. Katnelson, I. Grigorieva, S. Dubonos, A.A. Firsov, Two-dimensional gas of massless Dirac fermions in graphene, *Nature* 438 (2005) 197–200.
- [30] S.D. Sarma, S. Adam, E.H. Hwang, E. Rossi, Electronic transport in two-dimensional graphene, *Rev. Mod. Phys.* 83 (2011) 407–470.
- [31] L.A. O'Hare, A. Hynes, M.R. Alexander, A methodology for curve-fitting of the XPS Si 2p core level from thin siloxane coatings, *Surf. Interface Anal.* 39 (2007) 926–936.
- [32] S. Hüfner, *Photoelectron Spectroscopy*, Springer-Verlag, Berlin Heidelberg, 2003.
- [33] C.J. Yang, S.J. Huang, C.L. Kuo, The electronic property of graphene adsorbed on the siloxane and silanol surface structures of SiO₂: a theoretical prediction, *Appl. Phys. Lett.* 101 (2012), 253107(1–5).
- [34] K. Leung, I.M. Nielsen, L.J. Criscenti, Elucidating the bimodal acid-base behaviour of the water-silica interface from first principles, *J. Am. Chem. Soc.* 131 (2009) 18358–18365.
- [35] H. Fukidome, O. Pluchery, K.T. Queeney, Y. Caudano, K. Raghavachari, M.K. Weldon, E.E. Chaban, S.B. Christman, H. Kobayashi, Y.J. Chabal, In situ vibrational study of SiO₂/liquid interfaces, *Surf. Sci.* 502 (2002) 498–502.
- [36] T.O. Wehling, M.I. Katnelson, A.I. Lichtenstein, Adsorbates on graphene: impurity states and electron scattering, *Chem. Phys. Lett.* 476 (2009) 125–134.
- [37] T.O. Wehling, A.I. Lichtenstein, M.I. Katnelson, First-principles studies of water adsorption on graphene: the role of the substrate, *Appl. Phys. Lett.* 93 (2008), 202110(1–3).
- [38] A.K.M. Newaz, Y.S. Puzyrev, B. Wang, S.T. Pantelides, K.I. Bolotin, Probing charge scattering mechanisms in suspended graphene by varying its dielectric environment, *Nat. Commun.* 3 (2012), 734(1–6).
- [39] L. Bours, S. Guiducci, M-Kolasinski A, B. Szafran, J.C. Maan, S. Heun, Manipulating quantum Hall edge channels in graphene through scanning gate microscopy, *Phys. Rev. B* 96 (2017), 195423(1–10).
- [40] R. Nouchi, K. Tanigaki, Competitive interfacial charge transfer to graphene from the electrode contacts and surface adsorbates, *Appl. Phys. Lett.* 106 (2015), 083107(1–5).
- [41] G. Giovannetti, P.A. Khomyakov, G. Brocks, V.V. Karpan, J. van den Brink, P.J. Kelly, Doping graphene with metal contacts, *Phys. Rev. Lett.* 101 (2008), 026803(1–4).
- [42] P.A. Khomyakov, A.A. Starikov, G. Brocks, P.J. Kelly, Nonlinear screening of charges induced in graphene by metal contacts, *Phys. Rev. B* 82 (2010), 115437(1–6).
- [43] P.A. Khomyakov, G. Giovannetti, P.C. Rusu, G. Brocks, J. van den Brink, P.J. Kelly, First-principles study of the interaction and charge transfer between graphene and metals, *Phys. Rev. B* 79 (2009), 195425(1–12).
- [44] Y.S. Dedkov, A.M. Shikin, V.K. Adamchuk, S.L. Molodtsov, C. Laubschat, A. Bauer, G. Kaindl, Intercalation of copper underneath a monolayer of graphite on Ni(111), *Phys. Rev. B* 64 (2001), 035405(1–6).



Spectrum adapted expectation-maximization algorithm for high-throughput peak shift analysis

Tarojiro Matsumura, Naoka Nagamura, Shotaro Akaho, Kenji Nagata & Yasunobu Ando

To cite this article: Tarojiro Matsumura, Naoka Nagamura, Shotaro Akaho, Kenji Nagata & Yasunobu Ando (2019) Spectrum adapted expectation-maximization algorithm for high-throughput peak shift analysis, Science and Technology of Advanced Materials, 20:1, 733-745, DOI: [10.1080/14686996.2019.1620123](https://doi.org/10.1080/14686996.2019.1620123)

To link to this article: <https://doi.org/10.1080/14686996.2019.1620123>



© 2019 The Author(s). Published by National Institute for Materials Science in partnership with Taylor & Francis Group.



Accepted author version posted online: 20 May 2019.
Published online: 27 Jun 2019.



Submit your article to this journal [↗](#)



Article views: 566



View Crossmark data [↗](#)

Spectrum adapted expectation-maximization algorithm for high-throughput peak shift analysis

Tarojiro Matsumura^a, Naoka Nagamura^{b,c}, Shotaro Akaho^d, Kenji Nagata^{c,d} and Yasunobu Ando^a

^aResearch Center for Computational Design of Advanced Functional Materials (CD-FMat), National Institute of Advanced Industrial Science and Technology, Tsukuba, Japan;

^bResearch Center for Advanced Measurement and Characterization, National Institute for Materials Science (NIMS), Tsukuba, Japan;

^cJapan Science and Technology Agency, PRESTO, Saitama, Japan;

^dArtificial Intelligence Research Center (AIRC), National Institute of Advanced Industrial Science and Technology, Tokyo, Japan

ABSTRACT

We introduce a spectrum-adapted expectation-maximization (EM) algorithm for high-throughput analysis of a large number of spectral datasets by considering the weight of the intensity corresponding to the measurement energy steps. Proposed method was applied to synthetic data in order to evaluate the performance of the analysis accuracy and calculation time. Moreover, the proposed method was performed to the spectral data collected from graphene and MoS₂ field-effect transistors devices. The calculation completed in less than 13.4 s per set and successfully detected systematic peak shifts of the C 1s in graphene and S 2p in MoS₂ peaks. This result suggests that the proposed method can support the investigation of peak shift with two advantages: (1) a large amount of data can be processed at high speed; and (2) stable and automatic calculation can be easily performed.

ARTICLE HISTORY

Received 19 November 2018

Revised 14 May 2019

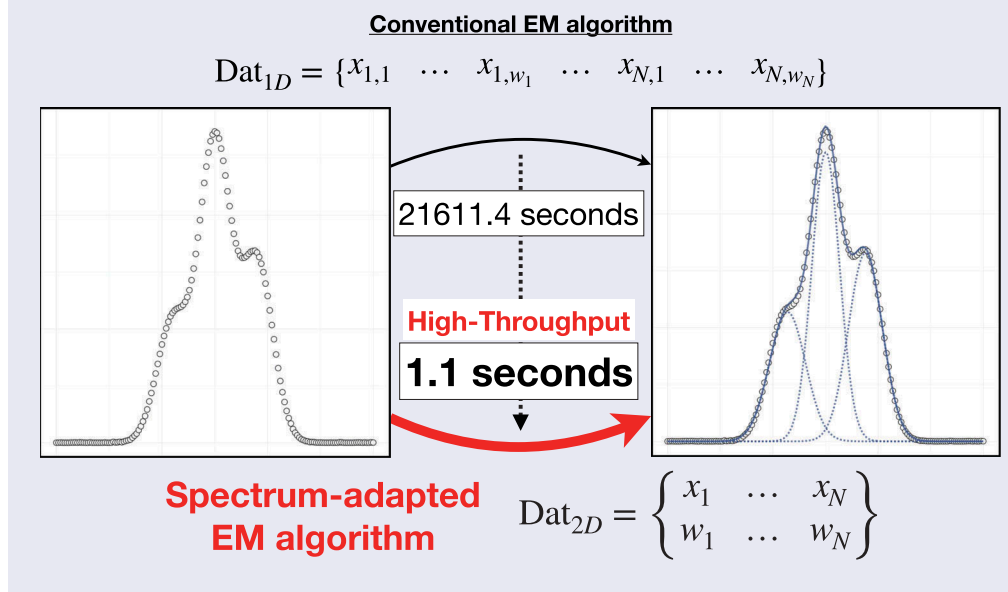
Accepted 14 May 2019

KEYWORDS

EM algorithm; peak separation; spectral data; XPS analysis; machine learning

CLASSIFICATION


60 New topics / Others; 502 Electron spectroscopy



1. Introduction

Interpretation of spectral data is essential in spectroscopy measurements for investigating electronic properties of new materials and devices [e.g. 1–4]. In the case of X-ray photoelectron spectroscopy (XPS), as researchers generally adopt suitable parameters of fitting curves according to previous reports and their experiences, peak assignment of core-level spectra in compounds strongly resorts to the manual trial and error. This procedure surely affects the efficiency of the spectral data analysis.

The method of spectral data analysis using machine learning technique has been studied to improve the resorting to the manual trial and error [5–11]. For example, Nagata et al. [7] proposed a Bayesian peak separation with the exchange Monte Carlo method [12] and estimated an appropriate number of peaks while avoiding parameter solutions trapped into local minima. The effectiveness of this method was practically demonstrated in the analysis of synthetic data and reflectance spectral data for olivine. Murata et al. [9] extended this method [7]

CONTACT Yasunobu Ando  yasunobu.ando@aist.go.jp

This article has been republished with minor changes. These changes do not impact the academic content of the article.

© 2019 The Author(s). Published by National Institute for Materials Science in partnership with Taylor & Francis Group.

This is an Open Access article distributed under the terms of the Creative Commons Attribution-NonCommercial License (<http://creativecommons.org/licenses/by-nc/4.0/>), which permits unrestricted non-commercial use, distribution, and reproduction in any medium, provided the original work is properly cited.

to time-series spectral dataset, and a highly accurate analysis was demonstrated to extract latent dynamics in the dataset. Moreover, Shiga et al. [10] proposed a new non-negative matrix factorization (NMF) technique to analyze spectral imaging data, namely electron energy-loss/energy-dispersive X-ray spectral datasets from a specified region of interest at an arbitrary step width. This technique has helped to resolve problems associated with previous NMF techniques, such as the calculation not always converging and the number of separated peaks being specified by the manual trial and error.

Little attention has been paid to the computational cost because the number of datasets is not so large in conventional spectroscopy measurements. Recently, as extremely high brilliant quantum beams such as synchrotron radiation (SR) X-rays, X-ray free electron lasers, and neutron beams are available for probes of spectroscopy, researchers can perform various kinds of high-resolution analysis (e.g. pump-probe method with sub-10 fs time resolution and imaging microscopy with spatial resolution of nm order) [see 1–4]. Such advanced spectroscopy measurements potentially produce huge number of datasets, and then the computational cost has become a serious problem in the spectral data analysis.

Developing an efficient method for the spectral data analysis is an urgent issue in the multi-dimensional measurements. For example, operando SR X-ray scanning photoelectron microscopy system, called ‘3D nano-ESCA’ (three-dimensional nanoscale electron spectroscopy for chemical analysis) [13], provides spatial, time and electric field dependence of photoemission spectra. Incident SR X-rays are focused by a Fresnel zone plate, and the photoemission spectra are obtained at the beam spot (~70 nm) on a sample. As a sample is scanned on a piezo-driven stage, high spatial resolution XPS analysis can be conducted during device operation by a bias voltage applying circuit induced in sample stage (i.e. operando analysis [14,15]). XPS analysis of core-level spectra typically means peak fitting and assignment of decomposed peak components determined by the chemical shifts that takes a particular value depending on a local chemical environment of a specific element. In contrast, the 3D nano-ESCA system also carries out the potential mapping of microstructures in operating devices by observing the spatial distribution of the core level peak shift. In other words, ‘the electric potential shift’ reflects the change of the vacuum level, the Fermi energy, and the local carrier density, and the value of the electric potential shift dynamically fluctuates, unlike the chemical shift. However, the 3D nano-ESCA has been performed only for the pinpoint or line-scan analysis that deals with few tens of spectral datasets by the inefficiency of peak fitting procedure, although spatial and time-

resolved measurement potentially provides over thousands of the datasets.

In this paper, we adapted an expectation-maximization (EM) algorithm for the spectral data to investigate the peak shift by the peak fitting and assignment of decomposed peak components. We derived the spectrum-adapted EM algorithm and demonstrated this method to the synthetic and experimental data. In the synthetic data analysis, we evaluated the performances of the analysis accuracy and calculation cost of the proposed method depending on the initialization procedure and compared the performances of the proposed method with those of the exchange Monte Carlo method, and Newton’s method. In the experimental data analysis, the proposed method was applied to the datasets that were collected previously from graphene [14,16] and MoS₂ [17] field-effect transistors (FETs) by 3D nano-ESCA.

2. EM algorithm adapted for the high-throughput peak separation

The EM algorithm is one of the machine learning techniques for estimating the parameters of the mixture model (i.e., Gaussian mixture model, GMM), including latent parameters, based on maximum likelihood estimation with iterative calculation between the expectation (E) step and the maximization (M) step [18–20]. This algorithm has been widely studied and applied in image processing [21–25].

When the conventional EM algorithm is applied to the peak separation using a linear superposition of distributions such as Gaussian distributions, the analyzed data are required to be one-dimensional (a_1, a_2, a_3, \dots). However, the spectral data consist of N measurement steps of energy ($\mathbf{x} = \{x_1, \dots, x_n, \dots, x_N\}$) corresponding to the intensity ($\mathbf{w} = \{w_1, \dots, w_n, \dots, w_N\}$). Hence, the spectral data (**Dat**) are represented in two dimensions:

$$\mathbf{Dat} = \begin{Bmatrix} x_1 & \dots & x_N \\ w_1 & \dots & w_N \end{Bmatrix}. \quad (1)$$

When using the conventional EM algorithm, as **Dat** (Equation 1) is converted to be one-dimensional ($\mathbf{x}^* = \{x_{1,1}, \dots, x_{1,w_1}, \dots, x_{n,1}, \dots, x_{n,w_n}, \dots, x_{N,1}, \dots, x_{N,w_N}\}$), the size of \mathbf{x}^* becomes the sum of the intensity $\left(\sum_{n=1}^N w_n\right)$. This size is significantly larger (10^3 times or more in general) than the total number of measurement steps (N), and the calculation cost increases greatly high. Therefore, the conventional EM algorithm is unsuitable for the high-throughput peak separation in terms of the calculation cost.

We solved this disadvantage by using the intensity (\mathbf{w}) as a weight for each measurement step (\mathbf{x}). Here,

we explain this procedure for the peak separation by using a GMM. The GMM can be written as a linear superposition of Gaussians ($\mathbf{N}(\mathbf{x}|\mu_k, \sigma_k)$) as follows:

$$\text{GMM}(\mathbf{x}|\pi_k, \mu_k, \sigma_k) = \sum_{k=1}^K \pi_k \mathbf{N}(\mathbf{x}|\mu_k, \sigma_k), \quad (2)$$

where K is the number of mixture Gaussian distributions corresponding to the number of separated peaks, and π_k , μ_k and σ_k are, respectively, the mixing-coefficient of k -th Gaussian distribution ($0 \leq \pi_k \leq 1$ and $\sum_{k=1}^K \pi_k = 1$), mean and standard deviation ($\sigma_k > 0$). For a given GMM, the aim of the EM algorithm is to maximize the log-likelihood function with respect to the parameters (π_k , μ_k and σ_k) by iterative calculation between the E-step and the M-step.

The E-step calculates responsibilities $\gamma(z_{nk})$, which correspond to posterior probabilities when the measurement steps (\mathbf{x}) are observed [26]; they are calculated using the current parameters (π_k , μ_k and σ_k) as follows:

$$\gamma(z_{nk}) = \frac{\pi_k \mathbf{N}(x_n|\mu_k, \sigma_k)}{\sum_{j=1}^K \pi_j \mathbf{N}(x_n|\mu_j, \sigma_j)}, \quad (3)$$

where z_{nk} is a latent variable associated with x_n . In GMM, x_n is assumed to be generated from one of the Gaussian components. z_{nk} represents the component that generated x_n ; i.e. z_{nk} is equal to 1 when x_n is generated from k -th component, otherwise z_{nk} is equal to 0. Theoretical details of z_{nk} are described by McLachlan and Krishnan, and Bishop [20,26].

Then, in the M-step, the parameters are updated by using the current responsibilities and intensities ($\mathbf{w} = \{w_1, \dots, w_n, \dots, w_N\}$) that correspond to the measurement steps of energy ($\mathbf{x} = \{x_1, \dots, x_n, \dots, x_N\}$) as follows:

$$\pi_k^{new} = \frac{N_k}{\sum_{n=1}^N w_n}, \quad (4)$$

$$\mu_k^{new} = \frac{1}{N_k} \sum_{n=1}^N w_n \gamma(z_{nk}) x_n \quad (5)$$

and

$$\sigma_k^{new} = \frac{1}{N_k} \sum_{n=1}^N w_n \gamma(z_{nk}) (x_n - \mu_k^{new})(x_n - \mu_k^{new})^T, \quad (6)$$

where

$$N_k = \sum_{n=1}^N w_n \gamma(z_{nk}). \quad (7)$$

Using these parameters (π_k^{new} , μ_k^{new} , σ_k^{new}), the log-likelihood value is updated as follows:

$$\begin{aligned} & \ln p(x_n|\pi^{new}, \mu^{new}, \sigma^{new}) \\ &= \sum_{n=1}^N w_n \ln \left\{ \sum_{k=1}^K \pi_k^{new} \mathbf{N}(x_n|\mu_k^{new}, \sigma_k^{new}) \right\}. \end{aligned} \quad (8)$$

The log-likelihood value monotonically increases in iterative calculation between E-step and M-step, and the parameters are converged to a local optimal solution [27].

Convergence criterion of the iterative calculation is defined as the distance of the log-likelihood values between Equation (8) and that at the step immediately before the update. When this distance is more than 1×10^{-8} after the M-step, the calculation is returned to the E-step. In contrast, when the distance is below 1×10^{-8} , the calculation is determined to have converged and the parameters (π_k^{new} , μ_k^{new} , σ_k^{new}) at that time are adopted as the solution.

Calculation was conducted by using our own source code developed in R (<http://cran.r-project.org/>). R is an open-source programming language and software environment for statistical analysis and graphics. The reason for using our own code is that major R packages for the calculation of the EM algorithm [e.g. 28] cannot deal with the weight at each data point. The computer carrying out the calculations had an Intel(R) Core(TM) i7 CPU with four cores at 2.9 GHz with 16 GB memory.

3. Application to the synthetic data

We applied the proposed method to synthetic data 1 and 2 in order to evaluate its spectral analysis capability. The synthetic data 1 were used for the examinations of initialization procedures in the proposed method. The synthetic data 2 were used for the comparison of the analysis accuracy and calculation time with the proposed method, exchange Monte Carlo method and, Newton's method (see also Appendix).

3.1. Synthetic data 1

Synthetic data 1 consist of step (x) and intensity (y), and true step-intensity function $g(x)$ was the sum of two Gaussian functions

$$g(x) = \sum_{k=1}^2 \pi_k^* \mathbf{N}(x|\mu_k^*, \sigma_k^*). \quad (9)$$

The parameters were given as $\{\pi_1^*, \pi_2^*\} = \{0.3, 0.7\}$, $\{\mu_1^*, \mu_2^*\} = \{1.0, 1.8\}$ and $\{\sigma_1^*, \sigma_2^*\} = \{0.3, 0.3\}$. Here, μ_2^* was increased by 0.02 from 1st to 100th of the spectral datasets. Hence, 100 sets of synthetic data 1 were generated and $\{\mu_1^*, \mu_2^*\}$ varies from $\{1.0, 1.8\}$ to $\{1.0, 2.0\}$.

The step (x) was collected from the range [0:3] in steps of 0.02 so that the total number of steps was 151. The intensity (y) was given by $10^6 \times g(x)$, and

each data point is added the noise following Gaussian that is one of the most common noise models [10]. The intensity including the noise of each data point (y^*) was calculated as follows:

$$y^* = \mathbf{N}(y|\mu, \sigma_e), \quad (10)$$

where σ_e is the magnitude of noise ($\sigma_e = \{10^3, 10^4, 5 \times 10^4\}$). These procedures generated the synthetic datasets practically simulating spectral datasets.

At the calculation, the number of peaks (K) were $K = 2$, and we demonstrated three initialization procedures; (1) manual, (2) random and (3) heuristic. In the manual initialization, the initial values of each parameter (π_k, μ_k and σ_k) were $\{0.5, 0.5\}$, $\{1, 1.9\}$ and $\{1, 1\}$, respectively. In the random initialization, the initial values of each parameter were randomly collected from the range $[0:1]$, $[0:3]$ and $[0.1:3.0]$, respectively. In the heuristic initialization, random initialization was repeated 5 times, and the result with the maximum value of Equation (8) was selected.

3.2. Synthetic data 2

Synthetic data 2 consist of step (x) and intensity (y), and true step-intensity function $h(x)$ was the sum of three Gaussian functions

$$h(x) = \sum_{k=1}^3 \pi_k^* \mathbf{N}(x|\mu_k^*, \sigma_k^*). \quad (11)$$

The parameters were $\{\pi_1^*, \pi_2^*, \pi_3^*\} = \{0.2, 0.5, 0.3\}$, $\{\sigma_1^*, \sigma_2^*, \sigma_3^*\} = \{0.15, 0.15, 0.15\}$ and $\{\mu_1^*, \mu_2^*, \mu_3^*\} = \{1.1, 1.5, 1.9\}$. The step (x) was collected from the range $[0:3]$ in steps of 0.02, so that the total number of steps was 151. The intensity (y) was given by $10^6 \times h(x)$, and the intensity including the noise (y^*) was calculated from Equation (10).

We generated three synthetic datasets with different magnitude of noise ($\sigma_e = \{10^3, 10^4, 5 \times 10^4\}$) and repeated the calculation 100 times. At the calculation, we set $K = 3$, and the parameters (π_k, μ_k and σ_k) were collected by the random initialization from the range $[0:1]$, $[0:3]$ and $[0.1:3]$, respectively.

3.3. Result in the analysis of synthetic data 1

Figure 1 shows the example of the peak separation for synthetic data 1. As fitting curves showed good fitting in each data (Figure 1), the proposed method could perform reasonable analysis. The relationship between estimated and true peak positions ($\mu_1^* = 1.0$ and $\mu_2^* = 1.8$ to 2.0) is shown in Figure (2). Analyzing low and medium noise data ($\sigma_e = 10^3$ and 10^4), estimated peak positions were close to the true; shifting peak ($\mu_2^* = 1.8$ to 2.0) and fixed peak ($\mu_1^* = 1.0$) were clearly observed. In contrast, when $\sigma_e = 5 \times 10^4$,

estimated peaks were occasionally deviated from the true position (Figure 2).

Table 1 respectively shows the root-mean-square error (RMSE) between the estimated and true peak position and the calculation time (s) in each initialization. There was almost no difference in the RMSE between these initializations when $\sigma_e = 10^3$. In contrast, the random initialization showed larger RMSE than the others when $\sigma_e = 10^4$, and the heuristic initialization showed smaller RMSE than the others when $\sigma_e = 5 \times 10^4$. The calculation times were 11.4–11.8 s, 11.4–12.4 s and 54.1–59.8 s in manual, random and heuristic initialization for analyzing 100 sets of synthetic data 1 with noise ($\sigma_e = 10^3, 10^4$ and 5×10^4), respectively. There is little difference in calculation time due to the magnitude of noise, although the heuristic initialization requires relatively large calculation time.

3.4. Result in the analysis of synthetic data 2

Figure 3 shows an example of the peak separation using the proposed method, exchange Monte Carlo method and Newton's method. The proposed method showed good fitting curve for synthetic data 2 with low noise, whereas unclear peak (= 1.1) could not be detected for the data with medium and high noise. In contrast, the exchange Monte Carlo method could detect an accurate peak position regardless of the magnitude of noise. Newton's method occasionally failed to detect the peaks because the parameter solution did not converge. For example, appropriate peaks were not detected for a set of data with medium and high noise (Figure 3).

Table 2 shows the median of RMSE and average calculation time (s) by using each method, respectively. The median of RMSE shows that the exchange Monte Carlo method could perform a more accurate analysis than the other methods. In contrast, the proposed method and Newton's method completed the calculation over 1000 times faster than the exchange Monte Carlo method. However, Newton's method showed significantly large RMSE. Thus, the proposed method could analyze more accurately than Newton's method at the same order of calculation time. This result strongly suggests that the proposed method, and the exchange Monte Carlo method have a trade-off relationship between the analysis accuracy and calculation time. In contrast, as Newton's method showed insufficient accuracy, it is difficult to use it for the high-throughput analysis.

We also examined the efficiency of the proposed method relative to the conventional EM algorithm by using synthetic data 2 in $\sigma_e = 10^3$. The proposed method and conventional EM algorithm with the same initial values required 1775 and 1166 iterations of the E- and M-step loop, respectively. However, the

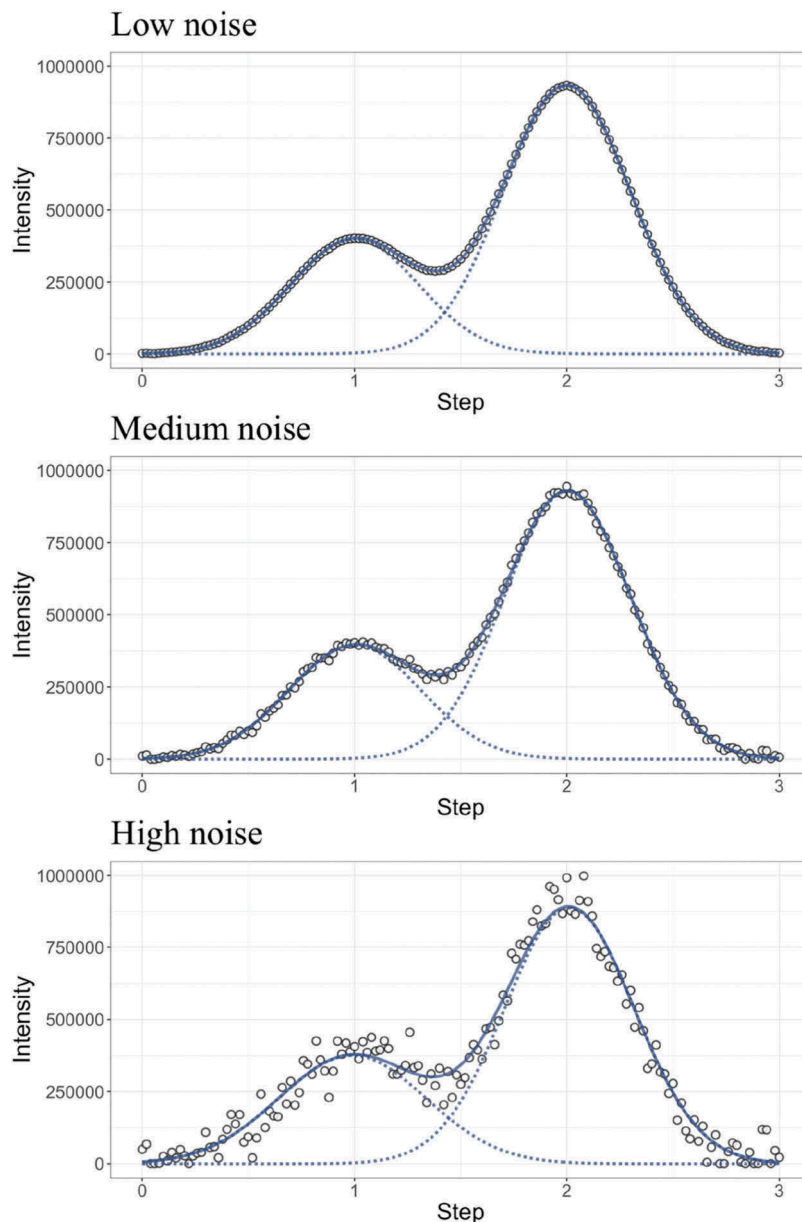


Figure 1. Example of the fitting curve for the sets of synthetic data 1 at each noise ($\sigma_e = 10^3$ (Low noise), 10^4 (Medium noise), 5×10^4 (High noise)) by using the random initialization. Circles show the generated intensity (y^*) at each step (x). Blue solid line is fitting curve, and the dotted blue line is each Gaussian distribution.

total calculation times to reach the convergence were 1.1 s and 21611.4 s, respectively. Therefore, the proposed method significantly improves the efficiency of the E- and M-step loops. Moreover, the accuracy of the proposed method is better than the conventional method; RMSE obtained by the proposed method is 8607.1, whereas that by the conventional method is 41371.9. These results suggest that the proposed method successfully adapted the conventional method to the spectrum fitting.

4. Application to the experimental data

4.1. Experimental datasets

The experimental datasets were systematically collected from the FETs [14,16,17] by the 3D nano-ESCA system

in order to investigate the local electronic states in the structures of devices [13,29,30]. Fukidome et al. [14] collected spectra for the graphene FET on the graphene channel region applying gate biases (V_g). Suto et al. [17] collected spectra by line scanning on the interface between a Ni electrode and a four-layer MoS₂ sheet. Nagamura et al. [16] collected spectra by line scanning on the interface between a metal electrode and a monolayer graphene sheet. The previous works [14,16,17] have reported systematic core level peak shifts (i.e. the electric potential shift) for the C 1s in graphene [14,16] and S 2p in MoS₂ [17] peaks. These datasets from Fukidome et al. [14], Suto et al. [17] and Nagamura et al. [16] are labeled here as Graphene FET-1, MoS₂ FET, and Graphene FET-2, respectively. The background was processed as a linear background.

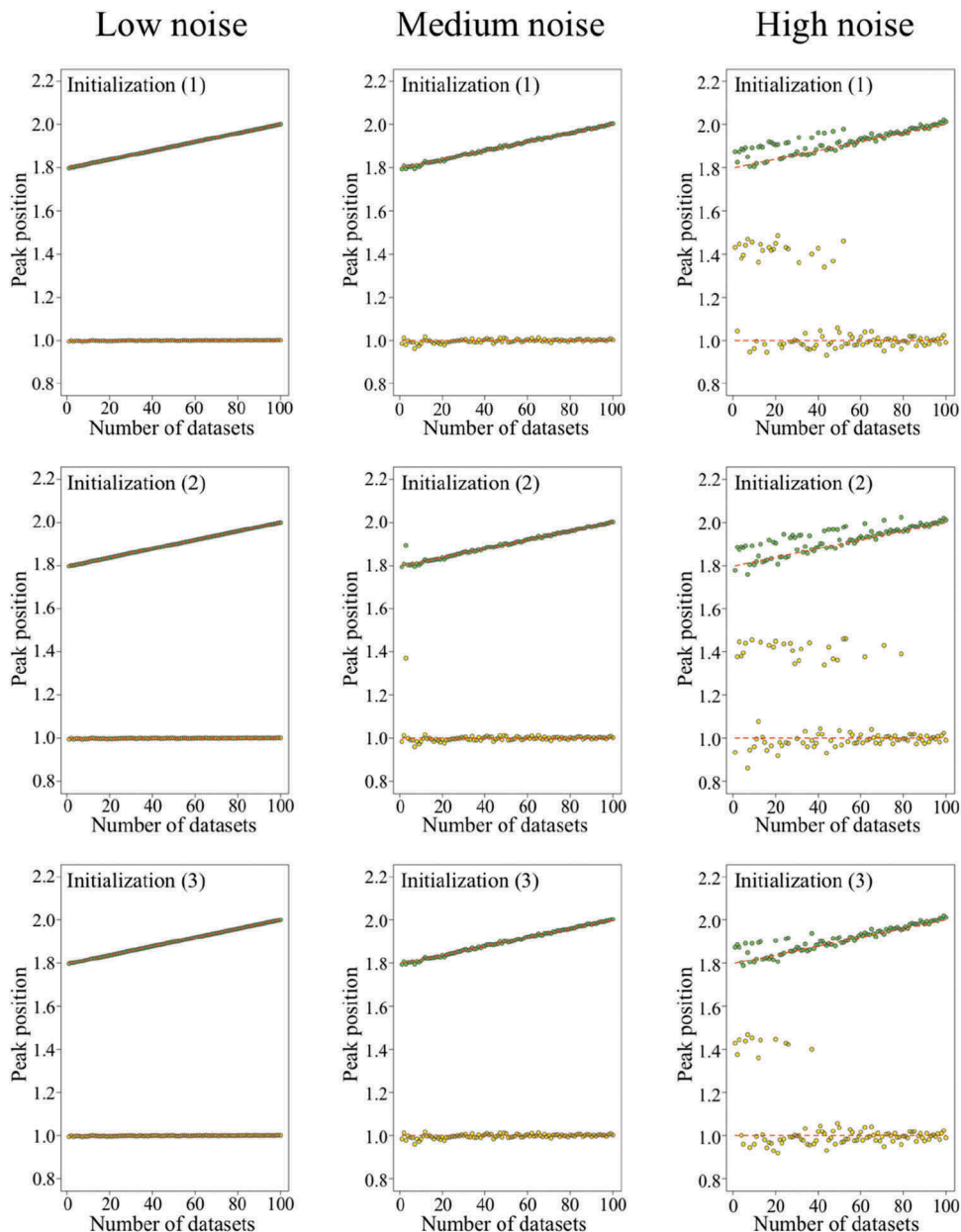


Figure 2. Relationship between the number of datasets and estimated two peak positions at each noise ($\sigma_e = 10^3$ (Low noise), 10^4 (Medium noise), 5×10^4 (High noise)). Initialization (1), (2) and (3) are manual, random and heuristic initialization, respectively. Green and yellow dots show each estimated peak position. Red dashed line represents the true peak position.

Table 1. Analysis accuracy and computational cost of each initialization. Initialization (1); manual, initialization (2); random, and initialization (3); heuristic. RMSE values were calculated from the difference between true peak position and estimated peak position. Time (s) represents the calculation time to complete the analysis for 100 sets of data.

	Low noise	Medium noise	High noise
RMSE in Peak 1			
Initialization (1)	0.002	0.009	0.203
Initialization (2)	0.002	0.038	0.212
Initialization (3)	0.001	0.009	0.151
RMSE in Peak 2			
Initialization (1)	0.001	0.004	0.036
Initialization (2)	0.001	0.010	0.041
Initialization (3)	0.001	0.004	0.027
Time (s)			
Initialization (1)	11.8	11.6	11.4
Initialization (2)	12.2	12.4	11.4
Initialization (3)	59.8	57.5	54.1

4.2. Initial condition for the analysis

Decomposed number of peaks (K) were $K = 2, 2$ and 3 for the Graphene FET-1, MoS₂ FET and Graphene FET-2, respectively. The initial values of the parameters (π_k, μ_k and σ_k) were, respectively, collected by the heuristic initialization from the range [0:1], [711:713 eV] and [1:3] for Graphene FET-1; [0:1], [832:834 eV] and [1:3] for MoS₂ FET; and [0:1], [709:713 eV] and [1:3] for Graphene FET-2.

4.3. Result in the analysis of experimental data

4.3.1. Graphene FET-1

Analysis using the spectrum-adapted EM algorithm for the Graphene FET-1 determined the fitting

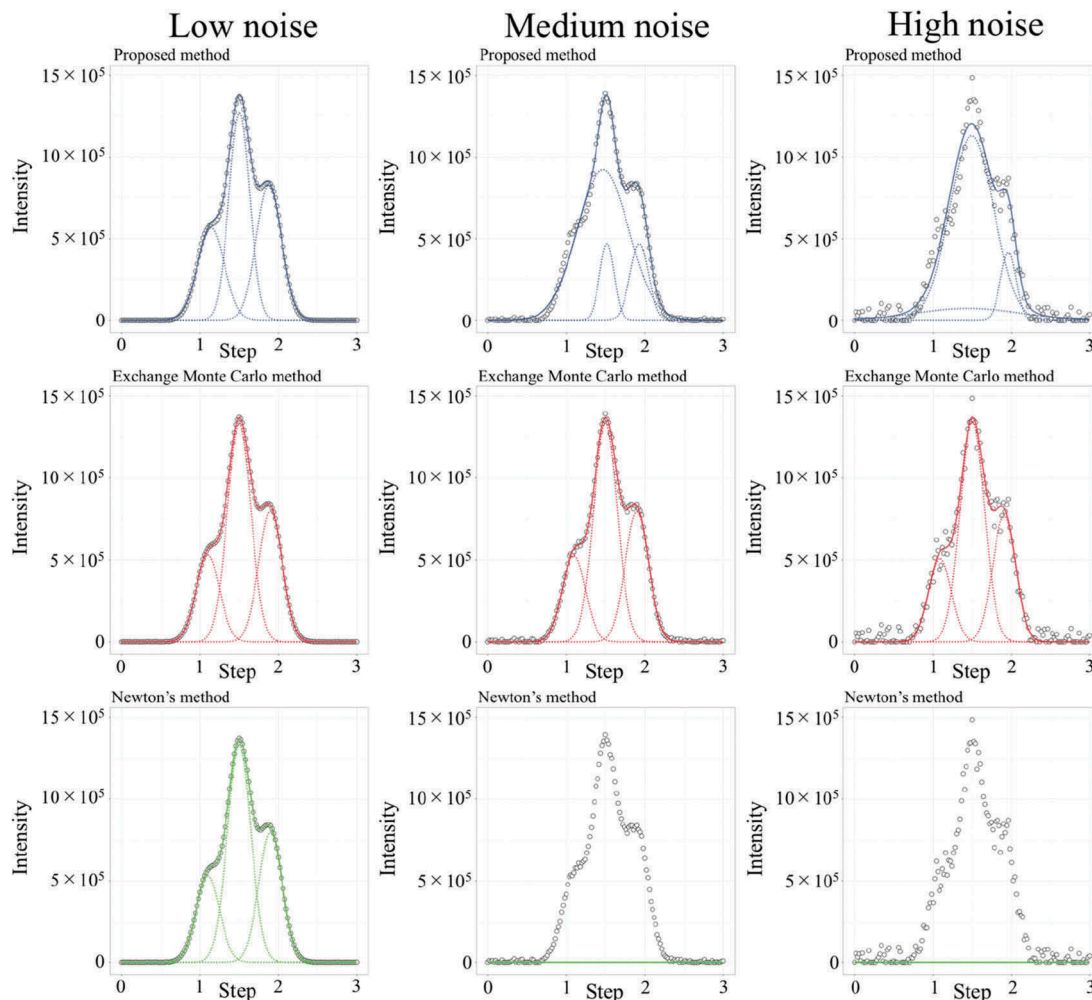


Figure 3. Example of fitting curve for synthetic data 2 at each noise ($\sigma_e = 10^3$ (Low noise), 10^4 (Medium noise), 5×10^4 (High noise)). Circles show the generated intensity (y^*) at each step (x). Blue solid and dotted line are fitting curve and each gaussian distribution estimated by the proposed method. Red solid and dotted line are fitting curve and each gaussian function estimated by the exchange Monte Carlo method. Green solid and dotted line are fitting curve and each gaussian function estimated by Newton's method.

Table 2. Analysis accuracy and computational cost of the proposed method, exchange Monte Carlo method and Newton's method. Median of RMSE was obtained from the 100 calculations of the peak separation. Each RMSE value was calculated from the difference between estimated and true fitting curve. Time represents the average calculation time (s) of the 100 calculations of the peak separation.

	Low noise	Medium noise	High noise
Proposed method			
Median of RMSE	8607	65,089	64,575
Time (s)	0.77	0.32	0.43
Exchange Monte Carlo method			
Median of RMSE	138	1375	6849
Time (s)	610.82	472.95	404.95
Newton's method			
Median of RMSE	537,532	533,865	537,728
Time (s)	0.17	0.18	0.48

curves of the GMM that fit the spectral data well. The calculation for 13 sets of spectral data (each with 211 measurement steps) was completed in 14.5 s (1.1 s per set) to separate each spectrum into two Gaussian distributions. Figure 4(a) shows the

example of the fitting curve and the two decomposed Gaussian distributions. In the previous study of Fukidome et al. [14], as peak fitting was performed with two components, we adopt $K = 2$. The component at higher kinetic energy is interpreted as C 1s core level spectrum derived from graphene sp^2 bonds, whereas that at lower kinetic energy is ascribable to carbon oxide contaminants. The fitting curves showed that the graphene peak position is systematically shifted by ~ 130 meV depending on the gate bias (V_g) in the range -40 to -5 V (Figure 4(b)). This peak shift is consistent with the peak shift of about 200 meV corresponding to the gate bias (in the range -40 to 0 V) in Fukidome et al. [14]. Here, the binding energy of graphene is expressed in terms of the gate bias (V_g) [14,31–33]:

$$E_{BE}(G) = E_{BE}(DP) - 6.0 \times 10^{-2} \sqrt{V_{CNP} - V_g}, \quad (12)$$

where the $E_{BE}(G)$ and V_{CNP} are the binding energy of the graphene and the charge neutrality point ($V_{CNP} = 28$ [14]), respectively. Also, $E_{BE}(DP)$ is the binding

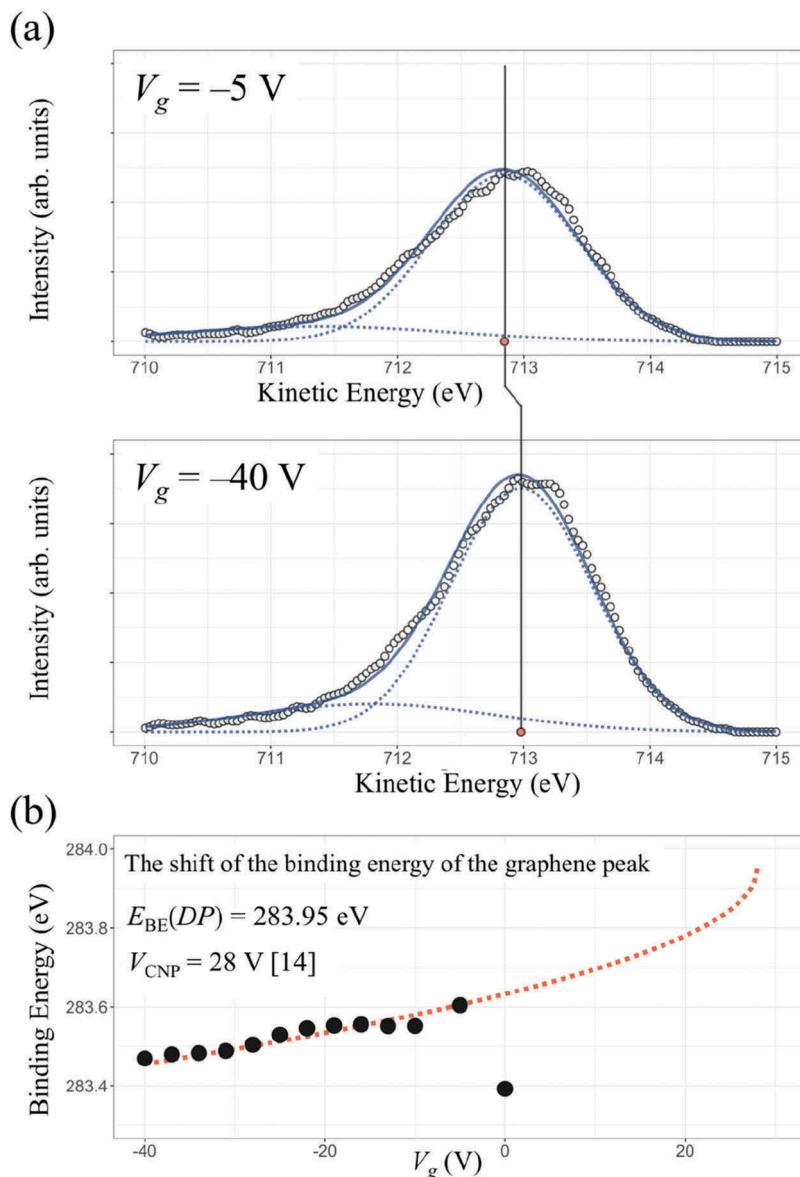


Figure 4. (a) Example of GMM fitting curve for the spectra of Graphene FET-1 at gate biases of -5 and -40 V. The horizontal axis is the kinetic energy (eV), the vertical axis is the intensity (arbitrary units), and the open black circles show the observed spectral data. Blue solid and dotted line are fitting curve and each Gaussian distribution. Red dot indicates the peak position of the graphene (712.85 and 712.98 eV at gate biases (V_g) of -5 and -40 V, respectively). (b) The graphene peak shift of the binding energy ($E_{BE}(G)$) against the gate bias (V_g). Red dotted curve is the fitting curve given by Equation (12) using $E_{BE}(DP) = 283.95$ eV and $V_{CNP} = 28$ V [14]. The binding energy (eV) is obtained by converting the kinetic energy; i.e., binding energy = $996.45 -$ kinetic energy.

energy of graphene when the Fermi level coincides with the Dirac point, i.e., the energy difference between the Dirac point energy and the C 1s core level of graphene [14]. The theoretical curve (Equation 12) fitted to the graphene peak position at $V_g = -40 - -5$ V shows $E_{BE}(DP)$ as 283.95 eV and V_{CNP} as 28 V [14] (Figure 4(b)). The value of $E_{BE}(DP)$ (283.95 eV) is close to the binding energy of neutral graphene (284.4 eV) [34]. The slight difference between the binding energy of $E_{BE}(DP)$ (283.95 eV) and neutral graphene (284.4 eV) may be ascribable to minute uncertainties in the incident photon energy or Fermi-edge measurements used to determine the binding energies [14]. However, the

binding energy of graphene peak at $V_g = 0$ was underestimated about 300 meV relative to the theoretical curve (Equation 12) in the previous study [14]. This is because that the contaminant component derived from the 0th order of diffracted beam of the Fresnel zone plate would be large in the case of $V_g = 0$. Estimation of the appropriate peak position using GMM may not be successful when the contaminant component is large or the asymmetry of the peak shape cannot be negligible.

4.3.2. MoS₂ FET

The proposed method showed GMM fitting curves and S $2p_{3/2}$ and S $2p_{1/2}$ peak positions from the MoS₂ FET

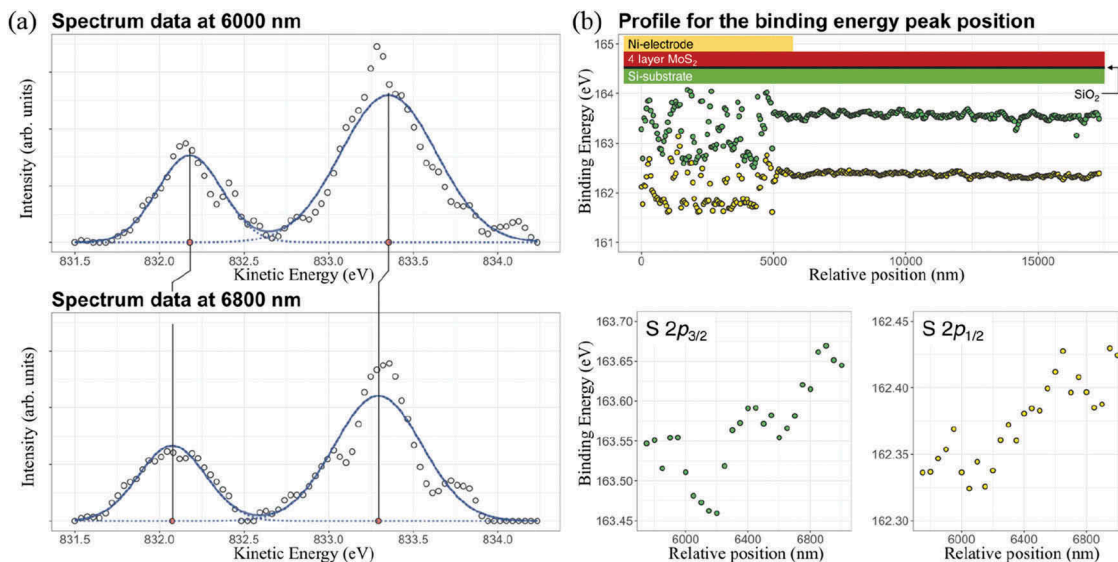


Figure 5. (a) Example of GMM fitting curve for the spectra of MoS₂ FET at the Ni/MoS₂ interface. The horizontal axis is the kinetic energy (eV), the vertical axis is the intensity (arbitrary units), and the open black circles indicate the observed spectral data. Blue solid and dotted line are fitting curve and each Gaussian distribution. Red dots indicate the positions of the S 2p_{1/2} and S 2p_{3/2} peaks of the MoS₂ sheet at 6000 nm (832.18 and 833.35 eV) and 6800 nm (832.08 and 833.29 eV) of the relative position (Figure 5(b)), respectively. (b) Plot of the S 2p_{3/2} (green point) and S 2p_{1/2} (yellow point) peak position of the binding energy against the relative position. The S 2p_{3/2} and S 2p_{1/2} peak position focusing on the spectral data at the vicinity of the contact of a Ni electrode with 4-layer MoS₂. The binding energy (eV) is obtained by converting the kinetic energy; i.e. binding energy = 995.690 – kinetic energy.

spectral data (Figure 5). In Suto et al. [17], peak fitting was performed with two components of S 2p_{3/2} and S 2p_{1/2}, so that we also adopt $K = 2$. The calculation to separate each of the 347 individual spectral data (each with 76 measurement steps) into two Gaussian distributions was completed in 30.6 s (0.09 s per set). This calculation completed in a significantly short time because the spectra of MoS₂ FET consists of relatively small measurement steps. Figure 5(a) shows the example of GMM fitting curves and the two decomposed Gaussian distributions. The fitting curves show that S 2p_{3/2} and S 2p_{1/2} peak positions systematically shifted by ~150 and ~100 meV from 5800 nm to 7000 nm, respectively (Figure 5(b)). This peak shift is observable near the interface between the Ni electrode and MoS₂ sheet (approximately 5750~ nm). Suto et al. [17] reported that such systematic peak shift overlaps with a charge transfer region; they detected this region at the MoS₂/metal–electrode interface expanding over ~500 nm, with the electrostatic potential variation of binding energy (~70 meV) mainly causing the transfer of charges by contacting MoS₂ with the Ni metal electrode. This peak shift has been considered due to band bending in the MoS₂ electronic structure with a Fermi level shift [17,35,36].

4.3.3. Graphene FET-2

Analysis using the proposed method for the Graphene FET-2 spectral data showed fitting curves, three decomposed Gaussian distributions

(Figure 6(a)) and the profile of the graphene peak positions (Figure 6(b)). The calculation to separate each of the 44 sets (each with 211 measurement steps) into three Gaussian distributions was completed in 589.7 s (13.4 s per set). Nagamura et al. [16] performed peak fitting to the Graphene FET-2 spectral data with two components: the higher-kinetic-energy component is interpreted as the C 1s core level spectrum derived from graphene sp² bonds, and the lower-kinetic-energy component is interpreted as that from surface contaminants. However, we adopt $K = 3$ in these data because it is better to consider multiple components of the surface contaminants from polymer residue in the device fabrication process and naturally involved amorphous carbon [37–39]. The graphene peak position is systematically shifted by ~140 meV to ~700 nm from the vicinity of the interface between the metal electrode and the monolayer graphene sheet (Figure 6(b)). Such a peak shift overlaps with a charge transfer region at the graphene/metal–electrode boundary [40,41]. Nagamura et al. [16] reported a ~60 meV peak shift at ~500 nm of the charge transfer region in graphene at a metal boundary. Assuming the measurement energy step containing ~±50 meV error due to the resolution of equipment, the proposed method could detect acceptable peak position and the same order of energy shift relative to the result in the previous research [16].

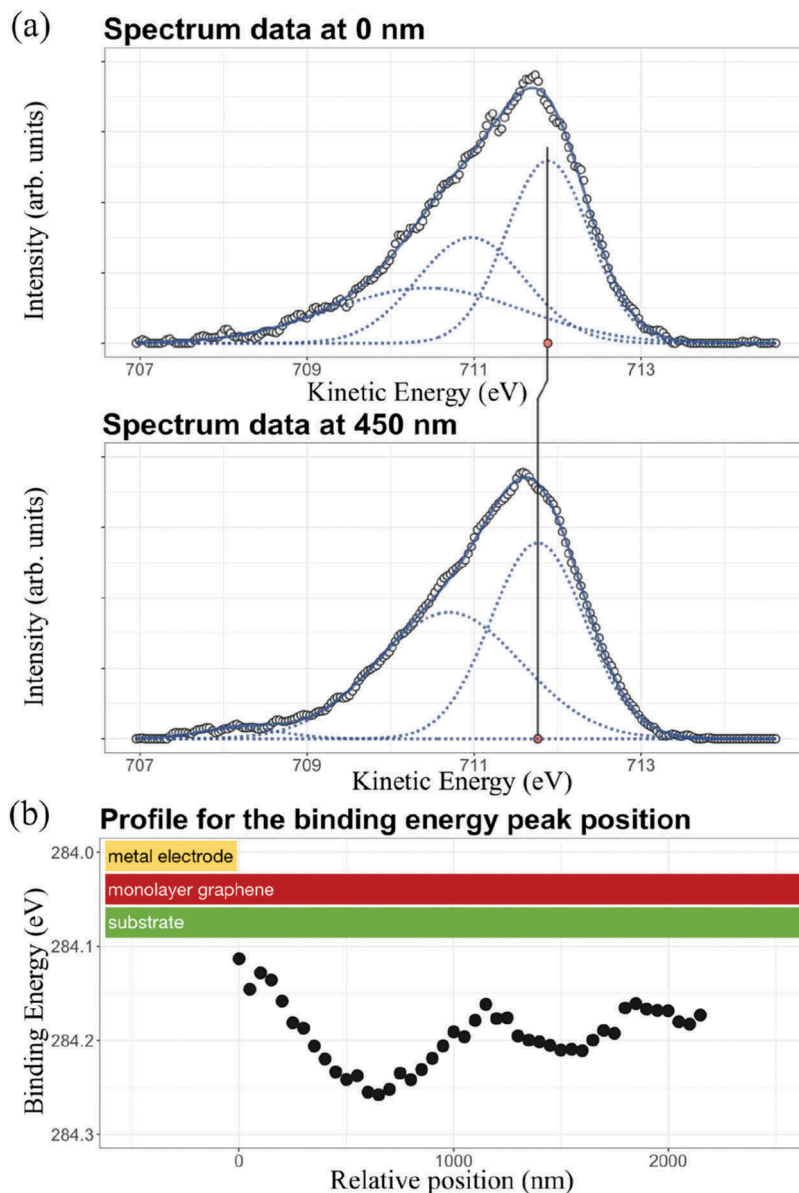


Figure 6. (a) Example of GMM fitting curve for the spectra of Graphene FET-2 at the interface between the metal electrode and the monolayer graphene sheet. The horizontal axis is the kinetic energy (eV), the vertical axis is the intensity (arbitrary units), and open black circles indicate the observed spectral data. Blue solid and dotted line are fitting curve and each Gaussian distribution. Red dot indicates the position of the C 1s peak of the graphene (711.88 and 711.76 eV at the 0 nm and 450 nm of the relative position (Figure 6(b)), respectively). (b) Profile for the binding energy of the graphene peak position (black dots) against the relative position of the spectra. The binding energy (eV) is obtained by converting the kinetic energy; i.e. binding energy = 995.996 – kinetic energy.

5. Discussion and implication

The spectrum-adapted EM algorithm was proposed and successfully applied to synthetic and experimental datasets. The advantage of the proposed method is the fast and stable calculation. The peak separation for the synthetic and experimental datasets was completed less than 1.0 and 13.4 s per set of the data, respectively. As the parameters are converged to a local optimal solution by monotonically increasing log-likelihood value in the iterative calculation, the proposed method can stably conduct the peak separation. Thus, it is unnecessary to conduct the manual trial and error in order to converge the parameter

solution in using ordinary gradient methods such as Newton’s method. In contrast, the exchange Monte Carlo method can perform a more accurate analysis than the proposed method (Figure 3). Moreover, the appropriate number of peaks can be determined by calculating the model selection criteria such as the marginal likelihood [7]. However, the exchange Monte Carlo method requires high computational cost, and it is not easy to set a suitable prior distribution and inverse temperature for non-expert. As such a setting is unnecessary to use the proposed method, the peak shift analysis can be performed easily.

The random and heuristic initialization are suitable initialization procedures for the high throughput

analysis because these procedures can automatically process the spectral data. Especially, heuristic initialization helped to find a reasonable solution in the analysis of noisy data (Figure 2) and showed acceptable performance in the peak shift analysis of the experimental data (Figures 4–6). These applications suggest that the proposed method with the heuristic initialization may be applicable to other spectral deconvolution problems for investigating electronic properties of materials and devices at an adequately small computational cost. However, it is necessary to sophisticate the initialization procedure because heuristic initialization cannot systematically select an appropriate number of peaks, and the computational cost remains relatively higher than the others (Table 1). Moreover, further studies are needed to be able to use other common fitting functions such as Lorentzian and Voigt function, and asymmetric line-shape functions such as the Doniach–Sunjic function [42] according to Section 4.3.1. To overcome these disadvantages is important for further improvement of the high throughput the method.

6. Conclusions

We proposed the spectrum-adapted EM algorithm as a high-throughput method to investigate the peak shift from a large number of spectral datasets. Application to the synthetic datasets suggested that heuristic initialization can perform more accurate analysis than other initializations with relatively large calculation time, and the proposed method, and the exchange Monte Carlo method have a trade-off relationship between the analysis accuracy and calculation time. Moreover, the proposed method was applied to experimental datasets collected from two graphene [14,16] and one MoS₂ [17] FETs and detected the systematic peak shifts close to the results in the previous works [14,16,17] in less than 13.4 s per set. These applications suggest that the proposed method has acceptable accuracy to investigate the peak shift at high speed. Even a non-expert analyst can easily and automatically use this method for the spectral data analysis.

Acknowledgments

This paper is based on results from a project (P16010) commissioned by the New Energy and Industrial Technology Development Organization (NEDO), JST CREST (JPMJCR1761), the ‘Materials Research by Information Integration’ Initiative project and PRESTO (Grant number: JPMJPR17NB), commissioned by the Japan Science and Technology Agency (JST), and the Research Program for CORE lab (2016002) of ‘Dynamic Alliance for Open Innovation Bridging Human, Environment and Materials’ of the ‘Network Joint Research Center for Materials and Devices’. We thank Prof. Kosuke Nagashio of the University of

Tokyo and Prof. Hirokazu Fukidome of Tohoku University for measuring the presented data. The spectral datasets were obtained with the support of the University of Tokyo outstation beamline at SPring-8 (Proposal Numbers: 2012B7402, 2013A7443, 2013B7451, 2014B7472, and 2015A7482).

Disclosure statement

No potential conflict of interest was reported by the authors.

Funding

This work was supported by the Precursory Research for Embryonic Science and Technology [JPMJPR17NB]; New Energy and Industrial Technology Development Organization [P16010]; Research Program for CORE lab [2016002]; Core Research for Evolutional Science and Technology [JPMJCR1761].

References

- [1] Hüfner S, editor. Very high resolution photoelectron spectroscopy. Berlin (GE): Springer; 2007.
- [2] Hüfner S. Photoelectron spectroscopy: principles and applications. 3rd ed. Berlin (GE): Springer; 2013.
- [3] Suga S, Sekiyama A. Photoelectron spectroscopy. Berlin (GE): Springer; 2014.
- [4] Attwood D, Sakdinawat A. X-rays and extreme ultraviolet radiation: principles and applications. 2nd ed. Cambridge (UK): Cambridge university press; 2017.
- [5] Jaumot J, Gargallo R, de Juan A, et al. A graphical user-friendly interface for MCR-ALS: a new tool for multivariate curve resolution in MATLAB. Chemom Intell Lab Syst. 2005;76(1):101–110.
- [6] Dobigeon N, Brun N. Spectral mixture analysis of EELS spectrum-images. Ultramicroscopy. 2012;120:25–34.
- [7] Nagata K, Sugita S, Okada M. Bayesian spectral deconvolution with the exchange Monte Carlo method. Neural Netw. 2012;28:82–89.
- [8] Kasai T, Nagata K, Okada M, et al. NMR spectral analysis using prior knowledge. J Phys Conf Ser. 2016 Mar;699(1):012003.
- [9] Murata S, Nagata K, Uemura M, et al. Extraction of latent dynamical structure from time-series spectral data. J Phys Soc Jpn. 2016;85(10):104003.
- [10] Shiga M, Tatsumi K, Muto S, et al. Sparse modeling of EELS and EDX spectral imaging data by nonnegative matrix factorization. Ultramicroscopy. 2016;170:43–59.
- [11] Jany BR, Janas A, Krok F. Retrieving the quantitative chemical information at nanoscale from scanning electron microscope energy dispersive X-ray measurements by machine learning. Nano Lett. 2017;17(11):6520–6525.
- [12] Hukushima K, Nemoto K. Exchange Monte Carlo method and application to spin glass simulations. J Phys Soc Jpn. 1996;65(6):1604–1608.
- [13] Horiba K, Nakamura Y, Nagamura N, et al. Scanning photoelectron microscope for nanoscale three-dimensional spatial-resolved electron spectroscopy for chemical analysis. Rev Sci Instrum. 2011;82(11):113701.

- [14] Fukidome H, Nagashio K, Nagamura N, et al. Pinpoint operando analysis of the electronic states of a graphene transistor using photoelectron nanospectroscopy. *Appl Phys Express*. 2014;7(6):065101.
- [15] Nagamura N, Kitada Y, Tsurumi J, et al. Chemical potential shift in organic field-effect transistors identified by soft X-ray operando nano-spectroscopy. *Appl Phys Lett*. 2015;106(25):251604.
- [16] Nagamura N, Horiba K, Toyoda S, et al. Direct observation of charge transfer region at interfaces in graphene devices. *Appl Phys Lett*. 2013;102(24):241604.
- [17] Suto R, Venugopal G, Tashima K, et al. Observation of nanoscopic charge-transfer region at metal/MoS₂ interface. *Mater Res Express*. 2016;3(7):075004.
- [18] Dempster AP, Laird NM, Rubin DB. Maximum likelihood from incomplete data via the EM algorithm. *J R Stat Soc Series B Stat Methodol*. 1977;39(1):1–38.
- [19] McLachlan G, Peel D. Finite mixture models. New York (NY): Wiley; 2000. Chapter 2, ML fitting of mixture models; p. 40–79.
- [20] McLachlan G, Krishnan T. The EM Algorithm and its Extensions. 2nd ed. New York (NY): Wiley; 2008. Chapter 1, General introduction; p. 1–37.
- [21] Akaho S. The EM algorithm for multiple object recognition. Proceedings of ICNN'95 – International Conference on Neural Networks; 1995 Nov 27–Dec 1; Perth (WA): IEEE; 1995. Vol. 5, p. 2426–2431.
- [22] Ayer S, Sawhney HS Layered representation of motion video using robust maximum-likelihood estimation of mixture models and MDL encoding. Proceedings of IEEE international Conference on Computer Vision; 1995 Jun 20–23; Cambridge (MA): IEEE; 1995. p. 777–784.
- [23] Fan CM, Namazi NM, Penafiel PB. A new image motion estimation algorithm based on the EM technique. *IEEE Trans Pattern Anal Mach Intell*. 1996;18(3):348–352.
- [24] Nowak RD. Distributed EM algorithms for density estimation and clustering in sensor networks. *IEEE Trans Signal Process*. 2003;51(8):2245–2253.
- [25] Gebru ID, Alameda-Pineda X, Forbes F, et al. EM algorithms for weighted-data clustering with application to audio-visual scene analysis. *IEEE Trans Pattern Anal Mach Intell*. 2016;38(12):2402–2415.
- [26] Bishop CM. Pattern recognition and machine learning. New York (NY): Springer; 2006. Chapter 9, Mixture models and EM; p. 423–455.
- [27] Wu CJ. On the convergence properties of the EM algorithm. *Ann Stat*. 1983;11(1):95–103.
- [28] Young D, Benaglia T, Chauveau D, et al. Mixtools [Package]. Version 1.1.0. Available from: <https://cran.r-project.org/web/packages/mixtools/mixtools.pdf>
- [29] Senba Y, Yamamoto S, Ohashi H, et al. New soft X-ray beamline BL07LSU for long undulator of SPring-8: design and status. *Nucl Instrum Methods Phys Res A*. 2011;649(1):58–60.
- [30] Yamamoto S, Senba Y, Tanaka T, et al. New soft X-ray beamline BL07LSU at SPring-8. *J Synchrotron Radiat*. 2014;21(2):352–365.
- [31] Novoselov KS, Geim AK, Morozov SV, et al. Two-dimensional gas of massless Dirac fermions in graphene. *Nature*. 2005;438(7065):197.
- [32] Sarma SD, Adam S, Hwang EH, et al. Electronic transport in two-dimensional graphene. *Rev Mod Phys*. 2011;83(2):407.
- [33] Kanayama K, Nagashio K, Nishimura T, et al. Large Fermi energy modulation in graphene transistors with high-pressure O₂-annealed Y₂O₃ topgate insulators. *Appl Phys Lett*. 2014;104(8):083519.
- [34] Emtsev KV, Speck F, Seyller T, et al. Interaction, growth, and ordering of epitaxial graphene on SiC {0001} surfaces: a comparative photoelectron spectroscopy study. *Phys Rev B*. 2008;77(15):155303.
- [35] Miwa JA, Dendzik M, Grönberg SS, et al. Van der Waals epitaxy of two-dimensional MoS₂-graphene heterostructures in ultrahigh vacuum. *ACS Nano*. 2015;9(6):6502–6510.
- [36] Wang Y, Yang RX, Quhe R, et al. Does p-type ohmic contact exist in WSe₂-metal interfaces? *Nanoscale*. 2016;8(2):1179–1191.
- [37] Lim H, Song HJ, Son M, et al. Unique photoemission from single-layer graphene on a SiO₂ layer by a substrate charging effect. *Chem Commun*. 2011;47(30):8608–8610.
- [38] Kim KJ, Lee H, Choi JH, et al. Scanning photoemission microscopy of graphene sheets on SiO₂. *Adv Mater*. 2008;20(19):3589–3591.
- [39] Peltekis N, Kumar S, McEvoy N, et al. The effect of downstream plasma treatments on graphene surfaces. *Carbon*. 2012;50(2):395–403.
- [40] Nagashio K, Toriumi A. Density-of-states limited contact resistance in graphene field-effect transistors. *Jpn J Appl Phys*. 2011;50(7R):070108.
- [41] Khomyakov PA, Giovannetti G, Rusu PC, et al. First-principles study of the interaction and charge transfer between graphene and metals. *Phys Rev B*. 2009;79(19):195425.
- [42] Doniach S, Sunjic M. Many-electron singularity in X-ray photoemission and X-ray line spectra from metals. *J Phys C*. 1970;3(2):285.
- [43] Nagata K, Watanabe S. Exchange Monte Carlo sampling from Bayesian posterior for singular learning machines. *IEEE Trans Neural Netw*. 2008;19(7):1253–1266.
- [44] Nagata K, Watanabe S. Asymptotic behavior of exchange ratio in exchange Monte Carlo method. *Neural Netw*. 2008;21(7):980–988.

Appendix. Procedure of the peak separation using the Newton's method and the exchange Monte Carlo method

Here, we describe the procedure of the peak separation using the Newton's and exchange Monte Carlo method to the synthetic data 2. The peak separation model is used the sum of three Gaussian functions $s(x)$:

$$s(x) = \sum_{k=1}^3 a_k \exp\left(-\frac{b_k}{2}(x - \mu_k)^2\right) \quad (\text{A1})$$

where a_k , b_k and μ_k are the strength, bandwidth, and center of k -th Gaussian function. The set of parameters $\theta = \{a_k, b_k, \mu_k\}_{k=1}^K$ are optimized by minimizing the mean-squared error function $E(\theta)$ between the synthetic data $\{x_n, y_n^*\}_{n=1}^N$ and the function (Equation A1):

$$E(\theta) = \frac{1}{2N} \sum_{n=1}^N (y_n^* - s(x_n; \theta))^2 \tag{A2}$$

We applied Newton’s method to the optimization of $E(\theta)$. The initial values of parameters $\{a_k, b_k, \mu_k\}$ are randomly chosen from the ranges [500,000–150,000], [1–100] and [0–3].

Using $E(\theta)$ (Equation A2), we also performed Bayesian peak separation by the exchange Monte Carlo method (theoretical details are shown in Nagata et al. [7]). Application of the exchange Monte Carlo method requires to set (1) Prior densities, (2) Inverse temperature, and (3) Initial condition. These settings are shown below.

(1) Prior densities

The prior densities $\varphi(a_k)$, $\varphi(b_k)$ and $\varphi(\mu_k)$ of the parameters were, respectively, defined in terms of the following Gamma, Gamma and Gauss distribution:

$$\varphi(a_k) = \text{Gamma} (a_k; \eta_a, \lambda_a) \tag{A3}$$

$$\varphi(b_k) = \text{Gamma} (b_k; \eta_b, \lambda_b) \tag{A4}$$

$$\varphi(\mu_k) = N (\mu_k; \eta_0, \lambda_0) \tag{A5}$$

The hyperparameters $\{\eta_a, \lambda_a\}$, $\{\eta_b, \lambda_b\}$ and $\{\eta_0, \lambda_0\}$ were {10, 1e-5}, {10, 1/5} and {1.5, 1/5}, respectively. The determination of the prior densities and hyperparameters is heuristics in this study.

(2) Inverse temperature

According to Nagata et al. [7] and Nagata and Watanabe [43,44], the number of inverse temperatures L was 24, and the inverse temperature was given by

$$\beta_l = \begin{cases} 0 & (\text{if } l = 1) \\ 1.5^{l-L} & (\text{otherwise}) \end{cases} \tag{A6}$$

β_l is each inverse temperature ($0 = \beta_1 > \beta_2 > \dots > \beta_{L-1} > \beta_L = 1$).

(3) Initial condition

The initial values of parameters $\{a_k, b_k, \mu_k\}$ are randomly chosen from the range [500,000–150,000], [1–100] and [0–3], respectively. The iteration was set as 10,000 steps for the burn-in period, and 2000 steps for the expectation value calculation.

6. Staff

Director: HARADA Yoshihisa, Professor

KOMORI Fumio, Professor

MATSUDA Iwao, Associate Professor

KONDO Takeshi, Associate Professor

NIIBE Masahito, Visiting Associate Professor

YAMAMOTO Susumu, Research Associate (~2019.10)

YAJI Koichiro, Research Associate

MIYAWAKI Jun, Research Associate

HIRATA Yasuyuki, Research Associate (~2019.9)

HARASAWA Ayumi, Technical Associate

SHIBUYA Takashi, Technical Associate

KUDO Hirofumi, Technical Associate

FUKUSHIMA Akiko, Technical Associate

Technical Assistant: FUJISAWA Masami

KOSEGAWA Yuka

ARAKI Mihoko

Secretary: AIHARA Yumiko

HARADA Misa

YOSHIZAWA Motoko

TSUTSUMI Yumiko

IKEDA Kuniko

Graduate Student: IKEDA Keisuke

WATANABE Ryusuke

UGALINO Ralph John

SATO Yusuke

ZHAO Yuhao

YANG Tianqi

Contract Researcher: OSHIMA Masaharu

AKADA Keishi

YAMAZOE Kosuke

YAMAGAMI Kohei (~2020.2)

OHDaira Takeshi

EL Moussaoui Souliman

ZHANG Wenxiong

KURAHASHI Naoya (2019.11~)

No	Title	Authors	Journal	Vol.	Page	Year
1	Ellipsometer Equipped with Multiple Mirrors for Element-selective Soft X-ray Experiments	Mihoko Araki, Junji Meikaku, Yuya Kubota, Jun Miyawaki, Yuka Kosegawa, Souliman El Moussaoui, Thomas Bouillaud, Paul Manset, Shigeki Owada, Kensuke Tono, Makina Yabashi, Iwao Matsuda	e-J. Surf. Sci. Nanotechnol.	18	231-234	2020
2	Electronic structure of a (3x3)-ordered silicon layer on Al(111)	Yusuke Sato, Yuki Fukaya, Mathis Cameau, Asish Kumar Kundu, Daisuke Shiga, Ryu Yukawa, Koji Horiba, Chin-Hsuan Chen, Angus Huang, Horng-Tay Jeng, Taisuke Ozaki, Hiroshi Kumigashira, Masahito Niibe, and Iwao Matsuda	Phys. Rev. Materials	4	064005	2020
3	Electronic-structure analyses for electrode materials of rechargeable batteries using soft X-ray absorption/emission spectroscopy	Daisuke Asakura, Eiji Hosono, Jun Miyawaki and Yoshihisa Harada	J. JSSRR	33	213-221	2020
4	The Atomistic-Level Description of GaN/Water Interface by a Combined Spectroscopic and First-Principles Computational Approach	M. Sato, Y. Imazeki, T. Takeda, M. Kobayashi, S. Yamamoto, I. Matsuda, J. Yoshinobu, Y. Nakano, M. Sugiyama	J. Phys. Chem. C	124	12466-12475	2020
5	Topological Dirac nodal loops in nonsymmorphic hydrogenated monolayer boron	N. T. Cuong, I. Tateishi, M. Cameau, M. Niibe, N. Umezawa, B. Slater, K. Yubuta, T. Kondo, M. Ogata, S. Okada, and I. Matsuda	Phys. Rev. B	101	195412 (1-11)	2020
6	Multiorbital bond formation for stable oxygenredox reaction in battery electrodes	Takaaki Sudayama, Kazuki Uehara, Takahiro Mukai, Daisuke Asakura, Xiang-Mei Shi, Akihisa Tsuchimoto, Benoit Mortemard de Boisse, Tatau Shimada, Eriko Watanabe, Yoshihisa Harada, Masanobu Nakayama, Masashi Okubo and Atsuo Yamada	Energy Environ. Sci.	13	1492-1500	2020
7	Element-selective tracking ultrafast demagnetization process in Co/Pt multilayer thin films by the resonant magneto-optical Kerr effect	Kohei Yamamoto, Souliman El Moussaoui, Yasuyuki Hirata, Susumu Yamamoto, Yuya Kubota, Shigeki Owada, Makina Yabashi, Takeshi Seki, Koki Takanashi, Iwao Matsuda, Hiroki Wadati	Appl. Phys. Lett.	116	172406 (1-5)	2020
8	ポストグラフェン材料の創製と用途開発最前線	松田巖 他	エヌ・ディー・エス		(448 pages)	2020
9	Surface-state Coulomb repulsion accelerates a metal-insulator transition in topological semimetal nanofilms	S. Ito, M. Arita, J. Haruyama, B. Feng, W.-C. Chen, H. Namatame, M. Taniguchi, C.-M. Cheng, G. Bian, S.-J. Tang, T.-C. Chiang, O. Sugino, F. Komori, I. Matsuda	Science Advances	6	5015 (1-7)	2020
10	Two-dimensional conducting layer on SrTiO ₃ surface induced by hydrogenation	Y. Takeuchi, R. Hobar, R. Akiyama, A. Takayama, S. Ichinokura, R. Yukawa, I. Matsuda and S. Hasegawa	Phys. Rev. B	101	085422 (1-6)	2020
11	Photoemission and dynamical mean field theory study of electronic correlations in a t_{2g}^5 metal SrRhO ₃ thin film	Yujun Zhang, Minjae Kim, Jernej Mravlje, Changhee Sohn, Yongseong Choi, Joerg Stempfer, Yasushi Hotta, Akira Yasui, John Nichols, Ho Nyung Lee, Hiroki Wadati	Phys. Rev. B	101	085134 (1-9)	2020
12	Geometrical Frustration of B-H Bonds in Layered Hydrogen Borides Accessible by Soft Chemistry	Satoshi Tominaka, Ryota Ishibiki, Asahi Fujino, Kohsaku Kawakami, Koji Ohara, Takuya Masuda, Iwao Matsuda, Hideo Hosono, Takahiro Kondo	Chem	6	406-418	2020
13	Direct observation of the electronic states of photoexcited hematite with ultrafast 2p3d X-ray absorption spectroscopy and resonant inelastic X-ray scattering	Ahmed S. M. Ismail, Yohei Uemura, Sang Han Park, Soonnam Kwon, Minseok Kim, Hebetalla Elnaggar, Federica Frati, Yasuhiro Niwa, Hiroki Wadati, Yasuyuki Hirata, Yujun Zhang, Kohei Yamagami, Susumu Yamamoto, Iwao Matsuda, Ufuk Halisdemir, Gertjan Koster, Bert M. Weckhuysen, Frank M. F. de Groot	Phys. Chem. Chem. Phys.	22	2685-2692	2020
14	A computational examination of the electric-field-induced proton transfer along the interface hydrogen bond between proton donating and accepting self-assembled monolayers	Yusuke Kanematsu, Hiroyuki S Kato, Shinya Yoshimoto, Akira Ueda, Susumu Yamamoto, Hatsumi Mori, Jun Yoshinobu, Iwao Matsuda, Masanori Tachikawa	Chemical Physics Letters	741	137091 (1-4)	2020
15	Symmetry-breaking and spin-blockage effects on carrier dynamics in single-layer tungsten diselenide	Ro-Ya Liu, Meng-Kai Lin, Peng Chen, Takeshi Suzuki, Philippa Clark, Nathan Lewis, Cephise Cacho, Emma Springate, Chia-Seng Chang, Kozo Okazaki, Wendy Flavell, Iwao Matsuda, Tai-Chang Chiang	Phys. Rev. B	100	214309	2019
16	Ultrafast demagnetization of Pt magnetic moment in L1 ₀ -FePt probed by magnetic circular dichroism at a hard x-ray free electron laser	Kohei Yamamoto, Yuya Kubota, Motohiro Suzuki, Yasuyuki Hirata, Karel Carva, Marco Berritta, Kou Takubo, Yohei Uemura, Ryo Fukaya, Kenta Tanaka, Wataru Nishimura, Takuo Ohkochi, Tetsuo Katayama, Tadashi Togashi, Kenji Tamasaku, Makina Yabashi, Yoshihito Tanaka, Takeshi Seki, Koki Takanashi, Peter M. Oppeneer, Hiroki Wadati	New J. Phys.	21	123010	2019
17	SACLAによる軟X線非線形光学現象の開拓 *ジャーナル表紙	山本真吾、松田巖	放射光	32	307 (7 pages)	2019

18	Operando soft X-ray emission spectroscopy of the Fe ₂ O ₃ anode to observe the conversion reaction	Daisuke Asakura, Yusuke Nanba, Masashi Okubo, Hideharu Niwa, Hisao Kiuchi, Jun Miyawaki, Masaharu Oshima, Eiji Hosono and Yoshihisa Harada	Phys. Chem. Chem. Phys.	21	26351-26357	2019
19	Intrinsic 2D Ferromagnetism in V ₅ Se ₈ Epitaxial Thin Films	Masaki Nakano, Yue Wang, Satoshi Yoshida, Hideki Matsuoka, Yuki Majima, Keisuke Ikeda, Yasuyuki Hirata, Yukiharu Takeda, Hiroki Wadati, Yoshimitsu Kohama, Yuta Ohigashi, Masato Sakano, Kyoko Ishizaka, Yoshihiro Iwasa	ACS Nano Lett.	19	8806-8810	2019
20	時間分解軟X線光電子分光による電子状態の動的観察	松田巖	応用物理	88	716-719	2019
21	Surface Chemistry of Carbon Dioxide on Copper Model Catalysts Studied by Ambient-Pressure X-ray Photoelectron Spectroscopy	Takanori Koitaya, Susumu Yamamoto, Iwao Matsuda, Jun Yoshinobu	e-J. Surf. Sci. Nanotechnol.	17	169-178	2019
22	Photoinduced hydrogen release from hydrogen boride sheets	Reiya Kawamura, Nguyen Thanh Cuong, Takeshi Fujita, Ryota Ishibiki, Toru Hirabayashi, Akira Yamaguchi, Iwao Matsuda, Susumu Okada, Takahiro Kondo and Masahiro Miyauchi	Nature Commun.	10	4880	2019
23	Nature of Carrier Doping in T'-La _{1.8-x} Eu _{0.2} Sr _x CuO ₄ Studied by X-Ray Photoemission and Absorption Spectroscopy	Chun Lin, Masafumi Horio, Takayuki Kawamata, Shin Saito, Keisuke Koshiishi, Shoya Sakamoto, Yujun Zhang, Kohei Yamamoto, Keisuke Ikeda, Yasuyuki Hirata, Kou Takubo, Hiroki Wadati, Akira Yasui, Yasumasa Takagi, Eiji Ikenaga, Tadashi Adachi, Yoji Koike, Atsushi Fujimori	J. Phys. Soc. Japan	88	115004 (1-2)	2019
24	Ultrafast unbalanced electron distributions in quasicrystalline 30° twisted bilayer graphene	Takeshi Suzuki, Takushi Iimori, Sung Joon Ahn, Yuhao Zhao, Mari Watanabe, Jiadi Xu, Masami Fujisawa, Teruto Kanai, Nobuhisa Ishii, Jiro Itatani, Kento Suwa, Hirokazu Fukidome, Satoru Tanaka, Joung Real Ahn, Kozo Okazaki, Shik Shin, Fumio Komori, Iwao Matsuda	ACS Nano	13	11981-11987	2019
25	Elucidation of Structure–Activity Correlations in a Nickel Manganese Oxide Oxygen Evolution Reaction Catalyst by Operando Ni L-Edge X-ray Absorption Spectroscopy and 2p3d Resonant Inelastic X-ray Scattering	Mustafa Al Samarai, Anselm W. Hahn, Abbas Beheshti Askari, Yi-Tao Cui, Kosuke Yamazoe, Jun Miyawaki, Yoshihisa Harada, Olaf Rüdiger, Serena DeBeer	ACS Appl. Mater. Interfaces	11	38595-38605	2019
26	Reversible low-temperature redox activity and selective oxidation catalysis derived from concerted activation of multiple metal species on Cr and Rh-incorporated ceria catalysts	S. Ikemoto, X. Huang, S. Muratsugu, S. Nagase, T. Koitaya, H. Matsui, G. Yokota, T. Sudoh, A. Hashimoto, Y. Tan, S. Yamamoto, J. Tang, I. Matsuda, J. Yoshinobu, T. Yokoyama, S. Kusaya, R. Matsuda, and M. Tada	Phys. Chem. Chem. Phys.	21	20868-20877	2019
27	Photoinduced valence dynamics in EuNi ₂ (Si _{0.21} Ge _{0.79}) ₂ studied via time-resolved x-ray Absorption spectroscopy	Y. Yokoyama, K. Kawakami, Y. Hirata, K. Takubo, K. Yamamoto, K. Abe, A. Mitsuda, H. Wada, T. Uozumi, S. Yamamoto, I. Matsuda, S. Kimura, K. Mimura, H. Wadati	Phys. Rev. B	100	115123 (1-6)	2019
28	A Surface Science Approach to Unveiling TiO ₂ Photocatalytic Mechanism: Correlation between Photocatalytic Activity and Carrier Lifetime	K. Ozawa, S. Yamamoto, K. Mase, I. Matsuda	e-J. Surf. Sci. Nanotechnol.	17	130-147	2019
29	偏光変調型軟X線を用いた複素誘電率の直接測定	久保田雄也、平田靖透、赤井久純、松田巖	日本物理学会誌	74	646	2019
30	Microscopic photoelectron analysis of single crystalline LiCoO ₂ particles during the charge-discharge in an all solid-state lithium ion battery	Keishi Akada, Takaaki Sudayama, Daisuke Asakura, Hirokazu Kitaura, Naoka Nagamura, Koji Horiba, Masaharu Oshima, Eiji Hosono & Yoshihisa Harada	Scientific Reports (nature research)	9	12452 (1-7)	2019
31	Do X-ray spectroscopies provide evidence for continuous distribution models of water at ambient conditions?	Lars G. M. Pettersson, Yoshihisa Harada, and Anders Nilsson	Proc. Nat. Acad. Sci. USA (LETTER)	116	17156-17157	2019
32	Mn 2p resonant X-ray emission clarifies the redox reaction and charge-transfer effects in LiMn ₂ O ₄	Daisuke Asakura, Yusuke Nanba, Eiji Hosono, Masashi Okubo, Hideharu Niwa, Hisao Kikuchi, Jun Miyawaki, Yoshihisa Harada	Phys. Chem. Chem. Phys.	21	18363-18369	2019
33	Modulation of Electronic States near Electrodes in Graphene Transistors Observed by Operando Photoelectron Nanospectroscopy	Hirokazu Fukidome, Kazutoshi Funakubo, Naoka Nagamura, Koji Horiba, Yasunori Tateno, Masaharu Oshima, Maki Suemitsu	Sensors and Materials	31	2303-2311	2019
34	High pressure synthesis of a quasi-one-dimensional GdFeO ₃ -type perovskite PrCuO ₃ with nearly divalent Cu ions	Masaharu Ito, Hidefumi Takahashi, Hideaki Sakai, Hajime Sagayama, Yuichi Yamasaki, Yuichi Yokoyama, Hiroyuki Setoyama, Hiroki Wadati, Kanako Takahashi, Yoshihiro Kusano and Shintaro Ishiwata	Chem. Commun. (Communication)	55	8931-8934	2019
35	Polarization control with an X-ray phase retarder for high-time-resolution pump–probe experiments at SACLA	Y. Kubota, M. Suzuki, T. Katayama, K. Yamamoto, K. Tono, Y. Inubushi, T. Seki, K. Takanashi, H. Wadati and M. Yabashi	J. Synch. Rad.	26	1139-1143	2019
36	Spectrum adapted the expectation-maximization algorithm for high-throughput peak shift analysis	Tarojiro Matsumura, Naoka Nagamura, Shotaro Akaho, Kenji Nagata & Yasunobu Ando	Sci. Technol. Adv. Mater.	20	733-745	2019

37	Magnetic and electronic properties of <i>B</i> -site-ordered double-perovskite oxide La ₂ CrMnO ₆ thin films	K.Yoshimatsu, J.Ishimaru, K.Yamamoto, Y.Hirata, H.Wadati, Y.Takeda, K.Horiba, H.Kumigashira, O.Sakata, A.Ohtomo	Phys. Rev. B	99	235129 (1-8)	2019
38	Influence of interface dipole layers on the performance of graphene field effect transistors	Naoka Nagamura, Hirokazu Fukidome, Kosuke Nagashio, Koji Horiba, Takayuki Ide, Kazutoshi Funakubo, Keiichiro Tashima, Akira Toriumi, Maki Suemitsu, Karstern Horn, Masaharu Oshima	Carbon	152	680-687	2019
39	時間分解X線磁気円二色性で見るスピンドYNAMIX	山本航平、和達大樹	まぐね	14	140-145	2019
40	Measurements of ultrafast dissociation in resonant inelastic x-ray scattering of water	Kosuke Yamazoe, Jun Miyawaki, Hideharu Niwa, Anders Nilsson, Yoshihisa Harada	J. Chem. Phys.	150	204201 (1-7)	2019
41	Superstructure-induced splitting of Dirac cones in silicene	B. Feng, H. Zhou, Y. Feng, H. Liu, S. He, I. Matsuda, L. Chen, E. F. Schwier, K. Shimada, S. Meng, and K. Wu	Phys. Rev. Lett.	122	196801 (1-6)	2019
42	Segmented Undulator for Extensive Polarization Controls in ≤ 1 nm-rad Emittance Rings	I. Matsuda, S. Yamamoto, J. Miyawaki, T. Abukawa, and T. Tanaka	e-J. Surf. Sci. Nanotechnol.	17	41-48	2019
43	Direct Evidence of Interfacial Hydrogen Bonding in Proton-Electron Concerted 2D Organic Bilayer on Au Substrate	Susumu Yamamoto, Hiroyuki S Kato, Akira Ueda, Shinya Yoshimoto, Yasuyuki Hirata, Jun Miyawaki, Kohei Yamamoto, Yoshihisa Harada, Hiroki Wadati, Hatsumi Mori, Jun Yoshinobu, Iwao Matsuda	e-J. Surf. Sci. Nanotechnol.	17	49-55	2019
44	Electronic structure of a monatomic Cu ₂ Si layer on a Si substrate	M. Cameau, R. Yukawa, S. Ito, R. Ishibiki, K. Horiba, Y. Obata, T. Kondo, H. Kumigashira, M. D'angelo, and I. Matsuda	Phys. Rev. Materials	3	44004 (1-5)	2019
45	CO ₂ Activation and Reaction on Zn-Deposited Cu Surfaces Studied by Ambient-Pressure X-ray Photoelectron Spectroscopy	T.Koitaya, S.Yamamoto, Y.Shiozawa, Y.Toshikura, M.Hasegawa, J.Tang, K.Takeuchi, K.Mukai, S.Yoshimoto, I.Matsuda, J.Yoshinobu	ACS Catalysis	9	4539-4550	2019
46	Half-metallicity of Mn ₂ VAl ferrimagnet revealed by resonant inelastic soft x-ray scattering in a magnetic field	R.Y. Umetsu, H. Fujiwara, K. Nagai, Y. Nakatani, M. Kawada, A. Sekiyama, F. Kuroda, H. Fujii, T. Oguchi, Y. Harada, J. Miyawaki, and S. Suga	Phys. Rev. B	99	134414 (1-10)	2019
47	<i>Operando</i> measurement of single crystalline Li ₄ Ti ₅ O ₁₂ with octahedral-like morphology by microscopic X-ray photoelectron spectroscopy	Keishi Akada, Takaaki Sudayama, Daisuke Asakura, Hirokazu Kitaura, Naoka Nagamura, Koji Horiba, Masaharu Oshima, Eiji Hosono, and Yoshihisa Harada	J. Electron Spectrosc. Relat. Phenom.	233	64-68	2019
48	Semimetallicity of free-standing hydrogenated monolayer boron from MgB ₂	I. Tateishi, N. T. Cuong, C. A. S. Moura, M. Cameau, R. Ishibiki, A. Fujino, S. Okada, A. Yamamoto, M. Araki, S. Ito, S. Yamamoto, M. Niibe, T. Tokushima, D. E. Weibel, T. Kondo, M. Ogata, and I. Matsuda	Phys. Rev. Materials	3	024004 (1-8)	2019
49	Mass transport in the PdCu phase structures during hydrogen adsorption and absorption studied by XPS under hydrogen atmosphere	Jiayi Tang, Susumu Yamamoto, Takanori Koitaya, Akitaka Yoshigoe, Takuma Tokunaga, Kozo Mukai, Iwao Matsuda, Jun Yoshinobu	Appl. Surf. Sci.	480	419-426	2019
50	Enhanced Photoresponsivity of Fullerene in the Presence of Phthalocyanine: A Time-Resolved X-ray Photoelectron Spectroscopy Study of Phthalocyanine/C ₆₀ /TiO ₂ (110)	Kenichi Ozawa, Susumu Yamamoto, Marie D'angelo, Yuto Natsui, Naoya Terashima, Kazuhiko Ma, and Iwao Matsuda	J. Phys. Chem. C	123	4388-4395	2019
51	Hydrogen adsorption and absorption on a Pd-Ag alloy surface studied using in-situ X-ray photoelectron spectroscopy under ultrahigh vacuum and ambient pressure	J. Tang, S. Yamamoto, T. Koitaya, Y. Yoshikura, K. Mukai, S. Yoshimoto, I. Matsuda, J. Yoshinobu	Appl. Surf. Sci.	463	1161-1167	2019
52	Site-sensitive X-ray photoelectron spectroscopy of Fe ₃ O ₄ by photoelectron diffraction	Yusuke Hashimoto Munetaka Taguchi Shun Fukami Hiroki Momono Tomohiro Matsushita Hiroyuki Matsuda Fumihiko Matsui Hiroshi Daimon	Surface and Interface Analysis	51	115-119	2019
53	Monatomic Two-Dimensional Layers: Modern Experimental Approaches for Structure, Properties, and Industrial Use	Iwao Matsuda ed.	Elsevier		(232 pages)	2019

E-labo. Paper 2019

No.	Title	Authors	Journal	Vol.	Page	Year
1	Multiple topological states in iron-based superconductors	Peng Zhang, Zhijun Wang, Xianxin Wu, Koichiro Yaji, Yukiaki Ishida, Yoshimitsu Kohama, Guangyang Dai, Yue Sun, Cedric Bareille, Kenta Kuroda, Takeshi Kondo, Kozo Okazaki, Koichi Kindo, Xiancheng Wang, Changqing Jin, Jiangping Hu, Ronny Thomale, Kazuki Sumida, Shilong Wu, Koji Miyamoto, Taichi Okuda, Hong Ding, G. D. Gu, Tsuyoshi Tamegai, Takuto Kawakami, Masatoshi Sato & Shik Shin	Nature Physics	15	41	2019

2	A weak topological insulator state in quasi-one-dimensional bismuth iodide	Ryo Noguchi, T. Takahashi, K. Kuroda, M. Ochi, T. Shirasawa, M. Sakano, C. Bareille, M. Nakayama, M. D. Watson, K. Yaji, A. Harasawa, H. Iwasawa, P. Dudin, T. K. Kim, M. Hoesch, V. Kandyba, A. Giampietri, A. Barinov, S. Shin, R. Arita, T. Sasagawa & Takeshi Kondo	Nature	566	518	2019
3	Coexistence of Two Types of Spin Splitting Originating from Different Symmetries	Koichiro Yaji, Anton Visikovskiy, Takushi Iimori, Kenta Kuroda, Singo Hayashi, Takashi Kajiwara, Satoru Tanaka, Fumio Komori, and Shik Shin	Phys. Rev.Lett.	122	126403	2019
4	Giant Rashba system on a semiconductor substrate with tunable Fermi level: Bi/GaSb(110)-(2×1)	Takuto Nakamura, Yoshiyuki Ohtsubo, Naoki Tokumasu, Patrick Le Fèvre, François Bertran, Shin-ichiro Ideta, Kiyohisa Tanaka, Kenta Kuroda, Koichiro Yaji, Ayumi Harasawa, Shik Shin, Fumio Komori, and Shin-ichi Kimura	Phys. Rev. Materials	3	126001	2019
5	Unified description of the electronic structure of M ₂ AC nanolamellar carbides	Damir Pinek, Takahiro Ito, Masashi Ikemoto, Koichiro Yaji, Masashi Nakatake, Shik Shin, and Thierry Ouisse	Phys. Rev. B	100	75144	2019